LATE-STAGE PROPAGATION OF THE GRENVILLE OROGEN: THERMOBAROMETRY AND TIMES OF PEAK METAMORPHISM FROM SUDBURY METADIABASE, GEORGIAN BAY, ONTARIO

by

Glenn G. Chapman

Submitted in partial fulfilment of the requirements
for the degree of Master of Science

at

Dalhousie University
Halifax, Nova Scotia
March 2017

What are men to rocks and mountains? Oh! what hours of transport we shall spend! And when we do return, it shall not be like other travellers, without being able to give one accurate idea of any thing. We will know where we have gone – we will recollect what we have seen.

Jane Austen

TABLE OF CONTENTS

LIST OF TABLES

LIST OF FIGURES

Chapter One

Chapter Two

Chapter Three

Chapter Four

Chapter Five

Chapter Six

ABSTRACT

Did the final (Rigolet) phase of the Grenvillian Orogeny result from renewed convergence or post-convergent ductile flow? This question remains unresolved in part because of limited data on the timing of late Grenvillian tectonism in the parautochthonous Britt Domain (BD) in central Ontario, which occupies the critical region between the Grenville Front and the orogenic core. This thesis presents P-T-t data from Sudbury metadiabase (SmD), part of a ca. 1235 Ma dyke swarm that intruded Laurentian crust after pre-Grenvillian tectonism, and records exclusively Grenvillian (< 1100 Ma) metamorphism.

Samples were collected along a 40 km transect representing the southern, central, and northern BD along Georgian Bay. All samples preserve relict igneous textures overprinted by granulite-facies corona assemblages including garnet + clinopyroxene ± orthopyroxene ± pargasite. Thermobarometry on equilibrated subdomains yielded T-P estimates of 785 °C and 15 kbar, 763 °C and 13.1 kbar, and 718 °C and 13.4 kbar for rocks from HA Gray Island in the southern BD, Byng Inlet in the central BD and Key Harbour in the northern BD, respectively. U-Pb geochronology of metamorphic zircon yielded weighted mean $^{206}Pb/^{238}U$ ages of 1033 ± 12 Ma, 1020 ± 8.7 Ma and 1011 ± 11 Ma for the southern, central, and northern BD samples, respectively.

Metamorphic ages from the southern and central BD (ca. 1033 and 1020 Ma) overlap with previously reported ages of syn-kinematic pegmatite dykes in the Shawanaga Shear Zone (ca. 1042-1019 Ma), which record normal-sense ductile reactivation of the Allochthon Boundary Thrust. The northern BD age (ca. 1011 Ma) is similar to other metamorphic ages from the Grenville Front Tectonic Zone (ca. 1010-980 Ma). These new ages are interpreted to reflect ca. 2 mm/y propagation of Grenvillian metamorphism and deformation from SE to NW across the parautochthon, compatible with model predictions for post-convergent ductile flow.

List of Abbreviations Used

α-Qtz	alpha quartz
Ab	albite
ABT	Allochthon Boundary Thrust
Alm	almandine
Amp	amphibole
Ann	annite
An	anorthite
Ap	apatite
BD	Britt Domain
Bdy	baddeleyite
Bt	biotite
CGB	Central Gneiss Belt
CMB	Central Metasedimentary Belt
Cpx	clinopyroxene
Di	diopside
EBC	effective bulk composition
EMP	Electron Microprobe
En	enstatite
Fe-prg	ferropargasite
Fs	ferrosilite
ΔG	change in Gibbs free energy
GB	Georgian Bay
GD	Grenville Diabase
GF	Grenville Front
GFTZ	Grenville Front Tectonic Zone
Grt	garnet
Grs	grossular
Hc	hercynite
Hd	hedenbergite

Hbl	hornblende
Ilm	ilmenite
K_D	distribution coefficient
KH	Key Harbour
LA-ICP-MS	Laser Ablation-Inductively Coupled Plasma-Mass Spectrometry
Mag	magnetite
Mnz	monazite
ND	Nipissing diabase
NISZ	Nares Inlet Shear Zone
Oam	orthoamphibole
Olg	oligoclase
Opx	orthopyroxene
P-T	Pressure-Temperature
P-T-t	Pressure-Temperature-time
PaB	Point au Baril
PB	Parautochthonous Belt
Phl	phlogopite
Prg	pargasite
Pyr	pyrope
Px	pyroxene
Qtz	quartz
REE	Rare Earth Elements
SD	Sudbury diabase
SIMS	Secondary Ion Mass Spectrometry
SmD	Sudbury metadiabase
Sp	spinel
Srp	serpentine
SSZ	Shawanaga Shear Zone
T-D	Theriak-Domino
TIMS	Thermal Ionization Mass Spectrometry
T-W	Tera-Wasserburg

Wo	wollastonite
X	Chemical composition
Zrn	zircon

ACKNOWLEDGEMENTS

First and foremost, I would like to thank Dr. Rebecca A. Jamieson for the opportunity to contribute, in some small way, to the legacy of Grenvillian research at Dalhousie University. Your singular patience, generosity, and support have enabled me to coax a rather compelling story out of a challenging set of pretty black rocks.

This study could not have been possible without the guidance and support of committee members Dr. Nicholas Culshaw and Dr. Jeffrey Marsh, field assistance by Jillian Kendrick, and technical assistance by laboratory technicians Dan MacDonald and Gordon Brown. Deep gratitude is also due to Dr. Chris McFarlane and Brandon Boucher at the LA-ICP-MS facility at UNB, who took a chance on some challenging material and contributed immeasurably to the resolution of this thesis.

I could not have carried through without the community of graduate and undergraduate students serving time in the LSC, the endless discussions and commiserations with my officemate and fellow Grenvillian, Samantha Van De Kerckhove, and, finally, Dr. Catherine Mottram for comments and suggestions, and bearing so many “important questions”.

Chapter 1: Introduction

1.1 Grenvillian Orogeny in Ontario

1.1.1 Overview

The Grenville Province in central Ontario offers spectacular access to the exposed mid-crust of a Himalayan-scale Mesoproterozoic collisional orogen that formed during the assembly of the supercontinent Rodinia (Condie, 2001; Gower et al., 2002; Tollo et al., 2004). In the Canadian Shield, the Grenville Province underlies a 2000 km long and several hundred kilometers wide NE-SW oriented belt extending from the Atlantic coast of Labrador to Georgian Bay on Lake Huron (Fig. 1.1) The Grenville Province is bounded to the NW by the Grenville Front (GF), a moderately-to-steeply dipping crustal-scale shear zone marking the farthest extent of Grenvillian deformation and metamorphism in the Laurentian craton. The SE half of the orogen, identified as Amazonia in most reconstructions (Hoffman, 1991; Tohver et al., 2006), was lost during the Neoproterozoic rifting that created the Iapetus ocean

The Laurentian margin was the locus of voluminous Paleo-to Mesoproterozoic arc and back-arc magmatism as an active continental margin from ca. 1900-1400 Ma (Slagstad et al, 2004; Davidson, 2008; Gower et al, 2008). Widespread high-grade metamorphism during the Pinwarian Orogeny (Krogh et al., 1996) affected the margin between ca. 1520- 1450 Ma (Ketchum et al., 1994; van Breemen and Corriveau, 2005). The Grenvillian Orogeny, *sensu lato*, comprises accretionary and collisional events along the Laurentian margin between ca. 1290 - 980 Ma (Rivers, 1997; Rivers and Corrigan,

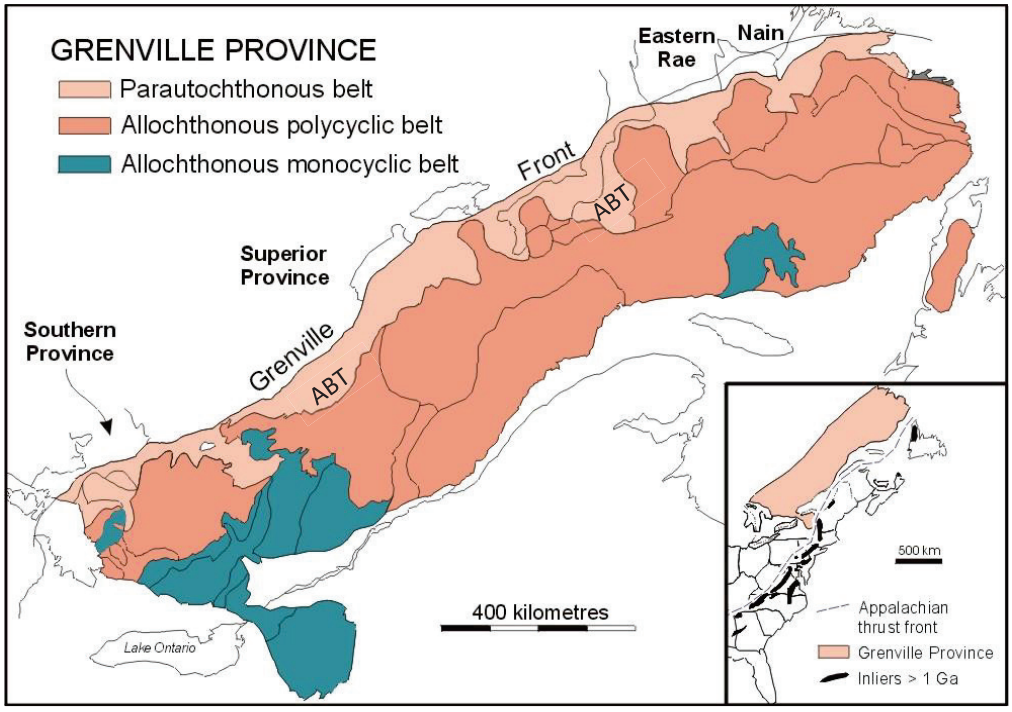

Figure 1.1 The Grenville Province and Appalachian inliers (inset) with first-order tectonic subdivisions and structures (ABT, Allochthon Boundary Thrust) after Rivers et al. (1989) modified from Carr et al. (2000).

2000; Carr et al., 2000; Rivers et al., 2012). Early events, at ca. 1290-1230 Ma and ca. 1190-1120 Ma, are called the Elzevirian and Shawinigan phases (Moore and Thompson, 1980; Rivers, 1997). The former is preserved primarily in the Composite Arc Belt and Frontenac belt in the southwest and represents formation and amalgamation of offshore arcs. The latter, preserved in the central and southwestern Grenville Province, represents the accretion of arc terranes to the Laurentian margin (Rivers, 1997, Carr et al., 2000). The Grenvillian Orogeny (sensu stricto; Rivers, 2012) refers to orogen-wide medium- and high-grade metamorphism and deformation in the orogenic core between ca. 1090-1020 Ma (Ottawan phase), followed by late-stage NW-directed propagation of the orogen into Laurentia until ca. 980 Ma (Rigolet phase).

The multiple phases of superimposed Grenvillian- and pre-Grenvillian orogenesis produced corresponding polyphase metamorphism and deformation across the southeast margin of Laurentia. In the resulting polycyclic rocks, the effects of Grenvillian metamorphism may be impossible to distinguish from those of earlier orogenic episodes. In contrast, monocyclic rocks that were affected only by the Grenvillian orogeny (sensu stricto), including rocks deposited on or intruded into the Laurentian margin after ca 1400 Ma, have the potential to record uniquely Grenvillian metamorphism and deformation. This thesis is primarily concerned with determining the relationship between the Ottawan and Rigolet phases of the Grenvillian orogeny, using the monocyclic Sudbury metadiabase dykes (ca. 1235 Ma; Krogh et al, 1987; Dudàs et al., 1994) to monitor the times and P-T conditions of late Grenvillian metamorphism along the NW flank of the orogen.

1.2 Regional Geology

1.2.1 Terminology

First-order subdivision of the Grenville Province was attempted by Wynne-Edwards (1972), who recognized the Grenville Front Tectonic Zone (GFTZ) along the northwest flank of the orogen (Fig. 1.2), the Central Gneiss Belt (CGB), and the Central Metasedimentary Belt (CMB) to the southeast. Rivers et al. (1989) refined this, recognizing orogen-scale units, the Parautochthonous Belt, the Allochthonous Polycyclic Belt, and the Allochthonous Monocyclic Belt (Fig. 1.1, 1.2), bounded by first-order structures, the GF, the Allochthon Boundary Thrust (ABT), and the Monocyclic Belt Boundary Zone. The Shawanaga Shear Zone (SSZ) (Fig. 1.2) is the local expression of the ABT. The Parautochthonous Belt in the northwest consists of reworked gneisses

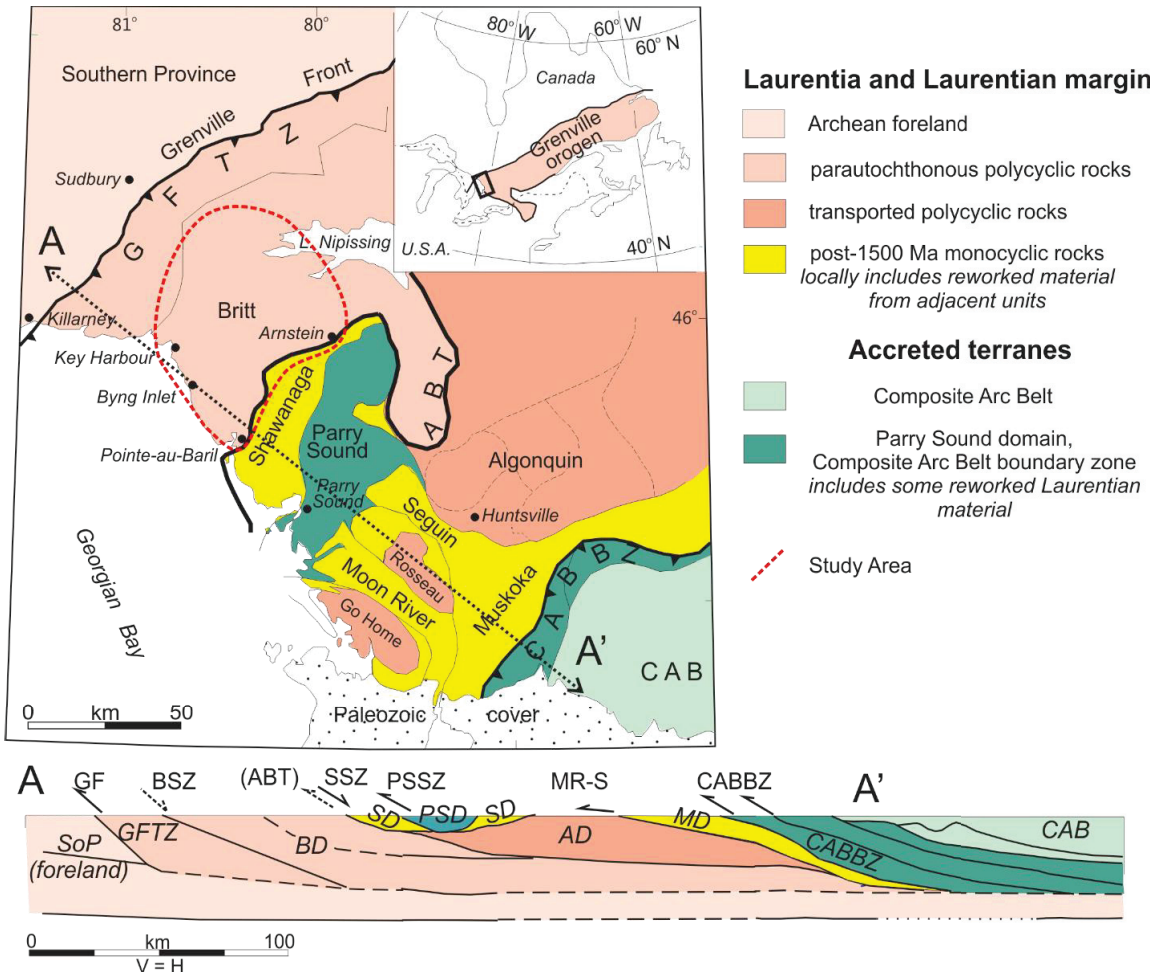

Figure 1.2 Simplified regional geology map of the western Grenville Orogen in Ontario (modified from Jamieson et al., 2007, after Culshaw et al., 1997; Ketchum and Davidson, 2000) showing the study area (dashed red line) with a crustal-scale cross section constructed from geological and seismic data by Culshaw et al. (1997), with modifications after White et al. (2000). Lithotectonic domains (e.g., Britt, Shawanaga) as defined by Culshaw et al. (1997); Allochthon Boundary Thrust (ABT) as defined by Ketchum & Davidson (2000).

unambiguously correlated with the Laurentian foreland, and interpreted to have been affected by relatively limited NW-directed transport. The Allochthonous Polycyclic Belt preserves pre-Grenvillian tectonism, but, while it contains rocks of similar age and type to the foreland and Parautochthonous Belt, neither specific rock units nor structures can be traced continuously from one to the other, implying more substantial tectonic transport. The Allochthonous Monocyclic Belt consists of transported (or far-travelled) supracrustal

and plutonic rocks affected only by the Grenvillian orogeny. Here, the term "allochthonous" does not imply exotic provenance (cf. “terrane”), as many of these units are interpreted to have formed on the distal margin of Laurentia or as peri-Laurentian arcs that were accreted and subsequently transported hundreds of kilometers toward the foreland. Carr et al. (2000) further refined the terminology in terms of provenance, referring to Laurentia (foreland and parautochthon), Laurentian margin (allochthonous belts), and Composite Arc belts. In addition, Culshaw et al. (1997) defined a number of mappable gneiss associations and lithotectonic domains along the shores of Georgian Bay. For purposes of this thesis, the original, largely non-genetic, terminology of Wynne-Edwards (1972) is preferred, along with the lithotectonic domains defined by Culshaw et al. (1997).

1.2.2 Southern Province

In the study area, the Southern Province (Fig. 1.2), comprising the Paleoproterozoic Huronian Supergroup and plutons of two distinct ages, including the Killarney complex (ca. 1740 Ma) and the Bell Lake, Ann Lake, and Chief Lake granites (ca. 1.47 Ga) (van Breemen and Davidson, 1988; Davidson and van Breemen, 1994) underlies the Grenville foreland. The Huronian supracrustal rocks and sills of Nipissing gabbro (ca. 2220 Ma, Corfu and Andrews, 1986) were folded and metamorphosed to greenschist facies during the Penokean Orogeny (1.9 – 1.83 Ga; van Schmus, 1980). Northwest of the study area, SE-striking dykes of the ca. 1235 Ma (Krogh et al, 1987; Dudàs et al., 1994) Sudbury swarm cut all lithologies of the Southern Province. South of the GF, the Sudbury dykes are highly disrupted, strongly folded, and progressively metamorphosed (Bethune and Davidson, 1988, 1997; Bethune 1989, 1997).

1.2.3 Grenville Front Tectonic Zone

The Grenville Front Tectonic Zone (GFTZ) (Fig. 1.2) is a steeply to moderately SE-dipping crustal-scale thrust-sense shear zone that that reworked portions of Laurentian crust along a continuous, narrow belt from Labrador to Georgian Bay between ca 1010 – 990 Ma (Figs. 1.2). Grenvillian metamorphic conditions within the GFTZ range from greenschist facies near the GF to granulite facies (ca. 800 °C, ca 11 kbar) in the SE (Jamieson et al., 1995; Bethune and Davidson, 1997). In the study area the southeast margin of the GFTZ is marked by the Boundary Shear Zone, a band of moderately dipping straight gneiss that marks the transition from moderately dipping thrust-sense shearing in the GFTZ to shallow-to-sub-horizontal deformation fabrics in the Britt Domain (Jamieson et al.,1995). The Boundary Shear Zone also displays a component of oblique-normal-sense top to the SSE slip (Jamieson et al., 1995).

1.2.4 Central Gneiss Belt

The Ottawan phase of Grenvillian orogenesis (ca. 1090-1020 Ma) resulted in high-grade metamorphism and protracted lateral ductile flow of partially molten hot mid-lower crust in the thickened orogenic core (Culshaw et al. 1997; Ketchum and Davidson 2000; Jamieson et al. 2007). Deformation propagated northwestward into the Laurentian foreland along a series of crustal scale ductile shear zones (Fig. 1.2). Late-Ottawan phase, normal-sense SE-directed shearing on the SSZ, the local expression of the ABT, is constrained by igneous U-Pb ages of pre/early syn-kinematic, late syn-kinematic, and post-kinematic pegmatite dykes of ca. 1042 +4/-2, 1019 ± 4, and 988 ± 2 Ma, respectively (Corrigan, 1990; Corrigan et al., 1994; Ketchum, 1994; Culshaw et al., 1997; Ketchum et al., 1998; Jamieson et al. 2010; Rivers et al. 2012).

1.2.5 Sudbury (meta)diabase

The NW-SE striking ca. 1235 Ma (Krogh et al., 1987; Dudàs et al., 1994) Sudbury diabase (SD) dykes in the Southern and Superior Provinces are truncated by the GF, across which correlated segments are progressively folded, boudinaged, and metamorphosed (Bethune and Davidson, 1988, 1997; Bethune, 1989, 1993, 1997; Jamieson et al., 1995). The dykes are medium to-to-fine-grained and subophitic, with distinctive olivine-normative geochemistry enriched in Fe, K, Ba, Ti, P, Zr, and LREE, (Bethune and Davidson 1997; Ketchum and Davidson, 2000).

Bethune (1993) correlated deformed metadiabases located up to 45 km south of the GF with the pristine, undeformed SD dyke swarm in the Superior Province north of the GF. The dykes are characterized and correlated on the basis of their distinct geochemistry. Emplaced 200-150 Myr before the GFTZ and parautochthonous underwent Grenvillian tectonism, the SD dykes represents the youngest pre-orogenic lithological unit in the Parautochthonous Belt in the study area. As they record exclusively Grenvillian metamorphism and deformation, and are readily identifiable in outcrop, Sudbury metadiabases Dykes (SmD) are ideal targets for examining unambiguous monocyclic P-T-t histories in otherwise complex polycyclic gneissic domains.

1.3 Thesis Problem: What was the Rigolet Phase?

1.3.1 The Rigolet Phase

Although it is widely agreed that the Grenville Orogen was a Himalayan-scale convergent orogenic system involving accretion and eventual collision between Laurentia and an unknown continent (probably Amazonia) to the south, there is less agreement on

the geodynamic significance of the various phases of the Grenvillian Orogeny. In particular, the nature of the terminal Rigolet phase, and its relationship to the preceding Ottawan phase, remains elusive.

Rivers (1997) defined the late-stage Rigolet "pulse" (later, phase) as "... a third cycle (of contraction) nearer the foreland of the orogen that involved crustal thickening at ~1000 Ma followed by granitoid plutonism in the interval 990-960 Ma." The late event mainly affected rocks near the GF along the entire length of the orogen, including the GFTZ in Ontario. The GFTZ is a crustal-scale thrust-sense shear zone that reworked older (≥ ca. 1450 Ma) Laurentian rocks. Peak Grenvillian metamorphism across the GFTZ grades from local greenschist facies near the GF to granulite facies over 15 km, and was reached between ca. 1010 – 990 Ma (Haggart et al., 1993; Krogh, 1994). Following peak metamorphism, the GFTZ underwent rapid cooling until ca. 980 Ma, followed by slower cooling (Haggart et al., 1993). This was interpreted to represent rapid exhumation in the hangingwall of a crustal-scale shear zone. Short-lived thrusting and metamorphism within the GFTZ is interpreted to be the final stage of propagation into the Laurentian foreland.

What is the connection between ductile flow associated with convergence during the Ottawan phase and late thrusting within the GFTZ? If these were discrete, temporally separate events, why did late convergence only affect a narrow, cold, and relatively rigid region of the foreland and not hot, relatively ductile rocks nearer the core? If, on the other hand, the Ottawan and Rigolet phases are continuous, is the age gap used by Rivers (1997) to define the phases real, or only apparent? This study addresses the link between the Ottawan and Rigolet phases by focussing on the Grenvillian metamorphic history of a critical region, the parautochthonous Britt Domain, situated between the GFTZ and the allochthonous Shawanaga Domain. Except where indicated, use of the term "Rigolet

phase", here, refers to post-Ottawan phase late-stage propagation of the Grenville Orogeny including, though not limited to, thrusting and metamorphism within the GFTZ.

Two competing models types, one conceptual and the other numerical, have been developed in efforts to explain these observations.

1.3.2 Conceptual Models

Rivers (2008, 2009, 2012) presented a conceptual model that sought to accommodate a perceived hiatus in tectonic activity between ca 1020 – 1000 Ma. This hiatus, it was argued, marked a transition from Ottawan phase ductile flow consistent with large hot orogens in the orogenic core, to a form of critical-wedge mechanics, characteristic of relatively small and cold orogens, in the foreland. This model suggests that melt-weakened mid-crust became sub-critical for ductile flow following extension and cooling of the foreland-directed mid-crustal channel as a result of gravitational "collapse" of the orogenic plateau. Subsequent rapid burial and exhumation along thrust-sense shear zones in the GFTZ was explained by renewed convergence.

Conceptual models present a difficulty in validation, in that processes are posited to fit the available data. The conceptual model proposed by Rivers (2008, 2009, 2012) predicts cooling and exhumation of the parautochthon south of the GFTZ during extension and normal-sense reactivation of the SSZ, not prograde metamorphism associated with crustal thickening and heating. Subsequent post-Ottawan metamorphism is predicted to be isochronous, between ca 1000-980 Ma.

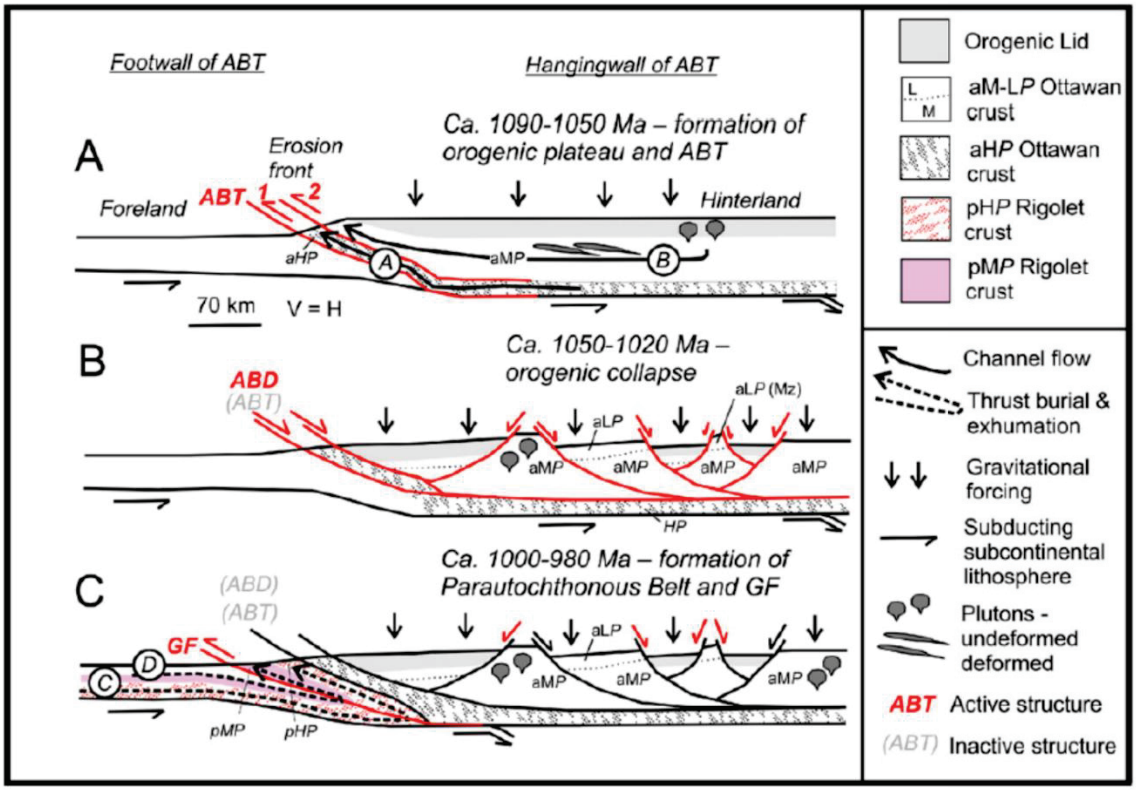

Figure 1.3. Conceptual model for Ottawan (1090-1020 Ma) and Rigolet (1000-980 Ma) phases of the Grenvillian orogeny (Rivers, 2008). In this case, the Rigolet phase represents renewed convergence that affected only the NW flank of the orogen, separated from main Ottawan phase by an episode of extension and crustal thinning (orogenic collapse, 1050-1020 Ma). According to this interpretation, the parautochthon south of the GFTZ should be undergoing cooling and thinning after ca 1050 Ma, not prograde metamorphism associated with crustal thickening and heating. Post-Ottawan structures in the orogenic core are predicted to be steep, with abrupt contrasts in metamorphic grade across normal faults, and there is no explanation for what happens to the material displaced by extension and thinning. The reason for the renewed convergence, and why it affected only the GFTZ, is not explained. LP,MP, and HP are low, medium, and high-pressure belts of the allochthon and parautochthon, denoted by the prefixes a and p, respectively. The Allochthon Boundary Thrust (ABT) reworked in normal-sense extension is referred to, in this model, as the Allochthon Boundary Detachment (ABD). The latter term is not used in this study.

1.3.3 Numerical Models

Coupled thermal-mechanical numerical models published by Jamieson et al. (2007, 2010) explained the crustal-scale structure of the Grenville Orogen as one margin of a convergent continental system, constructed of progressively weaker lower crustal blocks representing progressively weaker protoliths (Archean to accreted juvenile arcs). During convergence, the crustal blocks get progressively thicker and hotter by radioactive self-heating (Fig. 14.a). Underthrusting of a strong lower crustal indentor, the most external and strongest block, analogous to Archean crust, gravitational pressure gradients beneath the plateau, and focussed erosion in the foreland drive the extrusion of hot, ductile lower crust as a series of nappes toward the foreland (Fig. 1.4b).

Models involving constant convergence over ca. 100 My produced similar crustal geometries to models involving ca. 85 My of convergence followed by ca. 25 My of post-convergent ductile flow. Both produced crustal geometries for the western CGB that are remarkably consistent with cross-sections based on geological and seismic data (Fig. 1.2, 1.4c, Culshaw et al, 1997; White et al., 2000). However, the latter are considered more reliable, as only models which stop convergence after ca. 85 My produce late, normal-sense ductile shearing consistent with extension in the SSZ at ca 1025 Ma.

Numerical models for ductile flow in large hot orogens and subsequent orogenic propagation predict structural profiles and P-T-t paths for tracked particles, but models require sufficient correlative data from natural systems at the scale of the model for comparisons to be meaningful and robust. The most useful data include crustal-scale cross-sections based on geological observations coupled with geophysical surveys of the sub-surface, and geochronological data timing the deformation and metamorphic events

which produced the observed geometry (Jamieson et al., 2010). The consistency of metamorphic P-T estimates with regional-scale predictions provides further criteria for assessing and comparing model validity.

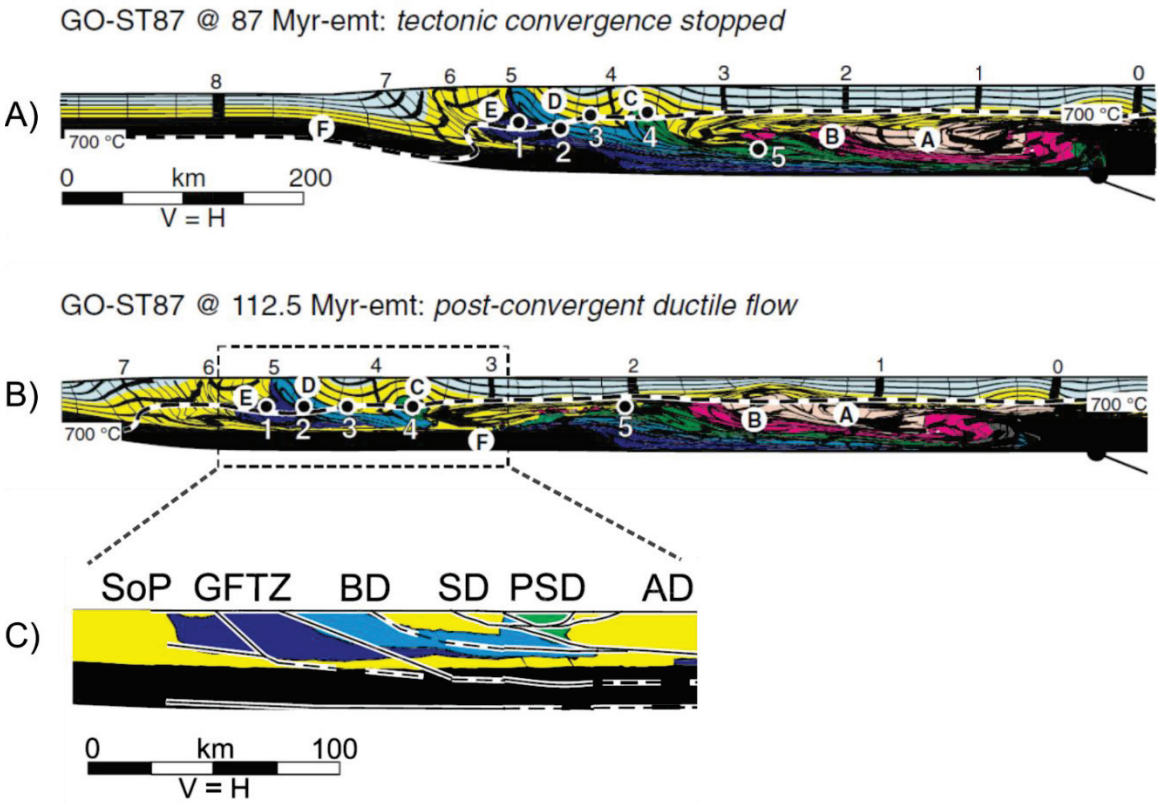

Figure 1.4 Results from numerical models of the Grenvillian Orogeny (Jamieson et al., 2010) showing 112.5 My-emt (elapsed model time). A) Deformed marker grid, crustal blocks, and 700 °C at time the time convergence is stopped, 87 My-emt. Strong lower crustal block F has started to underthrust blocks in the orogenic core. V = H, vertical scale = horizontal scale. B) At 112.5 My-emt, 25 My after convergence has stopped. Note blocks E,D, and C have be transported ca 200 km into the foreland over the lower crustal indentor F by thinning in the orogenic core. C) Detail of model at 112.5 My-emt with grid removed, truncated at present day surface, and with Georgian Bay cross section (Culshaw at al, 1997; White et al., 2000) superimposed. Note that foreland-directed thrusting continues after the end of convergence in response to ductile thinning in the core, demonstrating dynamically coupled thinning and extension in the core and thrusting in the flanks. This model predicts progressive deformation and prograde metamorphism, with post-convergent spreading driving thrusting in the flank of the orogen. No hiatus in tectonism is predicted.

Models for late-stage orogenic propagation make different predictions about the manner and rate at which metamorphism and deformation in the orogenic foreland progresses. Thus, distinguishing between contrasting models, numerical or otherwise, and testing those predictions with field data has direct implications for understanding how Himalayan-scale large, hot, collisional orogens, such as the Grenville Orogen, evolve.

Forward numerical models, in contrast to conceptual models, enable tracking particles to record the P-T conditions "seen" by various crustal materials through elapsed model time in addition to the resulting crustal geometries. Critically, these models predict progressive deformation and metamorphism of crustal blocks correlative with the Britt Domain (BD) and GFTZ in response to gravitational spreading of melt-weakened mid-crust from the orogenic core. Tight hairpin P-T-t paths calculated for parautochthon-correlative crustal blocks demonstrate relatively rapid burial and exhumation, reaching peak T of 732 °C and P at peak T of 9.6 kbar (Jamison et al., 2010; Jamieson and Beaumont, 2011). No hiatus in tectonic activity is indicated, suggesting the Rigolet and Ottawan "phases" are simply the early and late expressions of the same process, not discrete orogenic events.

1.4 Purpose, Objectives, and Approach

1.4.1 Hypothesis

The goal of this study is to resolve Grenvillian metamorphic histories across the polycyclic Britt Domain with sufficient precision to distinguish between predictions made by contrasting models of late-stage orogenic propagation. Sudbury metadiabase dykes (SmD) are the tectonized equivalents of the ca. 1235 Ma (Krogh et al., 1987; Dudàs et al., 1994) dyke swarm that intruded the Laurentian crust prior to the Grenvillian Orogeny.

These rocks therefore record exclusively Grenvillian metamorphism and deformation during reworking of the BD, the GFTZ, and adjacent parautochthonous domains. By linking well-constrained P-T data to the times of peak metamorphism, this study tests the hypothesis that deformation and metamorphism of the BD began first in the SE, close to and coeval with deformation along the SSZ, and propagated progressively to the NW, culminating with late, short-lived thrusting in the GFTZ.

1.4.2 Objectives

The study area lies within a critical region affected by late-stage propagation that separates the GFTZ from allochthonous domains metamorphosed during the Ottawan phase. Thus, the specific objectives of this study are: 1) to examine and characterise regional variations in the development of coronitic metamorphic assemblages in SmD across the BD; 2) to produce unambiguous and well-constrained peak P-T data from various regions across the Britt Domain; 3) to produce well-constrained ages of peak metamorphism across the BD for comparison with model predictions for Rigolet phase propagation of the Grenville Orogeny.

1.4.3 Approach

All known outcrops of metadiabase with potential SD affinity in the Britt Domain were examined and sampled during the summer of 2014. Macroscale features and host rock relations were documented to characterise regional-scale variations in metamorphism and deformation. Petrographic analysis was undertaken to characterise regional variations in metamorphic histories, and identify peak metamorphic

assemblages. Three key samples representing a 40 km front-normal transect along Georgian Bay were selected for detailed study.

A combination of multiequilibrium analysis, conventional thermobarometry, and phase equilibrium modelling was undertaken to identify well-equilibrated compositional subgroups in the metamorphic assemblage associated with peak conditions, and to produce reliable peak P-T estimates from these compositional subgroups.

Peak metamorphic ages for key SmD samples were produced using Laser Ablation-Inductively Coupled Plasma-Mass Spectrometry (LA-ICP-MS) U-Pb geochronology of metamorphic zircon. *In situ* analysis of metamorphic zircon was undertaken to ensure that each target was texturally associated with the peak metamorphic assemblage.

1.4.4 Thesis Organization

Field criteria for recognizing SmD and distinguishing them from other metabasite lithologies in the field area are presented in Chapter 2, including descriptions detailing host rock relations in key sample localities. Chapter 3 presents petrographic analysis of key samples outlining the development, and subsequent overprinting, of coronitic textures in SmD across the BD, and the identification of peak metamorphic mineral assemblages for use in thermobarometry. Bulk geochemical data are also presented in Chapter 3, confirming SD affinity of metadiabases sampled in this study. Chapter 4 discusses the challenges and limitations of extracting P-T estimates from metamorphic rocks dominated by disequilibrium textures. Mineral composition data from peak metamorphic assemblages and other compositional subsets in key SmD samples are presented and discussed, followed by P-T results from conventional and multiequilibrium

thermobarometry. Preliminary results of phase equilibrium modelling are presented for comparison. Chapter 5 presents the results of LA-ICP-MS U-Pb geochronology of metamorphic zircons in association with granulite-facies coronitic assemblages, interpreted to represent the timing of peak metamorphism in SmD. The conclusions reached by this study and a discussion of their implications regarding models of Grenvillian orogenesis and the late-stage evolution of large, hot, collisional orogens is presented in Chapter 6.

Chapter 2: Field Relations

2.1 Introduction

2.1.1 Overview

The Sudbury diabase (SD) dyke swarm is one of many volumetrically minor yet distinctive suites of mafic and ultramafic intrusive rocks that are widely distributed throughout the western CGB. Where domains of similar composition, age, metamorphic grade, and with similar structures are juxtaposed, the distribution of readily identifiable mafic lithologies with known, mutually exclusive domain associations provides an opportunity for confident approximations and mapping of major domain bounding structures and contacts.

The goal of this chapter is to introduce the characteristic features that provide field criteria for recognizing SD dykes and their metamorphosed correlatives throughout the Parautochthonous Belt (PB), and distinguish them from other, widely distributed mafic intrusions and metabasites in the western CGB. The following sections provide field descriptions including, but not limited to, characterization of regional variations in Grenvillian deformation and metamorphism across the Britt Domain by focussing on representative Sudbury metadiabase (SmD) localities selected for P-T work and U-Pb geochronology. A brief review of similar metabasite suites in the study area is provided for the sake of comparison.

2.1.2 Location and Access

The study area comprises a large, roughly 40 km transect of the northeast coast of Georgian Bay, extending from Key Harbour (KH) in the north, to the Point au Baril (PaB) archipelago in the south. The low, glaciated coastline is largely devoid of vegetation, affording remarkably complete exposure for examination of lithological and structural relationships.

Access is almost entirely by boat. Docking facilities and boat rentals are available from four locations. Highway 69 (extension of highway 400, north of Toronto) crosses Key River 14 km east of the KH archipelago, affording access to the northern region of the study area. The town of Britt on Byng Inlet provided access to both the northern and central regions of the study area. Islands and inlets south of Byng Inlet were accessed through a small private channel marked by home-made buoys 1.5 km south of the Gereaux Island lighthouse which is strongly recommended for travel by small watercraft. Good aerial photographs are strongly recommended for navigating the shoals and islands in this area, as marine charts do not represent the shoals in great detail. Marinas at Bayfield Inlet, off of highway 529, and the village of PaB afford access to the southern region.

Though the study area is predominantly crown land, many islands in the vicinity of KH and PaB are privately owned with cottages and small cabins. In addition, Henvey Inlet First Nation extends south of Key River, on the mainland, to a point on the coast roughly equidistant between Henvey Inlet and Byng Inlet. Magnetawa First Nation covers an area surrounding ~9 km of the Magnetawan river and a 2 km portion of the south-

shore at the head of Byng Inlet. All efforts should be taken to obtain permission before accessing First Nations lands and private properties.

2.1.3 Methods

Field work was carried out over 4 weeks in the summer of 2014, primarily along a ~40 km section of northeastern Georgian Bay (GB) shoreline. Roadcuts and lakeshore outcrops east of GB supplement regional data coverage, though poor inland exposure limited access, mapping, and sampling. Using 1:50,000 geological maps published by the Ontario Geological Survey (mapsheets P.3548, P.3549), copies of working maps on which these publications were based (provided by N. Culshaw), and annotated aerial photographs (also provided by N. Culshaw), all known outcrops of metabasite with potential SD affinity were examined and sampled. A limited number of samples up to 60 km east of the GB shoreline were collected from road cuts and shores of smaller lakes. Host rock field data were collected to provide context. Several kilograms of material were collected from each of three key locations.

2.2 Metabasites in the northwestern Grenville Province

Several suites of chemically and texturally distinct mafic intrusions, and their metamorphosed counterparts, are present throughout the northwestern Grenville Orogen. North of the Grenville Front (GF), Nippising diabase (ca. 2220 Ma; Buchan et al., 1998), SD (ca. 1235 Ma; Krogh et al, 1987; Dudàs et al., 1994), and Grenville diabase (GD) (ca. 590 Ma; Kamo et al., 1995) intruded the Archean Superior Province and Paleoproterozoic Huronian Supergroup of the Southern Province. Farther south, metamorphosed equivalents of SD are found south of the GF (Bethune and Davidson, 1988, 1997;

Bethune, 1993, 1997; Jamieson et al., 1995; Ketchum and Davidson, 2000). Algonquin metagabbro (ca. 1170-1150 Ma; Davidson and van Breemen, 1988; van Breemen and Davidson, 1990; Heaman and LeCheminant, 1993) is widely distributed throughout the allochthonous domains of the Central Gneiss Belt (CGB), with the notable exception of the Parry Sound Domain. Garnet- and clinopyroxene-dominated rocks interpreted as retrogressed eclogites ("meta-eclogite" of Culshaw et al., 1983; Grant, 1989) are present as isolated pods or lenses in the hanging walls of large shear zones, such as the ABT and bounding structures of the Go Home, Moon River, and Rosseau domains (e.g., Davidson et al., 1982; Culshaw et al., 1983, 1994, 1997; Davidson, 1990; Ketchum and Davidson, 2000; Marsh and Culshaw, 2014). Primary crystallization ages of the gabbroic protoliths of two retrogressed eclogite bodies from the CGB in western Quebec of ca. 1400 Ma, with a third yielding a slightly older age of 1470 Ma (Indares and Dunning, 1997; Ketchum and Krogh, 1997, 1998).

2.2.1 Nipissing diabase

The 2.22 Ga Nipissing diabase (ND) is the distal part of the radiating dyke swarm associated with the Ungava magmatic event of northern Quebec (Buchan et al., 1998)**.** Nipissing diabase crops out within the Proterozoic metasediments of the Huronian Supergroup and is known to cut Precambrian basement in a number of locations north of the Huronian basin (Lightfoot et al., 1993). Emplaced primarily as undulating sills, cone sheets, and dykes (Noble and Lightfoot, 1992), ND north of the GF preserves a greenschist to amphibolite facies pre-Grenvillian metamorphic overprint (Card, 1978; Blonde, 1996).

2.2.2 Sudbury diabase

The ca. 1235 Ma Sudbury swarm (Krogh et al., 1987; Dudàs et al., 1994) strikes uniformly SE, sub-vertically, cutting E-W folds in the Southern Province and E-dipping fabrics in Huronian metasediments and Proterozoic granites (Bethune and Davidson, 1988; Bethune, 1993; 1997). South of the GF, the Sudbury dykes are first cut by steeply SE-dipping brittle faults with minor offsets, then truncated abruptly by a mylonite zone across which no individual SD dyke has been traced continuously (Bethune, 1997). Immediately south of this mylonite zone, SD dykes are folded and highly irregular but relatively continuous over several kilometers. South of the Boundary Shear and transition zone marking the southern extent of the GFTZ (Jamieson et al., 1995), SD is tectonically segmented into discrete bodies that preserve a marked increase in metamorphic grade (Bethune, 1993, 1997; Jamieson et al., 1995; Bethune and Davidson, 1997). Here, metamorphosed dyke segments within the Grenville Orogen that can be shown unequivocally to have SD affinity are referred to as Sudbury metadiabase (SmD).

2.2.3 Algonquin metagabbro

Algonquin metagabbro and retrogressed eclogite suites are restricted to the allochthonous domains of the CGB, with the exception of the Parry Sound Domain. Sudbury metadiabase, in contrast, is restricted to the parautochthonous domains of the western GP, leading Ketchum (1994) to suggest that the observed distribution of these distinct metabasite lithologies defines the surface position of the Allochthon Boundary Thrust (ABT).

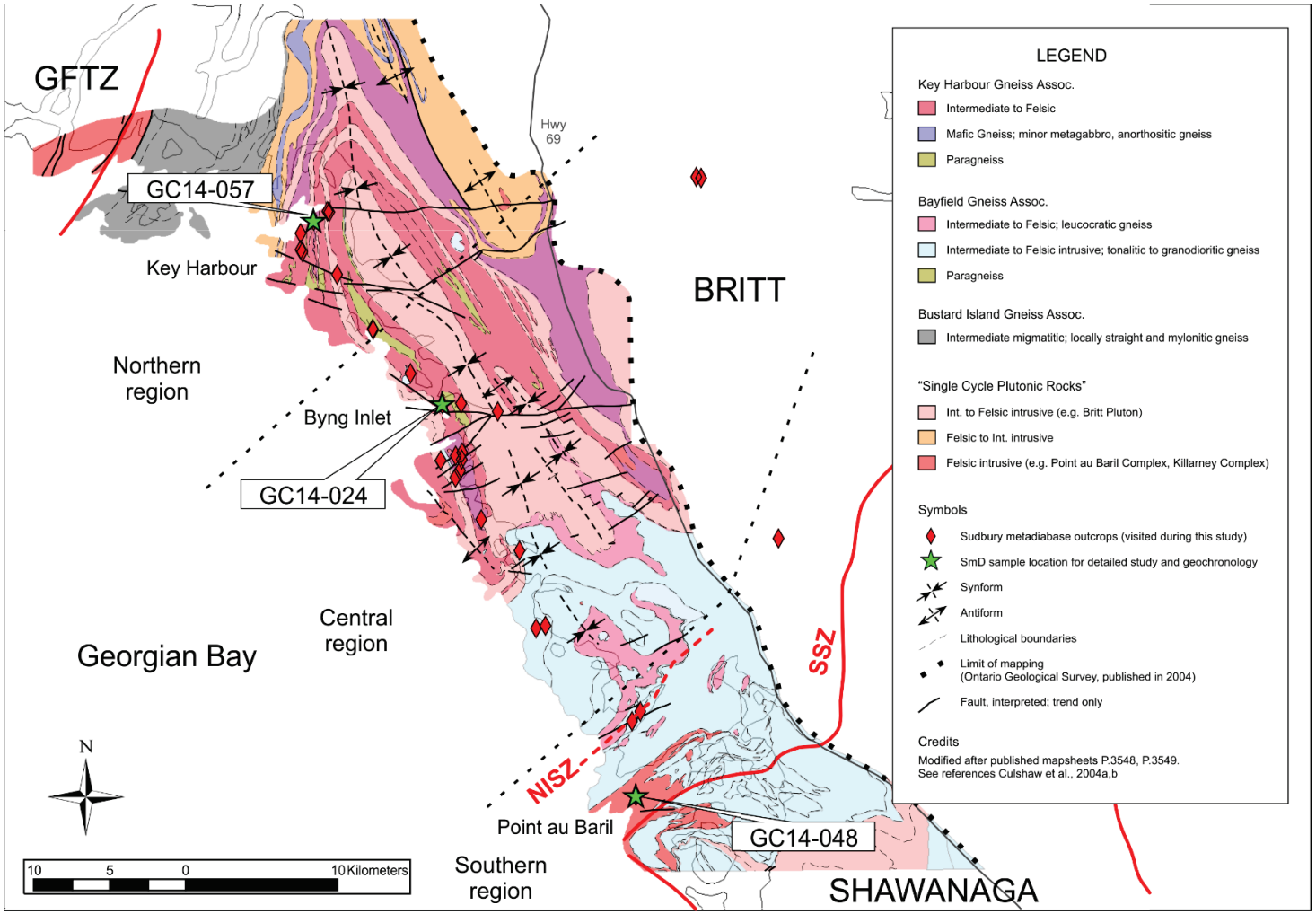

Figure 2.1 Geology of the Georgian Bay transect with SmD and representative sample locations indicated. Red diamonds show SmD outcrops. The GFTZ and SSZ (the local expression of the ABT) bound the parautochthonous Britt Domain to the north and south, respectively. Nares Inlet Shear Zone (NISZ) is a minor extensional shear zone coeval with the SSZ (Culshaw et al., 1994).

Table 2.1 Distinguishing features of common metabasite lithologies throughout the western GP, GFTZ, and Southern Province. Age references by Lithology follow. *SD/SmD*: 1. Krogh et al., 1987; 2. Dudàs et al., 1994. *Coronitic metagabbro*: 3. Davidson and van Breemen 1988; 4. van Breemen and Davidson 1990; 5. Heaman and LeCheminant 1993. *GD*: 6. Kamo et al., 1995.

	Sudbury (meta)diabase	Algonquin coronitic metagabbro	Grenville dykes
Age	ca. 1235 Ma (1,2)	ca. 1150-1170 Ma (3,4,5)	ca. 590 (+2-1) Ma (6)
Mineralogy 1. Igneous 2. Metamorphic	1. pl + aug + ol + ilm + ap ± bt, bdy 2. grt + cpx + opx + pl + bt + prg	1. ol + aug + pl + ilm 2. grt + cpx + opx + pl + bt + prg	1. pl + aug + mag ± srp (after ol), qtz, ab
Textures and colour	medium- to fine-grained subophitic chilled margins stippled weathered surface rusty red hue	coarse- to v. coarse-grained gabbroic dark grey-green hue	fine-grained ophitic green-grey hue
Megacrysts/ phenocryst	pl common ol uncommon	n/a	n/a
Chemistry	alkali-olivine diabase *high*: Fe, Ti, K, Zr, Ba, alkalis, LREE *low*: Mg, Ni, Cr	olivine-gabbro *high*: Ca, Al, Cr, Ni *low*: Fe, alkalis, LREE	Tholeiitic, qtz normative *high*: Mg, Ca *low*: alkalis
Provinces/Domains	Southern & Superior Pr. GFTZ, Britt	Algonquin, Kiosk, Moon River, Muskoka, Shawanaga, Rosseau, Seguin	Superior & Southern Pr. all GP from Sudbury to Montreal

2.2.4 Grenville dykes

The ca. 590 Ma Grenville dykes (Kamo et al., 1995; Seymour and Kumarapeli, 1995) follow similar SE-striking trends to the SD in the Southern Province. Grenville dykes, however, traverse the GF and the CGB without significant disruption or metamorphic overprint, and cut folded and metamorphosed SmD within the GFTZ. The Grenville dykes are tholeiitic and quartz-normative. In contrast, SD is strongly olivine-normative, and enriched in FeO, K_2O, P_2O_5, Ba, Zr, and LREE.

This study focuses on the parautochthonous domains composed of Laurentian crust reworked during late-stage propagation of the Grenville Orogen into its foreland, in particular, the unambiguous single-cycle tectono-metamorphic history recorded by the SmD within the polycyclic Britt Domain.

2.3 Sudbury metadiabase: field identification and sampling criteria

The criteria described by Davidson and Bethune (1988), Bethune (1993, 1997), and Ketchum and Davidson (2000) for field identification of SmD in the GFTZ and northern Britt Domain, based largely on distinctive relict igneous textures and features, have been adopted in this study. Characteristic features of SmD and other metabasite lithologies in the study area are summarised in Table 2.1.

2.3.1 Primary Igneous Features

Unmetamorphosed SD north of the GFTZ is sub-ophitic and medium- to fine-grained. South of the GF, coronitic textures after olivine, plagioclase, and Fe-Ti oxides

within the undeformed cores of SmD pods and dyke segments clearly overprint a relict sub-ophitic texture (Fig. 2.2b,c), both of which are readily visible in hand sample.

Where strain is low or absent, relict chilled margins are preserved as fine-grained to aphanitic sharp contacts cutting host gneissic fabrics (Fig. 2.2a) (Davidson and Bethune, 1988; Bethune 1997). Commonly, however, the margins of strain-enveloped dyke segments are completely converted to medium-grained, strongly foliated amphibolite that weathers recessively. In many places, host strain envelopes, where truncated gneissic fabrics are transposed parallel to the contact with the more competent mafic bodies, obscure cross-cutting relations.

Distinctive plagioclase megacrysts (locally ≤ 20 cm) (Fig. 2.2b) are common and generally concentrated at or near dyke margins. Their origin in SD is unclear, and the term megacryst is used here in preference to phenocryst to avoid the connotation that they formed from the diabase magma. Plagioclase megacrysts tend to be light-grey to dark greenish-grey, semi-translucent, and have waxy to resinous lustre. The dark grey-green colour is attributed to a high concentration or "dusting" of submicroscopic spinel (see Ch. 3). Primary multiple twinning in coarse plagioclase is visible locally, but typically obscured in dark-coloured megacrysts.

An unusual and conspicuous accumulation of megacrystic plagioclase ~ 0.5 m thick (Fig. 2.3a), surrounding a large ~ 1 m coherent xenolith of very coarse-grained anorthosite (highlighted by dashed red line, Fig. 2.3b) was observed in SmD at one location in the central region of the study area. Megacrysts at this locality are identical to those observed in SmD throughout the study area, strongly suggesting that disaggregation of similar anorthositic enclaves may be the source of this characteristic SD feature.

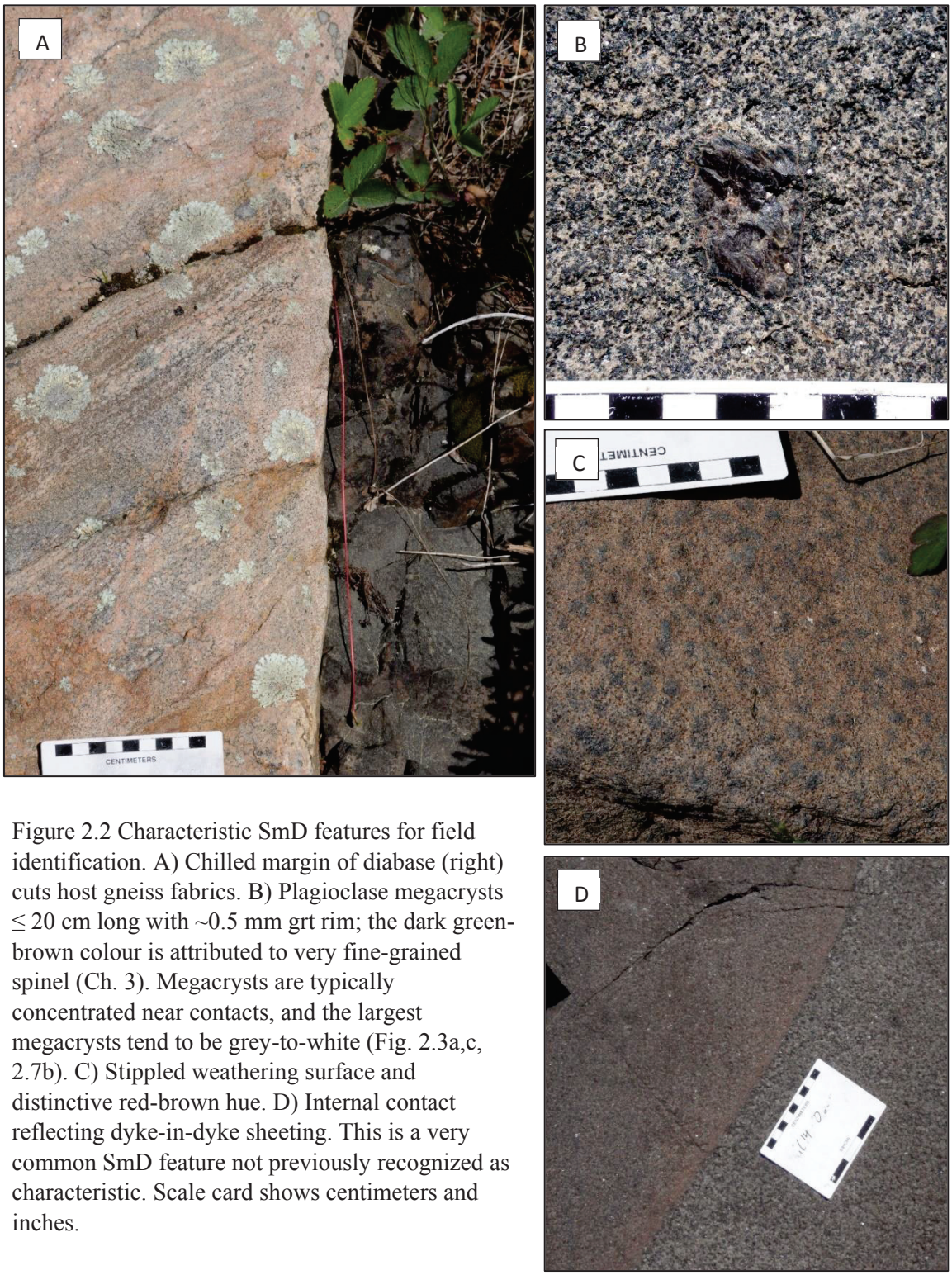

Figure 2.2 Characteristic SmD features for field identification. A) Chilled margin of diabase (right) cuts host gneiss fabrics. B) Plagioclase megacrysts ≤ 20 cm long with ~0.5 mm grt rim; the dark green-brown colour is attributed to very fine-grained spinel (Ch. 3). Megacrysts are typically concentrated near contacts, and the largest megacrysts tend to be grey-to-white (Fig. 2.3a,c, 2.7b). C) Stippled weathering surface and distinctive red-brown hue. D) Internal contact reflecting dyke-in-dyke sheeting. This is a very common SmD feature not previously recognized as characteristic. Scale card shows centimeters and inches.

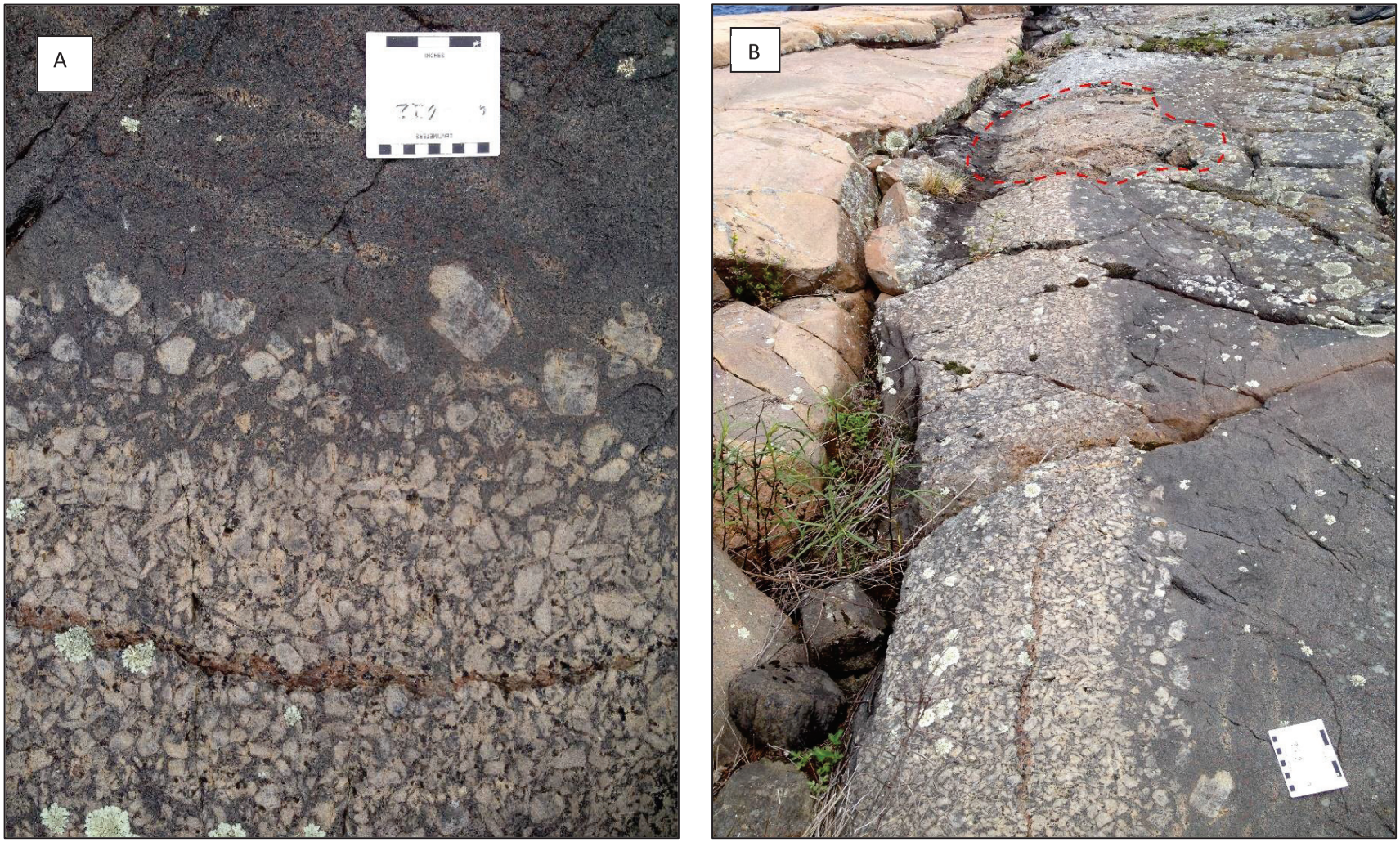

Figure 2.3 An unusual megacryst accumulation at SmD locality GC14-023, 3 km NW of Byng inlet. A) The accumulation lies within ~ 50 cm of the northern margin of the SmD dyke segment, and contains megacrysts up to 20 cm long. The accumulation is not found along the opposing, southern margin. B) 1 m wide, equant xenolith of very coarse-grained anorthosite (outlined by dashed red line) with crystals of comparable size and habit to the surrounding accumulation of megacrysts.

2.3.2 Weathering colours

Weathered surfaces of SmD display a rusty red-brown hue and commonly show a stippled "raisin-cake" or "leopard-spotted" texture (Fig. 2.2c). Weathering colours also serve to highlight the presence of internal contacts (Fig. 2.2d) and magma mingling, common features of dyke segments throughout the study area. In outcrop, these appear as sheeted, side-parallel units, and as elongate to rounded bulbous patches and small enclaves, respectively. Margins of relatively straight, sheeted contacts tend to be dark grey to black. Irregular magma mingling enclaves tend to be slightly lighter grey, possibly reflecting slightly higher proportions of plagioclase. Both show sharply defined margins and asymmetric, inwardly coarsening grain-size gradations from near-aphanitic and granular to typical medium-grained and sub-ophitic (relict). This indicates the dykes were filled by more than one pulse of mafic melt, a slightly cooled initial pulse providing for "chilling" of at least one successive fresh pulse(s) (Fig. 2.2d, 2.3 (b)). Internal contacts, not previously viewed as diagnostic of SmD affinity, are common throughout the study area.

2.4 Regional-scale variations

In the Southern Province north of the GF, SD consists of uniformly SE-striking vertical dykes that cut Huronian Supergroup metasediments and Proterozoic granites (Bethune and Davidson, 1988; Bethune 1993, 1997). Based on field observations of SmD and their host rocks, the following regional-scale variations are described here from north (GFTZ) to south (SSZ).

2.4.1 The Grenville Front Tectonic Zone

The GFTZ is a broad crustal-scale shear zone that developed at ca. 1000 Ma along the entire northern margin of the Grenville Orogen during the final stage (Rigolet Phase) of orogenic propagation into the Laurentian foreland (Wynne-Edwards, 1972; Rivers et al., 1989; Haggart et al. 1993; Krogh, 1994; Rivers, 2009).

The GF, the northwest boundary of the GFTZ, is marked by a zone of faults and mylonites up to 5 km wide that cuts NE-trending Paleo- and Mesoproterozoic granitoids, and E-W-trending folds in Huronian metasediment (Bethune and Davidson, 1988). The GF marks a sharp break in metamorphic grade from greenschist facies rocks in the Southern Province to upper amphibolite and granulite facies, NE-striking, steeply SE-dipping gneisses with S>>L fabrics (Bethune, 1997; Culshaw et al. 1997). Within the GFTZ, SD is folded and highly irregular, though relatively continuous over several kilometers. Road-cut outcrops of SD observed along Highway 637 northeast of Killarney contain numerous mm- to cm-scale, moderately to steeply dipping, ultra-mylonite bands. A structural and metamorphic analysis of SD in the GFTZ was reported in the PhD thesis of K.M. Bethune (1993) and associated publications (Bethune and Davidson, 1988, 1997; Bethune, 1989, 1997).

2.4.2 The Britt Domain

Along Georgian Bay, the Britt Domain is underlain mainly by migmatitic grey-to-pink tonalitic-to-granodioritic orthogneiss with subordinate, though volumetrically significant, paragneisses comprising semipelitic and psammitic lithologies. Stretching lineations plunge shallowly-to-subhorizontally to the SE, and NW-SE striking,

moderately dipping gneissosity reflects shallowly SE-plunging front-normal open folds (Culshaw et al., 1994) (Fig. 2.1). At outcrop scale, gneissic banding and outcrop-scale shear zones are deflected about large, tectonically segmented mafic bodies. The overall size of dyke segments decreases markedly southward within the BD, from ≥100 m to ≤1 m scale thickness, reflecting increased degrees of stretching and disaggregation. Generally, metadiabase segments hosted in pelitic lithologies display higher degrees of strain than blocks hosted in orthogneiss, and tend to have wider amphibolite selvages. For convenience, the general characteristics of SmD dyke segments and their host rocks are described below with respect to northern, central, and southern regions that reflect variations in metamorphic transformation of SmD and relation to host rocks from north to south across the region.

2.4.2.1 Northern Britt Domain

The northern region of the field area, between the southern boundary of the GFTZ and Henvey Inlet, is underlain by gneisses, plutons, and mafic intrusions with SmD hosted in several different gneiss associations (Fig. 2.1). Dyke segments in the Key Harbour area show the lowest degree of strain where hosted in leucogranite of the Key Harbour gneiss association. Orthogneiss-hosted, sharply rectangular blocks with long axes up to 135 m are clearly visible in satellite images (Fig. 2.5). *S*maller, paragneiss-hosted, boudinaged dyke segments also crop out near larger, orthogneiss-hosted segments, locally within the same island, suggesting the segments were once part of the same intrusion. Pegmatites syntectonic with the disaggregation of the dykes are found adjacent to dyke segments in strain shadows and within boudin necks (Fig.2.4). Granitic pegmatites in boudin necks of paragneiss-hosted segments form distinctive “fish mouth”

Figure 2.4 Contrasting habits of syntectonic pegmatite emplacement at SmD dyke segment margins in Key Harbour. A) Paragneiss-hosted boudinaged SmD necking into the strain shadow, forming distinctive 'fish mouth' morphologies filled with granitic pegmatite (lower left). Sledge hammer, top left, is 1 m long. B) Orthogneiss-hosted SmD is largely undeformed with megacrystic pegmatite pooled along relatively straight dyke margins with very narrow ~ 1 cm wide amphibolite selvage.

morphologies (Fig. 2.4a). In contrast, pegmatites adjacent to orthogneiss-hosted blocks tend to be much more voluminous and extremely coarse-grained, locally containing

metre-scale K-feldspar megacrysts (Fig. 2.4b).

2.4.2.2 Central Britt Domain

The central region of the study area encompasses ~30 km of the Georgian Bay coast between Henvey Inlet to the north and the Nares Inlet Shear Zone (NISZ) to the south (Fig. 2.1). The northern half of the central region is dominated by the Key Harbour gneiss association and the Britt Pluton. The southern half comprises the Bayfield gneiss association, composed primarily of tonalitic to granodioritic and pink granitic orthogneiss, and subordinate pelitic gneiss (Culshaw et al., 1991). Dyke segments within the central region are invariably lenticular to lozenge-shaped and rarely exceed 30 m in length. Commonly, several segments of comparable size, orientation, and aspect ratio can be observed along-strike, suggesting that they are boudins derived from a single continuous intrusion. The long axes of SmD segments in this area are mainly oriented NE-SW (Fig. 2.7), roughly orthogonal to SD orientation in the Southern Province, and oblique to SE-trending gneissic foliations, stretching lineations, and leucosomes. Bethune (1997) documented deviations in orientation of continuous SmD dyke segments in the Tyson Lake area of the GFTZ. While most variations in dyke orientation were attributed to folding, some were interpreted to reflect local irregularities in the trajectory of the initial intrusion. Similar intrusion-related variations cannot be ruled out in the central Britt Domain, though complexly folded intercalations of leucosome and amphibolitized diabase near thinned “necks” (Fig. 2.8e) indicate that most boudins rotated as coherent bodies within a host undergoing simple shear.

2.4.2.3 Southern Britt Domain

The southern region of the study area encompasses the relatively narrow region between the NISZ and the SSZ (Culshaw et al., 1994; Ketchum, 1994; Ketchum et al. 1994). Nares Inlet marks a transition from NNW-SSE trending tectonic fabrics and structures to SW-NE trending ones proximal to the SSZ near Point au Baril. Along the Georgian Bay shoreline, this region comprises the southern extent of the Bayfield gneiss association and ca. 1430-1460 Ma (T.E. Krogh, unpublished data cited in Culshaw et al., 1994) megacrystic granitoids of the Point au Baril complex (PBC). Pre-Grenvillian granulite assemblages (Ketchum et al., 1994) and foliations are well preserved in the region, possibly owing to regional strain partitioning between the SSZ and the NISZ. Two metadiabase pods several meters long within the NISZ are strongly deformed, partially disaggregated, and locally amphibolitized by fine-grained intrusions, preventing unequivocal confirmation of SD affinity. A single metadiabase dyke segment with confirmed Sudbury affinity, one of the best preserved in the entire study area, crops out within the Point au Baril archipelago on H. A. Gray Island, as discussed in detail in section 2.4.3 below.

2.5 Sampling Localities

To examine the record of how and when deformation and metamorphism propagated through the parautochthonous Britt Domain, three representative sites were selected for detailed P-T study and geochronology. Bigsby Island, containing several large (100 m-scale) diabase dykes of known Sudbury affinity, was selected to represent the northern region of the Britt domain, and was part of a previous detailed

geochronological study of the Key Harbour area (Corrigan, 1990; Corrigan et al., 1994). Lamondin Point on the north shore of Byng Inlet was selected to represent the central region. H.A. Gray Island in Point au Baril, the southernmost known outcrop of SmD, was selected to represent the southern region of the study area.

Together, these sampling locations record the pressure-temperature-time (P-T-t) history of orogenic propagation along a 40 km NE-SW transect of the parautochthonous Britt Domain.

2.5.1 Bigsby Island, Key Harbour

Key Harbour is located roughly 15 km southeast of the GFTZ and contains the highest concentration of SmD outcrops in the western Central Gneiss Belt (Fig. 2.1). The region comprises Paleoproterozoic migmatitic ortho- and paragneisses and Mesoproterozoic granitoids, deformed into GF-normal, SE-plunging folds (Culshaw et al., 1988, 1994, 1997). Grenvillian deformation in the area was partitioned between relatively strain-resistant panels along an anastomosing network of high-strain north-south trending shear zones (Corrigan, et al., 1994). Pre-Grenvillian features are preserved within shear-bounded and elongate strain-resistant panels.

Bigsby Island is situated within a strain-resistant panel roughly 2 km west of the mouth of Key River. Sample GC14-057 was collected from one of two large tectonically segmented blocks of SmD hosted in pink granitic orthogneiss. The sampled segment is approximately 100 m by 50 m, rectangular, and strikes roughly E-W (Fig. 2.5). Southeast-plunging fabrics are poorly developed in the host orthogneiss adjacent to the northern

Figure 2.5 Satellite image of Bigsby Island showing GC14-057 sample location. SmD outlined in red. OG: ca. 1694 Key Harbour leucogranite orthogniess, PG: pelitic paragneiss (after Corrigan, 1990). Image from Google Earth.

margin of the block, suggesting strain shielding in the lee of the large relatively competent mafic body. Host fabrics are truncated by the igneous contact in the lee of the block at a very low angle (Fig 2.6d).

Figure 2.6 GC14-057 sample locality and features, Bigsby Island, Key Harbour. A) SmD (left) cutting pink orthogneiss (right). B) Metre-scale elongate finer-grained enclaves (center left) suggest mingling of multiple magma injections. C) Subophitic texture is perfectly preserved, with garnet coronas clearly visible in medium-grained metadiabase and coarse-grained enclaves (top and bottom right). D) Igneous contact with county rock cuts poorly developed fabrics in orthogneiss (left) at a very low angle.

The block contains several small irregular enclaves of mafic pegmatite identical in composition to the main diabase body (Fig. 2.6c). Characteristic plagioclase megacrysts have not been found at this site. Primary medium-grained subophitic textures are well preserved throughout the block, with plagioclase laths averaging 3-4 mm long (Fig. 2.6c). Very fine-grained garnet coronas on primary plagioclase are ubiquitous and visible to the naked eye. Weathered surfaces display a distinctive spotted 'leopard skin' texture and rusty red-brown hue (Fig. 2.6c). Representative sample GC14-057 was collected from the core of the northernmost of two large SmD blocks (figure 2.4) hosted within 1694 Ma leucogranite of the Key Harbour gneiss association (Corrigan et al., 1994).

2.5.2 Lamondin Point, Byng Inlet

Lamondin Point, at the entrance to Byng Inlet, is located roughly 26 km southeast of the GFTZ (Fig. 2.1). The inlet itself cuts directly eastward, extending roughly 12 km inland, and exposes numerous, variably deformed SmD segments along its northern shore. The area comprises three main lithological units, comprising the monocyclic 1456 Ma Britt pluton (van Breemen et al., 1986), and the two dominant members of the Key Harbour gneiss association, the 1694 Ma Key Harbour leucogranite, and polycyclic leucocratic quartzo-feldspathic ortho- and paragneiss (Culshaw et al., 1988; Corrigan et al., 1994). All lithological units are elongate and trend NW-SE, with map patterns reflecting GF-normal, subhorizontally-to-shallowly SE-plunging folds (Fig. 2.1). Stretching lineations in all units are very shallowly SE-plunging to sub-horizontal, parallel to regional fold axes.

Numerous small islands immediately south of Byng Inlet contain boudinaged SmD segments hosted in leucocratic paragneiss of the Key Harbour gneiss association. The

largest and most clearly exposed segments of SmD near Byng Inlet crop out at Lamondin Point on the north shore of the North Channel at the mouth of the inlet, roughly 8 km west of the town of Britt. Two large lenticular dyke segments cut host fabrics and strike NE-SW, orthogonal to regional structural trends (Fig. 2.7).

The sampled dyke segment has a long axis of at least 120 m and a width of 60 m. Its full extent is unknown as the outcrop extends underwater to the south, though the satellite image shows that its length does not exceed 200 m (Fig. 2.7).

Primary igneous textures and features characteristic of SD are exceedingly well preserved at Lamondin Point. Intrusive contacts cutting orthogneiss foliations are visible locally (Fig. 2.8b), though much of the contact is obscured by cross-cutting pegmatite of unknown age (Fig. 2.8d). Primary sub-ophitic textures are perfectly preserved and show little evidence of retrograde recrystallization with the exception of broad zone, several metres thick, of amphibolite adjacent to the pegmatite.

Abundant subhedral plagioclase megacrysts up to 8 cm long (Fig. 2.8b, top right) rimmed by continuous coronas of very fine-grained garnet and opaque whitish-grey recrystallized plagioclase. Several internal contacts are clearly visible on weathered surfaces as described in section 2.2. Internal contacts within this dyke segment are continuous and straight, and appear to bisect the entire body (Fig. 2.8c). Unlike the small patches and enclaves observed elsewhere, contacts here appear to indicate volumetrically comparable pulses of mafic melt with relatively little mingling, in the manner of dyke-in-dyke sheeting.

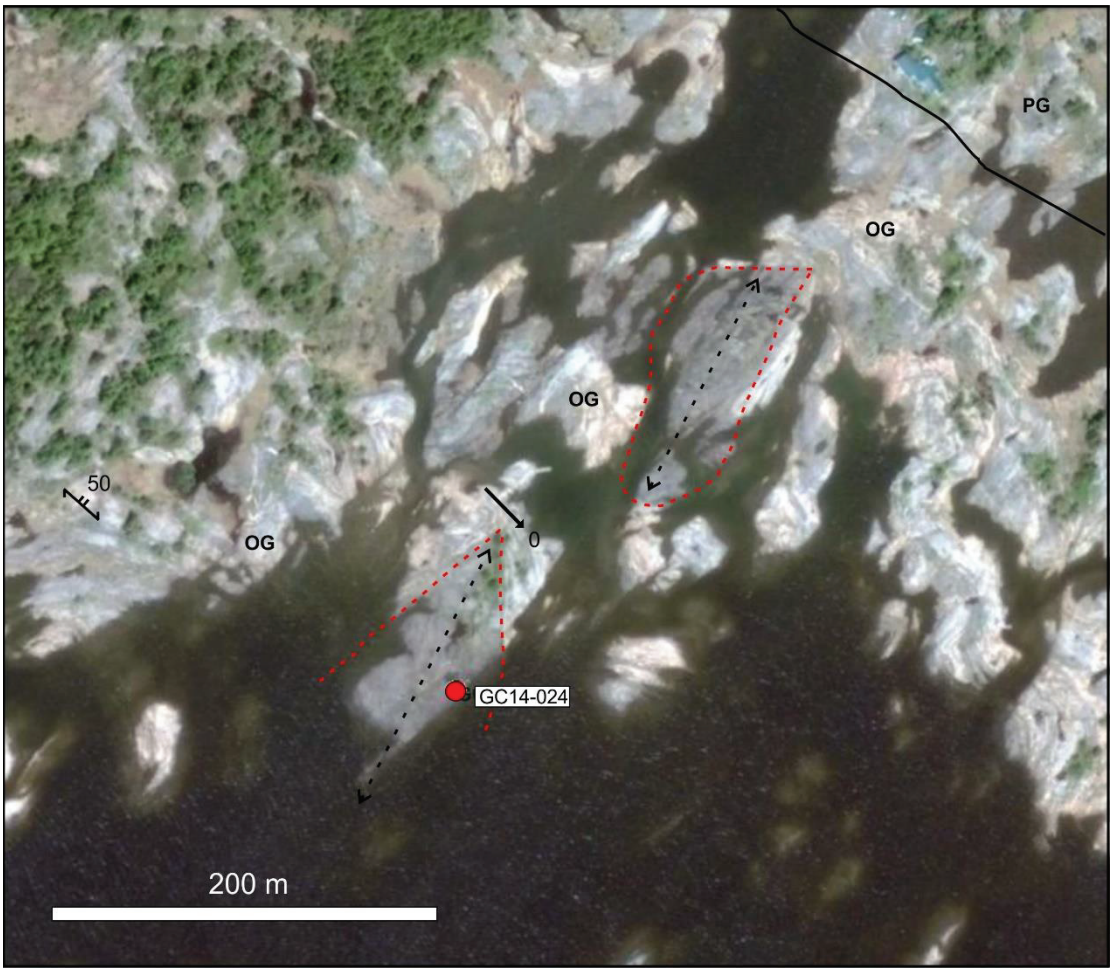

Figure 2.7 Satellite image of Lamondin Point, Byng Inlet, showing GC14-024 sample location. Two SmD segments are outlined in red. OG: Key Harbour leucocratic orthogneiss; PG: undivided paragneiss. Arrow indicates trend of sub-horizontal lineation. The long axes of dyke segments (back dashed line with arrows) are roughly orthogonal to the strike of gneissosity (strike and dip symbol at left) and lineation (center), and NW-SE orientations of SD north of the GF.

Diabase adjacent to the pegmatite dyke contains a dense network of leucosomes oriented at a high angle to the pegmatite contact. Leucosomes become less abundant and thinner away from the pegmatite dyke (Fig. 2.8d). Diabase within the leucosome-rich zone shows no evidence of the granulite facies assemblage, and is interpreted to have been amphibolitized by pegmatite-derived fluids (Fig. 2.8d,e).

Sample GC14-024 was collected from the southernmost of the two SmD segments at Lamondin Point (Fig. 2.7, 2.8a).

Figure 2.8 GC14-024 sample site. A) Small island composed mostly of SmD at Lamondin Point on the North Channel of Byng Inlet. B) Igneous contact cutting country rock fabrics at a low angle (bottom), with plagioclase megacrysts concentrated near the contact. C) Internal contacts within the metadiabase segment showing chilled margins. D) Leucosome-rich zone in amphibolitized SmD adjacent to a cross-cutting pegmatite dyke (right). E) Complexly folded intercalated leucosome and amphibolitized diabase adjacent to SmD the boudin neck. Scale card shows centimetres and inches. Hammer is ~35 cm long.

2.5.3 H. A. Gray Island, Point au Baril

The Point au Baril archipelago is situated immediately north of the SSZ (Culshaw et al., 1994; Ketchum, 1994; Ketchum and Davidson, 2000) and roughly 50 km SE of the GFTZ (Fig. 2.1). H.A Gray Island, roughly 1.5 km SE of the Coast Guard lighthouse at the mouth of Point au Baril harbour, contains the southernmost known outcrop of SmD in the CGB. The ~4 m by 240 m long intrusion bisects the western side of the island, cutting SW-striking foliations in the host orthogneisses of the Point au Baril Complex (Fig. 2.9, 2.10a). Though small, m-scale SmD segments, such as the dyke at H.A. Gray Island, are typically strongly deformed, boudinaged, and/or retrogressed, this segment is exceptionally well preserved, possibly because it lies within a shear-bounded block of relatively strong granitic orthogneiss. The relative times of foliation development in the Point au Baril Complex and deformation of the Gray's Island dyke segment are unclear, though some component of the former is likely synchronous with the latter (Ketchum et al., 1999).

An irregular accumulation of fine-grained leucocratic material is found within SmD along the dyke margins (Fig. 2.10c). Faint traces of compositional banding within the leucocratic material appear to be semi-continuous with, though strongly deflected from, host gneiss fabrics, which are otherwise truncated sharply along the igneous contact (Fig. 2.10c). Dyke margins are sharp, and do not weather recessively. Weathered surfaces display a prominent leopard-skin texture, and distinctive rusty red-brown hue.

Relict plagioclase laths average 2-3 mm in length and are largely to completely replaced by fine-grained garnet. Metallic oxides are rimmed by biotite and dark green amphibole. Abundant dark grey-green plagioclase megacrysts, rimmed by fine-grained

garnet (Fig. 2.10b), are readily identifiable in outcrop. Representative sample GC14-048 was collected from the core of the H. A. Gray Island dyke segment (Fig. 2.9), where fine-grained relict sub-ophitic textures are clearly preserved.

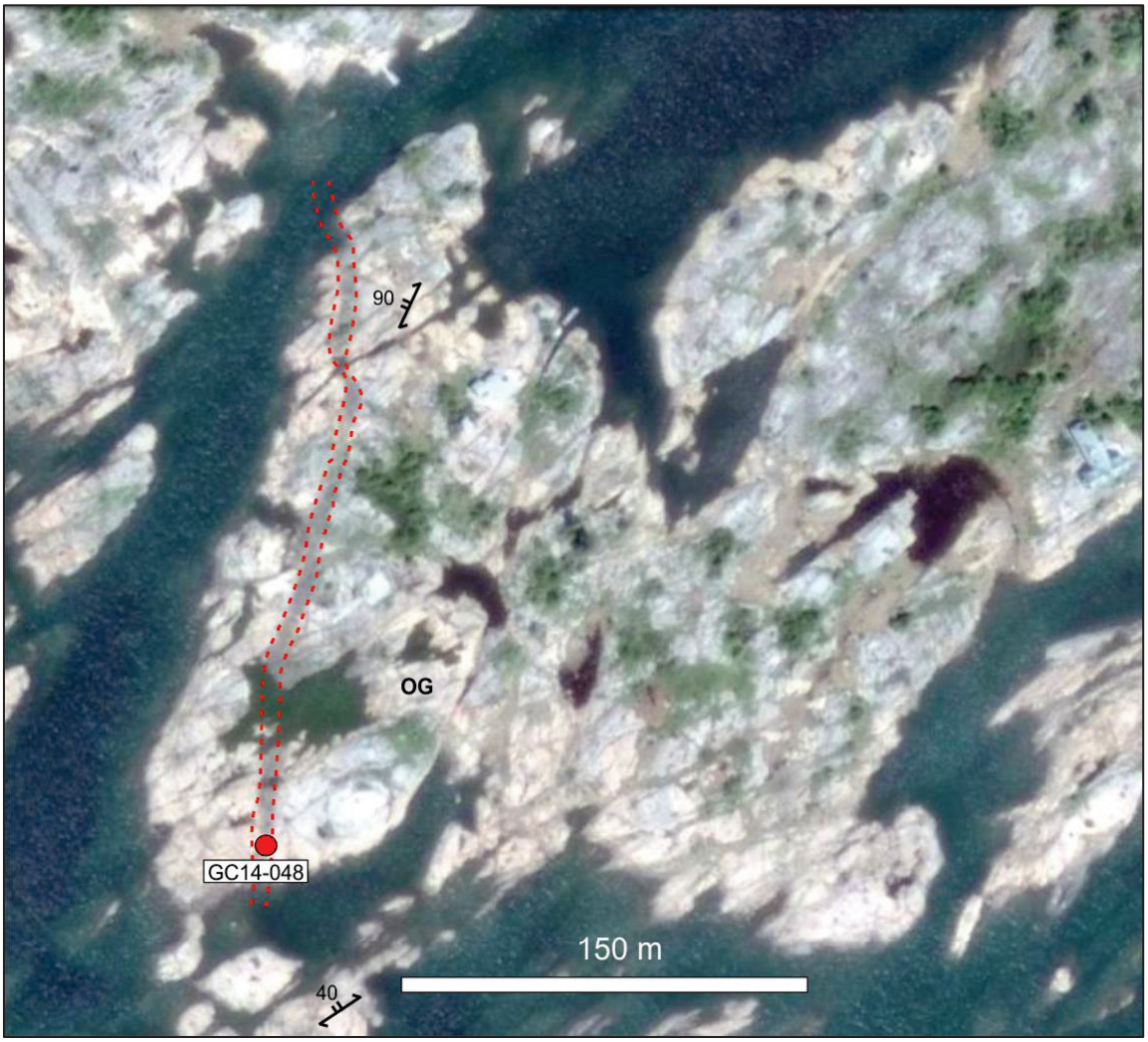

Figure 2.9 Satellite image of H. A. Gray Island, Point au Baril, showing GC14-048 sample location. This ~4 m wide dyke, hosted in 1430-1460 Ma leucocratic granite orthogneiss (OG) of the Point au Baril Complex, is the southernmost metadiabase body with confirmed SD affinity in the Britt Domain. It crops out < 2 km from the SSZ. Satellite image from Google Earth.

Figure 2.10 GC14-048 sample locality, H.A. Gray Island, Point au Baril. A) SmD cuts Point au Baril Complex orthogneiss fabrics sharply, at a high angle. B) Perfectly preserved subophitic texture with characteristic plagioclase megacryst (here quite small; lower center). Fine-grained garnet coronas are clearly visible throughout (scale card shows centimetres). C) A unique fine-grained concentration of leucocratic material, within SmD (centre) and along the contact, with faint foliation (dashed lines, center) oblique to host gneissosity (solid lines, left). Scale card shows centimeters (A-C) and inches (A).

2.6 Summary

The western CGB of the Grenville Province hosts numerous suites of mafic intrusions, most of which predate Grenvillian orogenesis. Emplaced within the Laurentian margin prior to the Grenvillian Orogeny, SmD records an exclusively Grevillian metamorphic history and is a potential, unambiguous monitor of the P-T conditions and times of peak metamorphism across the polycyclic parautochthonous BD.

Sudbury metadiabase is distinguishable from other, typically older, metabasite rocks in the field by a set of distinctive features related to primary igneous characteristics. These include a well preserved medium- to fine-grained sub-ophitic texture, chilled margins that cut host foliations, subhedral, grey-green plagioclase megacrysts, prominent and commonly stippled leopard-spotted weathering surfaces with a red-brown hue, and internal contacts indicating multiple phases of dyke injection and, locally, magma mingling. SmD samples were collected from Bigsby Island, Lamondin Point, and H. A. Gray Island at Point au Baril, to represent the northern, central, and southern regions of the study area, respectively.

Undeformed SD in the Southern and Superior Province north of the GF were progressively deformed and boudinaged southward across the GFTZ (Bethune and Davidson, 1988, 1997; Bethune, 1989, 1993, 1997). South of the GFTZ, tectonically segmented SmD appears to be progressively reworked from N to S across the BD. On the local scale, paragneiss-hosted SmD segments are invariably more deformed than orthogneiss-hosted segments, and overprinted by retrograde amphibolite-facies assemblages. Generally, neither peak granulite-facies assemblages nor primary subophitic textures are preserved in paragneiss-hosted SmD. Similarly, small (m-scale) SmD

segments and the margins of large, shear-bounded blocks are commonly amphibolitized and strongly foliated. The strain-resistant cores of large, well preserved SmD segments, however, clearly preserve granulite facies mineral assemblages overprinting the primary subophitic texture.

Chapter 3: Petrography and Geochemistry

3.1 Introduction

Regional metamorphism in very old continental crust commonly involves multiple phases of overprinting, reflecting polycyclic tectonic histories. Where multiple overprinting events involve similar metamorphic conditions, or produce tectonic fabrics of similar orientation, distinguishing discrete assemblages representing disparate orogenic events can be extremely challenging. The ca. 1235 Ma Sudbury Diabase (SD) dyke swarm, hosted in rocks of the Laurentian margin variably affected by previous high-grade regional metamorphic events, preserves an exclusively Grenvillian metamorphic overprint. This chapter focuses on documenting progressive changes in mineral assemblages and textures, and describing and assessing appropriate Sudbury metadiabase (SmD) metamorphic assemblages throughout the Britt Domain for the purposes of producing reliable pressure and temperature data.

Calculations for pressure and temperature information require thermodynamic equilibrium within a system. Textural equilibrium in metamorphic rocks requires, among other things, that all phases be in contact, and thus available to react, with all other phases. That portion of a mineral assemblage in a given rock which participates in metamorphic reactions is called the reaction volume. Corona textures are mono- or polymineralic rims that surround and isolate particular minerals, effectively removing them from the reaction volume. The presence of corona textures, by definition, implies disequilibrium. It is possible, however, to identify mineral associations in textural subdomains in local chemical equilibrium (Grant, 1987). A nuanced understanding of

metamorphic textural development and carefully targeted in situ microanalysis allows not only for the production of meaningful P-T estimates, but subsequent correlation of these estimates with age data.

This chapter begins with a summary of early metamorphic development of the SmD from igneous protolith to two-pyroxene coronitic metadiabase. Subsequent petrographic descriptions present textural and mineral assemblage information and mineral chemical data that will contribute to calculations of P-T for representative samples from the northern, central, and southern Britt Domain, respectively. Lastly, the geochemistry of characteristic major, trace, and rare earth elements is used to test the affinity of the sampled metabasites by comparison with the geochemical fingerprint of known SD and SmD outcrops.

3.2 SD in the Superior and Southern Provinces, and the GFTZ

Bethune (1989) and Bethune and Davidson (1997) defined four metamorphic zones describing a metamorphic field gradient across the GF and through the GFTZ based on the distribution of corona-forming assemblages and major shifts in metamorphic grade, microtexture, structural orientation, and lithological continuity of the SD dykes (Fig. 3.1). The primary features of each zone are summarised in Table 3.1. The following discussion is a summary of that work.

Zone I includes fresh, unaltered SD north of the GF. Dykes of the Sudbury swarm trend uniformly SE, cutting Huronian metasediments of the Southern Province and late Paleoproterozoic and early Mesoproterozoic granitic plutons of the Superior Province. The diabase tends to be fine- to medium-grained and subophitic, composed primarily of

plagioclase, augite, olivine, and Fe-Ti oxide. Accessory minerals include apatite, biotite, and variably perthitic K-feldspar interstitial to Plagioclase laths. Biotite is present as single crystals adjacent to and partly rimming Fe-Ti oxide. Present in trace amounts are sulphides (pyrite, pyrrhotite, and chalcopyrite), and baddeleyite (ZrO_2), which was dated to obtain the primary age of intrusion (ca. 1235 Ma., Krogh et al., 1987; Dudàs et al, 1994).

Porphyritic vs. non-porphyritic and enriched vs. normal varieties of SD in the Southern and Superior Provinces were distinguished by Bethune (1993) based on the presence or absence of plagioclase megacrysts (section 2.2), and relative enrichments in Fe, K, Ba, Ti, P, and LREE that are characteristic of SD and SmD. Optically, plagioclase megacrysts show no evidence of zoning from a calcic core (An_{60}) with the exception of a narrow sodic rind (An_{30-40}) associated with rounded, partially resorbed crystal margins (Bethune and Davidson, 1997). Matrix plagioclase laths in normal diabase are zoned, grading from An_{60} cores to An_{38} rims, while core-to-rim compositions in less common, enriched diabase grade from An_{54} to An_{30}. Primary olivine is present both as ≤ 5 mm inclusions within or adjacent to plagioclase megacrysts and as isolated phenocrysts ≤ 1 cm in diameter in the groundmass. Megacrysts and included olivine are chemically more primitive than the accompanying phases in the groundmass, with $\leq Fo_{70}$ and $\sim Fo_{40}$, respectively. Primary interstitial clinopyroxene falls within the augite field (e.g. $En_{35}Fs_{17}Wo_{35}$) with minor jadite and tschermakite components (e.g. Jd_4 and Tsc_9) and elevated titanium (Bethune and Davidson, 1997).

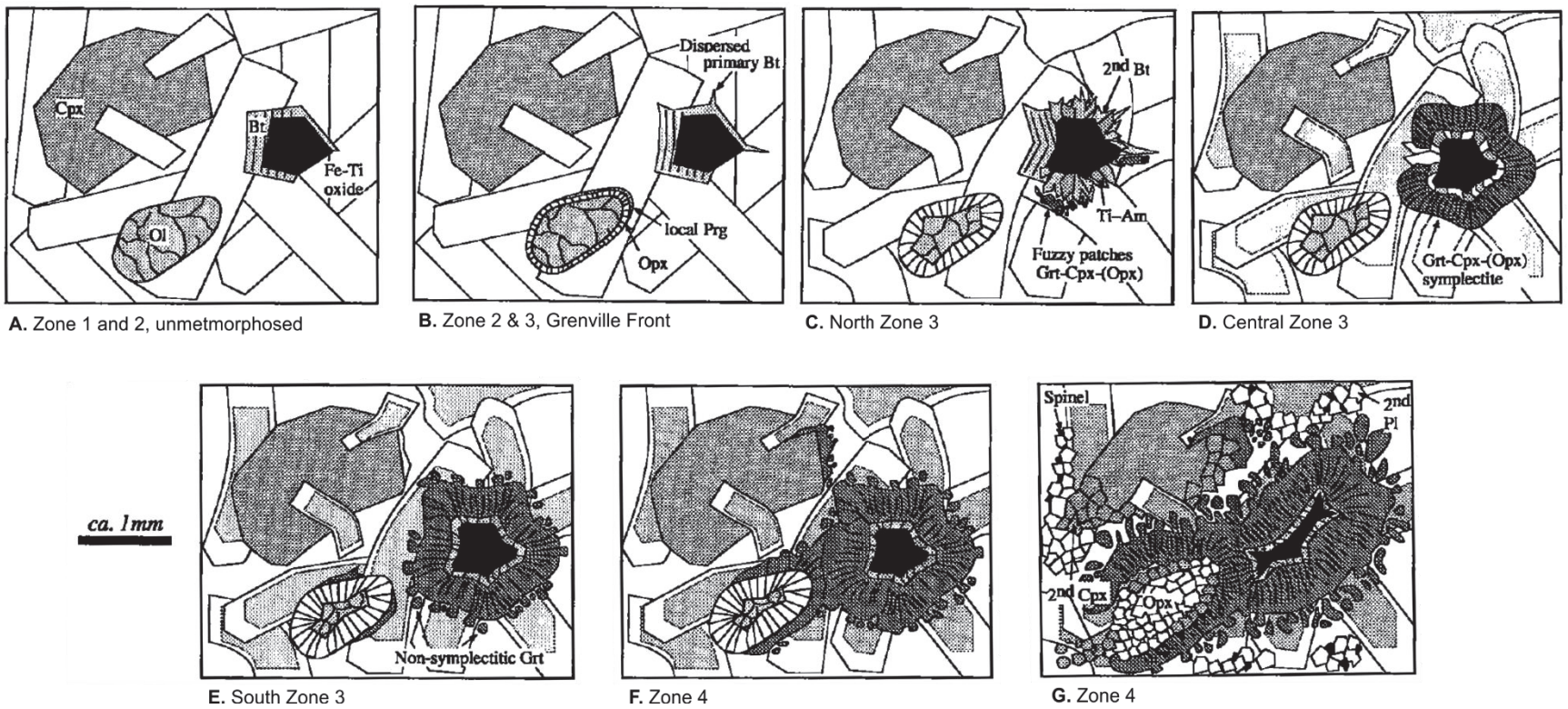

Figure 3.1 Schematic textural representation of progressive metamorphic sequence around primary Ol and Fe-Ti oxide in Sudbury diabase north of the study area (from Bethune and Davidson, 1997). A. Unmetamorphosed subophitic texture typical of Zone 1 and unaltered parts of Zone 2. B. Onset of corona-forming reactions at the Grenville Front. Narrow rim of Opx surrounds Ol. Primary Bt partly recrystallized and dispersed. C. Opx rims widen. Secondary Bt and olive-green Ti-Amph overgrow primary Bt. Fuzzy patches of garnet-pyroxene symplectite nucleate in Pl beside Fe-Ti coronas. D. Grt-Px symplectite forms complete rim. The cores of Pl laths begin to show distinct clouding by sub-microscopic spinel. E. Grt-Px symplectite rim widens, overprinting Pl laths. Outermost Grt growths are idioblastic, lack pyroxene intergrowths. F. Grt-Px symplectite is evident around Ol coronas and local insipient growth between Pl and other minerals. Core of Pl more strongly clouded. G. Grt-Px symplectite fully encircles both Fe-Ti oxide and Ol, which are strongly embayed. Ol "core" is replaced by granoblastic mosaic of fine Opx. Grt encroaches further on Pl laths, which has locally recrystallized, exsolving discrete grains of Sp.

The groundmass of porphyritic SD is texturally and mineralogically identical to non-porphyritic diabase. Given this, the lack of distinguishing chemical trends in the groundmasses of each variety, and compelling evidence from site GC14-023 for the xenocrystic nature of plagioclase megacrysts (Fig. 2.2), the term porphyritic and non-porphyritic are maintained, where convenient, for descriptive purposes only.

The boundary between zone I and II follows the NE trending northern contact of the ca. 1.47 Ga Bell Lake granite. SD in zone two shows no sign of metamorphism except near faults. Sheared SD near the faults contain chlorite, actinolite, and epidote. Olivine inclusions in plagioclase megacrysts are variably replaced by carbonate, serpentine, chlorite and cummingtonite, reflecting greenschist facies metamorphism strongly controlled by the availability of fluids (Bethune and Davidson, 1997).

The transition from zone II to III spans the GF, and corresponds to both the first development of metamorphic coronas around olivine and Fe-Ti oxides and the onset of penetrative deformation of primary minerals, principally plagioclase. Southward, the first corona textures to develop are narrow rims of orthopyroxene surrounding olivine, itself surrounded by thin, discontinuous rims of pale green amphibole. Farther south in zone III, this amphibole rim disappears as orthopyroxene coronas widen, further replacing the olivine. Primary augite throughout the study area becomes noticeably darker within and beyond zone III owing to the exsolution of very fine ilmenite and, rarely, rutile lamellae. Primary augite is readily identifiable in SmD throughout the parautochthon by the presence of these lamellae, and does not participate in corona-forming reactions despite varying degrees of resorption. Primary biotite becomes progressively overgrown by fine-grained granoblastic secondary biotite that is locally intergrown with green amphibole.

Garnet-pyroxene symplectite first forms as small, high-relief "fuzzy patches" within plagioclase near biotite and amphibole coronas around Fe-Ti oxide. Toward the centre of zone III, symplectites extend to form continuous rims overprinting primary plagioclase laths, features roughly coincident with the first formation of pervasive and highly concentrated sub-microscopic spinel "dust" in plagioclase laths.

Toward and within zone IV, spinel dusting becomes more intense in plagioclase laths and garnet-pyroxene symplectite coronas broaden around matrix olivine and Fe-Ti oxide. The outer surface of the garnet symplectite is generally free of pyroxene intergrowths and forms discrete, faceted garnet grains overprinting the relict laths. Matrix olivine is completely replaced by a mosaic of fine-grained granoblastic orthopyroxene that is commonly rimmed by a narrow band of equigranular granoblastic clinopyroxene (e.g. Fig. 3.3b). The clinopyroxene mosaic rim is typically separated from the garnet-pyroxene symplectite coronas by a narrow "moats" of oligoclase. Recrystallization is variable and restricted largely to the rims and twin planes of relict plagioclase laths (Bethune and Davidson, 1997). The coincident coalescence of spinel into coarser grains renders recrystallized plagioclase conspicuous both optically and in back-scatter electron (BSE) images by its lack of spinel dusting.

Table 3.1 Sudbury diabase metamorphic sequence north of the study area (Bethune and Davidson, 1997)

Zone	Location	Metamorphic Features
1	Southern Province	Unmetamorphosed and undeformed subophitic texture - matrix Pl core-rim An_{60}-An_{38} - matrix Ol Fo_{47-36}
2	Southern Province, < 4 km NW of the GF	Generally unmetamorphosed - local shearing and greenschist assemblage (Chl, Act, Ep) along steep faults - bound by broad mylonite zone to the south, the Grenville Front (GF)
	GF	
3	Northern GFTZ	Deformed Pl laths Initial coronas: - Opx on Ol - 2nd Bt on Ilm, followed by Grt-Cpx symplectite - Sp clouding Ca-rich Pl lath cores - non-symplectite Grt begins overgrowing Pl
4	Central to Southern GFTZ	- Granoblastic Px mosaics, Opx core with Cpx rim, after Ol - Grt-Cpx symplectite corona around Px mosaics - 2nd Pl, granoblastic

Bethune and Davdison (1997) suggested that the corona-forming metamorphic mineral assemblages around matrix olivine (1a,b) and Fe-Ti oxide (2a) observed in SmD within the GFTZ could be produced by the following generalized metamorphic reactions:

$$1a)\ Ol + Pl_1 = Opx + Cpx + Grt + Sp + Pl_2 \quad (3.1)$$

$$1b)\ Ol + Pl_1 = Opx + Prg + Sp + Pl_2 \quad (3.2)$$

$$2a)\ \text{Fe-Ti oxide} + Pl_1 = \text{Ti-Bt} + \text{Ti-Amp} + Grt + Pl_2 \quad (3.3)$$

where Pl_1 and Pl_2 refer to primary and secondary plagioclase, respectively, the latter which is part of the metamorphic assemblage.

3.3 Sudbury metadiabase across the Britt Domain

Corona textures observed in SmD throughout the Britt Domain are equivalent to those developed within metamorphic zone IV of Bethune (1997) and Bethune and Davidson (1997). Within strain-resistant cores of boudinaged and variably deformed SmD dyke segments immediately south of the GFTZ, early corona textures and assemblages observed within the GFTZ are partially overprinted by prograde metamorphic recrystallization and subsequent late alteration. When discussing microdomain textures specific to coronitic phases the term 'inner' is used to describe the margin of a particular layer that is closer to the core mineral (Fig. 3.3 a). Here, these minerals are olivine (mosaic Opx - Cpx pseudomorphs) and Fe-Ti oxide. The opposing margin, farther from the core mineral, is referred to as 'outer'.

The NW - to - SE-trending textural and metamorphic sequence reported for the GFTZ breaks down within the parautochthonous Britt Domain. Coronitic textural associations correlating to metamorphic zone IV are best preserved in the NW, where garnet-pyroxene symplectite and Opx + Cpx mosaic after olivine are largely unaltered. Upper amphibolite- to granulite-facies peak assemblages are preserved in all regions, but increasing degrees of garnet and plagioclase recrystallization toward the SE indicate more protracted residence at peak conditions than in the NW. Figure 3.3 illustrates the textural associations observed for each region of the study area. In contrast to the NW-to-SE progression presented for the GFTZ, the development of metamorphic assemblages and retrograde overprinting varies greatly on local scales, indicating that the Britt domain preserves a more complex metamorphic history.

Figure 3.2 (following page) Schematic illustration of coronitic textural associations in SmD of the Britt domain. (A) Garnet-pyroxene symplectite around Px mosaic after Ol is preserved as a highly irregular and inclusion-rich 'inner' surface of the garnet corona. The idiomorphic 'outer' surface is inclusion-free except for fine, regularly oriented Sp rods. B-D represent north, central, and southern regions, respectively. (B) Corona assemblage in the northern region is broadly consistent with metamorphic zone IV of Bethune and Davidson (1997; Fig. 3.1). Symplectite surrounding Ilm is very well preserved, though Px is largely replaced by Bt. (C) Grt corona is discontinuous and inclusion-rich, but commonly overprints the cores of relict Pl laths. Cpx outer rim is largely absent from mosaics, but present as inclusions and granoblastic intergrowths with Opx. Pargasite commonly overprints both Ol and Ilm corona assemblages. (D) The Grt coronas thicken and progressively overprint Pl laths. Symplectite is weakly preserved around Px mosaic as an irregular inner surface of the Grt corona with abundant inclusions of Pl. Corona of Bt around Ilm is strongly overprinted by Prg. Ilm is heavily embayed and replaced by granoblastic Bt. Relict Aug, though clouded by fine lamellae of Ilm, commonly displays a narrow lamellae-free rim but no obvious reaction rim textures.

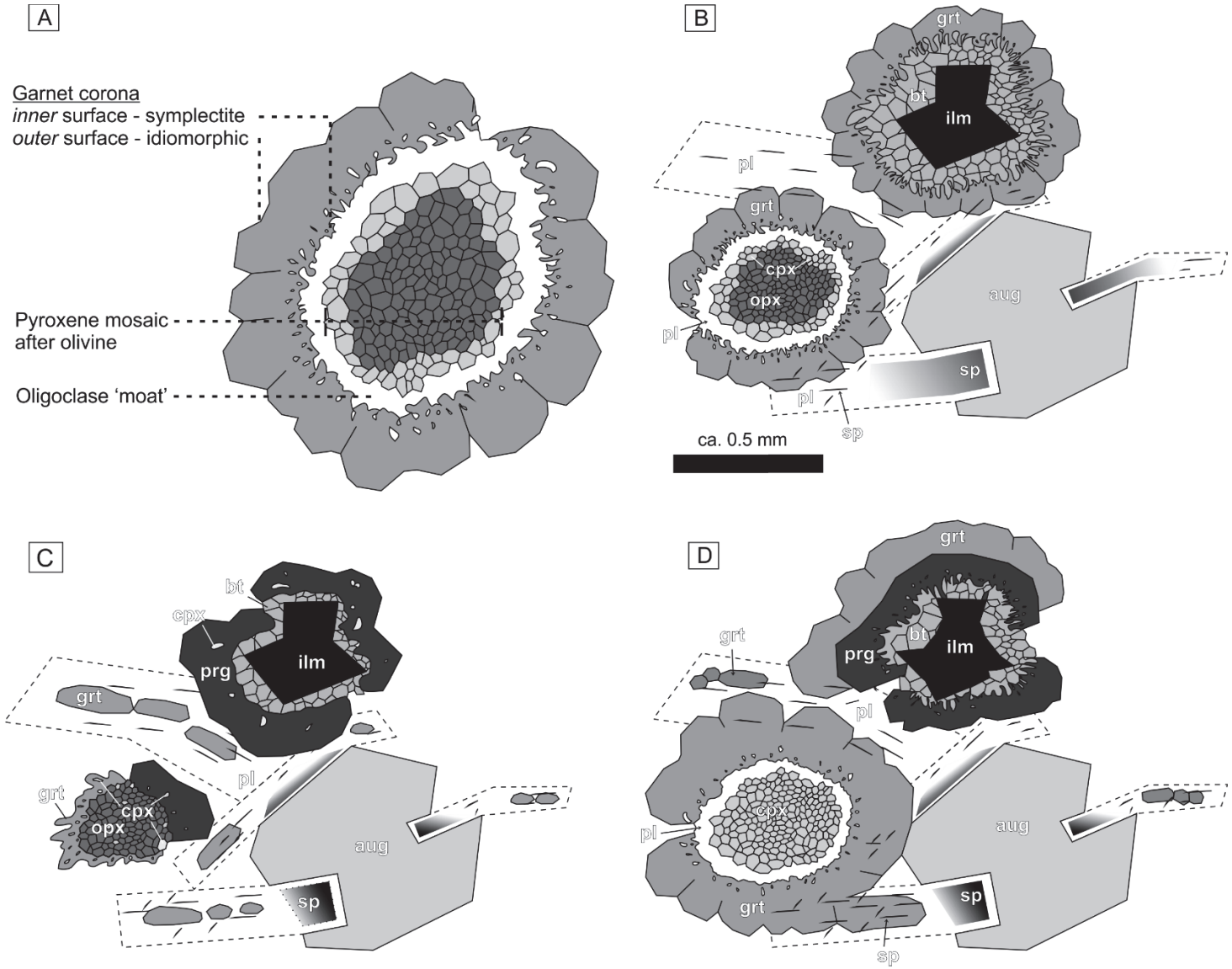
A
Garnet corona
inner surface - symplectite
outer surface - idiomorphic
Pyroxene mosaic
after olivine
Oligoclase 'moat'
B
grt
bt
ilm
pl
grt
cpx
opx
aug
pl
sp
pl
sp
ca. 0.5 mm
C
bt
cpx
ilm
prg
grt
pl
grt
cpx
opx
aug
sp
D
grt
grt
bt
ilm
prg
pl
cpx
aug
pl
grt
sp
sp

3.3.1 Northern Britt Domain: Key Harbour

The numerous well exposed outcrops of SmD in the Key Harbour archipelago (Corrigan, 1990; Corrigan et al., 1994) present a unique opportunity to examine heterogeneous development of coronitic textures. Diabase hosted in disparate rock types within local areas, such as a large island or group of islands, is assumed to have experienced similar pressures and temperatures. Samples GC14-055, -057 and -058 represent a spectrum of textures preserved in the strain-resistant cores of SmD hosted in granodiorite and leucocratic orthogneisses of the Key Harbour gneiss association. Sample GC14-057, from Bigsby Island, is considered representative of the northern region of the study area largely owing to its well preserved peak metamorphic assemblage and coronitic textural associations. Heterogeneous SmD metamorphism across Key Harbour is illustrated by samples from bodies hosted in leucocratic gneiss (GC14-058) roughly 800 m to the SW of Bigsby Island, and Mann Island granodiorite (GC14-055) 1 km to the NE.

3.3.1.1 GC14-057, Bigsby Island

The morphology of relict plagioclase laths is easily recognizable macroscopically, though large portions of the relict laths have been recrystallized and/or overprinted by garnet. Relict plagioclase laths (An_{28-30}) are most conspicuous, microscopically, by dense spinel dusting. Most virtually opaque, densely spinel-dusted plagioclase is partially enveloped by or immediately adjacent to coarse relict augite. Away from relict augite, plagioclase laths are bent and variably recrystallized to ~An_{16} metamorphic subgrains that are free of spinel inclusions and which show a distinct lattice preferred orientation

(observed optically, using a retardation plate in cross-polarized light). This suggests that coarse, relatively competent relict augite shielded the enveloped and adjacent plagioclase laths from deformation-induced recrystallization, allowing the retention of spinel-dusted cores. Metamorphic plagioclase grains are roughly equant, range in size from ~30-60 μm, and are generally equigranular with metamorphic pyroxene and biotite. Locally, spinel inclusions coalesce and coarsen, forming extremely fine, consistently oriented rods proximal to the recrystallized sectors of larger relict plagioclase laths. In places, these rods can be found as inclusions in coarser overprinting garnet and within the outer margin of garnet coronas. Oligoclase moats (An_{12-18}) < 0.1 mm wide separate granoblastic clinopyroxene from the inner margin of garnet coronas. The irregular inner margins of garnet coronas contain abundant micron-scale inclusions of oligoclase.

Coronitic textures around primary Fe-Ti oxides accord largely with those observed in GFTZ zone IV. Primary biotite is almost entirely replaced by fine-grained granoblastic biotite ranging Phl_{56-65}. Significantly, biotite closely intergrown with garnet is the least Fe-rich, with Phl_{65}: all other biotite compositions for GC14-057 fall within Phl_{56-62}. Where primary ilmenite and biotite were initially in contact with plagioclase, the outer margin of granoblastic biotite coronas is finely intergrown with clinopyroxene and garnet, interpreted to be the recrystallized remnants of early pyroxene-garnet symplectites (Fig. 3.2a). These relict symplectites are coarser than those preserved between metamorphic pyroxenes after olivine and adjacent to plagioclase, and commonly contain very fine inclusions of pyroxene and biotite. Locally, individual biotite grains are intergrown with metamorphic clinopyroxene, and less commonly form fine, irregular growths around relict augite. No amphibole is found in this sample.

Coarse relict augite (originally titanaugite) in sample GC14-057 ($Wo_{45}En_{38}Fs_{17}$) is strongly clouded by submicroscopic ilmenite. Variations in ilmenite lamellae density within relict augite reflect primary igneous sector zonation, and less commonly, simple twin boundaries. Local neoblasts of clinopyroxene are found as small aggregates on apices of the relict grains. Minor fine, metamorphic biotite fringes relict augite. Beyond this, coarse relict augite shows no evidence of resorbtion and does not appear to participate significantly in corona-forming reactions. Metamorphic pyroxene is largely restricted to granoblastic pseudomorphs after olivine consisting of an orthopyroxene core (En_{56-59}) rimmed by clinopyroxene ($Wo_{43-45}En_{36-38}Fs_{18-20}$). Individual grains are ≤ 80 μm across, generally show straight boundaries with clear triple-point junctions, and are virtually inclusion-free. Though not visible optically, back-scatter electron (BSE) images show faint lamellae in the cores of the coarsest metamorphic clinopyroxene grains. Neither pyroxene phase shows evidence of retrograde overprinting or late alteration.

Garnet is the dominant corona-forming phase in SmD, forming virtually continuous rims around all primary Fe-Ti oxides and pyroxene pseudomorphs after olivine (Fig. 3.3a,b). Compositions are relatively homogenous ($Grs_{16-18}Pyr_{22-25}Alm_{58-62}$), showing no significant chemical zonation or compositional trends across textural microdomains. A highly irregular, inclusion-rich inner margin dominated by extremely fine (≤ 5 μm) plagioclase and clinopyroxene inclusions is interpreted to represent the progressive growth of early, vermicular garnet overprinting and isolating other early symplectite phases (Fig. 3.3a). The coarsest garnets extend from outer corona margin or form idioblastic grains within relict plagioclase cores. The idioblastic garnets are generally texturally and compositionally homogenous with minor inclusions of spinel and

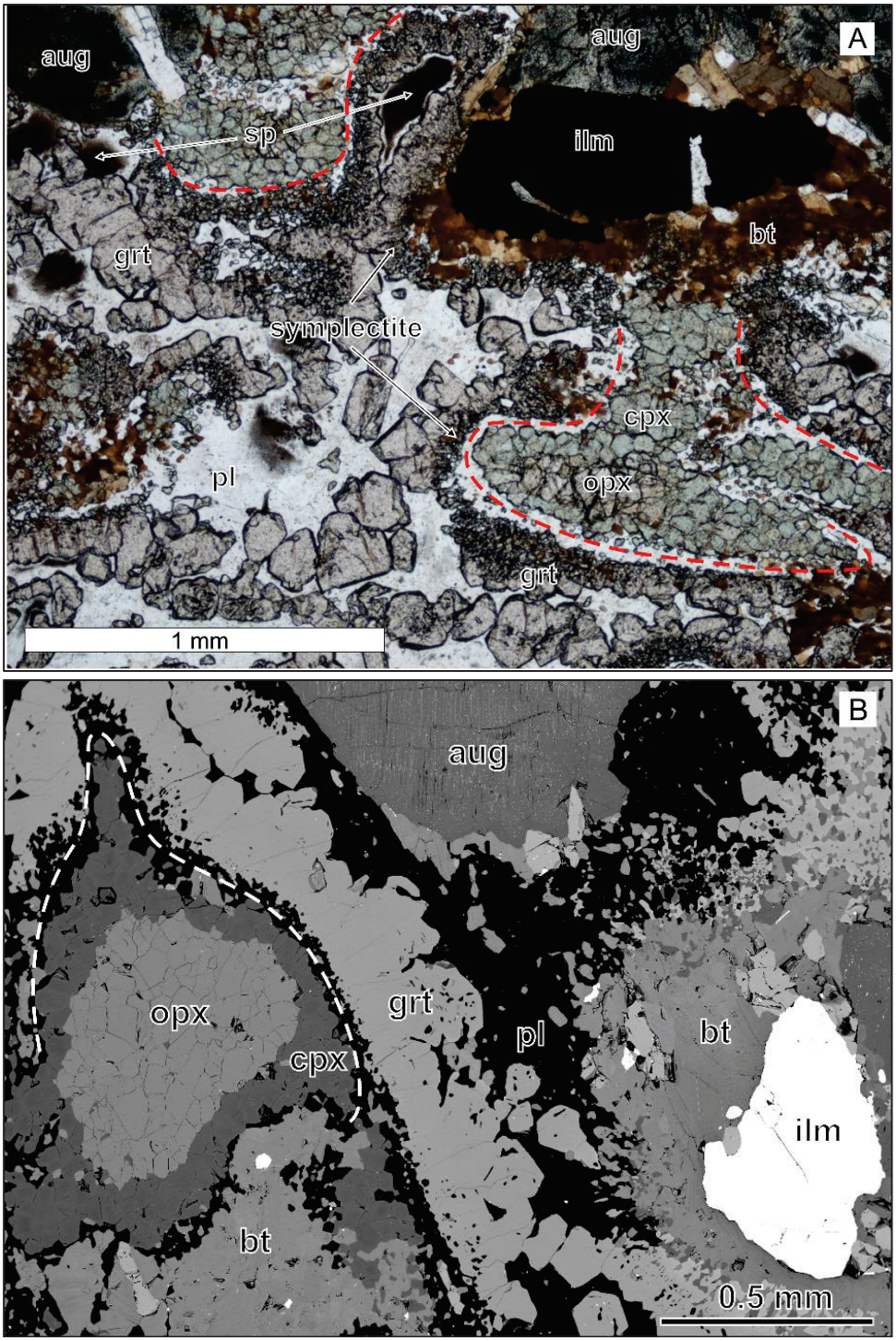

Figure 3.3 Corona textures, sample GC14-057, northern Britt Domain. Relict Aug is clouded with Ilm lamellae (A, top left and right; B, top centre). Relict Pl is strongly overprinted by Grt; dense Sp dusting proximal to relict Aug (A, top left). Granoblastic Opx + Cpx mosaic pseudomorphs after Ol (A, lower right; B, centre left). Olg moat (dashed line A, red; B, white) separates metamorphic Cpx from recrystallized Grt symplectite coronas.

plagioclase, and preferentially overgrow densely spinel-dusted regions of relict

plagioclase laths (Fig. 3.3b). Locally, garnet completely overprints primary plagioclase laths to form tabular pseudomorphs after plagioclase.

Main accessory phases include apatite, Fe-sulphide, zircon, and rare monazite. Apatite forms conspicuous mm-scale, clear, inclusion-free columns that show no reaction textures with adjacent minerals. Monazite is present almost exclusively within Ap fractures. Zircons are concentrated where ilmenite has been resorbed and replaced by biotite and amphibole. They invariably form small grains decorating the edges of, or less commonly, removed from but aligned parallel to the boundaries of Fe-Ti oxides. The latter, referred to as a 'string of beads' texture, is interpreted to indicate the previous extent of the oxide grain boundary prior to embayment and retreat (Corfu et al., 2003; Austrheim et al., 2008). Zircons rarely exceed 40 μm in size, and most are < 20 μm. Zircon textures in samples selected for geochronology are discussed in detail in chapter 5.

3.3.1.2 GC14-055, Mann Island

Spinel dusting of relict plagioclase is subdued in GC14-055, rarely approaching the opacity observed elsewhere. Laths are neither bent nor kinked, and show no lattice preferred orientation. Primary igneous zoning patterns are preserved, though compositional ranges (An_{22-31}) are much narrower and lower than those reported for the GFTZ (Bethune and Davidson, 1997).

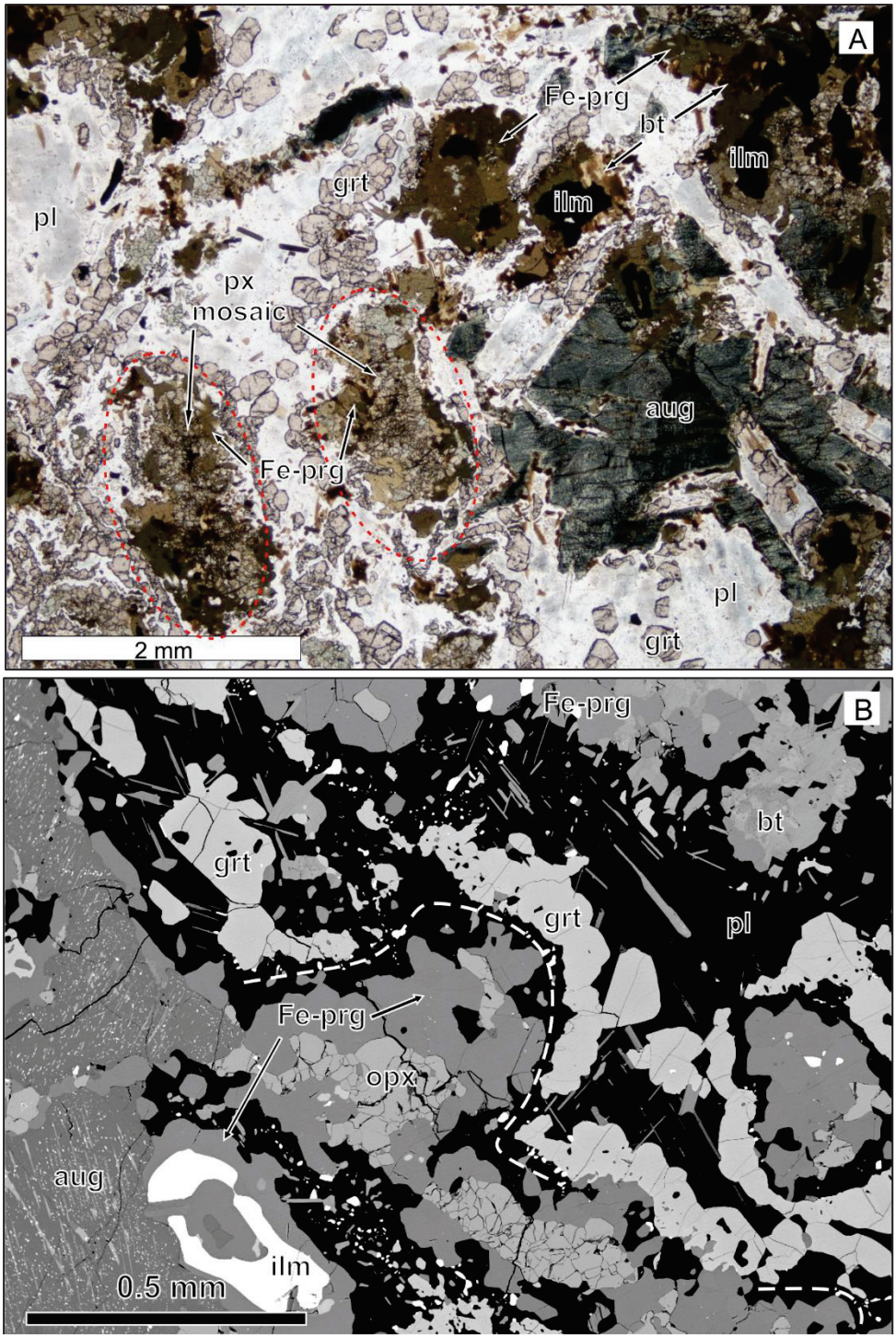

Figure 3.4 Corona textures, sample GC14-055, northern Britt Domain. A) Optical image in PPL. Undeformed relict Pl laths only slightly Sp dusted (A, upper left and lower right) with fine, needle-like inclusions of regularly oriented Bt. Remnants of Olg moat (B, dashed white line). Relict Aug clouded by very fine lamellae of Ilm and Opx. Granoblastic Cpx virtually absent from pyroxene mosaic after Ol (A, dashed red ovals) following overprint by dark brown-green Fe-Prg that semi-continuously envelope Opx (A and B). Sporadic inclusions of Pl in garnet adjacent Fe-Prg (B, lower right) are remnants of recrystalized Grt - Px symplectite.

The main difference between SmD from Bigsby Island vs. Mann Island is a strong retrograde overprint of the peak assemblage in the latter, with abundant dark green-brown amphibole (potassic-ferro-pargasite; Leake, 1997) (Fig. 3.3a). Biotite coronas around Fe-Ti oxide are almost entirely replaced by relatively coarse (≤ 0.5 mm) single crystals of amphibole. Ilmenite embayment is more advanced, with some xenoblastic amphibole porphyroblasts containing only small relicts of the original oxide grains (Fig. 3.3b).

Pyroxene mosaics after olivine are still recognizable but variably affected by retrograde alteration (Fig. 3.4a). Locally, rims of granoblastic clinopyroxene remain unaltered. Core orthopyroxene grains (En_{51-54}), however, are strongly retrogressed and converted to fibrous ortho-amphibole. More commonly, metamorphic clinopyroxene is completely overprinted by coarse ferro-pargasite, leaving granoblastic orthopyroxene entirely unaffected (Fig. 3.4b). In this sample, the composition of metamorphic clinopyroxene is indistinguishable from the relict augite ($Wo_{46-47}En_{35-36}Fs_{17-19}$).

Garnet coronas ($Grs_{16-18}Pyr_{18-21}Alm_{59-62}$) surrounding the pyroxene mosaics are texturally well equilibrated, forming semi-continuous bands of idioblastic to subidioblastic grains. Garnet-pyroxene symplectite is almost totally obliterated, preserved only as uncommon, slightly irregular garnet grain boundaries proximal to hornblende porphyroblasts and pyroxene mosaics. Discontinuous plagioclase moats separate garnet from the remnants of the pyroxene mosaics (Fig. 3.4a).

3.3.1.3 GC14-058, Keefer Island

Like sample GC14-057, GC14-058 is hosted in leucocratic gneiss, but in contrast, overprinting of relict plagioclase (An_{32}) laths by garnet and spinel is almost complete.

Garnet-pyroxene symplectites are perfectly preserved proximal to both pyroxene mosaic pseudomorphs and Fe-Ti oxides (Fig. 3.5c). Growth of garnet ($Grs_{16-18}Pyr_{18-23}Alm_{60-64}$) into adjacent plagioclase appears to be coeval with pervasive nucleation of new garnet within the lath cores, as both are densely overprinted by idioblastic garnet (Fig. 3.5a). Spinel dusting in the remaining relict plagioclase renders it virtually opaque. Metamorphic plagioclase (An_{16-20}) is difficult to identify optically, owing to the pervasive garnet overprint and general lack of spinel dusting. The boundary between overprinting garnet and opaque relict plagioclase is marked by a zone roughly 0.5 mm wide in which spinel coalesces and coarsens proximal to the garnet.

Despite the preservation of delicate symplectite textures, pyroxene mosaic pseudomorphs are strongly retrogressed. Orthopyroxene in the core is completely altered to pseudomorphs of carbonate and fibrous ortho-amphibole, as are the exsolved cores of granoblastic clinopyroxene ($Wo_{43-46}En_{35-38}Fs_{17-21}$) (Fig. 3.5a). Clinopyroxene rims around orthopyroxene mosaics are commonly no wider than a single grain.

The corona textures surrounding primary Fe-Ti oxides are similar to those in GC14-057. Ilmenite is variably embayed though largely intact. Primary, single-crystal biotite is largely recrystallized to aggregates of equant grains (Phl_{54-58}), roughly equigranular with metamorphic clinopyroxene in the same sample.

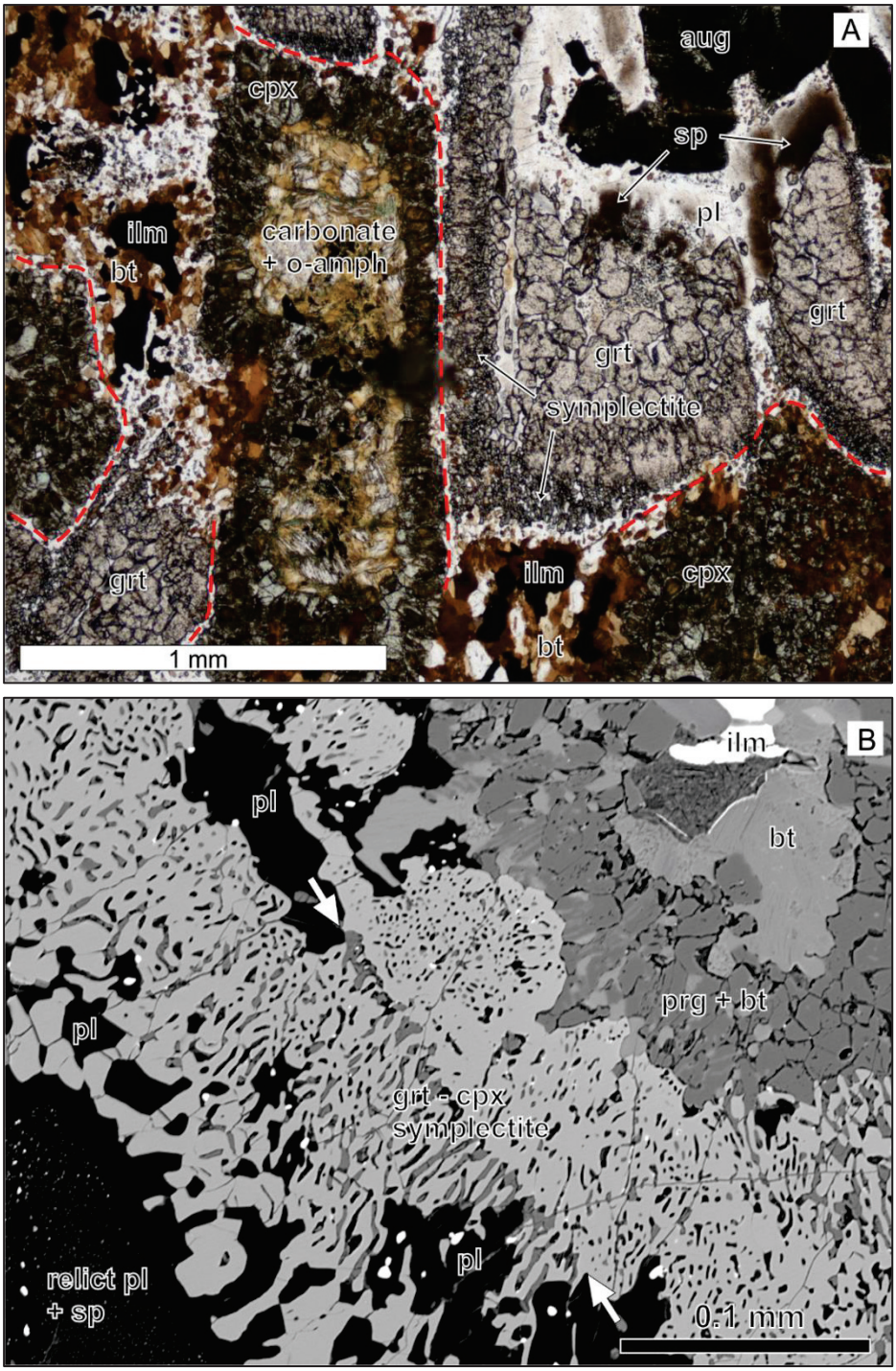

Figure 3.5 Corona textures, sample GC14-058, northern Britt Domain. A) photomicrograph in PPL showing heavily altered Px mosaics after Ol (left of center, bottom right) with the core minerals completely altered to a fine intergrowth of Oam and carbonate. Note the altered cores of Cpx grains around the mosaic rim. Pl laths strongly overprinted by Grt (A, center right, far right, bottom left) Dashed line (A, red) indicates oligoclase moats separating mosaic pyroxene from garnet symplectite. Sp dusting renders relict laths opaque (upper right). B) BSE image detail of corona sequence and Grt-Px symplectite around heavily embayed Ilm grain (upper right). Original Pl lath boundary indicated between white arrows.

3.3.2 Central Britt Domain

The central domain is represented by sample GC14-024, taken from Lamondin Point at the mouth of Byng Inlet. Early coronitic textures are moderately well preserved, although strongly overprinted by ferropargasite.

Unlike relict plagioclase in representative SmD samples to the north and south, plagioclase laths preserve relict igneous zoning and generally show very little spinel dusting (Fig. 3.6a). Metamorphic plagioclase compositions are tightly clustered (An_{12-15}). Relict laths show no evidence of bending or kinking, and neither a shape nor lattice preferred orientation is visible petrographically.

Relict primary augite is conspicuous both by its size and moderately dense clouding by fine exsolution lamellae of ilmenite. In contrast to samples to the north and south, relict augite in sample GC14-024 contains less exsolved ilmenite, a broad lamellae-free margin, and local, ilmenite-free sectors. Relict augite is not affected by corona-forming reactions (Fig. 3.6a, center right; b, upper left).

Relict Fe-Ti oxide retains the early corona of granoblastic biotite (Phl_{43-45}), which is, in turn, rimmed by relatively coarse, single crystals of ferropargasite. No garnet-pyroxene symplectite is preserved; only discontinuous bands of inclusion-rich, xenoblastic garnet proximal to the amphibole corona hint at early garnet coronas (e.g. 'fuzzy patch' symplectite illustrated in figure 3.1c). Coarse primary ilmenite is commonly intergrown with mag, and xenoblastic zircon is found along and proximal to primary oxide grain boundaries.

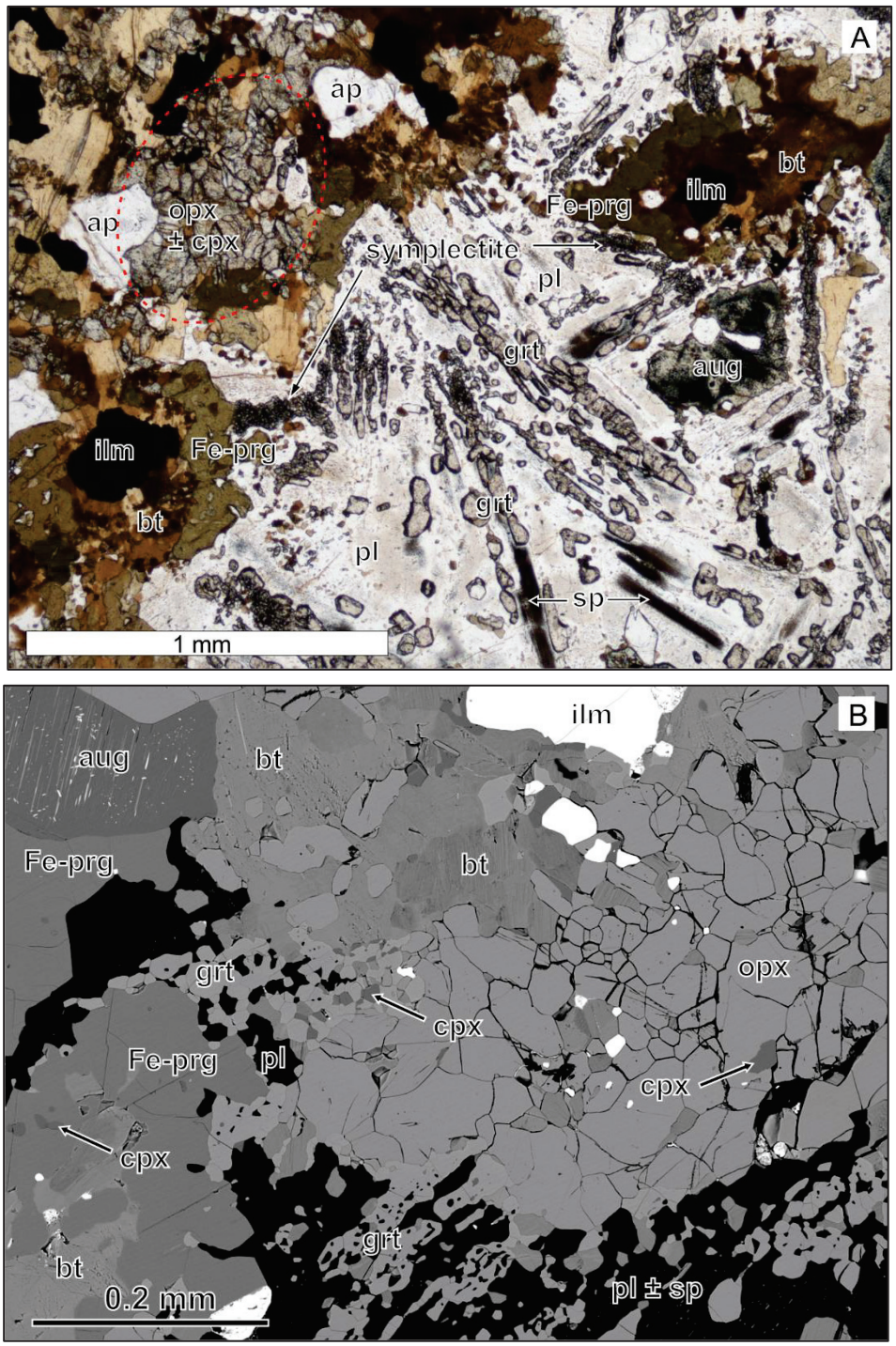

Figure 3.6 Sample GC14-024 from Lamondin Point, Byng Inlet. A) Optical photomicrograph in PPL showing remnants of Px mosaic after Ol (dashed red ellipse, upper left), heavily overprinted by Fe-Prg. Elongate idiomorphic Grt preferentially overprints Ca-rich Pl lath cores (center). Relict Aug (center right) is moderately dusted with Ilm lamellae and displays a narrow, lamellae-free rim. Note that Fe-Prg completely envelops Bt coronas around primary oxide (bottom left, top right). B) SE image showing unaltered granoblastic Opx with subordinate Cpx (center, center right) and Pl inclusion-rich Grt proximal to remnants of Px mosaic, possible recrystallized relicts of early discontinuous 'fuzzy patch' symplectites (Fig. 3.1c; Bethune and Davidson, 1997).

Garnet ($Grs_{19-22}Pyr_{11-15}Alm_{67-69}$) is concentrated in the cores of plagioclase laths and commonly displays a xenomorphic, elongate habit (Fig. 3.6a). In contrast to samples from the northern and southern regions of the study area, inclusion-rich margin-parallel bands of garnet around Fe-Ti oxide or pyroxene mosaics are rare. Inclusion-free, elongate garnet grains are commonly laterally continuous with the spinel-dusted cores of zoned relict plagioclase laths (Fig. 3.6a), suggesting that garnet overprinted densely spinel-dusted cores of relict plagioclase laths preferentially. This overprinting may account, in part, for the general paucity of visible dusting in GC14-024 as compared to samples elsewhere.

Metamorphic pyroxene is mostly represented by granoblastic aggregates of orthopyroxene (En_{45-46}) with subordinate fine intergrowths of clinopyroxene ($Wo_{44-46}En_{31-32}Fs_{22-25}$) (Fig. 3.1c, 3.6a,b). It is not clear whether the mosaic pseudomorph sequence described in section 3.2 and illustrated in figure 3.1 (i.e. granoblastic pyroxene mosaics with an orthopyroxene core and a clinopyroxene rim) failed to develop, or metamorphic clinopyroxene was preferentially overprinted by ferropargasite.

3.3.3 Southern Britt Domain

The southern Britt Domain is represented by relatively few samples. Sample GC14-048 is from a superbly preserved SmD dyke segment on H.A. Gray island near Point au Baril that has undergone relatively little deformation. A second set of SmD samples, GC14-008 and RJ07-AR5, was collected from an outcrop in the village of Arnstein, 60 km NE of Point au Baril, less than 5 km northwest of known outcrops of Algonquin coronitic metagabbro and a dated sample of retrogressed eclogite (Davidson and van Breemen, 1988; Ketchum, 1994; Ketchum and Davidson, 2000). As discussed in chapter

2 (section 2.1), ca. 1150-1170 Ma Algonquin metagabbro and retrogressed eclogite with protolith ages of ca. ~1400-1470 Ma are associated with allochthonous domains of the CGB, while the ca. 1235 Ma SmD is exclusive to parautochthonous domains. The distribution of these distinctive mafic intrusions serves to constrain the location of the ABT. The ABT, the southern boundary of the Britt Domain, is located just southeast of the GC14-008/RJ07-AR5 outcrop and runs NE-SW through the village of Arnstein. Owing to the distance of this locality from the Georgian Bay transect, the Arnstein outcrop is not considered representative of the southern Britt Domain, and is treated separately, for comparison.

3.3.3.1 GC14-048 Point au Baril

Relict plagioclase laths (An_{29-36}) are easily recognizable macroscopically despite extensive replacement by garnet. Finer laths < 1mm long are commonly bent and largely recrystallized (An_{19-20}). Narrow oligoclase moats, compositionally identical to recrystallized granoblastic plagioclase, separate mosaic pyroxene from garnet coronas. Locally, relict laths are completely overprinted by garnet, forming tabular garnet pseudomorphs after plagioclase. Coarser grains, several millimeters in length, are less strongly deformed, rimmed entirely by overprinting idioblastic garnet, and contain abundant, regularly oriented rod-shaped spinel inclusions that are commonly coarse enough to identify optically. Spinel dusting is less common in relict plagioclase than in samples to the north, though small sectors of dense spinel dusting are found proximal to relict augite. Coarser spinel rods within finely dusted sectors of relict plagioclase are surrounded by thin, < 5 μm wide inclusion-free halos. While submicroscopic spinel dust is generally far too fine to analyse in situ, coarse spinel here is Hc_{65}, contrasting with

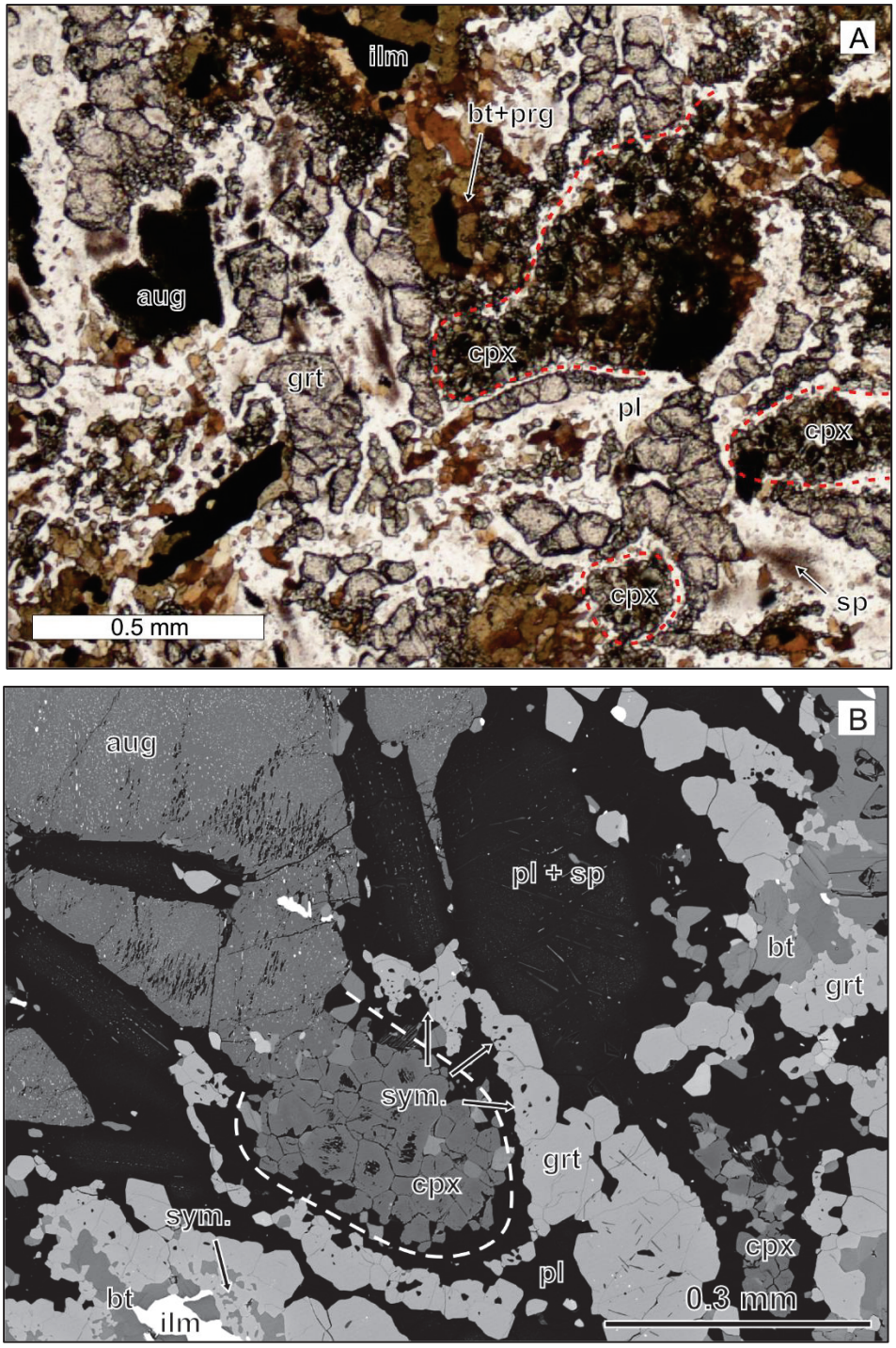

Figure 3.7 Coronitic textures, sample GC14-048 from H.A. Gray Island, Point au Baril. A) Photomicrograph in PPL shows granoblastic Cpx mosaics surrounded by narrow Pl moats (red dashed lines) and strongly recrystallized Grt coronas. Primary Aug is virtually opaque (centre left). Bt corona around Ilm is almost completely replaced by Fe-Prg (top centre). B) BSE image showing remnants of Grt symplectite as Pl inclusion-rich inner surface of Grt corona. Note the preservation of Sp-dusted relict Pl laths enveloped by relict Aug (top centre and left), while recrystallized Pl (lower right) is completely overprinted by Grt with regularly oriented very fine Sp rod inclusions.

compositions of texturally similar spinel from the GFTZ of Hc_{71-74} (Bethune and

Davidson, 1997). Since it is invariably included within relict plagioclase laths, spinel is interpreted to be isolated from the system.

Coronas around primary oxides are entirely composed of intergrown pargasite and biotite. Relative proportions of the two vary throughout, though pargasite tends to predominate. Biotite (Phl_{63-68}) is granoblastic, and roughly equigranular with metamorphic clinopyroxene and plagioclase. Primary oxide-rimming biotite, characterised by coarser single crystal habit and high Ti content, is completely replaced by granoblastic biotite, or overprinted by pargasite. Pargasite, in contrast, is slightly coarser with single porphyroblasts partially to completely enveloping smaller and more heavily embayed ilmenite. Garnet symplectite is generally well preserved along the inner margin of oxide-rimming garnet coronas, but is typically less continuous than the equivalent coronas around pyroxene mosaic pseudomorphs.

Pyroxene is only present in GC14-048 as relict augite and granoblastic clinopyroxene ($Wo_{46-47}En_{39-40}Fs_{14}$) mosaics. No orthopyroxene has been found in this sample, though heavily retrogressed remnants may remain elsewhere. Relict augite preserves an interstitial subophitic habit and shows no evidence of deformation or significant participation in corona-forming reactions. Partially enveloped and relict plagioclase adjacent to relict augite is very densely dusted with spinel and practically opaque. Notably, the only petrographic domain where relict plagioclase is not rimmed by a corona of overprinting garnet is along grain boundaries shared with relict augite. This interface tends to remain unchanged, with the exception of minor, sporadic biotite growth. Metamorphic pyroxene is restricted to mosaics consisting entirely of granoblastic clinopyroxene with strongly exsolved and variably retrogressed cores. Mosaic

pseudomorphs after olivine are smaller and less abundant than those observed elsewhere, though this may simply reflect a sampling bias. Local incipient recrystallization of relict augite apices form granoblastic aggregates much smaller than pseudomorphs after olivine.

Garnet ($Grs_{16-18}Pyr_{27-28}Alm_{54-57}$) preferentially overprints the cores of relict plagioclase laths in GC14-048, extensively enough, locally, to be considered pseudomorphs. Coarser spinel rods, retaining plagioclase-lattice-controlled orientations, are commonly found as inclusions in idioblastic garnet which has overprinted lath cores. Garnet symplectite intergrowths are moderately well preserved around primary Fe-Ti oxides, though clinopyroxene is largely overprinted by pargasite and biotite. By comparison, garnet symplectite textures proximal to clinopyroxene mosaics are very poorly preserved. Little more than slightly irregular inner garnet corona margins with sporadic, extremely fine plagioclase inclusions adjacent oligoclase-moat microdomains remain as strongly recrystallized vestiges of garnet-pyroxene symplectite.

3.4 Whole-rock geochemistry

No single Sudbury diabase dyke can be traced continuously across the Grenville Front (GF) from the Southern Province. Within the Grenville Province, deformed and tectonically segmented bodies of coronitic metadiabase are correlated with the Sudbury swarm on the basis of distinctive geochemistry and the age of primary crystallization (Bethune and Davidson, 1988, 1989; Bethune 1993, 1997; Dudas et al. 1994). While macroscopic features are suitable for field identification, SmD retains the characteristic

enrichment of Fe_2O_3, K_2O, TiO_2, P_2O_5, Ba, Zr, and LREE (Fig. 3.8a-e) and impoverishment of MgO, Ni, and Cr that distinguishes SD swarm geochemistry relative to other intrusive suites in the Canadian Shield (Condie et al., 1987; Ketchum and Davidson, 2000). After primary crystallization ages, chemical fingerprinting provides the strongest confirmation of Sudbury affinity within the Britt Domain.

In addition to chemical fingerprinting, geochemical data provide constraints on the effective bulk composition (EBC) of a rock for use in phase equilibrium modelling. The selection of EBCs and phase equilibrium modelling for the purposes of this project are discussed in chapter 4.

3.4.1 Methodology

Fourteen SmD samples selected for bulk geochemistry were chipped, crushed, and pulverized at the St. Mary's University Department of Geology in Halifax, Nova Scotia. All material exhibiting surficial weathering, visible alteration, veining, or secondary mineralization along fractures was separated manually. Crushed samples were pulverized using a tungsten carbide puck mill. Components of the mill were cleaned between each pulverization cycle by hand with ethanol and an approximately 45 second cycle with highly pure silica sand. Three hundred gram pulps from each sample, plus 2 duplicates, were separated and sent for whole-rock analysis by inductively coupled plasma (ICP) analysis at Bureau Veritas Mineral Laboratories in Vancouver, British Columbia. Appendix B contains details regarding analytical precision and reproducibility of the results.

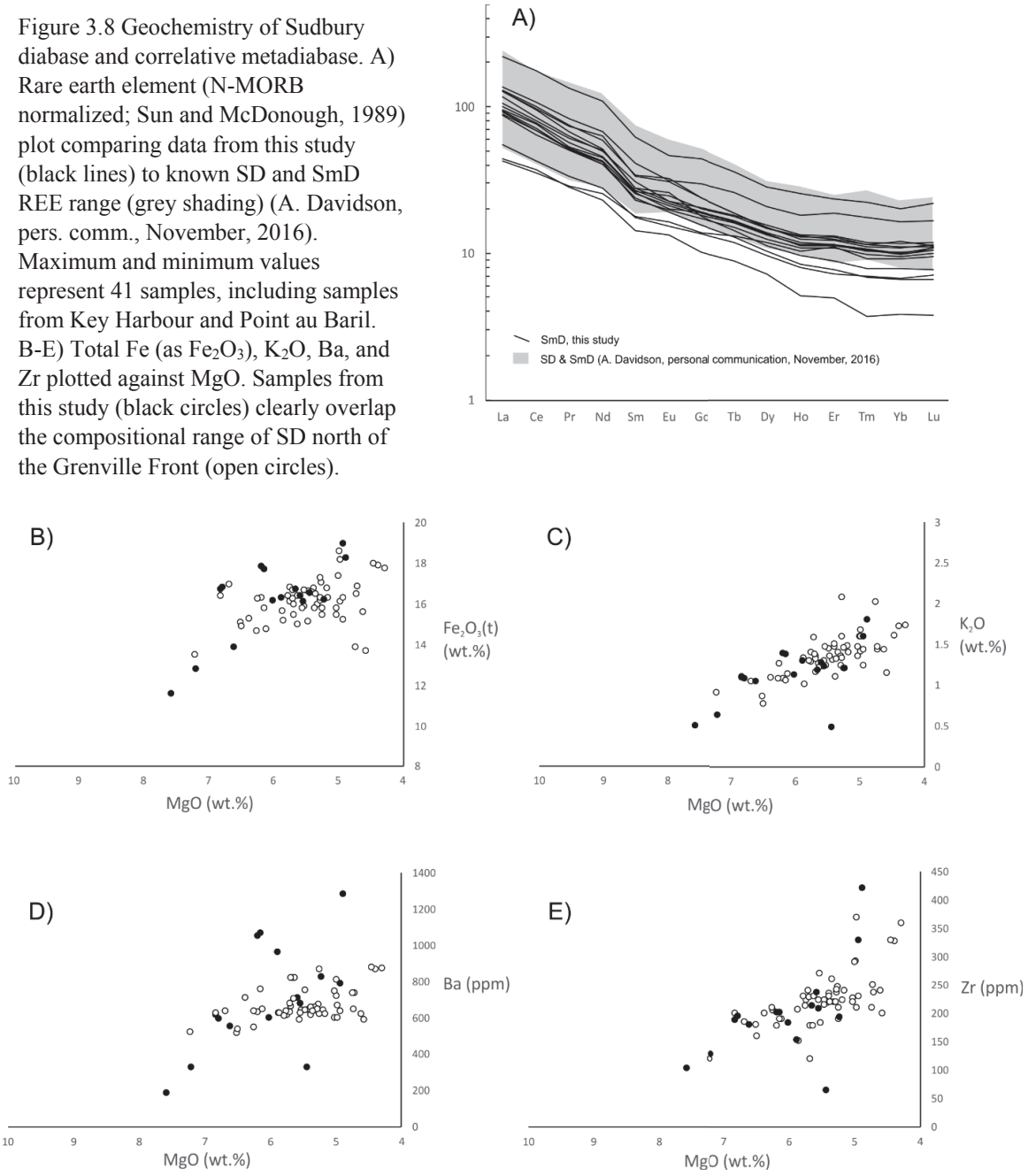

Figure 3.8 Geochemistry of Sudbury diabase and correlative metadiabase. A) Rare earth element (N-MORB normalized; Sun and McDonough, 1989) plot comparing data from this study (black lines) to known SD and SmD REE range (grey shading) (A. Davidson, pers. comm., November, 2016). Maximum and minimum values represent 41 samples, including samples from Key Harbour and Point au Baril. B-E) Total Fe (as Fe_2O_3), K_2O, Ba, and Zr plotted against MgO. Samples from this study (black circles) clearly overlap the compositional range of SD north of the Grenville Front (open circles).

3.4.2 Results

With the exception of two samples, all sampled metabasite lithologies show characteristic enrichment in rare earth elements (REE) elements, and profiles that fall within range of minimum and maximum REE values from SD north of the GF and

metabasites of known Sudbury affinity from Key Harbour and Point au Baril (Fig. 3.8 a, grey envelope). Total Fe (as Fe_2O_3), K_2O, Ba, and Zr vs. MgO from this study (Fig. 3.8 b-e, closed circles) directly overlap values from SD north of the GF (open circles). Two samples showing slightly lower Fe_2O_3, K_2O, Ba, and REE profiles correspond to samples from the Nares Inlet Shear Zone (NISZ), and a poorly exposed outcrop along highway 522. While both outcrops show characteristic Sudbury features, they are strongly deformed and show evidence of retrogression and possible melting.

3.5 Conclusions

Within the GFTZ, metamorphic grade of SD increases sharply southward, from greenschist facies proximal to the Grenville Front to two-pyroxene, granulite facies metadiabase between 7 and 16 km SE of the GF. The peak metamorphic assemblage observed in the representative sample for the northern Britt domain is identical to that of metamorphic zone IV within the GFTZ (Fig. 3.1f,g) (Bethune and Davidson, 1997), implying the same generalised reactions (3.1, 3.2, and 3.3).

Within the Britt domain, the southward progression of metamorphic grade is less pronounced. Samples from the northern and southern regions, proximal to the GFTZ and the ABT respectively, contain well preserved granulite facies peak metamorphic assemblages. The central region, in contrast, has undergone significant overprinting by pargasite, which appears to have replaced clinopyroxene preferentially. While orthopyroxene appears to be stable in the peak assemblage, it is unclear whether two-pyroxene mosaics developed in SmD at Lamondin Point.

Strong overprinting of classic mafic granulite assemblages (Opx + Cpx + Pl + Grt + Bt) by amphibole (here, pargasite) is, ostensibly, a retrograde reaction overprinting biotite, plagioclase, and clinopyroxene preferentially, following the general reactions:

1c) Opx + Cpx + Pl = Prg + Qtz (3.4)

2b) Bt + Pl = Prg + Qtz (3.5)

where (1c) is associated with primary olivine and (2b) is associated with Fe-Ti oxide. Pattison et al. (2003) explored Opx-free high-P metabasite assemblages, modelling stability fields that demonstrated the stability of amphibole in transitional and granulite facies, assemblages. The typical prograde amphibolite-granulite transition is given by the reaction:

Hbl + Qtz = Opx + Cpx + Pl + H_2O and/or melt (3.6)

The high-P equivalent, they show, is given by the equation:

Hbl + Pl + Qtz = Grt + Cpx + H_2O and/or melt (3.7)

which may relate to the orthopyroxene-free assemblage observed in sample GC14-048 from the southern BD.

Defining reactions involving spinel is problematic. Garnet, particularly in samples GC14-024 and -048, appears to overprint the Ca-rich cores of relict plagioclase laths preferentially where spinel-dusting is most dense. However, as inclusions in plagioclase, hercynitic spinel remains isolated from the corona-forming system, and coarser spinel rods (relative to more pervasive “dust”) are commonly found as inclusions in garnet, inherited from the overprinted relict laths. The submicron-scale spinel (hercynite) dust precipitated in direct response to the coupled substitution of (Na + Si) for (Ca + Al) in plagioclase as lath-core chemistry changed with increasing metamorphic grade from a

more calcic primary composition (ca. An_{60}) to a more sodic composition (ca. An_{25}). The uptake of Si by plagioclase, by far the dominant phase in the protolith, during this change may account for the lack of modal quartz in SmD by the general reaction:

$$An + Qtz = Ab + Hc \quad (3.8)$$

Though amphibole can be stable in mafic rocks at high-P and high-T, preference is given to Cpx + Pl + Grt + Bt ± Opx assemblage for the calculation of peak P-T. To explore the possibility that pargasite is part of the peak assemblage, P-T calculations involving pargasite are made for comparison with conditions calculated for the anhydrous mafic granulite assemblage.

The preservation of fine coronitic textures is strongly controlled by diffusion. In the absence of melt, fluids, or strong deformation, diffusion of components in SmD was slow enough to allow grain-scale recrystallization of garnet within early, delicate symplectite textures on the inner margin of the garnet corona while progressively overprinting adjacent recrystallized relict plagioclase.

Limited deformation of relict plagioclase laths facilitated local plagioclase recrystallization and coalescence of spinel in coarse (relative to submicron scale 'dust') rods. Continued growth of idioblastic garnet following plagioclase recrystallization is indicated by spinel rod inclusions in garnet. Relicts of garnet-pyroxene symplectite, spinel dusting, and plagioclase and biotite recrystallization indicate that SmD in the Britt domain experienced comparable sequences of corona development to those reported for the GFTZ by Bethune and Davidson (1997).

As indicated in figure 3.2, these textures and are well preserved in the northern Britt domain, but less well preserved in the south. If the assumption can be made that diffusion rates were comparable across samples, then SmD near the ABT in the southern Britt domain appear to have a more protracted metamorphic history, involving longer residence time at high P-T conditions, than SmD in the north, near the GFTZ.

An obvious difference between the corona textures reported for SmD in the GFTZ and those reported here for the Britt domain is the oligoclase moat between pyroxene mosaics and garnet coronas. A similar feature observed in metagabbros in the Snowbird tectonic zone in northern Saskatchewan (Baldwin et al., 2003) and was attributed to the transition from the high-pressure to the moderate-pressure granulite facies by the reaction:

$$Grt + Cpx + Qtz = Opx + Pl \quad (3.9)$$

Secondary plagioclase formed by reactions of this type, however, is predicted to be Ca-rich, contrary to Na-rich trends for oligoclase moats in SmD, and no later generation of orthopyroxene in association with them has been observed. Kendrick (2015) argued that the formation of albitic moats along the interface between garnet and amphibole coronas in coronitic metagabbro could be explained by decompression by the general reaction:

$$Grt + Amp_1 = Pl + Amp_2 \quad (3.10)$$

where subscripts 1 and 2 denote different compositions of amphibole. This, however, is inconsistent with oligoclase moats observed in SmD which invariably separate pyroxene mosaic from garnet coronas and are present in amphibole-free assemblages such as

GC14-057. In addition, pargasite in samples GC14-024 and -048 is compositionally homogenous and displays no textural evidence of diachronous amphibole growth.

With the exception of the two outcrops discussed above, geochemical fingerprinting confirms that the sampled metabasites are metamorphosed segments of ca. 1235 Ma Sudbury Diabase dyke swarm.

Chapter 4: Thermobarometry and thermodynamic modelling

4.1 Background

Metamorphic mineral assemblages form in response to changes in pressure (P), temperature (T), and chemical composition (X) within a chemical system. The following discussion, based on Spear (1993), introduces the fundamentals of thermodynamics pertaining to stable mineral assemblages and the derivation of P-T information from those assemblages.

When a chemical system undergoes changes in P-T-X conditions, the system adjusts to re-establish equilibrium by consuming unstable phases (reactants) and forming new stable phases (products), and/or by adjusting compositions of solid solution phases. Within rocks, these phases include minerals, fluids, and melt. Chemical reactions in nature proceed toward a state of minimum energy, termed the Gibbs free energy (G). For pure phases, this is described by the equation:

$$\Delta G^{\circ} = \Delta H^{\circ} + P\Delta V^{\circ} - T\Delta S^{\circ} \quad (4.1)$$

where ΔH° is enthalpy (J/mol) at 0.1 MPa (1 atm) for a T(°K) of interest; ΔV° is the change in volume of the system (m^3) produced by the reaction; $\Delta S^{\circ}$is the change in entropy (J/°K·mol) at a T of interest. Where the change in heat capacity is negligible ($\Delta C_P = 0$), ΔH° and ΔS° are independent of T, and ΔV° is considered independent of P and T. Where solid solutions are involved:

$$\Delta G_{rxn} = \Delta G^{\circ} + RTlnK_{eq} \quad (4.2)$$

where R is the gas constant and K_{eq} is the equilibrium constant. For a simple, hypothetical reaction:

$$A + 4B = 2C + 3D \quad (4.3)$$

the equilibrium constant is calculated by:

$$K_{eq} = \frac{a_C^2 \bullet a_D^3}{a_A \bullet a_B^4} \quad (4.4)$$

where a is the activity of each component raised to the power of their stoichiometric coefficients for the reaction. Where K_{eq} describes the ratio of measured component concentrations in coexisting phases at equilibrium, it is referred to as the partition or distribution coefficient (K_D). The distribution coefficient is calculated by:

$$K_D = \frac{X_C^2 \bullet X_D^3}{X_A \bullet X_B^4} \quad (4.5)$$

where X is the mole fraction of each component.

For ideal solutions, $a_i = X_i$ where a is the activity of component i and X is the corresponding mole fraction (e.g. equation 4.5). Minerals, however, rarely behave as ideal solutions, and the relationship between mineral composition and component activity is $a_i = \gamma \cdot X_i$ where γ is the activity coefficient. Activity coefficients are poorly constrained for some minerals of interest in thermobarometry and subject to continuing revision as new data become available. Activity-composition relationships are used to replicate this non-linear relationship for common metamorphic solid solutions, and are included in all

current thermodynamic calculation software packages. Solution models used in this study are compiled in Table 4.1.

Of particular interest to metamorphic petrologists, for the purposes of thermobarometry, are polymorphic transformations, ion exchange reactions, solid-solid net transfer reactions. The first, not relevant to this study, involves the reconfiguration of a crystal lattice with no change in the chemical composition of the mineral. The second and third kinds of reaction involve the redistribution of elements between phases, the former by direct exchange of cations between solid solutions, the latter by growth of new and stable phases from the breakdown components of unstable ones, providing petrologists with the means to derive quantitative estimates of P and T, and are the basis of all thermobarometric techniques.

4.2 Assessment of Equilibrium

The first step in deriving P-T information is the identification of an equilibrium assemblage, as implied by equation 4.1. Where an assemblage is in equilibrium ($\Delta G_{rxn} = 0$), P-T conditions can be determined as a function of mineral compositions through the distribution coefficient (K_D).

$$\Delta G_{rxn} = \Delta G^{\circ} + RTlnK_D = 0 \tag{4.6}$$

4.2.1 Equilibrium Criteria

4.2.1.1 Textural equilibrium

Metamorphic equilibration can be considered for systems spanning a wide range of scales, from regional or outcrop-scale to micron-scale subdomains smaller than individual

crystals. Textural equilibrium generally requires: 1) commonly shared grain boundaries between all phases in the assemblage; 2) stable microstructures including planar grain boundaries, forming ~120° triple junctions between equant polygonal grains (classic granoblastic texture); 3) no obvious replacement textures, such as reaction rims or alteration along fractures. Where local equilibrium can be demonstrated, quantitative estimates of metamorphic P-T conditions can be obtained even from rocks exhibiting disequilibrium textures on larger scales.

In general, SmD displays disequilibrium textures on both meso- and microscopic scales. Coronitic textures (Chapter 3) commonly include metamorphic phases insulated from the bulk rock by (semi-) continuous reaction rims. Mosaics of granoblastic ortho- and clinopyroxene after primary olivine display ideal granoblastic textures, but are commonly isolated from the system by continuous to semi-continuous rims of garnet. Granoblastic clinopyroxene rims, typically only a single grain thick, also isolate orthopyroxene from plagioclase, garnet, and other Fe-Mg minerals in the assemblage. Primary igneous textures are well preserved, with relict augite, plagioclase, Fe-Ti oxide, and apatite remaining prominent in most samples.

4.2.1.2 Compositional Equilibrium

Calculating P-T as a function the distribution of elements between coexisting phases entails the assumption that chemical potential of all elements among the mineral assemblage is equal, and, therefore, in the lowest energy configuration possible for those P-T conditions, and the Gibbs free-energy of the products and reactants is equal ($\Delta G_{rxn} = 0$). Unequal chemical potential of elements between coexisting phases at P-T of interest violates the assumption that the $\Delta G = 0$, and P-T values calculated from such an

assemblage are meaningless. While it is relatively easy to prove thermodynamic disequilibrium within an assemblage, it is impossible to prove, absolutely, that an assemblage was in equilibrium. The absence of compelling evidence for disequilibrium, however, provides grounds to claim that the observed assemblage is consistent with a system that has reached equilibration (Spear and Peacock, 1989).

Compositional equilibrium requires a lack of compositional zonation within minerals, and general homogeneity of mineral compositions on the scale of observation. Temperatures at granulite facies, for example, are sufficiently high (> 750 °C) to obliterate early growth-zonation in garnet and other Fe-Mg phases by diffusion, a process termed homogenisation.

Exchange and net-transfer reactions also operate on the retrograde portion of the P-T path, and can create localized zones of compositional heterogeneity. This is especially problematic for Fe-Mg phases with shared grain boundaries such as garnet and biotite, where late exchange upon cooling renders garnet more Fe-rich and biotite more Mg-rich, yielding lower T estimates (Spear and Peacock, 1989). While diffusion within biotite is generally rapid enough to alter the composition of an entire grain in contact with a large garnet, slower diffusion in garnet can result in a localized zonation halo along the exchange interface that is readily distinguishable by point analysis and/or chemical mapping. Additionally, the Ca content of the garnet, free to vary along with Fe and Mg during equilibration of the system, is unaffected by late Fe-Mg exchange with biotite, possibly providing further evidence for late exchange where correlations in component concentrations are incongruous.

Metamorphic phases in SmD are compositionally well equilibrated, with little to no compositional zonation or grain-to-grain variation. Metamorphic pyroxenes in mosaic pseudomorphs after olivine show minimal compositional variation within samples, although clinopyroxene is locally altered (GC14-048; section 3.3.3). Garnet shows no systematic compositional variation across textural subdomains, and no appreciable internal chemical zonation.

Metamorphic plagioclase and biotite show significant variations in composition related to distinct textural microdomains and late ion-exchange, respectively. Plagioclase in SmD is represented by three distinct populations: 1) coarse relict laths, locally preserving primary zonation; 2) granoblastic, metamorphically recrystallized plagioclase, roughly the same size as pyroxene grains in mosaics after olivine; 3) narrow oligoclase moats, separating pyroxene mosaics from the garnet coronas. Relict laths tend to exhibit higher Ca content ($\geq An_{20}$) than granoblastic grains. As the latter are clearly metamorphic, their compositions have been used in P-T calculations.

Metamorphic biotite is not restricted to textural subdomains, and is commonly intimately intergrown with other Fe-Mg minerals. Biotite compositions used in P-T compositions are generally single analyses of specific grains sharing minimal visible contact with Fe-Mg minerals to avoid the effects of late cation exchange.

Multiequilibrium modelling programs such as TWQ (Berman, 1991) provide an additional, robust method for assessing compositional equilibrium between selected mineral phases in texturally correlated subdomains. The program calculates the position of all possible reactions for phases of measured composition, plotting the resulting curves in P-T space. If the plotted reactions all intersect at a single point (perfect convergence),

this indicates that the specified mineral compositions could have equilibrated together at the P-T of the intersection. This is discussed in detail in Section 4.5.

Where rocks are texturally and compositionally well equilibrated, identifying the equilibrium assemblage and the effective bulk composition (EBC) of the assemblage may be trivial. Where several points on a P-T-t (time) path are being examined, and/or where rocks display obvious disequilibrium textures (e.g. coronas and symplectites) multiequilibrium modelling software such as TWQ provides a robust method for assessing the state of local equilibrium between select mineral phases in spatially correlated subdomains.

4.2.2 Limitations

4.2.2.1 Activity of SiO_2

Quartz is a product or reactant in many calibrated thermobarometers. However, as shown in chapter 3, samples from the strain-resistant cores of tectonically segmented SmD are entirely free of quartz. Though SiO_2 is clearly participating in corona-forming metamorphic reactions, lack of modal quartz indicates that the system is SiO_2-undersaturated. When quartz is present in the assemblage, $a_{SiO2} = 1$ and calculations of distribution coefficient (K_D) can be simplified. For SiO_2-undersaturated systems, such as those considered in this study, either a_{SiO2} must be estimated, or the calculated P-T conditions represent minima or maxima.

To constrain a_{SiO2} a series of multiequilibrium plots was generated for the granulite facies assemblage Grt + Opx + Cpx + Pl + Bt + Qtz with incrementally reduced activities ($a_{SiO2} = 1, 0.9, 0.7$). Reaction lines showed identical degrees of convergence, regardless of

a_{SiO2} value, though calculated estimates for P were reduced by approximately 0.5 kbar for each increment (14.0 ± 1.6, 13.6 ± 1.7, and 13.0 ± 1.7 kbar, respectively). T estimates remained virtually unchanged, though uncertainties increased (734 ± 54, 733 ± 63, and 737 ± 77 °C, respectively). The effect of $a_{SiO2} < 1$ on the Grt-Cpx-Pl-Qtz reaction as calculated by TWQ and the Newton and Perkins (1982) conventional geobarometer is illustrated in Figure 4.4. The ~0.25 kbar reduction in P at 700 °C is within the reported precision of ± 1.6 kbar for the conventional calibration.

4.2.2.2 Ferric Iron

Mg^{2+}/Fe^{2+} exchange forms the basis of many thermobarometers. However, microprobe analysis does not distinguish between Fe^{3+} and Fe^{2+}. The ratio of Fe^{3+}/Fe^{2+}, particularly in complex minerals with multiple cation sites such as amphibole and biotite, can significantly affect the P-T results produced by lowering the Fe^{2+} component, potentially overestimating pressures by several hundred bars and temperatures by more than 60˚C (Schumacher, 1991). Fe^{3+} can be calculated stoichiometrically on a basis of charge balance. However, this is subject to poorly constrained assumptions for minerals with variable stoichiometry and multiple cation sites. For this reason, P-T calculators often give the option to approximate Fe^{3+} in biotite using a simple percentage of "total" Fe, usually reported as FeO from EMP analysis (e.g. PTQuick, 11.6%; TWQ, 12%) (Dolivo-Dobrovolsky, 2016; Berman, 2007).

Most conventional thermobarometers, including those based on Mg^{2+}/Fe^{2+} exchange, were calibrated using EMP analyses and therefore assume $Fe_{total} = Fe^{2+}$. Consequently, reducing Fe^{2+} by calculating Fe^{3+} can lead to T estimates lower than those predicted by the thermometer. To illustrate the difference, it is useful to compare results

from the Krogh Ravna (2000) Grt - Cpx geothermometer applied to sample GC14-057 from the northern Britt domain. Using a reduced value of Fe^{2+}, with a stoichiometric calculation for Fe^{3+} produces a T estimate of 590 °C at 14.4 kbar (P estimate from TWQ multiequilibrium calculation; Table 4.1). Assuming $Fe^{2+} = Fe_{total}$ for the same compositions results in a T estimate of 724 ˚C (Fig. 4.3). Predictably, the T estimate for $Fe^{2+} = Fe_{total}$ by this method agrees well with results from Grt - Bt and Grt - Hbl geothermometers (Graham & Powell, 1984; Bhattacharya et al., 1992; Spear, 1993), while using calculated Fe^{2+} produces T ≥ 100˚ C lower than other thermometers (Fig. 4.3).

All conventional thermobarometers employed in this study were calibrated on the assumption that $Fe^{2+} = Fe_{total}$. For consistency, all P-T estimates using these thermobarometers, unless indicated otherwise, were calculated assuming $Fe^{2+} = Fe_{total}$. These results were used to obtain first-order P-T estimates and/or for assemblages where more sophisticated thermodynamic calculators were not applicable.

Multiequilibrium calculators such as winTWQ (Berman, 2007) allow the option of calculating mineral formula input files with and without Fe^{3+} calculations. Ferric iron, if measured independently, may be entered manually. Figure 4.1 demonstrates the effect of Fe^{3+} calculated by the winCMP module on the position of equilibrium reactions in P-T space for sample GC14-057.

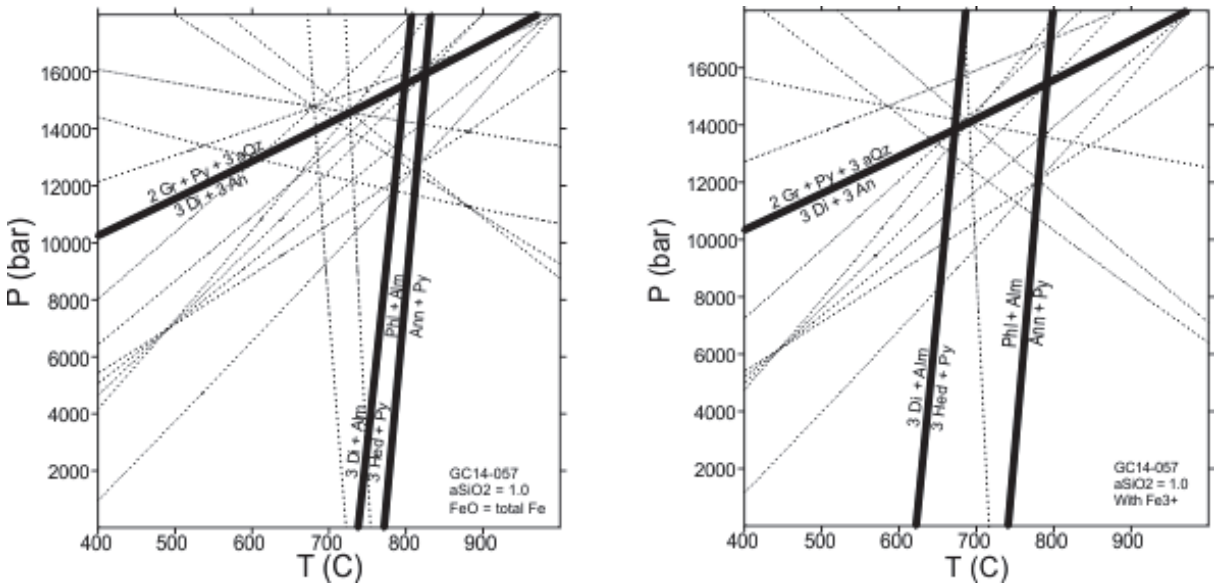

Figure 4.1 TWQ multiequilibrium plots of GC14-057, A) with $Fe^{2+} = Fe^{total}$, B) with Fe^{3+} calculated by the winCMP module. Heavy lines correspond to reactions calibrated for conventional thermobarometry (*Grt-cpx-pl-qtz barometer; Grt - Cpx and Grt - Bt thermometers*). Formula and multiequilibrium calculations for this study were performed with version 2.32 of the winTWQ software based on solution and thermodynamic data from the 2006 database (DEC06.DAT) (Berman, 1991, 2007; see Table 4.1 for solution models applied)

4.2.2.3 Solution models

The non-linear relationship between component activity and mineral composition was discussed in Section 4.1. Modelling of a-X relationships is a major source of uncertainty for thermodynamic calculators. While solution models are subject to periodic revision as new experimental data become available, many are considered reliable and included as default options in various thermobarometry software packages (e.g. Fuhrman and Lindsley, 1988, for plagioclase); solution models used in this study are listed in Table 4.1.

Table 4.1 *Solution models applied for multiequilibrium calculations (TWQ) and phase equilibrium modelling (Theriak-Domino)*

Mineral	Solution models applied	
	winTWQ	**Theriak-Domino**
plagioclase	*Fuhrman and Lindsley (1988)*	*Fuhrman and Lindsley (1988)*
clinopyroxene	*Berman et al. (1995)*	*Meyre et al (1997)*
orthopyroxene	*Berman and Aranovich (1996)*	*Ideal mixing*
biotite	*Berman et al. (2007)*	*Ideal mixing*
garnet	*Berman and Aranovich (1996)*	*Berman (1990)*

4.3 Representative Compositions

The selection of representative mineral compositions for calculating P-T conditions is the greatest source of variability and potential error. The early coronitic textures developed in SmD violate textural criteria for equilibrium in that certain phases, in this case, Fe-Ti oxides, biotite, and pyroxenes, become isolated from the chemical system. Progressive metamorphism has largely homogenized important solid solution phases of early coronitic phases, such as garnet. Where textural microdomains, outlined in Chapter 3, retain early and disparate compositional ranges (e.g. highly sodic An_{12-13} "moats" versus granoblastic An_{16-19} recrystallized plagioclase adjacent to relict laths, GC14-057), it is crucial to identify which compositional subsets represent the components of the equilibrium assemblage. The following section details compositional variations in the context of textural microdomains. Representative mineral compositions are compiled in Table 4.2.

Mineral compositions were measured using the JEOL 8200 Superprobe at the Robert M. MacKay Electron Microprobe Laboratory in the Department of Earth Sciences at Dalhousie University. Standard operation conditions include 15 kV accelerating voltage and a beam current of approximately 20 nA. Standard ZAF corrections were applied, and mineral-specific calibrations were used to calculate element concentrations for major silicate phases. Analytical uncertainty for major elements is in on the order of ±1% of the reported value.

4.3.1 GC14-057 – Key Harbour

The representative SmD sample from Key Harbour is composed of relict phases augite, plagioclase, ilmenite, biotite, and apatite. Metamorphic minerals include garnet, plagioclase, biotite, ortho- and clinopyroxene, hercynitic spinel, zircon, and rare monazite and sulphides. The granulite facies metabasite assemblage Grt + Pl + Cpx + Opx + Bt, representing peak metamorphism, was used for thermobarometry.

Two distinct populations of plagioclase, An_{12-20} and An_{28-30}, represent recrystallized and relict grains, respectively. Plagioclase from the highly sodic "moat" domains (An_{12-13}) was excluded as a late generation, locally Na-enriched by the breakdown of metamorphic clinopyroxene (Grant, 1988; Johnson and Carlson, 1990). Granoblastic recrystallized plagioclase, generally conspicuous by the lack of spinel dusting, displays no obvious chemical zonation or compositional trends. An average of seven analyses produced a representative plagioclase composition of An_{17}.

Of all samples collected south of the Grenville Front Tectonic Zone, metadiabase from Bigsby Island in Key Harbour most clearly preserves early coronitic textures (see

Section 3.2). No relict olivine is present south of the GFTZ, and pseudomorphs after inferred primary olivine are composed of very fine-grained mosaics of granoblastic ortho- and clinopyronxene. Metamorphic pyroxene, both ortho- and clinopyroxene, form clear triple-point junctions within their respective monomineralic domains, and show little evidence of retrogression or chemical zonation. Though clinopyroxene shows some variation in Na content (2.2 - 3.2 wt.% Na_2O) efforts to calculate multiequilibrium plots based on high-Na clinopyroxene compositions did not produce meaningful results. Averages for metamorphic clino- and orthopyroxene, based on 9 and 7 analyses, respectively, were taken as representative of peak metamorphic compositions.

Garnet forms continuous to semi-continuous coronas rimming pyroxene mosaics after olivine and, less continuously, outboard of metamorphic biotite rimming primary ilmenite. Both types have variably embayed and inclusion-rich inner boundaries, the remnants of variably recrystallized symplectites (Fig. 3.2a,b). In contrast, outer surfaces are idioblastic and generally inclusion-free. Neither individual garnet grains nor coronas show significant compositional variation within of between grains (Fig. 4.2). All microprobe analyses of garnet, with the exception of grains in visible contact with biotite, were averaged for a representative peak metamorphic composition ($Grs_{16}Py_{24}Alm_{58}Sps_1$).

Biotite is less common than other metamorphic phases in GC14-057, and readily distinguished from igneous biotite as granoblastic grains with lower Ti content (5.1-6.5 wt.% TiO_2 vs. 7.0 wt.%) and slightly higher Al content (14.3-14.9 wt.% Al_3O_3 vs. 14.0 wt.%). Commonly, fine biotite aggregates are intergrown with the inner edge of garnet coronas around primary Fe-Ti oxides (Fig. 3.2). Because biotite in direct contact with other Fe-Mg phases is susceptible to retrograde cation exchange, an analysis from a grain

not in visible contact with garnet or pyroxene was selected to represent the peak biotite composition.

4.3.2 GC14-024 – Byng Inlet

Sample GC14-024 from Lamondin Point at Byng Inlet in the central region of the Britt domain is composed of relict augite, plagioclase, ilmenite, biotite, and apatite. Metamorphic phases include garnet, ortho- and clinopyroxene, plagioclase, pargasite, biotite, magnetite, hercynitic spinel, zircon, and rare monazite and sulphides. The metamorphic assemblage Grt + Pl + Opx + Cpx + Bt was used for thermobarometry, because pargasite is interpreted as retrograde.

Relict plagioclase laths are less obvious in this sample, indicating a greater degree of recrystallization. The oligoclase moat microdomain is not present in GC14-024. Granoblastic plagioclase compositions are remarkably consistent, ranging from An_{12-15}; a simple average of ten analyses (An_{13}) was used for thermobarometric calculations.

Coronitic textures are not clearly represented in section, except where biotite and amphibole occlude strongly embayed and largely resorbed primary ilmenite. Orthopyroxene and biotite are largely granoblastic and commonly intergrown with pargasite. Clinopyroxene is a subordinate phase locally intergrown with granoblastic orthopyroxene and forming inclusions in pargasite.

Orthopyroxenes form distinct granoblastic aggregates commonly intergrown with smaller grains of metamorphic clinopyroxene, biotite, and pargasite. Analyses show virtually no variation in composition, with Mg/Fe ratios of 0.45 to 0.46. A simple average of 12 analyses was used for thermobarometric calculations.

Relict augite, though relatively small compared to augite in other SmD samples, is conspicuous petrographically and in BSE images by abundant lamellae of very fine ilmenite. Metamorphic clinopyroxene forms small, ovoid inclusions in pargasite, xenoblastic intergrowths with recrystallized garnet symplectites, and less commonly granoblastic grains within orthopyroxene aggregates. Compositions cluster very tightly on the Fe-Ca-Mg ternary plot (Fig. 4.2), and Mg/Fe ratio ranges from 0.56 to 0.60. The composition of metamorphic clinopyroxene and relict augite is remarkably similar, with identical Mg/Fe ratios of 0.57, indicating that relict augite in this sample has re-equilibrated to metamorphic conditions. An average of 16 analyses, excluding relict augite, was used in the calculations.

Garnet data for GC14-024 cluster very tightly on Fe-Ca-Mg ternary plots, except for grains completely included in biotite, which show a slightly higher Fe content ($Grs_{16}Py_{11}Alm_{69}Sps_4$). Given the general lack of a close textural association between garnet and biotite and the tight clustering of garnet compositions, an average of 15 analyses was used in the calculations.

Amphibole compositions in section GC14-024 are virtually homogenous, yielding Mg/Fe ratios of 0.42 - 0.43, and can be classified as titanian-potassian-ferroan-pargasite (Leake et al., 1997). While interpreted to be retrograde and excluded from the peak metamorphic assemblage, an average of 7 amphibole analyses was used in thermobarometric calculations for post-peak P-T.

4.3.3 GC14-048 – Point au Baril

Sample GC14-048 from H. A. Gray Island at Point au Baril in the southern Britt Domain contains the relict phases augite, plagioclase, ilmenite, biotite and apatite.

Metamorphic phases include garnet, plagioclase, clinopyroxene, pargasite, biotite, hercynitic spinel, zircon, and trace monazite, sulphides, and orthoamphibole. The peak metamorphic assemblage Grt + Pl + Cpx + Bt was used for thermobarometry.

Plagioclase falls within two compositional groups. Relict grains, conspicuously clouded with hercynitic spinel, are An_{29-36}. Notably, plagioclase grains from both the 'oligoclase moat' microdomain and granoblastic recrystallized portions of relict laths have identical compositions (An_{19-20}) and show no evidence of zoning. An average of 5 metamorphic plagioclase analyses (An_{20}) was used in the calculations.

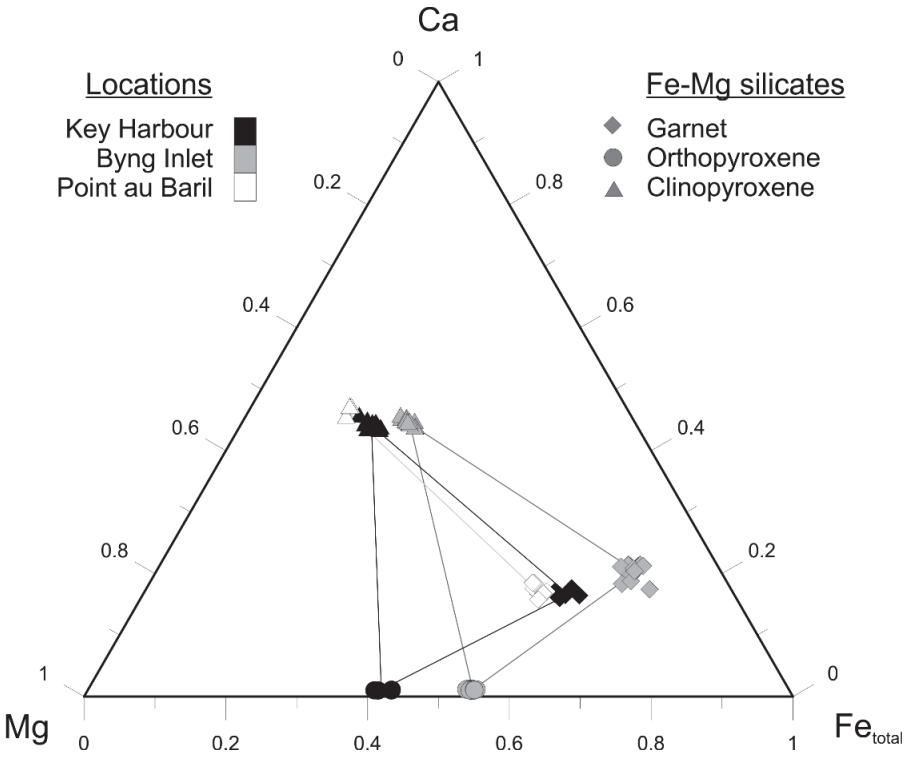

Figure 4.2 Ternary diagram showing the compositions of all Grt, Opx, and Cpx analyzed from samples GC14-057 from Key Harbour, GC14-024 from Byng Inlet, and GC14-048 from Point au Baril. Note that compositions are tightly clustered, regardless of textural association. Averages used for P-T calculations reflect subsets of these analyses.

Granoblastic clinopyroxene grains in sample GC14-048 exhibit fresh, inclusion-free rims surrounding variably altered, possibly exsolved cores. Close textural association of clinopyroxene and biotite in GC14-048 provided few targets for analyses of the former not in visible contact with the latter. Regardless, Mg/Fe ratios from all clinopyroxene analyses fall within the range 0.73 – 0.75. An average of 4 analyses from the unaltered rims of grains not in visible contact with biotite represents peak clinopyroxene composition for thermobarometric calculations. Orthopyroxene is not present in sample GC14-048.

Coronitic textures are well preserved in GC14-048, though garnet recrystallization has all but obliterated early symplectite. Garnet is compositionally homogenous throughout the scale of the thin section, though grains in visible contact with biotite are Fe-enriched (Alm_{60}) relative to the contrary (Alm_{55}). A garnet composition ($Grs_{17}Py_{27}Alm_{55}Sps_{1}$) represents the average of 7 analyses from grains not in visible contact with biotite, and is used to represent peak composition.

Biotite is closely associated with metamorphic pyroxene and amphibole in GC14-048. All analyzed biotites yield Ti and Al contents of 5.2-6.5 wt.% TiO_2 and 14.3-14.9 wt.% Al_2O_3. Igneous biotite, in contrast, has higher Ti (~7.0 wt.% TiO_2) and lower Al (~14.0 wt.% Al_2O_3) contents. In order to avoid the effects of late cation exchange, a single analysis from a biotite grain not in visible contact with other Fe-Mg minerals was selected to represent the peak composition.

Table 4.2 WDS-EMP chemical analyses of peak metamorphic assemblage, with amphibole, for Sudbury metadiabase across the Britt domain. GC14-057, from Bigsby Island in Key Harbour, represents the northern region. GC14-024 from Lamondin Point, Byng Inlet represents the central region. GC14-048, from H.A. Gray Island in Point au Baril, represents the southern region. Cations are calculated for the following oxygens p.f.u.: garnet = 12; biotite = 22; pyroxene = 6; plagioclase = 8; amphibole = 23.

	GC14-057					GC14-024						GC14-048				
Analysis	Avg (7)	057_16	Avg (9)	Avg (7)	Avg (7)	Avg (15)	Avg (8)	Avg (16)	Avg (12)	Avg (10)	Avg (7)	Avg (7)	048_2_32	Avg (4)	Avg (5)	048_1_5
Oxides (wt.%)	Garnet	Biotite	Cpx	Opx	Plag	Garnet	Biotite	Cpx	Opx	Plag	Amph	Garnet	Biotite	Cpx	Plag	Amph
SiO_2	38.70	36.08	52.29	52.12	63.94	36.74	35.55	51.53	50.61	64.70	40.51	39.22	36.84	52.56	63.27	41.33
TiO_2	0.03	6.34	0.15	0.04	0.00	0.08	6.47	0.25	0.15	0.00	3.08	0.06	5.36	0.39	0.07	3.13
Al_2O_3	21.96	14.40	4.76	0.89	22.49	20.68	13.87	2.85	0.58	21.74	11.80	22.15	14.62	5.50	22.93	13.07
FeO	27.24	14.57	10.17	26.57	0.25	30.53	21.83	13.63	33.08	0.54	19.67	25.90	13.24	7.59	0.34	12.65
MnO	0.69	0.03	0.08	0.23	0.00	1.59	0.06	0.20	0.50	0.00	0.11	0.61	0.02	0.07	0.00	0.04
MgO	6.43	13.48	11.29	20.25	0.00	3.09	9.56	10.43	15.35	0.00	8.14	7.16	14.38	11.94	0.00	11.82
CaO	5.92	0.05	18.75	0.51	3.16	6.58	0.03	20.45	0.53	2.78	11.12	6.29	0.05	19.87	4.13	11.54
BaO	0.00	1.11	0.00	0.00	0.00	0.00	0.83	0.00	0.00	0.00	0.00	0.04	0.67	0.00	0.00	0.00
Na_2O	0.00	0.00	2.61	0.02	9.64	0.00	0.00	1.63	0.02	10.27	2.81	0.00	0.00	2.33	9.05	2.56
K_2O	0.00	9.53	0.00	0.00	0.46	0.00	9.38	0.00	0.00	0.32	1.41	0.00	9.63	0.00	0.27	1.34
Total	100.97	95.60	100.10	100.63	99.94	99.29	97.58	100.96	100.81	100.35	98.64	101.43	94.82	100.25	100.06	97.48
Cations (p.f.u.)																
Si	2.984	5.434	1.945	1.966	2.821	2.963	5.416	1.943	1.971	2.853	6.179	2.992	5.524	1.933	2.799	6.157
Ti	0.002	0.717	0.004	0.001	0.000	0.005	0.741	0.007	0.004	0.000	0.354	0.004	0.605	0.011	0.002	0.352
Al	1.996	2.556	0.209	0.040	1.176	1.967	2.490	0.127	0.027	1.130	2.123	1.991	2.585	0.238	1.196	2.295
Fe	1.756	1.835	0.316	0.838	0.010	2.060	2.782	0.430	1.077	0.020	2.509	1.652	1.661	0.234	0.012	1.576
Mn	0.045	0.004	0.002	0.007	0.000	0.109	0.007	0.006	0.016	0.000	0.014	0.039	0.002	0.002	0.000	0.005
Mg	0.739	3.027	0.626	1.138	0.000	0.371	2.170	0.586	0.891	0.001	1.851	0.814	3.214	0.654	0.000	2.627
Ca	0.489	0.007	0.747	0.021	0.166	0.569	0.005	0.826	0.022	0.131	1.818	0.514	0.009	0.783	0.196	1.842
Ba	0.002	0.066	0.000	0.000	0.000	0.001	0.050	0.000	0.000	0.000	0.000	0.001	0.040	0.000	0.000	0.000
Na	0.003	0.000	0.188	0.002	0.809	0.001	0.000	0.119	0.001	0.878	0.832	0.000	0.000	0.166	0.776	0.738
K	0.003	1.833	0.001	0.000	0.025	0.003	1.823	0.000	0.000	0.018	0.274	0.002	1.841	0.001	0.015	0.255
Total	8.018	15.479	4.039	4.012	5.008	8.0488	15.4839	4.04385	4.0093	5.03032	15.95	8.009	15.481	4.021	4.996	15.847

Amphibole in GC14-048 is intergrown with metamorphic biotite. While interpreted to be retrograde, a single amphibole analysis from a grain with a single small inclusion of biotite was selected for use in post-peak P-T calculations. The selected analysis agrees with the average Mg/Fe ratio of 0.63 for amphiboles in the sample, and can be classified as titanian-ferroan-pargasite (Leake et al., 1997).

4.4 Conventional thermobarometry: Calibrated reactions

4.4.1 Background

Conventional geothermometers and geobarometers are used to calculate temperature (T) and pressure (P) from T- and P-sensitive reactions that have been calibrated either experimentally or empirically from natural assemblages (Spear, 1993). Most widely used thermometers are based on T-sensitive cation exchange (e.g. Fe^{2+}-Mg). Barometers generally rely on net-transfer reactions involving significant volume change (e.g., reactions involving grossular and anorthite). Uncertainties for conventional thermobarometers are nominally +/- 50° C and +/- 1 kb (e.g. Essene, 1989), but can be much higher depending on the type of calibration (experimental vs empirical), reliability of thermodynamic data and solution models, and analytical uncertainty associated with microprobe data (Powell, 1985; Powell and Holland, 1994, 2008).

Net transfer reactions involve solid phases of differing compositions. An example of this type of reaction is one of two Grt - Pl - Hbl - Qtz geobarometers of Kohn & Spear (1990):

$$6CaAl_2Si_2O_8\ (anorthite) + 3Ca_2Mg_5Si_8O_{22}(OH)_2\ (tremolite)$$
$$= 2Ca_3Al_2Si_3O_{12}\ (grossular) + Mg_3Al_2Si_3O_{12}\ (pyrope)$$
$$+ 3Ca_2Mg_4Al_2Si_7O_{22}(OH)_2\ (tschermakite) + 6SiO_2\ (quartz)$$

Ion-exchange reactions involve the reciprocal exchange of components of two or more minerals and are especially useful for conventional geothermometry as the partitioning of cations depends strongly on T. Calibrated exchange geothermometers typically involve the partitioning of Fe and Mg, e.g., between garnet and biotite (Spear, 1993):

$$Fe_3Al_2Si_3O_{12}\ (almandine)\ +\ K_2Mg_6[Si_2Al_2O_{20}](OH)_4\ (phlogopite)$$
$$=\ Mg_3Al_3Si_3O_{12}\ (pyrope)\ +\ K_2Fe_6[Si_2Al_2O_{20}](OH)_4\ (annite)$$

Comparisons between directly calibrated thermobarometers are illustrated in Fig. 4.3. A selection of Grt - Bt and Grt - Cpx exchange thermometers, calculated using the program PTQuick (Dolivo-Dobrovolsky, 2016) shows the spread of T estimates produced using the same compositional data (Figure 4.3).

4.4.2 Uncertainties

Garnet-biotite exchange reactions are typically calibrated assuming $Fe^{2+} = Fe_{tot}$. Using Fe^{2+} calculated from Fe_{tot} on a stoichiometric basis for calibrated geothermometers lowers T estimates by lowering the Fe^{2+}/Mg ratio of the mineral.

The simple stoichiometry of ideal clinopyroxene (4 cations : 6 oxygens) allows more confident calculations of Fe^{3+} based on charge balance. In reality, the actual Fe^{3+} content is almost certainly less than the calculated proportion, but without in independent measurement of ferric iron, it is difficult to determine a correct temperature. Most Grt -

Cpx thermometers were calibrated assuming $Fe^{2+} = Fe_{tot}$. Incorporating Fe^{3+} produces very little change in the spread of calibrations, giving T estimates of 597 – 677 °C at 14 kbar, as compared to 725 – 827 °C at 14 kbar when $Fe^{2+} = Fe_{total}$ (Fig. 4.3).

The same reactions calculated with TWQ (Fig. 4.3, dashed lines), with and without Fe^{3+}, are compared with envelope predicted by directly calibrated reactions (Fig. 4.3, solid lines). The slope of the Grt - Bt reaction mirrors most calibrated reaction curves. The TWQ calculated curve, assuming $Fe^{2+} = Fe_{total}$ yields a T estimate of ~825 °C at 14 kbar. The same reaction, incorporating a calculation of Fe^{3+} (using the method of Berman and Aranovich, 2007), gives a T estimate of 790 °C at 14 kbar. The former ($Fe^{2+}=Fe_{tot}$) exceeds the highest conventional calibration curve by 50 °C. The latter, with Fe^{3+}, exceeds the highest conventional calibration by 30 °C. The Grt - Cpx thermometer calculated using TWQ is roughly parallel to directly calibrated reaction curves, and plots within their envelope (Fig. 4.3). Assuming $Fe^{2+} = Fe_{tot}$ gives a T estimate of 790 °C while incorporating Fe^{3+} reduces the estimate to 675 °C.

For $Fe^{2+} = Fe_{tot}$, calibrated Grt - Cpx and Grt - Bt thermometers generally overlap. Reaction curves for the calibrated Grt - Bt thermometer (Spear, 1993; Kleemann & Rienhardt, 1994; Holdaway, 2000; calculated with PTQuick) yield slightly reduced T and narrower spread with the incorporation of Fe^{3+}. The same reactions calculated using TWQ yield a T reduction from 825 °C to 790 °C, the latter falling closer to results from both conventional thermometers. In contrast, T calculated from Grt - Cpx thermometers incorporating Fe^{3+} are ca. 100 °C lower than those suggested by granulite facies assemblage. With the exception of Sengupta et al. (1989), the TWQ calculated Grt - Cpx reaction yields the highest T estimate, regardless of Fe^{3+}. In contrast to the Grt - Bt curve,

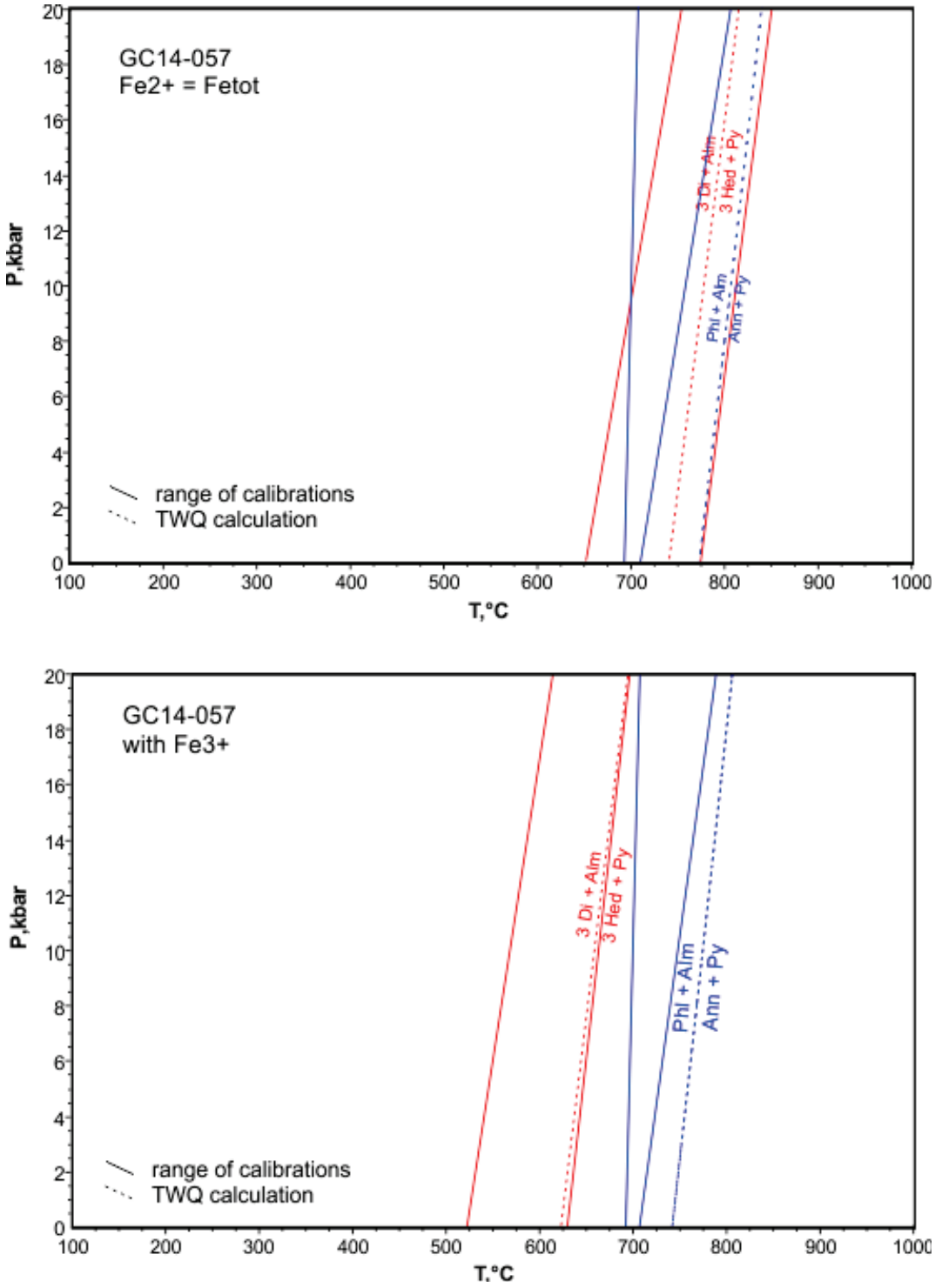

Figure 4.3 Range of reaction curves for conventional thermobarometers (see calibrations for reactions 1 and 2 in Table 4.3) calculated using PTQuick (Dolivo-Dobrovolsky, 2016). Solid lines envelope calibrations for Grt - Bt (blue) and Grt - Cpx (red). TWQ calculated T estimates (dashed line lines): Grt - Bt exceeds all conventional calibrations, while Grt - Cpx falls within their envelope. Note that Grt - Cpx thermometers are affect more than Grt - Bt thermometers by the incorporation of Fe^{3+}.

the Grt - Cpx curve overlaps the calibrated reaction curves, and, in both instances, is

virtually indistinguishable from the Nakamura (2006) calibration.

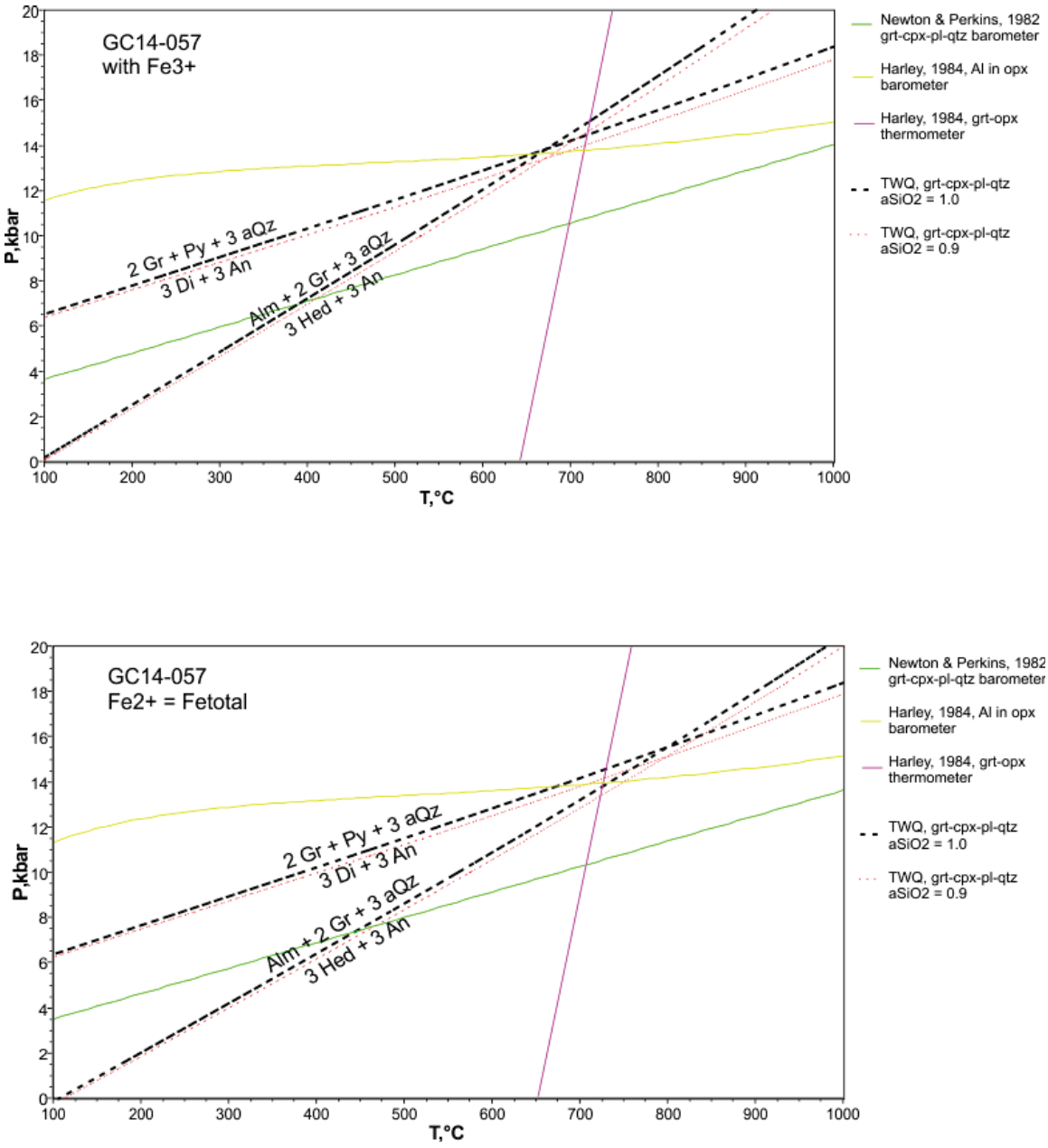

Figure 4.4 Conventional geobarometers (calculated using PTQuick) compared to equivalent reactions calculated by TWQ. Newton and Perkins (1982), mirrors the Mg end-member Grt-cpx-pl-qtz reaction, within errors, and would overlap with a prescribes + 1.6 kbar empirical correction. Negligible reduction in P indicted by dashed red line for reduced $aSiO_2$ = (0.9). Note the precise agreement of Harley (1984a,b) calibrations with TWQ calculated P-T values for GC14-057 (Table 4.3).

The disparity between Grt - Pl - Px - Qtz geobarometer reaction curves from a classic conventional calibration (Newton & Perkins, 1982) and a TWQ calculation is substantial, giving P estimates of 10.5 ± 1.6 kbar and 14.5 kbar, respectively, at 700 °C (Fig. 4.4). The latter agrees well with results from the calibrated Grt - Opx thermometer (Harley, 1984a) and Al-solubility in Opx barometer (Harley, 1984b), which intersect at 728 °C at 13.9 kbar ($Fe^{2+} = Fe_{tot}$) or 716 °C at 13.7 kbar (with Fe^{3+}). While the calibrated Grt-Opx P-T estimates appear indistinguishable from TWQ multiequilibrium results (718 °C at 13.8 kbar), errors associated with both barometers are large, ± 2 kbar (Harley, 1984b).

Reductions in P with incorporation of Fe^{3+} in the Grt - Cpx - Pl - Qtz (Newton and Perkins, 1982) and Al-solubility in Opx barometer (Harley, 1984b) are insignificant (~0.2 kbar) given uncertainties. TWQ calculations of the Grt - Cpx - Pl - Qtz barometer with $Fe^{2+} = Fe_{tot}$ and with Fe^{3+} show similar, negligible reductions in P, well within multiequilibrium based uncertainties, ± 1 kbar, calculated by the INTERSX program.

Conventional thermobarometers produce a broad range of P-T estimates. The inherent ambiguity of comparing values from different calibrations and mineral pairs is compounded by large errors associated with even the most recent calibrations. Conventional P-T estimates are, nevertheless, expedient indicators of the P-T range of interest. The multiequilibrium P-T calculations of TWQ provide more robust estimates based on all possible reactions for the given mineral assemblage and compositions. Calculating P-T based on all potential equilibria eliminates the potential for cross-calibration ambiguity, as only one reaction curve is modelled for each equilibrium, calculated from the same, internally consistent set of thermodynamic mineral properties

and solid solution models. Also, the ability to identify and omit equilibria involving potentially problematic and/or poorly constrained mineral end-members minimizes deviations form the "true" P-T of the system may become pronounced by focussing primarily on independent sets of reactions (Berman, 1991).

The geometric mean values for P-T calculated by INTERSX from TWQ plots are estimates of the uncertainties on the position of the "ideal" intersection of calculated reactions. They are not, strictly speaking, true statistical uncertainties of P-T, as they do not account for uncertainties in analytical and thermodynamic data (e.g. Hodges and McKenna, 1987). Despite this, P-T values for samples GC14-057 describes a plausible degree of precision and is likely accurate. Lack of preserved orthopyroxene from the peak assemblage of sample GC14-048 in the southern region, however, results in very few potential equilibria for the assemblage Grt + Cpx + Pl + Bt, and the resulting yielding estimates of 16.1 ± 0.6 kbar and 825 ± 31 °C. For comparison, amphibole, though appearing to be texturally retrograde, is compositionally equilibrated (Fig. 4.5c) with the peak granulite assemblage (Grt + Cpx + Pl + Bt) for GC14-048. Including amphibole in the assemblage provided a third independent reaction, yielding an estimate of 15.0 ± 0.2 kbar and 785 ± 4 °C (Table 4.3). As stated earlier, the implausibly precise errors (conservative estimates of uncertainty are ± 1 kbar and 50 °C) are strongly indicative of compositional equilibration of the assemblage, and may indicate that pargasite, contrary to textural evidence, is part of a high-P peak assemblage (Pattison, 2003).

Table 4.3 *Calibrated reactions for conventional thermobarometers*

1. *garnet-biotite* (Spear, 1993; Bhattacharya et al., 1992)

$$Fe_3Al_2Si_3O_{12}\ (almandine)\ +\ K_2Mg_6[Si_2Al_2O_{20}](OH)_4\ (phlogopite) = Mg_3Al_2Si_3O_{12}\ (pyrope)\ +\ K_2Fe_6[Si_2Al_2O_{20}](OH)_4\ (annite)$$

2. *garnet-clinopyroxene* (Powell, 1985; Krogh Ravna, 2000)

$$Fe_3Al_2Si_3O_{12}\ (almandine) + 3CaMgSi_2O_6\ (diopside) = Mg_3Al_2Si_3O_{12}\ (pyrope) + 3CaFeSi_2O_6\ (hedenbergite)$$

3. *garnet-hornblende* (Graham and Powell, 1984)

$$3NaCa_2Fe_4Al_3Si_6O_{22}(OH)_2\ (ferro\text{-}pargasite) + 4Mg_3Al_2Si_3O_{12}\ (pyrope) = 3NaCa_2Mg_4Al_3Si_6O_{22}(OH)_2\ (pargasite) + 4Fe_3Al_2Si_3O_{12}\ (almandine)$$

4. *garnet-orthpyroxene* (Harley, 1984a)

$$2Mg_3Al_2Si_3O_{12}\ (pyrope) + 3Fe_2Si_2O_6\ (ferrosilite) = 2Fe_3Al_2Si_3O_{12}\ (almandine) + 3Mg_2Si_2O_6\ (enstatite)$$

5. *garnet-hornblende-plagioclase-quartz* (Kohn and Spear, 1990) Fe end members

$$6CaAl_2Si_2O_8\ (anorthite) + 3Ca_2Fe_5Si_8O_{22}(OH)_2\ (Fe\text{-}actinolite) = 2Ca_3Al_2Si_3O_{12}\ (grossular) + Fe_3Al_2Si_3O_{12}\ (almandine) + 3Ca_2Fe_4Al_2Si_7O_{22}(OH)_2\ (Fe\text{-}tschermakite) + 6SiO_2\ (quartz)$$

6. *garnet-hornblende-plagioclase-quartz* (Kohn and Spear, 1990) Mg end members

$$6CaAl_2Si_2O_8\ (anorthite) + 3Ca_2Mg_5Si_8O_{22}(OH)_2\ (tremolite) = 2Ca_3Al_2Si_3O_{12}\ (grossular) + Mg_3Al_2Si_3O_{12}\ (pyrope) + 3Ca_2Mg_4Al_2Si_7O_{22}(OH)_2\ (tschermakite) + 6SiO_2\ (quartz)$$

7. *garnet-clinopyroxene-plagioclase-quartz* (Newton and Perkins, 1984)

$$3CaAl_2Si_2O_8\ (anorthite) + 3CaMgSi_2O_6\ (diopside) = 2Ca_3Al_2Si_3O_{12}\ (grossular) + Mg_3Al_2Si_3O_{12}\ (pyrope) + 3SiO_2\ (quartz)$$

Reactions on which the calibrated thermobarometers are based are compiled in table 4.2. Peak temperatures were calculated using the garnet – clinopyroxene (Krogh Ravna, 2000), and garnet – biotite (Bhattacharya, 1992; Spear 1993) thermometers. The garnet – hornblende (Graham and Powell, 1984) thermometer was applied for comparison, as textural evidence suggest that amphibole is retrograde. Several thermometers (Bhattacharya et al., 1992; Spear, 1993; Krogh Ravna; 2000) calculate temperature at a given pressure. Preliminary winTWQ derived multiequilibrium estimates were used where approximations of P (14.4, 14.0 and 16.1 kbar for the north, central and south samples, respectively) were required to calculate T, and vice versa.

4.4.3 Results, conventional thermobarometry

4.4.3.1 Northern Britt Domain, GC14-057

All temperature data are summarized in Table 4.3 and Figure 4.7. Three Grt - Bt thermometers were applied, using a P estimate of 14.0 kbar derived from preliminary multiequilibrium calculations using winTWQ. The Spear (1993) calibration produced the highest T at 763 °C. Bhattacharya et al. (1992) employed two different solution models (Hackler and Wood, 1989; Ganguly and Saxena, 1984; HW and GS, respectively) yielding estimates of 703 °C (HW) and 722 °C (GS). The Grt - Opx thermometer of Harley (1984a) gives a T estimate of 730 °C at 14.0 kbar. The Grt - Cpx calibration of Krogh Ravna (2000), gives an estimate of 721 °C. Assuming minimum T uncertainties of ± 50 °C, all estimates overlap within uncertainty. Though Fe-Mg exchange thermometers are all susceptible to post-peak thermal reequilibration, pyroxene is more resistant to retrograde exchange then biotite, and is considered a more reliable monitor of peak T.

That Grt - Cpx and Grt - Opx thermometers yield comparable results also supports their reliability.

The geobarometer of Harley (1984b), based on Al solubility in orthopyroxene (Al - Opx barometer) in the presence of garnet, gives a P estimate of 13.9 kbar at 734 °C. Errors for this calibration however, are large, and especially so for Fe-rich compositions. Since no amphibole is present in the representative northern sample, the Al - Opx barometer provides the only conventional P estimate for this sample.

4.4.3.2 Central Britt Domain, GC14-024

Garnet-biotite geothermometers, using winTWQ based P estimates, consistently produced T estimates 50 - 90 °C lower than winTWQ based average T. Spear (1993) produced the highest estimate, at 713 °C. The Bhattacharya et al. (1992) calibrations produced virtually identical results (669 °C and 667 °C) based on the (HW) and (GS) mixing models, respectively. The Krogh Ravna (2000) Grt - Cpx calibration produced an estimate of 702 °C. The presence of retrograde pargasite allows for the application of the garnet-hornblende calibration of Graham and Powell (1984), producing a post-peak T estimate of 631 °C.

As discussed in section 4.2.2, P estimates for quartz-free assemblages calculated using net-transfer reactions involving quartz indicate a maximum value. The Grt – Hbl – Pl – Qtz geobarometer of Kohn and Spear (1990) is a widely used calibration that produces two independent P estimates based on reactions described by equation 5 (Table 4.2) for Fe and Mg end members. Despite the relatively low T produced by the garnet-hornblende thermometer, P estimates are relatively high, 14.9 and 14.0 kbar based on Fe

and Mg end members, respectively, with $aSiO_2 = 1$. For comparison, applying an $aSiO_2 = 0.9$ in the reaction, on par with that applied in multiequilibrium, lowers the resulting P estimates to 14.5 and 13.5 kbar, based on Fe and Mg end members, respectively. Differences between Fe and Mg end member based reactions is related to poorly constrained Fe^{3+} content of amphibole.

4.4.3.3 Southern Britt Domain, GC14-048

The Spear (1993) Grt - Bt calibration produced the highest T estimate, at 770 °C. The Bhattacharya et al. (1992) calibrations yielded estimates of 706 °C (HW) and 729 °C (GS). The Krogh Ravna (2000) Grt - Cpx thermometer yields a T estimate of 684 °C (at 13.5 kbar, from winTWQ multiequilibrium calculations). The Graham and Powell (1984) Grt - Hbl thermometer produced a T estimate of 670 °C.

Sample GC14-048 does not contain modal quartz and the Kohn and Spear (1990) Grt – Hbl-based P estimates are maxima. Using $a_{SiO2} = 1.0$ produced P estimates of 13.3 and 14.4 kbar based on the Fe and Mg end member calibrations, respectively. Using $a_{SiO2} = 0.9$, P estimates are reduced to 12.8 and 13.8 kbar.

4.5 Multiequilibrium modelling: winTWQ

4.5.1 Background

P-T estimates from calibrated reactions rely on intersections of reaction curves in P-T space involving independent calibrations that may be inconsistent with each other in term of experimental method or thermodynamic constraints. Additionally, there is no guarantee that P or T assumed for the purpose for calculations based on these calibrations

is correct, though intersections in P-T space can be calculated by solving thermometers and barometers iteratively (i.e. using calculated P to solve for T and vice versa, until the results converge). Ambiguity of P or T results also arises from inconsistencies between various calibrations for the same mineral pairs, such as the garnet – biotite geothermometers of Spear (1993) and Bhattacharya et al. (1992) used in this study (Berman, 1991).

An alternative approach is to use multiequilibrium models, which operate by calculating all possible reactions between an assemblage of specified components of measured composition. The intersections of reaction curves in P-T space define the conditions of equilibration for the specified assemblage. Chemical systems are defined by the minimum number of components necessary to represent the system. The positions of potential reactions are calculated using thermodynamic properties of the minerals drawn from an internally consistent database compiled from reliable experimental and empirical data (Berman, 1988, 1991). Fundamental thermodynamic properties (e.g. ΔH_f°) are calculated from experimentally and empirically derived values of comparable reliability using the same algorithm. The resulting properties are then used in all equilibrium calculations, ensuring consistent application of end member activities between different reactions. The use of internally consistent databases to calculate reactions and potential equilibration conditions alleviates the consistency problems with conventional, calibrated thermobarometers.

Table 4.4 *Multiequilibrium and conventional thermobarometry P-T estimates*

Area	**Northern Britt Domain**				**Central Britt Domain**				**Southern Britt Domain**			
	Key Harbour				**Byng Inlet**				**Point au Baril**			
Sample	GC14-057				GC14-024				GC14-048			
		±				±				±		
T (TWQ)	718	44			763	12			785	4		
P (TWQ)	13.8	1.0			13.1	0.3			15.0	0.2		
Garnet - biotite	P	T	±		P	T	±		P	T	±	
T (S93)	14.0	760	50		13.5	713	50		16.1	770	50	
T (B92, HW)	14.0	703	50		13.5	671	50		16.1	706	50	
T (B92, GS)	14.0	722	50		13.5	670	50		16.1	729	50	
Garnet - clinopyroxene			±				±				±	
T (KR00)	14.0	721	50		13.5	702	50		16.1	684	50	
Garnet - orthopyroxene	P	±	T	±								
T (H84a)	14.0	-	730	50								
P (H84b)	13.9	2	734	-								
T (AB97)	14.0	-	627	50	13.5	626	50					
Garnet - hornblende							±				±	
T (GP84)	-	-			-	631	50		-	670	50	
Garnet - hornblende - plagioclase - quartz					P	±	T		P	±	T	
P (KS90, Fe)	-				14.9	1	764		13.3	1	825	
P (KS90, Mg)	-				14	1	764		14.4	1	825	

TWQ, Berman (2007); S93, Spear (1993); B92, Bhattacharya et al., 1992, with solutions models by Hackler and Wood (1994, HW) and Ganguly and Saxena (1984, GS); KR00, Krogh Ravna, (2000); H84a, Harley (1994a); H84b, Harley (1994b); GP84, Graham and Powell, (1984); KS90, Kohn and Spear (1990) with reactions for Fe and Mg end-members, respectively. T and P refer to geothermometer and barometer, respectively, with the accompanying P or T assumed for purposes of calculation. ± 1 kbar and 50 °C errors are a minimum as per Powell and Holland (2008)

4.5.2 WinTWQ

The program winTWQ (Berman, 1991, 2007) operates by modelling all possible reactions for a defined set of components within P-T-X-activity space. In this case, the system NCKFMASH (SiO_2-Al_2O_3-FeO-MgO-CaO-Na_2O-K_2O-H_2O) was selected to represent mafic granulite metamorphic assemblages including the end member

components of garnet (grossular, pyrope, almandine), clinopyroxene (diopside, hedenbergite), orthopyroxene (enstatite, ferrosilite), biotite (phlogopite, annite), and plagioclase (anorthite, albite). Solution models are applied through an integrated program (winCMP) that calculates mole fractions, site distributions, and activities from composition files containing wt.% oxide analyses. The same program can be used to calculate Fe^{3+}. Solution models can be selected or omitted if ideality is assumed. Assuming that: 1) the thermodynamic data are accurate, 2) the mineral analyses are accurate, and 3) the mineral assemblage is in equilibrium, then the intersection of component reactions around a single point in P-T space indicates that the mineral assemblage could have equilibrated at those P-T conditions. The failure of reaction lines to intersect at a single point indicates that one of these assumptions is invalid. Though it is impossible to tell which is in error, uncertainties associated with complicated geological systems are, generally, more problematic than uncertainties in thermodynamic data. In practice, the plotted reaction curves rarely intersect at a single point.

The INTERSX program analyzes winTWQ output to calculate average P-T data statistically from all reaction intersections. The algorithm progressively excludes outlying reaction intersections until included intersections fall within 2σ of the average point in P-T space. The uncertainties in P-T calculated by INTERSX are purely geometrical,

Figure 4.5 (following page) Multiequilibrium plots calculated in TWQ for the A) northern, B) central, and C) southern regions of the Britt domain (Berman, 1991, 2007; version 2.31, using the DEC06 database. See Table 4.1 for solution models applied). Equilibria involving Hd are excluded from all calculations. All models use calculated Fe^{3+} and $a_{SiO2} = 1.0$. Note that amphibole, interpreted texturally to be retrograde is all sections, is compositionally well equilibrated (near perfect convergence of equilibria) with the peak assemblage for GC14-048.

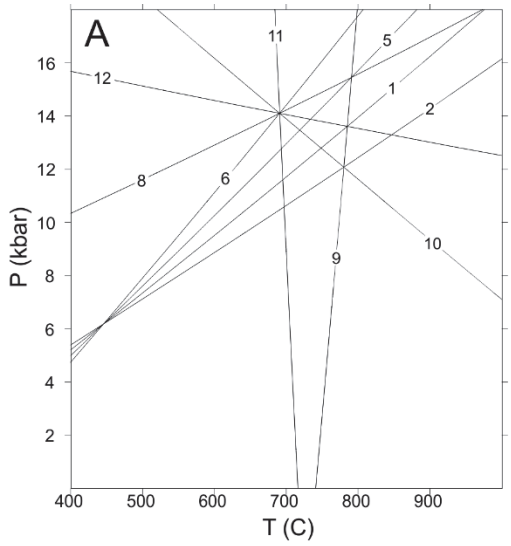

Sample: GC14-057
P: 13.8 ± 1.0 kbar
T: 718 ± 44 C
IR: 4

Equilibria:
1. 2 Alm + Gr + 3 α-Qtz = 6 Fs + 3 An
2. 3 α-Qtz + 3 Di + Ann + 3 Alm = 3 An + 12 Fs + Phl
5. 3 α-Qtz + Phl + 2 Gr + Alm = Ann + 3 An + 3 Di
6. 6 Fs + 3 Gr + 2 Phl + 3 α-Qtz = 6 Di + 3 An + 2 Ann
8. 3 α-Qtz + Py + 2 Gr = 3 An + 3 Di
9. Alm + Phl = Py + Ann
10. 3 α-Qtz + 3 Py + 3 Di + 4 Ann = 3 An + 12 Fs + 4 Phl
11. Py + 3 Di + 2 Ann = 6 Fs + Gr + 2 Phl
12. 2 Ann + Gr + 2 Py + 3 α-Qtz = 2 Phl + 6 Fs + 3 An

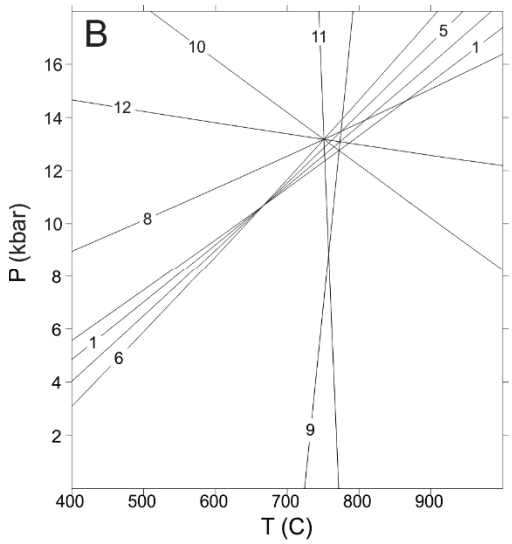

Sample: GC14-024
P: 13.1 ± 0.3 kbar
T: 763 ± 12 C
IR: 4

Equilibria:
1. 2 Alm + Gr + 3 α-Qtz = 6 Fs + 3 An
2. 3 α-Qtz + 3 Di + Ann + 3 Alm = 3 An + 12 Fs + Phl
5. 3 α-Qtz + Phl + 2 Gr + Alm = Ann + 3 An + 3 Di
6. 6 Fs + 3 Gr + 2 Phl + 3 α-Qtz = 6 Di + 3 An + 2 Ann
8. 3 α-Qtz + Py + 2 Gr = 3 An + 3 Di
9. Alm + Phl = Py + Ann
10. 3 α-Qtz + 3 Py + 3 Di + 4 Ann = 3 An + 12 Fs + 4 Phl
11. Py + 3 Di + 2 Ann = 6 Fs + Gr + 2 Phl
12. 2 Ann + Gr + 2 Py + 3 α-Qtz = 2 Phl + 6 Fs + 3 An

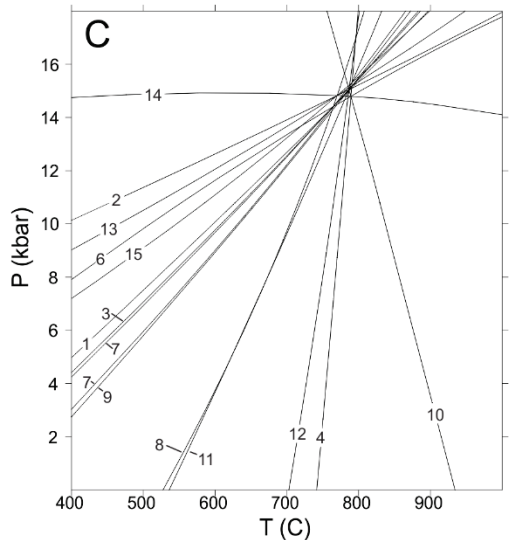

Sample: GC14-048
P: 15.0 ± 0.2 kbar
T: 785 ± 4 C
IR: 3

Equilibria:
1. 3 aQz + Phl + 2 Gr + Alm = Ann + 3 An + 3 Di
2. 3 aQz + Py + 2 Gr = 3 An + 3 Di
3. 3 Ab + 4 Alm + 8 Gr + 3 aQz + 3 Tsc = 3 FePa + 9 Di + 15 An
4. Alm + Phl = Py + Ann
5. 3 Ab + 3 Alm + Ann + 6 Gr + 3 Tsc = 3 FePa + Phl + 6 Di + 12 An
6. 3 FePa + 12 aQz + 5 Phl + 2 Gr + Alm = 3 Ab + 5 Ann + 6 Di + 3 Tsc
7. 3 Ab + Alm + 3 Ann + 2 Gr + 3 Tsc = 3 FePa + 6 aQz + 3 Phl + 6 An
8. 3 Ab + 4 Ann + 3 Di + 3 Tsc = 3 FePa + 9 aQz + 4 Phl + 3 An
9. 3 Ab + 4 Alm + 6 Gr + 3 Tsc = 3 FePa + Py + 6 Di + 12 An
10. 3 FePa + 12 aQz + 5 Py + 2 Gr = 3 Ab + 4 Alm + 6 Di + 3 Tsc
11. 3 Ab + 4 Alm + 2 Gr + 3 Tsc = 3 FePa + 6 aQz + 3 Py + 6 An
12. 3 Ab + 4 Alm + 3 Di + 3 Tsc = 3 FePa + 9 aQz + 4 Py + 3 An
13. 3 Ab + 4 Ann + 6 Gr + 3 Py + 3 Tsc = 3 FePa + 4 Phl + 6 Di + 12 An
14. 3 FePa + 12 aQz + Py + 4 Phl + 2 Gr = 3 Ab + 4 Ann + 6 Di + 3 Tsc
15. 3 Ab + 4 Ann + 2 Gr + Py + 3 Tsc = 3 FePa + 6 aQz + 4 Phl + 6 An

describing the spread of reaction intersections about the average point, and do not reflect

analytical or thermodynamic uncertainties. Calculated P-T data using the INTERSX program for samples GC14-057, 024, and 048, are summarised in Table 4.3 and Figure 4.9. Except where indicated, the following winTWQ results were calculated with Fe^{3+} calculated by winCMP and $a_{SiO2} = 1$.

4.5.3 Results

4.5.3.1 Northern Britt Domain, GC14-057

Multiequilibrium calculations using winTWQ (Berman, 2007) indicate that a good approximation of local equilibrium is given by representative analysis of the assemblage Grt + Pl + Opx + Cpx + Bt ± α-Qtz.

P-T estimates using the INTERSX program for multiequilibrium plots using carefully selected, averaged compositions for garnet, pyroxene, and plagioclase give a poorly constrained pressure of 14.0 ± 1.7 kbar, and a temperature of 734 ± 54 °C. The exclusion of reactions involving jadeite, hedenbergite, and pargasite (phases with relatively poorly constrained thermodynamic property data and high sensitivity to Fe^{3+}) dramatically increased the convergence of reactions, yielding estimations of 13.8 ± 1.0 kbar and 719 ± 44 °C (Fig. 4.5a). Calculated values and uncertainties are comparable to conventional thermobarometers and probably realistic. These estimates provide an approximation of the region in P-T space in which the assemblage may have equilibrated, and were used for those calibrated thermobarometers where approximations of P are required in order to calculate T, and vice versa, in section 4.4.

4.5.3.2 Central Britt Domain, GC14-024

The representative sample from the central Britt Domain contains significant modal pargasite overprinting peak Fe-Mg phases. The peak metamorphic assemblage mirrors that of Key Harbour, including Grt + Opx + Cpx + Pl + Bt ± α-Qtz. As with sample GC14-057, quartz is absent from the assemblage. Reactions involving hedenbergite were strongly divergent. Due to poorly constrained thermodynamic data and sensitivity to Fe^{3+} content, hedenbergite was excluded from the calculation. Excluding pargasite, as a retrograde phase, and hedenbergite from the assemblage improved the precision of estimates significantly, from 13.5 ± 1.4 kbar at 764 ± 40 °C to 13.1 ± 0.3 kbar at 763 ± 12 °C (Fig. 4.5b).

4.5.3.3 Southern Britt Domain, GC14-048

Pargasite is a major phase in SmD in the southern Britt Domain. Pargasite in sample GC14-048, however, does not strongly overprint pyroxene mosaics, and early corona textures are relatively well preserved. As with GC14-024, pargasite is interpreted, texturally, as retrograde, and initially excluded from the peak assemblage. Multiequilibrium TWQ plots show relatively strong agreement between reactions based on representative compositions for the assemblage Grt + Cpx + Pl + Bt ± a-Qtz. The number of reactions available to the system is reduced by two-thirds relative to samples from the northern and central regions due to the lack of orthopyroxene. The remaining 6 reactions provide a P-T estimate of 16.0 ± 1.0 kbar at 821 ± 57 °C. The exclusion of hedenbergite produced slightly lower P-T estimate of 15.1 kbar at 790 °C based on the perfect intersection of only three reactions. Regardless, both estimates involve only 2 independent reactions and 3 are necessary for TWQ results to be meaningful.

As an alternative, plots including pargasite in the peak assemblage were calculated for comparison. Though it was necessary to assume ideal mixing for amphiboles, the resulting plots show almost perfect convergence, strongly indicating equilibration at 15.0 ± 0.2 kbar at 785 ± 4°C (Fig. 4.5c).

4.6 Phase Equilibrium Modelling: Theriak-Domino

4.6.1 Background

Reverse modelling techniques such as conventional thermobarometry and multiequilibrium calculations assume equilibrium and calculate P-T conditions directly from mineral analyses. Standard petrogenetic grids plot all possible reactions for a given set of components, irrespective of their relative abundances in the system. The vast majority of reactions contained in petrogenetic grids are not experienced by the specific rock composition of interest, and the stability fields and reactions indicated may not be consistent with that system.

Phase equilibrium analysis is a forward modelling technique that uses internally consistent thermodynamic data sets to predict equilibrium assemblages, reaction boundaries, mineral compositions, and modal proportions for specified bulk compositions (de Capitani and Brown, 1987; Connolly, 1990, 2005; Powell et al, 1998; Powell and Holland, 2008, 2010; de Capitani and Petrakakis, 2010). This involves defining both the components of the system and their molar proportions. The resulting composition-specific diagrams, called pseudosections, are more useful than petrogenetic grids, and differ fundamentally from multiequilibrium calculations, in that only reactions actually seen by

the bulk composition of interest are modelled. The resulting diagrams are compared against observed mineral assemblages and compositions from natural samples.

Two widely used forward modelling programs for the generation of pseudosections are Thermocalc (Powell and Holland, 1988) and Theriak-Domino (de Capitani and Petrakakis, 2010). Both calculate mineral assemblage stability fields separated by reaction boundaries compatible with a specified bulk composition, but use very different computational techniques to generate the diagrams. Thermocalc calculates user-defined univariant reaction boundaries, where $\Delta G_{rxn} = 0$, between stability fields, one reaction boundary at a time. The process is user intensive and time-consuming.

4.6.2 Theriak-Domino

Theriak-Domino (T-D) (de Capitani & Petrakakis, 2010) is an efficient thermodynamic software package that generates pseudosection plots by iteratively solving for minimum Gibbs free energy (ΔG) across a grid. The program then defines stability fields of assemblages by drawing reaction boundaries between regions of the grid with common predicted assemblages. Boundary locations are then refined using an algorithm which smooths curves by calculating ΔG within progressively higher-resolution nested grids. The process is entirely automated, and diagrams can be generated in a matter of minutes. Like Thermocalc, the plots can be contoured for mineral compositions and mode for comparison with observations. The primary weakness of this technique (relative to Thermocalc) is the potential to miss stability fields smaller than the resolution of the grid (de Capitani & Petrakakis, 2010). A strength of T-D, relative to Thermocalc, is that pseudosections can be generated fairly rapidly, with a reduced potential for human error,

allowing for the efficient modelling of several possible systems. For this reason, T-D was chosen for thermodynamic modelling.

Two different approaches were used to determine the effective bulk compositions (EBC), the bulk chemistry of the modelled system, to be used in T-D calculations. The first was to use the whole rock compositions acquired from SmD samples (Appendix B). Given the large contribution of relict phases (e.g. Aug, Ilm, Pl), refractory accessory phases (e.g. Ap), and unequilibrated metamorphic phases (e.g. high-Na Pl in Olg-moats, Sp) to the bulk composition of SmD, the results were not useful (Section 4.6.2), indicating the need to define an EBC specific to textural and compositional subdomains observed in SmD.

Coronitic textures characteristic of these samples indicate that equilibration was restricted to compositional and textural subdomains and therefore the effective bulk composition involved in the corona-forming reactions was not the whole rock composition. Because olivine and plagioclase are the dominant phases participating in early corona-forming reactions, an alternative approach was adopted based on a range of Pl:Ol ratios and assumed primary mineral compositions.

While corona-forming reactions take place along the original shared grain boundary, the original proportions of the two primary minerals participating in the reaction are unknown. For purposes of defining an EBC, variable proportions of olivine (matrix olivine and olivine xenocrysts, Fo_{44} and Fo_{60}, respectively), and plagioclase (matrix lath cores and rims, An_{60} and An_{40}, respectively) in normal unenriched SD north of the GF (Bethune and Davidson, 1997) were combined. Enriched SD compositions differ slightly, with matrix olivine compositions in the range Fo_{25-35} and plagioclase core

and rim compositions of An_{54} and An_{30}. A sensitivity analysis was undertaken using primary olivine and plagioclase compositional ranges of normal diabase combined in 60:40, 50:50, and 40:60 proportions to produce bulk compositions representing the primary corona-forming interface. As enriched SD and SmD are fairly uncommon, T-D modelling was performed using primary compositional ranges from normal, unenriched SD.

4.6.3 Results

4.6.3.1 EBC: Whole rock geochemistry

Pseudosections for each region of the study area using an EBC based on the whole rock geochemistry of each sample contain very similar stability fields, with roughly identical equilibrium assemblages. The assemblages produced, however, are inconsistent with petrographic observations (section 3.3.1). Assemblages predicted invariably contain modal olivine and feldspathoid minerals over the entire P-T of interest, neither of which are present in SmD south of the GFTZ (Bethune, 1993; Jamieson et al., 1995; Bethune & Davidson, 1997; Ketchum & Davidson, 2000; this study). In addition, modal K-feldspar is predicted to be stable at pressures above 11 - to - 15 kbar. Rare accessory K-feldspar is present in SD north of the GF, but has not been found as a metamorphic phase in SmD. Adjustments to the EBC for abundant refractory apatite had little effect on the position of stability fields, and did not remove the incompatible phases.

4.6.3.2 EBC: The plagioclase – olivine interface

Proportions of the plagioclase + olivine system (% plagioclase : % olivine; 60:40, 50:50, 40:60) produced phase equilibria more consistent with the observed coronitic

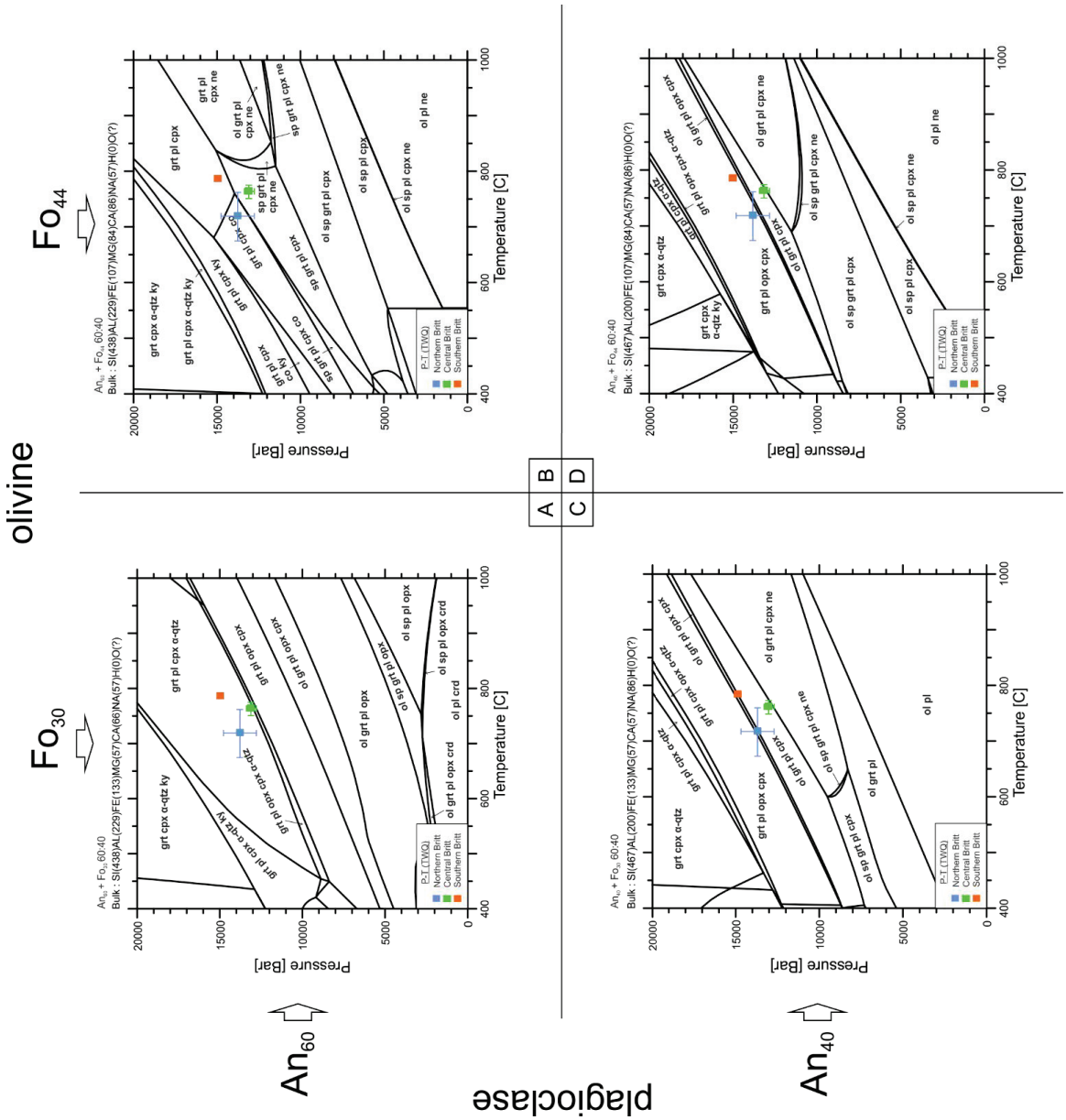

Figure 4.6 Phase equilibrium diagrams modelled for bulk compositions 60% plagioclase and 40% olivine (60:40) for all combinations of An_{60}, An_{40}, Fo_{44} and Fo_{30}. Multiequilibrium based P-T results from winTWQ are plotted with errors for comparison against predicted stability fields. All plots generated using Theriak-Domino (de Capitani and Petrakakis, 2010) using a modified version of the JUN92.bs database (Berman, 1988). Note that only systems incorporating An_{40} (c,d) predict the peak assemblage including garnet + plagioclase + 2 pyroxenes. Model (C) was selected for detailed examination (figure 4.7).

assemblage than those based on bulk geochemistry. Feldspathoid minerals are stable near

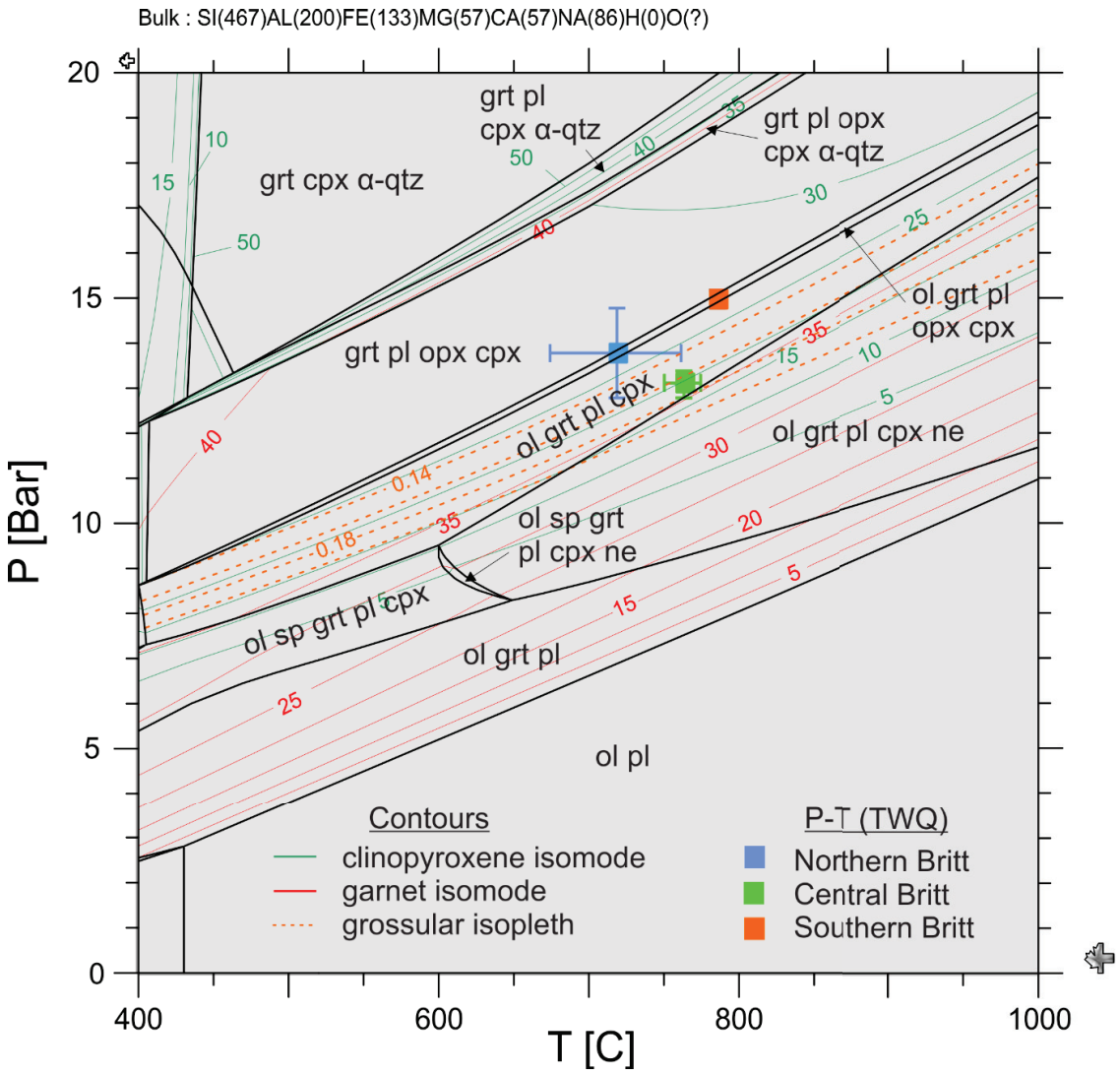

Figure 4.7 Detail of figure 4.6c contoured for isomodes (volume %) of the primary corona forming phases clinopyroxene (solid green) and garnet (solid red). Note the steady increase indicated for both with increasing P. P-T estimates (within range) for northern and central Britt domain fall within measured grossular composition of garnets (dashed orange). P-T estimates for the southern Britt domain are likely excessive, and would fall within range of measured grossular compositions given reasonable P-T uncertainties.

the P-T region of interest, though generally limited to higher temperatures. The observed Grt + Pl + Px coronitic assemblage is generally replicated close to the P-T range of interest (Figure 4.5).

Diagrams produced using olivine-rich systems (40:60) predict that modal olivine remains stable through the entire range of modelled P-T space, and are were not

considered further. Diagrams produced using plagioclase-rich (60:40) and equal-proportioned (50:50) systems, by contrast, indicate loss of olivine above ~11-15 kbar (between ~600 – 800 °C). Quartz is predicted to be stable (≤ 6 vol.%) above ~ 15-19 kbar for the same temperature range. Modal quartz is entirely absent from SmD assemblages described from any location throughout the parautochthon, though it is likely SiO_2 is participating in, and being consumed during, the various metamorphic reactions.

Systems composed of equal parts of olivine and plagioclase (50:50), regardless of mineral composition, are also problematic. Olivine is predicted to remain stable up to pressures of ~12-16 kbar through temperatures of ~ 600-800 °C, roughly within the P-T region of interest. A more problematic inconsistency with 50:50 systems is the prediction that plagioclase is only stable in the presence of olivine. Modal quartz is not predicted to be stable for 50:50 systems throughout the P-T range considered.

Systems composed of 60% plagioclase and 40% olivine replicate stability fields consistent with the early corona assemblage (Bethune, 1993; Jamieson et al, 1995; Bethune and Davidson, 1997), and the peak metamorphic assemblage Grt + Px + Pl. However, only 60:40 systems using An_{40} produce broad stability fields in which two pyroxenes (Cpx + Opx) are stable together. Results from peak P-T multi-equilibrium calculations generally lie within the broad stability field containing the two-Px + Grt + Pl assemblage (figure 4.6 c,d), and the predicted X_{Grs} corresponds roughly (within uncertainties) to the measured X_{Grs} of garnet from each region: Grs_{16}, Grs_{19}, and Grs_{17} for north, central, and southern samples, respectively (Figure 4.7). Spinel ‘dust’ in relict plagioclase laths, stable as a product of early Al exsolution during the couple substitution

(Ca + Al → Na + Si) by which igneous An_{60} lath cores changed to ~An_{25} measured in SmD, is represented in stability fields at lower P-T.

4.7 Discussion

Thermobarometric results from this study are plotted for comparison with P-T estimates from previous work on SmD and other monocyclic metabasites of the CGB (Fig. 4.8, 4.9). Temperature estimates for Key Harbour are generally ≤ 100 °C lower than the highest T estimates from previous work on SmD (Jamieson et al., 1995) but are comparable within errors. A southward increase in peak T, from 718 to 820 °C, across the Britt domain is indicated by winTWQ-based estimates. Conventional thermometers, with the exception of the Grt - Cpx calibration (Krogh Ravna, 2000), suggest virtually identical T estimates for the northern and southern samples, with a lower peak T for the central Britt Domain. While winTWQ estimates are considered more reliable, the calculated uncertainty is simply the geometric distribution of reaction intersections about the mean point in P-T space: uncertainties in analytical or thermodynamic data are not considered (Hodges and McKenna, 1987). Realistic uncertainties associated with multiequilibrium calculations and conventional thermobarometers are roughly equivalent (Essene, 1989; Berman, 1991). Considering this, results indicate that late-stage Grenvillian metamorphism produced identical peak T within the range 720 – 820 °C across the entire Britt Domain.

4.7.1 Peak T

Peak T estimates from Grenvillian metamorphic assemblages in coronitic metagabbro (coronite) and calc-silicate paragneiss within the Shawanaga domain

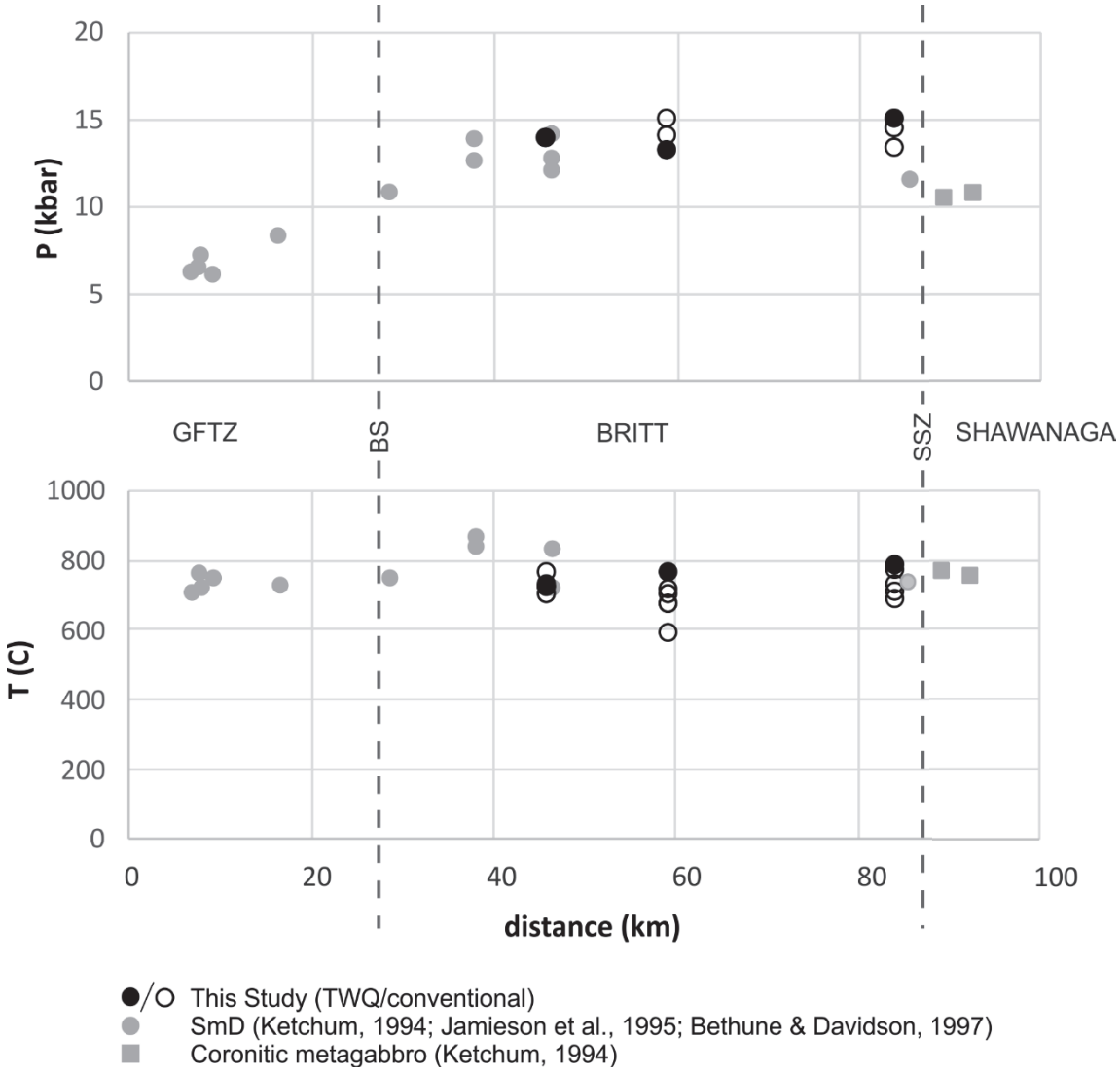

Figure 4.8 Comparison of peak P (a) and T (b) vs. distance from the GF across the GFTZ, and the Britt and Shawanaga domains. Dashed lines correspond to the Boundary shear (BS) separating the GFTZ and Britt Domain (Jamieson et al., 1995), and the Shawanaga Shear Zone (SSZ) separating the Britt and Shawanaga domains, marking the local expression of the ABT (Culshaw et al, 1994; Ketchum 1994). P-T estimates from this study are plotted in black. Estimates from previous studies are plotted in grey. GFTZ data from Jamieson et al. (1995), Bethune and Davidson (1997); Britt domain data from Jamieson et al. (1995), Ketchum (1994), and this study; Shawanaga data from Ketchum (1994). SmD are denoted by circles and ca. 1150-1170 Ma coronitic metagabbro by squares. All data represented here, with the exception of conventional P-T estimates from this study (open circles), were calculated using winTWQ (Berman, 1991, 2007), though previous studies used older versions of the software. Note the steady increase in peak P across the GFTZ, reaching a plateau in the northern Britt Domain, and a sharp decrease across the SSZ. Peak T, in contrast, remains consistent throughout, within the range ~730-820 °C.

immediately south of the SSZ fall within the range 720 – 820 °C (Fig. 4.9b) (Ketchum,

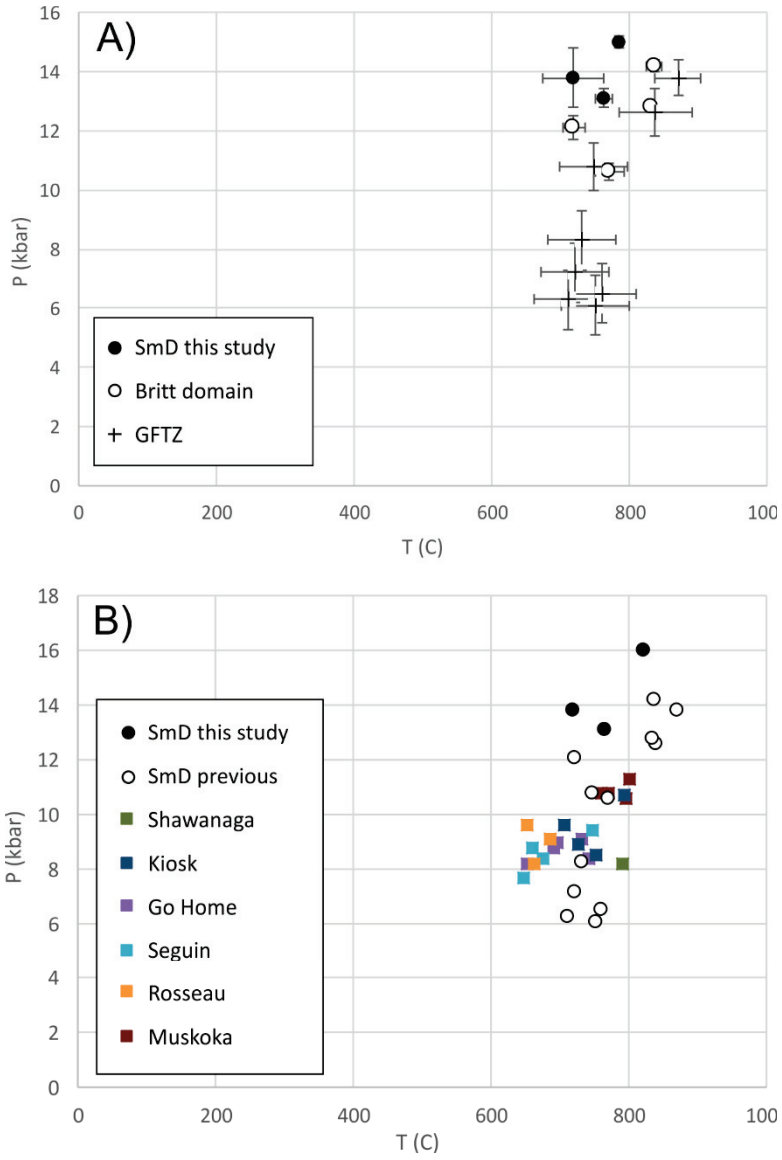

Figure 4.9 P-T diagrams comparing estimates from this study (solid circles) to previous work on SmD (open circles and plus symbols) and 1150 - 1170 Ma coronitic metagabbro (solid coloured squares) throughout the CGB. (A) P-T diagrams comparing winTWQ-based P-T estimates from the GFTZ and Britt Domain. Error bars represent geometric uncertainties from multiequilibrium calculations. (B) The range of P-T estimates for SmD compared to coronites from various allochthonous domains of the CGB. (Sources for both diagrams as follows: GFTZ - Jamieson et al., 1995, Bethune and Davidson, 1997; Britt - Ketchum, 1994, Jamieson et al., 1995, this study; Go Home, Rosseau, Seguin - Grant, 1987; Muskoka - Timmerman, 1998; Kiosk – Grant, 1987, Kendrick, 2015)

1994). Correlative coronites throughout the allochthonous Go Home, Rosseau, Seguin, and Kiosk domains, however, yield slightly lower peak T in the range 640 – 750 °C (Grant, 1987) with the exception of a coronite within the Novar subdomain of the Kiosk domain, roughly 14 km south of the ABT, recording peak T of 790 °C (Kendrick, 2015).

4.7.2 Peak P

Previous P estimates across the GFTZ and northern Britt domain indicate an increase from 6.1 kbar near the GF to 14.2 kbar in the northern Britt domain (Jamieson et

al., 1995; Bethune and Davidson, 1997). Peak P calculations for Bigsby Island SmD produce values virtually identical to the highest P estimates previously reported for the northern Britt domain (Jamieson et al., 1995). As with T estimates, a southward increase in P across the Britt Domain is indicated from 13.8 kbar in the north to 15 kbar in the south.

Results from H.A. Gray Island in the southern BD exceed previous P estimates for SmD near the SSZ by 4 kbar, and coronite in the Shawanaga domain by 7 kbar (Ketchum, 1994). Coronites in the Go Home, Rosseau, Seguin, and Kiosk domains record peak P in the range 7.7 – 9.6 kbar, which were calculated using a variety of conventional thermobarometers. Only coronites in the Muskoka Domain, 125 km SE of the Britt domain, yield P estimates consistently in excess of 10 kbar (10.6 – 11.3; Timmerman, 1998). P estimates for H.A. Gray Island are high (15.0 kbar). However, the estimation is unlikely to be excessive, given that the Grt - Pl - Hbl - Qtz barometer (Kohn and Spear, 1992), produces P estimates of 13.3 and 14.4 kbar from Fe and Mg end members of this sample, respectively. Near-perfect convergence of equilibria for GC14-048 for the assemblage including pargasite strongly suggests that it is, contrary to the textural interpretation, in compositional equilibration with the peak assemblage. Pattison (2003) showed that high-P mafic assemblages (> 16 kbar) can contain stable pargasite without stable orthopyroxene. P-T calculated for the southern BD for an assemblage including pargasite (15.0 ± 0.2 kbar and 785 ± 4 °C; Fig. 4.5c) is considered reliable.

The T-D phase equilibria models (Fig. 4.6, 4.7) are consistent with TWQ P-T estimates, but do not provide sufficient constraints to produce independent P-T estimates.

4.8 Conclusions

1. Peak P-T estimates are relatively consistent across the entire Britt domain, with the highest P conditions recorded in the immediate footwall of the SSZ.

2. While Grenvillian peak T conditions are comparable across the SSZ, P estimates from monocyclic mafic rocks are widely divergent, corresponding to burial differences of 20-25 km. This suggests that the SSZ, reactivated during extension, accommodated ca. 40 km of top-to-the-south normal-sense displacement.

Timing is everything, and in order to understand the tectonic implications of these trends and variations, it is necessary to determine the corresponding age of peak metamorphism for these rocks, across the Britt Domain.

Chapter 5: Geochronology

5.1 Introduction

It has been shown that the Grenville Front Tectonic Zone (GFTZ) records a late phase of deformation, termed the Rigolet phase (ca 1000 – 980 Ma), during which NW-directed thrusting propagated into the Laurentian foreland (Rivers et al., 1989, 2012, and references therein; Jamieson et al., 1992, 1995, 2010; Culshaw et al., 1997). The metamorphism, structure, and age of amphibolite- and granulite-facies domains of the orogenic core (Culshaw et al., 1983, 1988, 1990, 1994, 1997; Jamieson et al., 1992; Ketchum et al., 1994, 1998; Wodicka et al., 1996, 2000; Ketchum and Davidson, 2000) and the transition from craton to orogen in the GFTZ (Davidson and Bethune, 1988; Haggart et al., 1993; Jamieson et al., 1995; Bethune, 1997; Bethune and Davidson, 1997) are well documented, yet the P-T conditions and timing of metamorphism and structures related to Rigolet phase deformation are poorly documented for the Britt domain.

Grenvillian metamorphism of the polycyclic parautochthonous Britt domain gneisses overprinted metamorphic assemblages and textures formed during earlier tectonic episodes (ca. 1450, 1650, 1800 Ma; Corrigan, 1990; Tuccillo et al, 1992; Corrigan et al., 1994; Carr et al., 2000, and references therein). Obtaining P-T and age data relevant to the late-stage evolution of the Grenville orogeny requires analysis of assemblages not affected by previous tectonic events. The emplacement age (1238 ± 4 Ma, Krogh et al., 1987; 1235 +7/-3 Ma, Dudàs et al, 1994) of the Sudbury diabase (SD) dyke swarm has been determined by U-Pb geochronology on igneous baddeleyite.

Sudbury diabase is the only lithology in the Britt Domain to record an exclusively Grenvillian metamorphic history.

Samples from Key Harbour, Byng Inlet, and Point au Baril represent a 40 km transect of the western Central Gneiss Belt, spanning the parautochthonous Britt domain from north to south. Metamorphic mineral assemblages and associated P-T estimates for each sample are described in Chapters 3 and 4 and summarised in Table 5.1. This chapter describes the results of U-Pb geochronology of metamorphic zircons on the same samples.

5.2 Zircon Petrography

This section builds upon petrographic descriptions presented in Ch. 3 with particular emphasis on zircon growth habit and abundance. Salient features and lithological details from each sample are compiled in Table 5.1.

Zircon was found along ilmenite grain boundaries and within the adjacent biotite coronas. These are interpreted as overgrowths, which preserve the original oxide grain boundaries (Fig. 5.1b), or replacements, which deflect the relict oxide grain boundaries inward (Fig. 5.1c) (Bingen et al., 2001). Though overgrowth textures dominate, many zircon grains, especially the coarser grains targeted for U-Pb dating, exhibit a combination of the two (Fig. 5.1d). Rare “string of beads” textures (Corfu et al., 2003) are interpreted to show the extent of the ilmenite grain boundary at the time of zircon growth prior to replacement of the oxide by biotite.

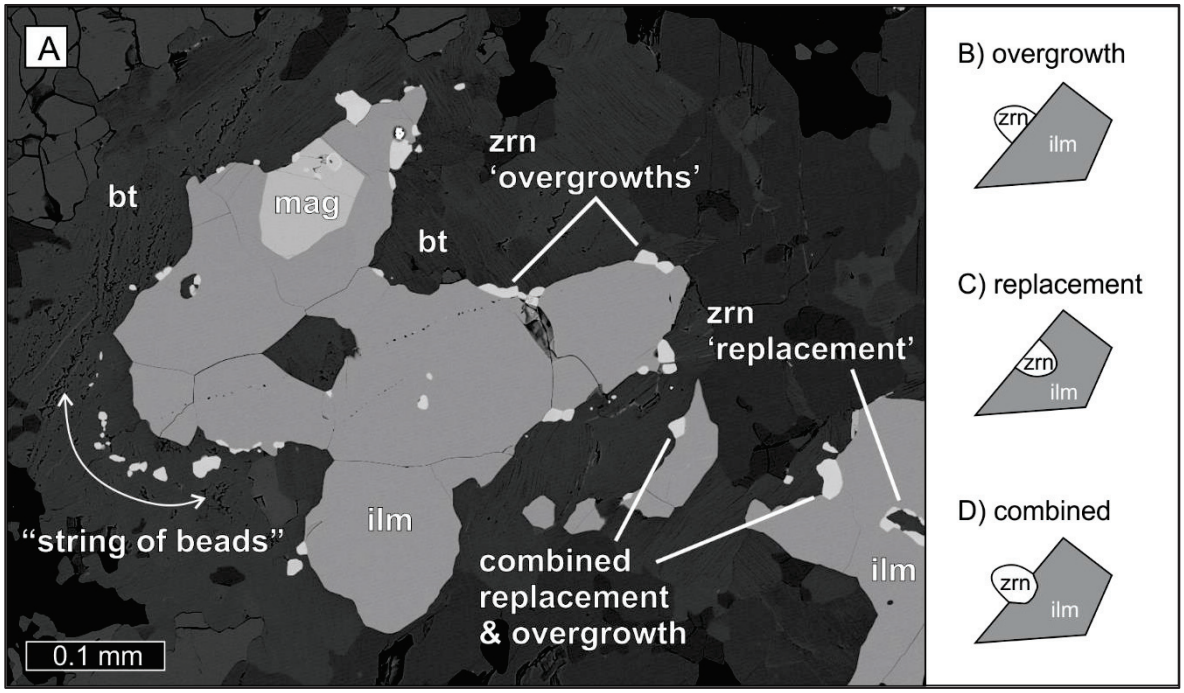

Figure 5.1 BSE image from sample GC14-024 and illustration showing typical zircon (all bright grey minerals pictured) habits and textural associations. A) "String of beads" texture (centre left) is interpreted to represent zircon nucleation at the previous extent of the Fe-Ti oxide grain boundary, which has subsequently receded during overprinting by biotite (Corfu et al., 2003). B) Overgrowth indicates zircon growth into the biotite corona, leaving the ilmenite grain-boundary intact. C) Replacement indicates zircon overprinting of ilmenite, where the oxide grain-boundary is deflected inward, away from the biotite corona. D) The coarsest zircon grains commonly display a combination of overgrowth and replacement (e.g. A, top centre and lower right).

5.2.1 GC14-057, Key Harbour

Sample GC14-057 was collected from the strain-resistant core of a large SmD dyke segment hosted in pink granitic orthogneiss on Bigsby Island in Key Harbour. The rectangular dyke segment is ~100 m long and 50 m wide, with the long axis oriented E-W. The contact between the dyke segment and host gneiss is mostly overgrown or underwater. A narrow, < 20 cm, amphibolite selvage is visible along a small portion of the contact with host gneiss visible near the eastern margin of the segment. Macroscale

textures and features are discussed in detail in Chapter 2 (section 2.4.2.1), and detailed petrography of the sample is discussed in Chapter 3 (section 3.3.1).

Zircons in sample GC14-057 are invariably located along the interface between primary Fe-Ti oxide and the biotite corona, with zircon commonly concentrated within embayed portions of the relict oxide. Most zircons are ≤ 15 μm wide, equant-to-elongate, xenoblastic overgrowths on ilmenite and locally form "string of beads" textures within biotite coronas. Less common, coarser zircon grains are ≤ 45 μm across and generally exhibit a combination of overgrowth and replacement textures. Zircon shows no evidence of zoning in high-contrast BSE images. Ilmenite breakdown during peak metamorphism (13.8 kbar at 718 °C) almost certainly provided Zr for zircon precipitation (Bingen et al., 2001; Corfu et al., 2003).

5.2.2 GC14-024, Byng Inlet

Sample GC14-024 was collected from a large lenticular SmD boudin, roughly 120 long and 60 m wide, hosted in leucocratic orthogneiss at Lamondin Point at the mouth of Byng Inlet. The NE portion of the SmD boudin is cut by an undeformed pegmatite dyke of undetermined age. Samples were collected several tens of meters south of the pegmatite, in an undeformed portion of the boudin core. Macroscale textures and features are discussed in section 2.4.2, and detailed petrography of the sample is discussed in section 3.3.2.

Zircons in sample GC14-024 are larger and more abundant than those observed in samples from the northern and southern regions of the study area. They are primarily found along the interface between igneous Fe-Ti oxide, here ilmenite intergrown with

magnetite, and the corona of intergrown biotite and pargasite. Less commonly, trails of fine zircon ≤ 10 µm ("string of beads" texture) are found extending from the rims of embayed zircons as inclusions in the biotite + pargasite corona.

Table 5.1 Summary of zircon and host rock petrographic information

Sample	Mineral assemblage & textures	Zircon textures
GC14-057 Bigsby Island Key Harbour - 46 km SE of GF 14 km SE of GFTZ - E 518225 N 5081051	Relict: Pl + Cpx + Ilm + Bt + Ap sub-ophitic Metamorphic: Grt + Pl + Cpx + Opx + Bt + Sp Ilm (2-3%), weakly embayed, mantled entirely by successive Bt and Grt coronas	Coarse grains (> 10 µm) elongate, ≤ 45 x 15 µm replacement > overgrowth. Finer grains (< 10 µm) equant overgrowth >> replacement
GC14-024 Lamondin point Byng Inlet - 59 km SE of GF 30km SE of GFTZ - E 526568 N 5069122	Relict: Pl + Cpx + Ilm + Bt + Ap Sub-ophitic Metamorphic: Grt + Pl + Opx + Cpx + Bt + Prg + Sp Ilm-Mag (3-5%) mantled by intergrown Bt ± Prg, semi-continuously enveloped by Prg	Coarse grains (> 10 µm) equant to elongate ≤ 40 x 20 µm overgrowths ≥ replacement Finer grains (< 10 µm) equant to elongate combined replacement + overgrowth
GC14-048 HA Gray Island Point au Baril - 84 km SE of GF 55km SE of GFTZ - E 539185 N 5043624	Relict: Pl + Cpx + Ilm + Ap Sub-ophitic Metamorphic: Pl + Grt + Prg + Cpx + Bt + Sp Ilm (2-3%) mantled by intergrown Bt ± Prg, semi-continuously enveloped and/or overprinted by Prg	Coarse grains (> 10 µm) generally equant, ≤ 35 µm replacement > overgrowth Finer grains (< 10 µm) generally equant overgrowth >> replacement

5.2.3 GC14-048, Point au Baril

Sample GC14-048 was collected from a relatively narrow, exceptionally well-preserved dyke segment in the southernmost portion of the parautochthonous belt, approximately 1.5 km NW of the ABT. The ~4 m wide dyke cuts NE-trending foliations

in the host orthogneisses of the Point au Baril complex, bisecting the western portion of H. A. Gray Island continuously for approximately 240 m.

Zircons from GC14-048 are neither particularly small, nor rare, relative to samples from the northern and central Britt domain. The coarsest zircons observed were typically ≤ 35 μm long and equant to elongate. Unlike elsewhere, zircon locally forms thin < 10 μm rims around small primary Fe-Ti oxides. Rare "string of beads" zircons are also found.

5.3 Methods

5.3.1 Isotopic decay systems

In U-bearing minerals, the radiogenic Pb isotopes of U decay (^{206}Pb,^{207}Pb, ^{208}Pb) accumulate over time at a constant, known rate. For the ^{238}U-^{206}Pb system, this is given by the equation:

$$^{206}Pb_r = {}^{238}U\left(e^{\lambda_{238}t} - 1\right)$$

where λ_{238} is the decay constant for ^{238}U-^{206}Pb, and ^{206}Pb$_r$ designates radiogenic lead. Similar equations describe the decay series for ^{235}U-^{207}Pb, and ^{232}Th-^{208}Pb. In a closed system, in which the only Pb present is radiogenic, three ages can be calculated from U, Th, and Pb isotopic data by the simple equations:

$$t_{206} = \frac{1}{\boldsymbol{\lambda}_{238}} ln\left(\frac{^{206}\mathrm{Pb}_r}{^{238}\mathrm{U}} + 1\right)$$

$$t_{207} = \frac{1}{\boldsymbol{\lambda}_{235}} ln\left(\frac{^{207}\mathrm{Pb}_r}{^{235}\mathrm{U}} + 1\right)$$

$$t_{208} = \frac{1}{\boldsymbol{\lambda}_{232}} ln\left(\frac{^{208}\mathrm{Pb}_r}{^{232}\mathrm{Th}} + 1\right)$$

where λ_{235} and λ_{232} are the decay constants of ^{235}U and ^{232}Th, respectively.

In addition to the analytical requirements for measuring parent-daughter ratios, radiogenic dating faces two fundamental complications: the incorporation of initial lead (Pb_0) from the environment during mineral growth, and gain or loss of parent or daughter isotopes after crystallization. The general term common lead (Pb_c) includes laboratory blanks and background signals, and is used here when referring to corrections for radiogenic Pb. Many datable minerals, including zircon, incorporate some Pb_0 during crystallization. Lead-loss results from efficient Pb diffusion through the crystal lattice. This may be the product of one or more recrystallization events, strain, lattice defects, and/or alteration (e.g. radiation-damaged metamict zircon grains) (Schoene, 2014).

In ideal, closed systems, the ages indicated by ratios of ^{206}Pb/^{238}U and ^{207}Pb/^{235}U are equal, and define a curve of equivalent ages referred to as "concordia" (Wetherill, 1956; e.g. Fig. 5.3c); dates that plot on concordia are referred to as "concordant".

5.3.2 Sources of discordance and Pb_c correction

Deviations from corcordia indicate departure from ideal closed-system behaviour. Ages that fall below concordia indicate Pb-loss or U-gain, and ages that fall above concordia indicate Pb-gain or U-loss. If a single linear regression can be drawn through data ellipses that fall below concordia, then the upper intercept is commonly interpreted as the age of initial formation (e.g. magmatic crystallization) and the lower intercept as the age of Pb loss.

Because most minerals incorporate Pb_c, corrections are always applied where possible. On standard concordia diagrams, the effect of Pb_c can be difficult to detect for Paleoproterozoic and Archean samples as the discordant array produced is nearly parallel to concordia. For younger samples the discordant array intercepts concordia at a higher angle, allowing for discernment between the effects of Pb_c and Pb loss. Conversely, when plotted on inverse concordia or Tera-Wasserburg (T-W) plots, analyses affected by Pb_c will show strong, distinct linear trends above the concordia curve, as Pb_c strongly affects the $^{207}Pb/^{206}Pb$ ratio (Tera and Wasserburg, 1972a,b). On the same diagram, provided analyses are not strongly affected by Pb_c, Pb loss produces a similar discordant linear array with upper and lower intercepts defining the age of initial formation and age of lead loss, respectively (Schoene, 2014).

Three types of corrections are possible when dealing with Pb_c. The most direct is to measure Pb isotope concentrations in coexisting K-feldspar, which incorporates significant Pb, but no U or Th, during its formation; the measured Pb_r of the datable mineral is corrected accordingly. This method is standard for direct measurement techniques such as thermal ionization mass spectrometry (TIMS), but not suitable for quadrupole inductively coupled plasma mass spectrometry (ICP-MS), which cannot resolve isobaric interference from ^{204}Hg (Parrish and Noble, 2003; Schoene, 2014, and references therein).

Alternatively, T-W plots can be used to correct for Pb_c. Regression lines are drawn that connect the y-axis at the $^{206}Pb/^{207}Pb$ composition of Pb_o (i.e. where U = 0, so there is no Pb_r; based on the model of Stacey and Kramers, 1975) through data ellipses that

follow linear trends above concordia. The resulting age is given by the intersection of the regression line with concordia.

A third technique for Pb_c correction, appropriate where measurements for ^{204}Pb are unavailable, is the method of Andersen (2002). This method assumes that all discordance in U/Pb and U/Th isotopic ratios is the sum of the effects of Pb_c and Pb loss, and employs all three isotopic systems to correct for those effects. The main weakness of this technique is that it requires an external constraint or reasonable assumption of the time of Pb loss. Analyses performed in this study showed strong evidence of Pb_c and very little evidence of Pb loss. The correction method of Andersen (2002) was applied to analyses in this study.

5.3.3 Sample preparation

Large samples (~10 kg) were collected from the strain-resistant cores of SmD dyke segments targeted for dating. A standard thin and three corresponding polished sections (30 and 50 μm thick, respectively) were cut from the cleanest portion of each sample (no evidence of veins or alteration) (see Ch. 3, section 3.3). Metamorphic zircons (≤ 50 μm) were identified optically and imaged by BSE to reveal textural details. The zircon is exceedingly fine-grained, and forms overgrowths on and/or replacements of coarse primary Fe-Ti oxides, invariably between the oxide and biotite. Rare monazites were found within fractures in primary apatite, but were too small (ca. 1 μm) to target for electron microprobe chronology.

Zircons in polished sections were imaged by BSE and analysed to confirm their identity. Following BSE imaging and EMP analysis, each section was repolished using

0.25, 0.05 and 0.01 μm diamond paste to remove any residual Pb from the lap used in the initial section preparation process.

5.3.4 LA-ICP-MS zircon analysis

Three techniques are currently available for U-Pb dating of zircons. They are, in order of decreasing analytical precision: 1) thermal ionization mass spectrometry (TIMS), 2) secondary ion mass spectrometry (SIMS), and 3) laser ablation - inductively coupled plasma - mass spectrometry (LA-ICP-MS). U-Th-Pb geochronology typically involves separated grains using magnetic and density techniques and dissolving single hand-picked grains, or measuring grains in epoxy mounts or in situ in polished sections.

In situ U-Pb dating using coupled laser ablation systems with plasma mass spectrometers has been available since the early 1990`s (Feng et al., 1993; Fryer et al., 1993; Hirata and Nesbitt, 1995). While the sensitivity of this technique is significantly lower than ID-TIMS, fine spatial resolution, short analytical time, minimal sample preparation, and affordability (relative to SIMS) has resulted in wide and growing application (Schoene, 2014). The process involves ablating a small volume of material from the mineral surface (pit diameter ≥ 5μm, though typically > 20 μm) inside of an ablation chamber through a laser-transparent window. Ablation pits vary in diameter depending on the target material and concentration of elements of interest. The aerosols produced by the laser are swept through the ablation chamber with a carrier gas, usually ultra-pure He, and carried to a plasma torch which ionizes the elements in the aerosol. The ionized particles are then drawn through a mass spectrometer for measurements calibrated against standards of known age and composition, which are analyzed regularly throughout the analytical session.

LA-ICP-MS analyses were performed by the author at the University of New Brunswick Department of Earth Sciences using a COMPexPro 102 F 193 nm excimer laser ablation system coupled to an Agilent 7700x quadrupole ICP-MS. Low concentrations of U (generally < 150 ppm) in the zircons required a minimum ablation diameter of 17µm. Isotopic data were calibrated against FC-1 (1099 Ma) as a primary zircon standard and NIST610 (U 461.5 ppm; Th 457.2 ppm; Pb 426 ppm) as the primary concentration standard. Secondary standards 91500 (1055 Ma) and Plesovice (337 Ma) were used to track reproducibility. A full list of analytical conditions is compiled in Table 5.2.

5.4 Results

Analytical data with 2σ uncertainties are reported in Table 5.3, and plotted on Wetherill concordia and Tera-Wasserburg plots (Figs. 5.2, 5.4, and 5.6). Data reduction and correction for Pb_c using the method of Andersen (2002) was performed by Dr. Christopher McFarlane at the University of New Brunswick. Additional plots and weighted mean calculations were done by the author using Isoplot 4.15™ for MS Excel 2016™ (Ludwig, 2012).

Tera-Wasserburg plots of the uncorrected isotopic data display linear discordant arrays indicative of Pb_c (Fig. 5.2a, 5.4a, 5.6a). The majority of data point ellipses, however, cluster just above concordia for each sample, limiting the reliability of ages calculated by regression (e.g. Fig. 5.2a).

Table 5.2 LA-ICP-MS Running conditions

Laser	
Model	COMPexPro 102 F 193 nm excimer laser
Laser energy used	100 mJ with 50% attenuation
BDU Demag position	20x
Laser fluence	~2.3 J/cm^2
Repetition rate	3 Hz
Spot diameter	17 μm
Ablation time (seconds)	30s background, 30s mineral ablation
Standards used	FC-1 (primary zircon standard, 1099 Ma) 91500 (secondary zircon standard, 1055 Ma) Plesovice (secondary zircon standard, 337 Ma) NIST610 (primary concentration standard)
ICP-MS	
Model	Agilent 7700
RF power	1550 W
Sampling depth (Torch position)	4 mm
Carrier gas (Ar)	0.93 L/min
ThO/Th	<0.2%
22/44 (Doubly charged ion ratio)	<0.3%
Tuning protocol	Tuned for heavy elements (207, 238 monitored during tuning)
Gas flow rate (ablation cell)	He (300 ml/min), N2 (2 ml/min) 2nd pump used (increases sensitivity)
Data acquisition parameters	
Protocol	Time resolved analysis
Sampling time	0.283 seconds
Dwell time per isotope (sec)	^{90}Zr (0.01), ^{202}Hg (0.04), ^{204}Pb (0.07), ^{206}Pb (0.04), ^{207}Pb (0.07), ^{208}Pb (0.01), ^{232}Th (0.01), ^{238}U (0.015)

Table 5.3: U-Th-Pb analytical data for SmD samples across the Britt domain

	Concentration			Corrected isotopic ratios					Age (Ma)													
				Statard Concordia (Wetherill)					Inverse Concordia (Tera-Wasserburg)													
	U	Th	Th/U	^{207}Pb	±2σ	^{206}Pb	±2σ	Error	^{238}U	±2σ	^{207}Pb	±2σ	^{208}Pb	±2σ	^{206}Pb	±2σ	^{207}Pb	±2σ	conc.	^{207}Pb	±2σ	^{208}Pb	±2σ
Analysis	(ppm)	(ppm)		^{235}U	abs.	^{238}U	abs.	Corr.	^{206}Pb	abs.	^{206}Pb	abs.	^{232}Th	abs.	^{238}U	abs.	^{235}U	abs.	%	^{206}Pb	abs.	^{232}Th	abs.
Bigsby Island, Key Harbour																						
GC14-057C - 8	166	105	1.58	1.4720	0.090	0.1470	0.0069	0.977	6.93	0.30	0.0721	0.0013	0.1040	0.029	883	38	913	35	96.7	983	37	2000	530
GC14-057C - 1	700	397	1.76	1.4130	0.083	0.1491	0.0062	0.931	6.79	0.25	0.0689	0.0015	0.0640	0.012	895	35	890	32	100.6	902	41	1250	240
GC14-057C - 10	253	136	1.87	1.5720	0.073	0.1595	0.0054	0.871	6.30	0.19	0.0710	0.0012	0.0550	0.011	953	30	955	26	99.8	952	36	1090	210
GC14-057C - 7	127	51	2.49	1.6500	0.130	0.1628	0.0090	0.972	6.30	0.35	0.0725	0.0019	0.1100	0.065	971	50	979	47	99.2	993	55	2100	1200
GC14-057C - 12	129	54	2.39	1.7020	0.100	0.1643	0.0073	0.983	6.17	0.25	0.0748	0.0013	0.1400	0.140	980	40	1004	35	97.6	1060	35	2700	2700
GC14-057C - 9	178	111	1.60	1.6230	0.098	0.1661	0.0079	0.775	6.11	0.26	0.0712	0.0021	0.0560	0.011	990	43	974	36	101.6	954	66	1090	220
GC14-057C - 4	153	59	2.62	1.7700	0.120	0.1677	0.0080	0.994	6.10	0.27	0.0771	0.0015	-	-	998	44	1036	40	96.3	1118	39	-	-
GC14-057C - 6	109	38	2.84	1.6540	0.088	0.1680	0.0061	0.903	6.06	0.19	0.0709	0.0016	0.0690	0.019	1000	34	984	29	101.6	954	45	1330	350
GC14-057C - 11	120	41	2.89	1.7020	0.071	0.1703	0.0057	0.884	5.98	0.18	0.0721	0.0012	0.0940	0.027	1013	31	1004	24	100.9	981	35	1790	490
GC14-057C - 3	221	97	2.29	1.6820	0.082	0.1705	0.0062	0.936	5.81	0.26	0.0725	0.0021	0.0780	0.032	1014	34	1010	37	100.4	991	60	1490	580
GC14-057C - 2	244	119	2.05	1.6940	0.080	0.1713	0.0058	0.883	5.94	0.19	0.0718	0.0013	0.0690	0.011	1018	32	1000	26	101.8	974	39	1350	210
GC14-057C - 15	167	75	2.22	1.7500	0.078	0.1719	0.0055	0.916	5.87	0.16	0.0740	0.0010	0.0930	0.016	1021	30	1021	25	100.0	1037	27	1780	290
GC14-057C - 5	142	50	2.83	1.7800	0.085	0.1743	0.0058	0.884	5.80	0.17	0.0743	0.0011	0.0730	0.017	1034	32	1031	27	100.3	1046	29	1420	310
GC14-057C - 13	132	41	3.25	1.9730	0.087	0.1881	0.0059	0.897	5.35	0.15	0.0751	0.0013	0.1010	0.017	1110	32	1101	24	100.8	1071	34	1940	300
Lamondin Point, Byng Inlet																						
GC14-024B - 19	86	81	1.07	1.5200	0.120	0.1533	0.0087	0.982	6.70	0.37	0.0712	0.0016	0.0530	0.063	918	49	928	49	98.9	959	46	1000	1200
GC14-024C - 23	77	52	1.49	1.5120	0.080	0.1583	0.0060	0.876	6.48	0.23	0.0688	0.0015	0.0540	0.014	946	34	927	32	102.0	887	49	1060	270
GC14-024C - 11	51	37	1.37	1.5860	0.110	0.1588	0.0085	0.961	6.58	0.32	0.0720	0.0014	0.1000	0.042	947	47	949	42	99.8	988	40	1890	750
GC14-024B - 5	119	97	1.23	1.5640	0.063	0.1593	0.0047	0.924	6.31	0.15	0.0714	0.0012	0.0590	0.013	956	25	954	26	100.2	966	35	1150	250
GC14-024B - 14	43	31	1.35	1.7600	0.170	0.1630	0.0120	0.955	6.65	0.55	0.0758	0.0021	0.1260	0.060	967	68	994	65	97.3	1069	57	2400	1100
GC14-024B - 13	81	44	1.81	1.6030	0.077	0.1624	0.0062	0.919	6.28	0.24	0.0718	0.0011	0.0500	0.016	969	35	965	31	100.4	975	32	980	300
GC14-024A-Zr12 - 1	106	96	1.10	1.6590	0.260	0.1636	0.0130	0.978	6.18	0.18	0.0735	0.0009	0.0690	0.042	976	66	989	68	98.7	1026	67	1360	750
GC14-024A-Zr13 - 5	89	28	3.13	1.5910	0.046	0.1645	0.0040	0.885	6.07	0.12	0.0705	0.0011	0.0559	0.010	984	21	969	20	101.5	953	28	1090	180
GC14-024B - 7	87	59	1.47	1.6650	0.083	0.1658	0.0063	0.918	6.11	0.21	0.0731	0.0010	0.0680	0.021	988	35	988	32	100.0	1012	30	1320	400
GC14-024B - 21	76	54	1.41	1.6880	0.094	0.1667	0.0064	0.976	6.05	0.21	0.0733	0.0011	0.0680	0.031	993	35	996	35	99.7	1025	34	1320	590
GC14-024B - 17	80	55	1.47	1.6820	0.088	0.1671	0.0069	0.889	6.11	0.22	0.0740	0.0012	0.0620	0.015	994	38	998	35	99.6	1034	34	1210	290
GC14-024B - 15	81	52	1.55	1.7040	0.095	0.1666	0.0069	0.948	6.13	0.23	0.0739	0.0012	0.0920	0.020	997	36	1005	34	99.2	1032	34	1760	360
GC14-024A-Zr5 - 2	91	90	1.02	1.6760	0.460	0.1679	0.0300	0.900	6.00	0.19	0.0728	0.0012	0.0540	0.047	1000	140	996	94	100.4	1006	89	1070	790
GC14-024B - 8	96	91	1.06	1.6090	0.061	0.1682	0.0061	0.797	6.02	0.19	0.0706	0.0014	0.0564	0.010	1001	33	978	27	102.4	954	39	1100	190
GC14-024B - 1	87	52	1.68	1.6400	0.079	0.1681	0.0057	0.807	6.04	0.18	0.0704	0.0018	0.0630	0.016	1001	31	980	30	102.1	935	57	1220	300
GC14-024C - 14	91	65	1.40	1.7300	0.089	0.1692	0.0067	0.906	6.08	0.22	0.0749	0.0012	0.0610	0.013	1006	37	1015	33	99.1	1058	33	1200	250
GC14-024B - 3	41	19	2.19	1.7000	0.100	0.1695	0.0075	0.889	6.10	0.27	0.0721	0.0018	0.0580	0.031	1007	41	995	37	101.2	995	51	1120	580
GC14-024A-Zr2 - 2	79	87	0.91	1.6140	0.048	0.1696	0.0042	0.646	5.92	0.12	0.0690	0.0013	0.0437	0.004	1009	23	972	19	103.8	890	47	864	83
GC14-024B - 9	79	78	1.01	1.6530	0.083	0.1698	0.0067	0.803	5.98	0.22	0.0703	0.0019	0.0610	0.018	1010	37	985	31	102.5	924	60	1190	340
GC14-024B - 18	74	103	0.71	1.8080	0.093	0.1712	0.0062	0.974	5.90	0.21	0.0759	0.0012	0.0730	0.028	1017	34	1039	34	97.9	1085	35	1410	520
GC14-024B - 20	56	50	1.11	1.5930	0.100	0.1715	0.0075	0.783	5.96	0.23	0.0684	0.0024	0.0700	0.010	1019	41	965	40	105.6	853	83	1370	190
GC14-024A-Zr13 - 2	51	21	2.40	1.5830	0.058	0.1717	0.0045	0.636	5.87	0.13	0.0668	0.0018	0.0510	0.007	1020	25	958	22	106.5	806	60	1000	130
GC14-024C - 9	93	53	1.75	1.7490	0.090	0.1718	0.0065	0.941	5.95	0.20	0.0743	0.0012	0.0980	0.021	1020	36	1024	34	99.6	1045	34	1880	380
GC14-024C - 5	33	16	1.99	1.6600	0.120	0.1719	0.0090	0.868	6.04	0.33	0.0693	0.0024	0.0260	0.014	1020	49	977	45	104.4	889	80	510	280
GC14-024C - 3	71	35	2.03	1.6260	0.086	0.1720	0.0065	0.812	5.95	0.21	0.0690	0.0019	0.0530	0.011	1022	36	976	34	104.7	876	65	1030	220
GC14-024A-Zr4 - 1	39	20	2.01	1.6600	0.070	0.1724	0.0057	0.860	5.95	0.24	0.0693	0.0018	0.0530	0.011	1024	31	984	27	104.1	900	43	1030	210
GC14-024A-Zr5 - 1	75	56	1.35	1.6740	0.064	0.1727	0.0050	0.847	5.89	0.17	0.0703	0.0014	0.0558	0.007	1026	27	992	24	103.4	932	35	1090	130
GC14-024C - 1	96	78	1.23	1.7670	0.094	0.1728	0.0068	0.900	5.92	0.21	0.0744	0.0014	0.0580	0.018	1026	37	1024	34	100.2	1054	35	1130	350
GC14-024C - 22	63	58	1.08	1.8400	0.140	0.1738	0.0093	0.962	5.87	0.28	0.0753	0.0016	0.0950	0.032	1029	51	1046	49	98.4	1072	46	1820	580

Table 5.3: U-Th-Pb analytical data for SmD samples across the Britt domain

	Concentration			Corrected isotopic ratios					Age (Ma)													
				Statard Concordia (Wetherill)					Inverse Concordia (Tera-Wasserburg)													
Analysis	U (ppm)	Th (ppm)	Th/U	$^{207}Pb/^{235}U$	±2σ abs.	$^{206}Pb/^{238}U$	±2σ abs.	Error Corr.	$^{238}U/^{206}Pb$	±2σ abs.	$^{207}Pb/^{206}Pb$	±2σ abs.	$^{208}Pb/^{232}Th$	±2σ abs.	$^{206}Pb/^{238}U$	±2σ abs.	$^{207}Pb/^{235}U$	±2σ abs.	conc. %	$^{207}Pb/^{206}Pb$	±2σ abs.	$^{208}Pb/^{232}Th$	±2σ abs.
GC14-024B - 12	57	42	1.36	1.7600	0.120	0.1737	0.0081	0.934	5.76	0.26	0.0732	0.0018	0.0800	0.016	1031	45	1029	48	100.2	1009	54	1550	300
GC14-024A-Zr13 - 4	97	84	1.15	1.7810	0.049	0.1737	0.0040	0.953	5.82	0.17	0.0744	0.0009	0.0520	0.012	1032	22	1035	18	99.7	1049	18	1030	230
GC14-024A-Zr13 - 1	86	53	1.61	1.6430	0.041	0.1740	0.0040	0.611	5.79	0.13	0.0684	0.0016	0.0611	0.006	1034	22	984	16	105.1	877	39	1200	110
GC14-024C - 10	122	94	1.30	1.6300	0.082	0.1742	0.0061	0.706	5.82	0.18	0.0675	0.0021	0.0486	0.007	1034	33	976	32	105.9	832	74	960	140
GC14-024C - 4	39	18	2.12	1.7400	0.150	0.1750	0.0110	0.934	6.02	0.37	0.0707	0.0024	0.0570	0.019	1037	59	1001	55	103.6	925	74	1110	360
GC14-024A-Zr13 - 3	80	54	1.49	1.6800	0.095	0.1756	0.0065	0.737	5.77	0.17	0.0691	0.0019	0.0519	0.008	1042	37	995	32	104.7	884	57	1020	150
GC14-024B - 4	68	41	1.66	1.7800	0.120	0.1777	0.0078	0.897	5.75	0.23	0.0722	0.0020	0.0700	0.017	1053	43	1026	43	102.6	976	65	1360	320
GC14-024A-Zr2 - 1	68	46	1.50	1.7110	0.063	0.1792	0.0051	0.739	5.64	0.14	0.0691	0.0016	0.0610	0.008	1061	28	1006	23	105.5	898	52	1190	160
Lamondin Point, Byng Inlet, cont.																							
GC14-024C - 8	45	33	1.38	1.7300	0.110	0.1793	0.0087	0.810	5.77	0.28	0.0695	0.0024	0.0470	0.012	1061	48	1009	41	105.2	888	78	920	240
GC14-024C - 2	62	35	1.79	1.8300	0.110	0.1800	0.0076	0.873	5.66	0.22	0.0734	0.0018	0.0680	0.016	1064	42	1041	40	102.2	1007	56	1310	300
GC14-024B - 11	67	40	1.66	1.7380	0.073	0.1797	0.0060	0.650	5.67	0.18	0.0699	0.0020	0.0600	0.011	1064	33	1016	27	104.7	899	67	1170	210
GC14-024C - 13	61	38	1.60	1.7570	0.089	0.1810	0.0070	0.796	5.62	0.20	0.0704	0.0020	0.0580	0.011	1070	38	1020	33	104.9	937	59	1130	210
GC14-024C - 21	60	39	1.54	1.7600	0.120	0.1788	0.0095	0.831	5.61	0.30	0.0717	0.0024	0.0700	0.012	1072	58	1034	49	103.7	979	68	1360	230
GC14-024C - 7	31	18	1.67	2.1900	0.220	0.1850	0.0130	0.939	5.85	0.40	0.0832	0.0028	0.1680	0.065	1085	72	1146	71	94.7	1272	70	3100	1100
GC14-024C - 17	32	27	1.20	1.9200	0.180	0.1840	0.0130	0.914	5.81	0.42	0.0741	0.0026	0.0560	0.028	1086	69	1061	62	102.4	1019	78	1090	530
GC14-024C - 18	44	29	1.50	1.8900	0.110	0.1858	0.0088	0.865	5.54	0.23	0.0740	0.0020	0.0900	0.026	1096	48	1065	39	102.9	1056	53	1710	480
GC14-024B - 22	29	19	1.56	1.9900	0.150	0.1861	0.0100	0.927	5.67	0.31	0.0770	0.0021	0.0660	0.029	1096	56	1091	51	100.5	1115	54	1270	560
GC14-024B - 2	54	72	0.75	2.0100	0.120	0.1839	0.0084	0.905	5.51	0.26	0.0779	0.0017	0.0720	0.022	1106	53	1107	40	99.9	1144	41	1400	420
GC14-024C - 6	26	18	1.42	1.9400	0.130	0.1883	0.0100	0.898	5.59	0.28	0.0744	0.0018	0.0800	0.029	1107	54	1082	45	102.3	1049	51	1500	540
GC14-024C - 24	19	15	1.21	2.1800	0.200	0.2020	0.0140	0.937	5.35	0.34	0.0783	0.0026	0.0670	0.027	1177	75	1159	66	101.6	1161	64	1280	500
H.A. Gray Island, Point au Baril																							
GC14-048B - 1	97	56	1.75	1.5110	0.094	0.1540	0.0068	0.952	6.70	0.28	0.0709	0.0012	0.0460	0.020	921	38	923	37	99.8	946	35	910	390
GC14-048C - 9	140	108	1.30	1.6500	0.110	0.1590	0.0084	0.987	6.50	0.31	0.0754	0.0015	0.0750	0.076	948	47	986	47	96.1	1076	41	1500	1500
GC14-048C - 12	118	62	1.92	1.4930	0.059	0.1586	0.0049	0.871	6.39	0.17	0.0694	0.0013	0.0592	0.010	948	27	931	26	101.8	909	38	1160	190
GC14-048A - 8	124	114	1.09	1.5990	0.100	0.1594	0.0073	0.995	6.38	0.26	0.0724	0.0011	0.0600	0.019	953	41	964	39	98.9	994	31	1180	350
GC14-048C - 3	86	59	1.47	1.7800	0.110	0.1653	0.0075	0.955	6.27	0.26	0.0774	0.0014	0.0640	0.029	984	41	1023	40	96.2	1124	35	1250	560
GC14-048C - 8	66	59	1.11	1.6900	0.130	0.1658	0.0095	0.949	6.21	0.32	0.0738	0.0015	0.0750	0.024	986	52	991	48	99.5	1030	41	1460	460
GC14-048C - 1	100	76	1.31	1.7500	0.140	0.1680	0.0110	0.917	6.13	0.40	0.0749	0.0022	0.0337	0.010	1000	62	1018	52	98.2	1057	62	670	190
GC14-048B - 3	70	44	1.60	1.6490	0.082	0.1694	0.0065	0.851	5.99	0.20	0.0703	0.0016	0.0474	0.009	1007	36	985	32	102.2	939	46	930	180
GC14-048B - 5	81	54	1.49	1.6350	0.078	0.1704	0.0062	0.871	5.98	0.20	0.0705	0.0014	0.0533	0.007	1013	34	985	32	102.8	929	47	1050	140
GC14-048A - 5	73	40	1.81	1.7300	0.120	0.1712	0.0089	0.946	5.96	0.31	0.0738	0.0020	0.0830	0.039	1017	49	1018	49	99.9	1024	57	1600	720
GC14-048C - 4	112	56	1.98	1.8700	0.140	0.1718	0.0086	0.991	6.04	0.28	0.0774	0.0015	0.2470	0.013	1019	47	1051	47	97.0	1122	41	4460	210
GC14-048C - 10	100	62	1.61	1.8700	0.130	0.1719	0.0080	0.963	6.02	0.26	0.0779	0.0017	0.1290	0.078	1020	44	1056	43	96.6	1132	45	2400	1400
GC14-048B - 4	52	20	2.63	1.6510	0.091	0.1761	0.0072	0.828	5.86	0.22	0.0688	0.0021	0.0400	0.011	1043	39	985	35	105.9	863	69	790	220
GC14-048A - 6	118	54	2.18	1.7930	0.086	0.1763	0.0060	0.905	5.75	0.17	0.0737	0.0012	0.0549	0.009	1045	33	1036	31	100.9	1025	36	1080	170
GC14-048C - 5	77	38	2.03	1.7370	0.082	0.1768	0.0071	0.868	5.81	0.20	0.0716	0.0013	0.0660	0.017	1048	38	1019	31	102.8	964	41	1390	380
GC14-048C - 13	72	46	1.58	1.8700	0.130	0.1772	0.0092	0.936	5.84	0.30	0.0757	0.0018	0.0790	0.056	1048	51	1057	48	99.1	1111	48	1470	980
GC14-048A - 3	129	76	1.70	1.9000	0.170	0.1772	0.0100	0.995	5.75	0.27	0.0771	0.0020	0.0670	0.068	1050	54	1072	54	97.9	1119	51	1300	1300
GC14-048A - 1	114	62	1.83	1.8670	0.094	0.1775	0.0071	0.959	5.69	0.20	0.0759	0.0012	0.0800	0.026	1052	39	1063	34	99.0	1089	33	1540	490
GC14-048B - 2	77	49	1.58	1.7270	0.086	0.1784	0.0065	0.821	5.74	0.19	0.0703	0.0018	0.0610	0.012	1056	35	1010	31	104.6	924	60	1190	230
GC14-048C - 6	51	22	2.30	1.8500	0.120	0.1815	0.0080	0.901	5.65	0.22	0.0736	0.0019	0.0890	0.020	1073	44	1056	41	101.6	1033	52	1700	360
GC14-048C - 11	69	35	2.00	1.8100	0.095	0.1853	0.0075	0.800	5.56	0.22	0.0711	0.0019	0.0820	0.016	1094	41	1045	35	104.7	949	59	1570	300
GC14-048A - 7	92	52	1.77	2.0000	0.110	0.1864	0.0070	0.951	5.48	0.20	0.0772	0.0014	0.0950	0.027	1100	38	1105	37	99.5	1117	38	1810	480
GC14-048C - 2	93	41	2.25	1.9580	0.095	0.1890	0.0064	0.836	5.35	0.16	0.0747	0.0015	0.0750	0.011	1114	35	1093	33	101.9	1050	48	1460	210

The Pb_c-corrected analyses from all samples produced a broad spread of ages, scattered about a central, concordant cluster. Owing to this scatter, weighted mean $^{206}Pb/^{238}U$ ages were calculated in lieu of calculated concordia ages. Concordia ages assume, at least provisionally, that the included analyses represent repeated measurements of the same point, and that the resulting spread of data is owing to analytical errors (Ludwig, 2012). To calculate a concordant age, all analyses must be concordant and overlap within errors. Excessive scatter (analyses which do not overlap within 2σ error) precludes the concordia age calculation.

Linearized probability plots of Pb_c-corrected $^{206}Pb/^{238}U$ ages for each sample show smooth, continuous distributions, indicating that data represent normal distribution for single age populations interpreted here to be the age of peak metamorphism, free of inheritance from the igneous protolith or country rock. For comparison, weighted mean $^{206}Pb/^{238}U$ ages were calculated for each sample from whole datasets, from all analyses < 5% discordant, and from all analyses < 2% discordant. A preferred age each sample was reached by simple and systematic method of data reduction. First, an anchored age and associated uncertainty were calculated using an anchored (at 0 Ma) regression through all analyses < 5% discordant (Fig. 5.3d, 5.5d, 5.7d). Analyses with $^{206}Pb/^{238}U$ ages outside of the 95% confidence range were then excluded, and a weighted average $^{206}Pb/^{238}U$ age was calculated from the remaining analyses (Fig. 5.3f, 5.5f, 5.7f). The following results are presented in order of increasing age, from N to S.

5.4.1 Key Harbour, SmD sample GC14-057

Zircon in GC14-057 shows combinations of overgrowth and/or replacement of ilmenite by zircon. Clear replacement textures are observed interspersed with

overgrowths, and commonly a combination of replacement and overgrowth is evident (Fig. 5.7a,b). Unfortunately, the exceedingly fine-grained habit of zircons in sample GC14-057 restricted the number of useful analyses to 14 points (Fig. 5.6).

Tera-Wasserburg and standard concordia plots of the uncorrected U-Pb isotopic data show slight discordance, with most (11 of 14) analyses clustering parallel to, though slightly off, concordia (Fig. 5.2a,b). Three analyses plot outside this grouping, in a cluster located roughly along a regression line anchored at an assumed $^{207}Pb/^{206}Pb$ composition for Pb_0 of 0.83, symptomatic of the effects of Pb_c. Figure 5.2a shows the provisional, unanchored age of 1024 ± 53 Ma.

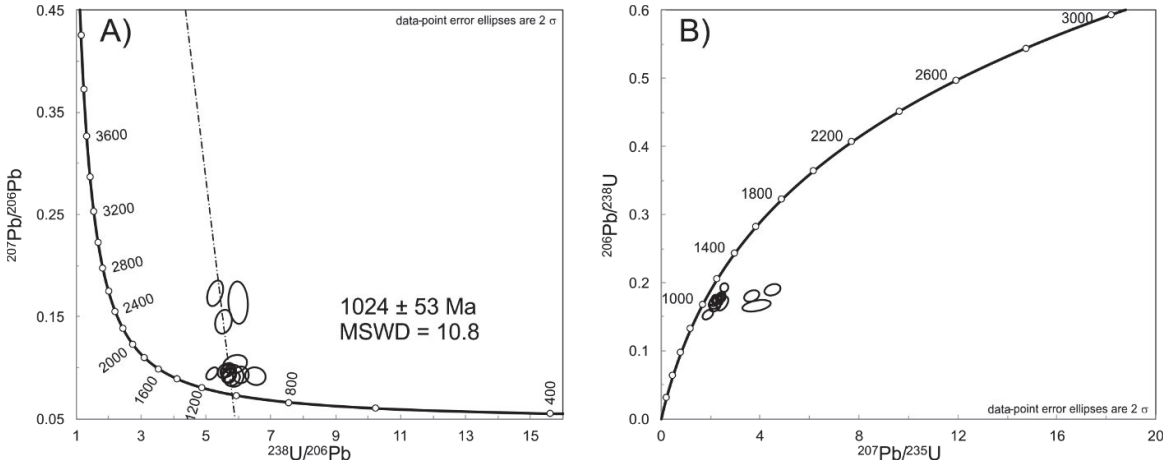

Figure 5.2 Uncorrected LA-ICP-MS results for sample GC14-057. A) Inverse concordia (Tera-Wasserburg) diagram regressed through all analyses, yielding the age 1022 ± 54 Ma. Deviation of analyses from concordia along this line is symptomatic of Pb_c. B) Standard concordia (Wetherill) diagram. Both plots indicate some Pb-loss as data lie slightly above (A) and below (B) concordia.

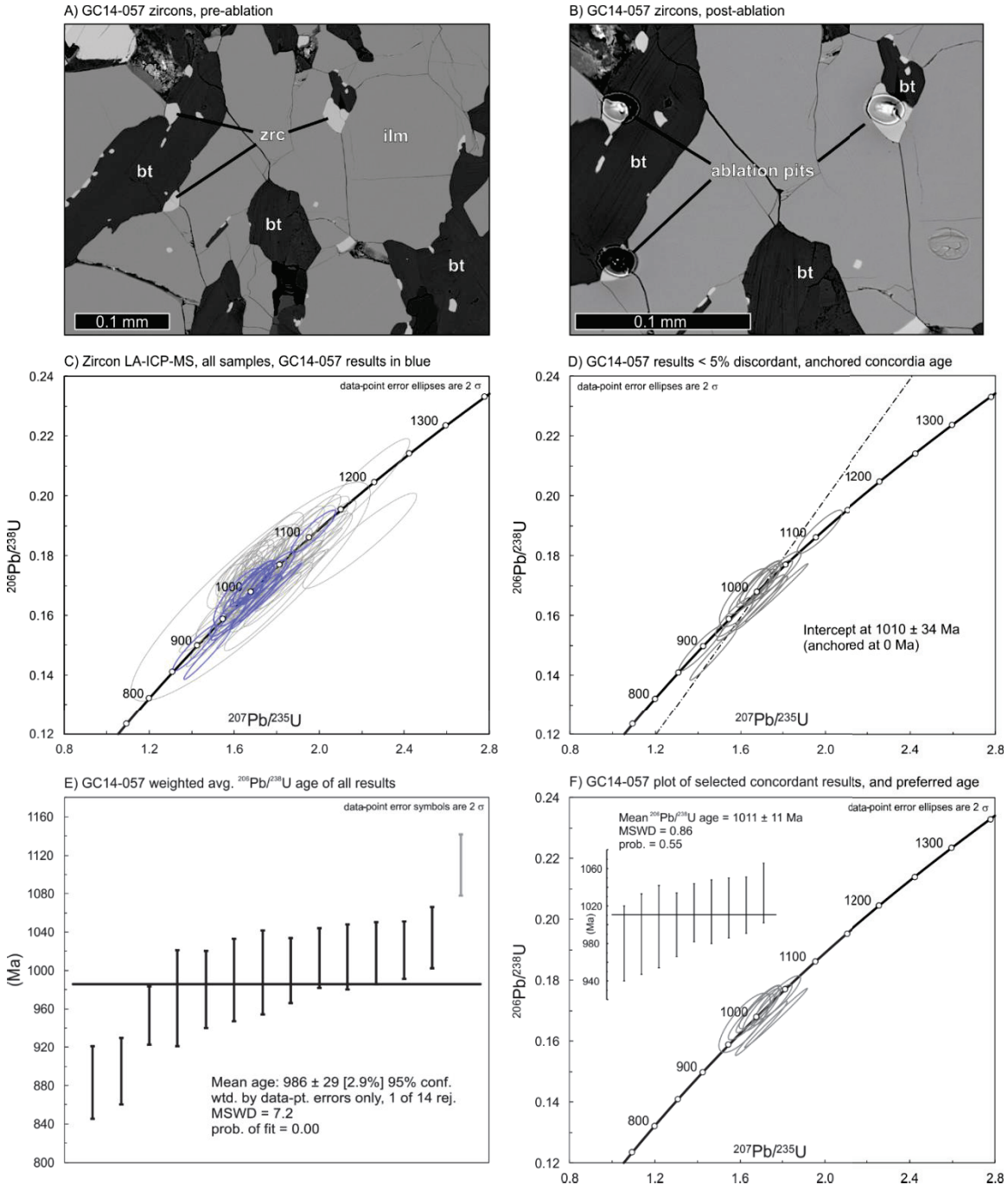

Figure 5.3 LA-ICP-MS results for sample GC14-057. A) BSE image of target zircons, pre-ablation. B) BSE image of the same zircons, post-ablation. C) Standard concordia diagram of all Pb_c-corrected analyses with results from GC14-057 shown in blue. D) Concordia diagram showing all analyses < 5% discordant and the anchored (at 0 Ma) regression intercept age range (1010 ± 34 Ma) used for further data reduction. E) A weighted average $^{206}Pb/^{238}U$ age plot using all analyses. F) A concordia plot and weighted average $^{206}Pb/^{238}U$ age plot showing the analyses used to calculate the preferred age for this sample (1011 ± 11 Ma, inset).

Correction for Pb_c, using the method of Andersen (2002) renders all analyses < 5%

discordant (Fig. 5.3c,d), though scatter among the data prevents calculation of a concordia age using the whole data set. A linearized probability plot of all ^{206}Pb-^{238}U ages with 1σ errors shows the data belong to a single age population.

Weighted average ^{206}Pb-^{238}U ages and concordia ages (anchored at 0 Ma) calculated for the whole data set (Table 5.4) yielded ages with unacceptable MSWD values >> 1. The calculation was then refined by excluding ages > 5% discordant, yielding a concordia age (anchored at 0 Ma) of 1010 ± 34 Ma (MSWD = 6.6; Fig. 5.3d). The weighted average calculated for all ages (9 of 14) lying within this 2σ range of uncertainty yielded the preferred age of 1011 ± 11 Ma (MSWD = 0.86; Fig 5.3f).

5.4.2 Byng Inlet, SmD sample GC14-024

High contrast BSE images of GC14-024 zircons show some evidence of zoning in several of the largest zircons, possibly relating to formation by a combination of replacement and overgrowth of the host oxide. As these zircons are generally too fine to

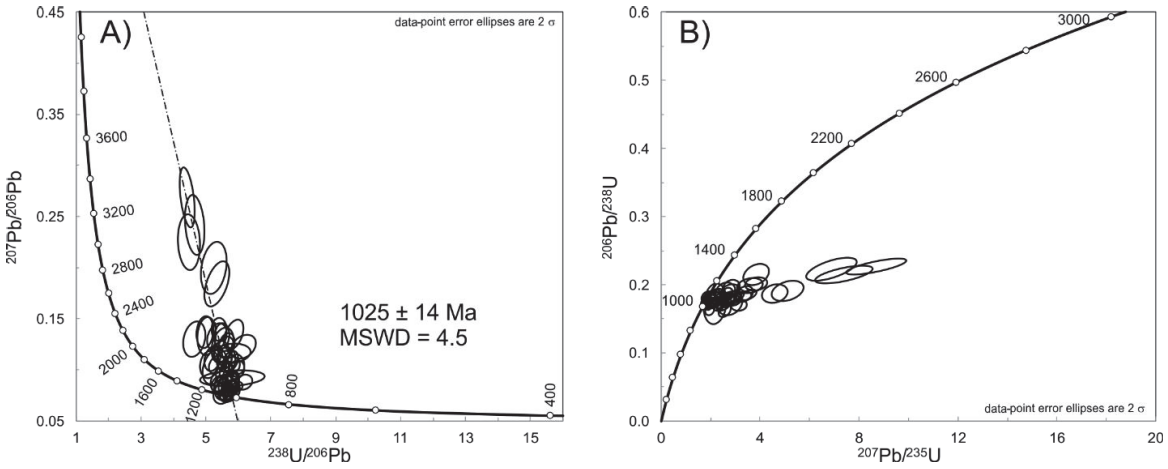

Figure 5.4 Uncorrected LA-ICP-MS results for sample GC14-024. A) Inverse concordia (Tera-Wasserburg) diagram regressed through all analyses, yielding the age 1025 ± 14 Ma. Deviation of analyses from concordia along this line is symptomatic of Pb_c. B) Standard concordia (Wetherill) diagram. Both plots indicate some Pb-loss as data lie slightly above (A) and below (B) concordia.

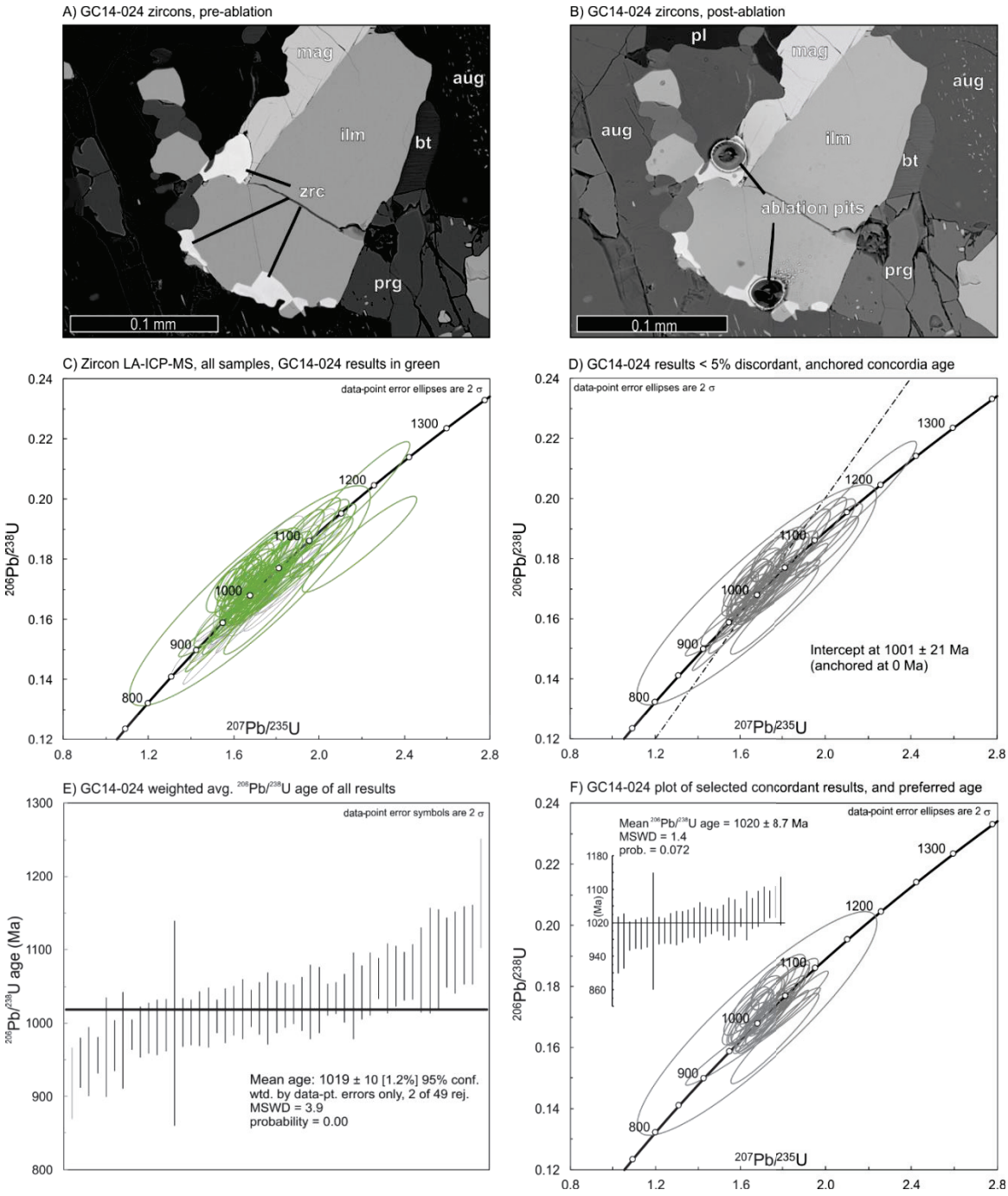

Figure 5.5 LA-ICP-MS results for sample GC14-024. A) BSE image of target zircons, pre-ablation. B) BSE image of the same zircons, post-ablation. C) Standard concordia diagram of all Pb_c-corrected analyses with results from GC14-024 shown in green. D) Concordia diagram showing all analyses < 5% discordant and the anchored (at 0 Ma) regression intercept age range (1001 ± 21 Ma) used for further data reduction. E) A weighted average $^{206}Pb/^{238}U$ age plot using all analyses. F) A concordia plot and weighted average $^{206}Pb/^{238}U$ age plot showing the analyses used to calculate the preferred age for this sample (1020 ± 8.7 Ma, inset).

accommodate more than a single 17 µm ablation pit, no further investigation into

compositional variations of these apparent "zones" was undertaken.

Tera-Wasserburg and standard concordia plots of uncorrected analyses for GC14-024 display a linear array of discordance symptomatic of the effects of Pb_c (Fig. 5.4a,b). In addition, despite the presence of a small concordant subset, data ellipses generally cluster about a center slightly above (Fig. 5.4a) concordia. A provisional regression through this array yields an age of 1025 ± 14 Ma with a MSWD = 4.5.

Corrected for Pb_c (Andersen, 2002), 7 of the 49 analyses are > 5% discordant. A further 21 of the remaining 42 analyses are > 2% discordant. A linearized probability plot of $^{206}Pb/^{238}U$ ages for the whole dataset shows a single, smooth trend in the data, with a regression line that intersects the 1σ error bars of all but one analysis, indicating that the data likely represent a single age population.

Weighted average ^{206}Pb-^{238}U ages and concordia ages (anchored at 0 Ma) calculated for the whole data set (Table 5.4) yielded ages with unacceptable MSWD values >> 1. The calculation was then refined by excluding ages > 5% discordant, yielding a concordia age (anchored at 0 Ma) of 1001 ± 21 Ma (MSWD = 7.7; Fig. 5.5d). The weighted average calculated for all ages (27 of 49) lying within this 2σ range of uncertainty yielded the preferred age of 1020 ± 8.7 Ma (MSWD = 1.4; Fig 5.5f).

5.4.3 Point au Baril, SmD sample GC14-048

Zircon in sample GC14-048 is comparable in coarseness to zircon in sample GC14-024, though slightly less abundant. Zircons coarse enough to accommodate ablation pits 17 µm in diameter are predominantly replacements after ilmenite (Fig. 5.7a,b). Despite this, zircon analyses from GC14-048 show the greatest degree of scatter, and produced the least well-constrained ages.

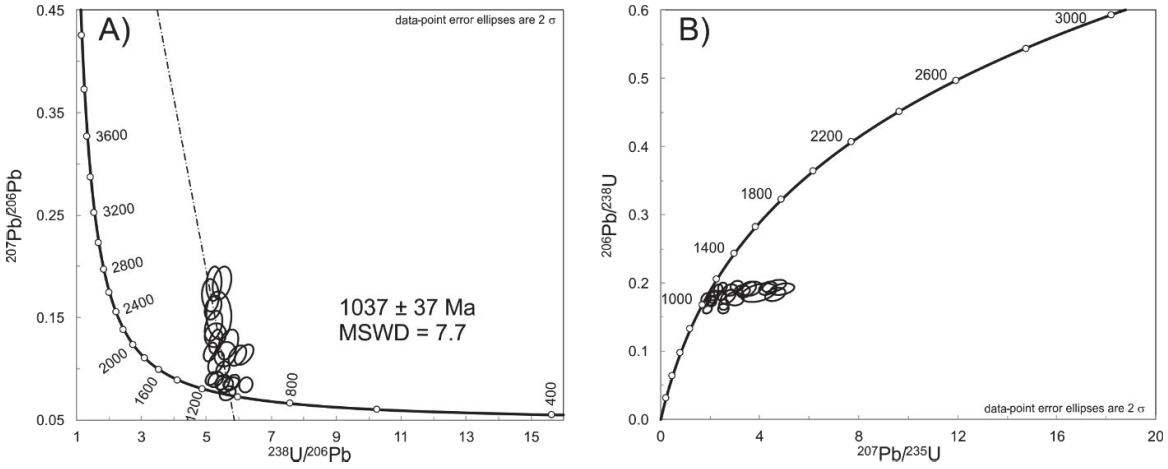

Figure 5.6 Uncorrected LA-ICP-MS results for sample GC14-057. A) Inverse concordia (Tera-Wasserburg) diagram regressed through all analyses, yielding the age 1037 ± 37 Ma. Deviation of analyses from concordia along this line is symptomatic of Pb_c. B) Standard concordia (Wetherill) diagram. Both plots indicate some Pb-loss as data lie slightly above (A) and below (B) concordia.

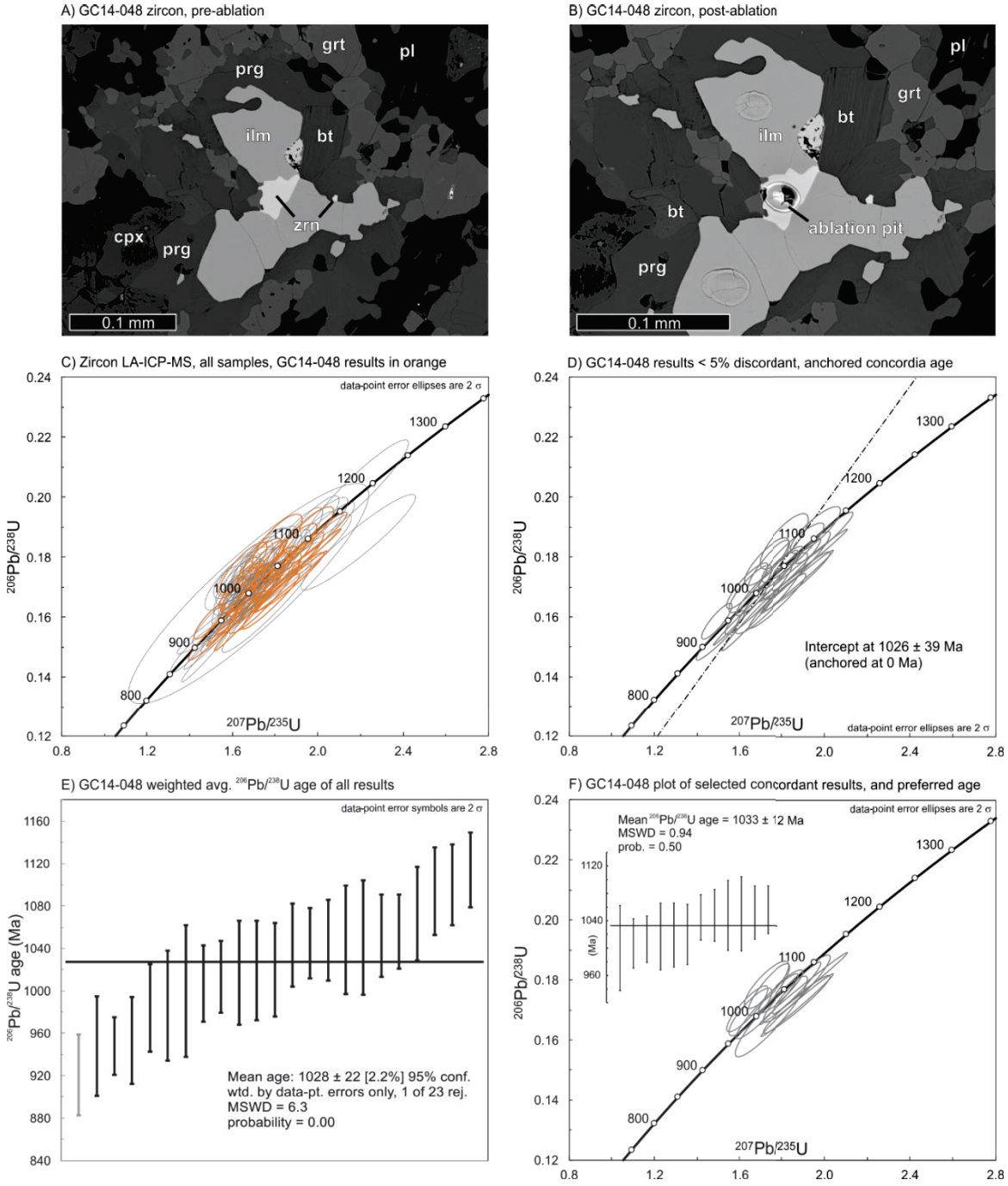

Figure 5.7 LA-ICP-MS results for sample GC14-048. A) BSE image of a target zircon, pre-ablation. B) BSE image of the same zircon, post-ablation. C) Standard concordia diagram of all Pb_c-corrected analyses with results from GC14-048 shown in orange. D) Concordia diagram showing all analyses < 5% discordant and the anchored (at 0 Ma) regression intercept age range (10026 ± 39 Ma) used for further data reduction. E) A weighted average $^{206}Pb/^{238}U$ age plot using all analyses. F) A concordia plot and weighted average $^{206}Pb/^{238}U$ age plot showing the analyses used to calculate the preferred age for this sample (1033 ± 12 Ma, inset).

Twenty-three analyses were produced from sample GC14-048. Uncorrected data display a distinct linear array of discordance that is symptomatic of Pb_c (Fig. 5.6). A regression though this array on a T-W plot intersects concordia at an age of 1037 ± 37 Ma (Fig. 5.6a).

A linearized probability plot of the Pb_c-corrected data shows that the all analyses fall within 1σ of a regression line, indicating that the data belong to a single age population. Of the 23 analyses, only one was found to be > 5% discordant, and a further 10 analyses were > 2% discordant.

Weighted average ^{206}Pb-^{238}U ages and concordia ages (anchored at 0 Ma) calculated for the whole data set (Table 5.4) yielded ages with unacceptable MSWD values >> 1. The calculation was then refined by excluding ages > 5% discordant, yielding a concordia age (anchored at 0 Ma) of 1026 ± 39 Ma (MSWD = 12; Fig. 5.7d). The weighted average calculated for all ages (12 of 23) lying within this 2σ range of uncertainty yielded the preferred age of 1033 ± 12 Ma (MSWD = 0.94; Fig 5.7f).

Table 5.4 Metamorphic ages (Ma) based on subsets of Andersen-corrected U-Pb data. The final column is the preferred age for each. The low anchored concordia age for GC14-024 reflects numerous reversely discordant analyses resulting from the Pb_c correction.

sample	wtd. avg. $^{206}Pb/^{238}U$ age (all analyses)	Anchored concordia age (< 5% disc.)	refined wtd. avg. $^{206}Pb/^{238}U$ (preferred age)
GC14-057	986 ± 29	1010 ± 34	1011 ± 11
GC14-024	1019 ± 10	1001 ± 21	1020 ± 8.7
GC14-048	1028 ± 22	1026 ± 39	1033 ± 12

5.5 Discussion

5.5.1 Comparison with previous geochronology

Corrigan et al. (1994) reported zircon, monazite, and titanite U-Pb TIMS data from Key Harbour, ~ 15 km south of the GFTZ, in the same area as sample GC14-057. Monazite separated from polycyclic migmatitic paragneiss yielded $^{207}Pb/^{206}Pb$ ages of 1035 ± 1 Ma and 1037 ± 1 Ma. While the monazite ages are concordant, it is impossible to tell whether the grains were Grenvillian in origin. Moreover, the latter age was derived from a single monazite analysis. Without petrographic information on internal texture and chemical zoning, the significance of this monazite age is very difficult to interpret.

Titanite in pegmatitic leucosome from internal boudin necks in the ca. 1442 Ma Mann Island granodiorite (van Breemen et al., 1986; Corrigan et al., 1994) yielded an age of 1003 ± 9 Ma, interpreted as the age of cooling through *c.* 600 °C. Zircons in pegmatite post-dating late-Grenvillian structures yield ages of 990 ± 2 Ma. The zircon $^{206}Pb/^{238}U$ age (1011 ± 11 Ma) reported in this study is the first age derived from a lithology with an exclusively Grenvillian metamorphic history. While zircon xenocrysts have been found in Sudbury Diabase, rare inherited grains are generally conspicuous by their size (> 100 μm), higher length:width ratios (3 to 5), striated faces, and highly fractured nature (Dudàs et al., 1994). Zircons in this study (mostly ≤ 20 μm and equant) formed within coronas and are clearly metamorphic.

A metadiabase body near Key Harbour, with coronitic mineralogy, relict subophitic texture, and geochemistry indistinguishable from SmD was described by Davidson and van Breemen (2001). The metamorphic zircon fraction yielded a U-Pb TIMS age of 1013

± 2.4 Ma (1.4% discordant), identical to the preferred age of peak metamorphism in the Key Harbour sample reported in this study. However, igneous baddeleyite in the sample yielded ages of ca. 1287 Ma, ca. 1343 Ma, and 1454 Ma. The ages are highly discordant (4.6 to 7.4%) and the younger ones are interpreted to reflect some degree of Pb loss (Davidson and van Breemen, 2001). The third age is interpreted to indicate a minimum emplacement age ca. 200 My older than the ca. 1235 Ma SD (Krogh et al., 1987; Dudàs et al., 1994), possibly calling into question the validity of geochemical correlations for defining SD affinity. This age is contemporaneous with the emplacement age of numerous Mesoproterozoic plutonic orthogneisses in the area, such as the ca 1450 Ma Britt Pluton (van Breemen et al., 1986) and ca. 1440 Mann Island granodiorite (Corrigan et al., 1994). If 1450 Ma really does represent the age of intrusion, these data cast doubt on the validity of geochemical data for identifying metadiabase correlative with the SD suite.

No previous detailed metamorphic or geochronological studies have been conducted on the central region of the Britt domain. Sample GC14-024, from the central Britt domain, is considered to yield the most robust age (1020 ± 8.7 Ma) of the three dated samples from this study. As the Pb_c correction applied affects the $^{207}Pb/^{235}U$ ratio more strongly than the $^{206}Pb/^{238}U$, the low anchored concordia age for this sample (1001 ± 21 Ma) is interpreted to reflect the numerous reversely discordant analyses resulting from the correction. No previous U-Pb metamorphic ages for SmD in the Point au Baril area have been published. However, the timing of ductile normal-sense displacement along the Shawanaga Shear Zone, immediately to the south, is constrained by zircon ages in pre- or early syn-kinematic, late syn-kinematic, and post-kinematic granitic pegmatites

(Ketchum, 1994; Ketchum et al., 1998). These yielded ages of 1042 +4/-2, 1019 ± 4, and 988 ± 2 Ma, respectively (Fig 5.8). Here, the reported weighted average $^{206}Pb/^{238}U$ age (1033 ± 12 Ma) from sample GC-048 agrees remarkably well with the range of pre-to-early syn-kinematic and late syn-kinematic ages reported by Ketchum et al. (1998).

5.5.2 Timing of metamorphism in the Britt domain

Data from these three samples show significant scatter, covering a broad range of ages between ca 1100-950 Ma, with considerable overlap among samples given large uncertainties in some analyses. If the method of calculation described in Section 5.4 and the resulting preferred ages are robust, then the ages for each sample, 1011 ± 11 Ma, 1020 ± 8.7 Ma, and 1033 ± 12 Ma indicate a systematic younging of granulite facies metamorphism from south to north across the Britt Domain. While the uncertainties are

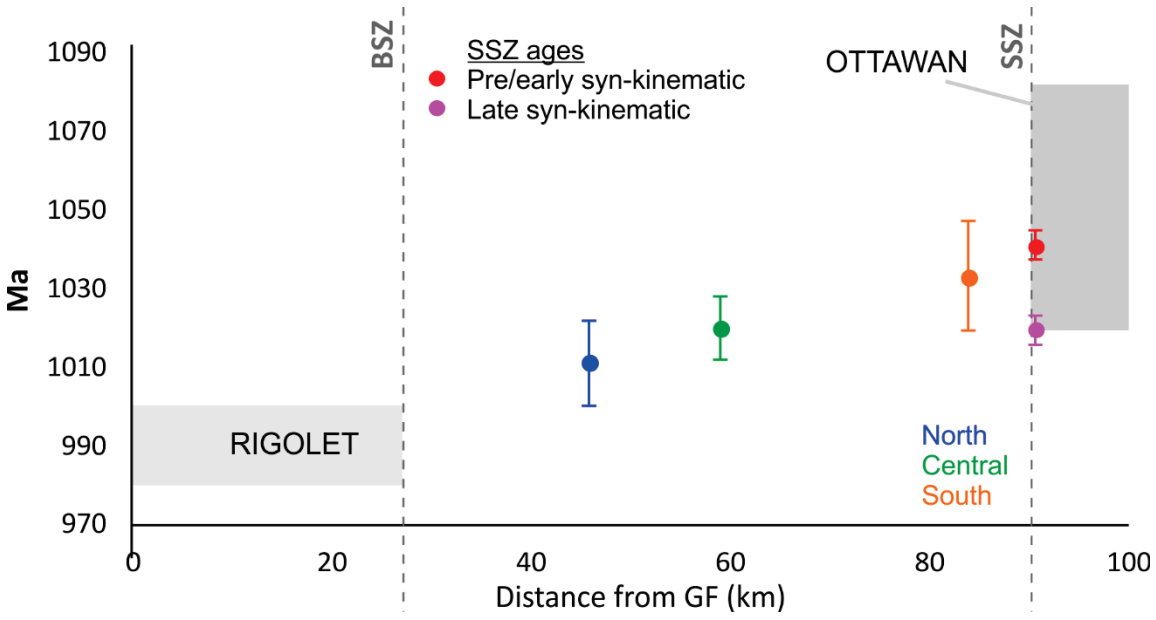

Figure 5.8 Age vs. distance plot showing the relationship of peak metamorphic ages from the Britt domain (in blue, green, and orange; this study) to age ranges defined for the Rigolet and Ottawan phases of the Grenvillian Orogeny (Rivers, 1997) in the GFTZ and Shawanaga Domain, respectively. Peak metamorphic age for the southern BD (orange) overlaps the ages of pre/early (red) and late (purple) syn-kinematic pegmatites injected during extension on the SSZ (Ketchum et al., 1998).

large enough to permit marginal overlap among the ages from all three samples, the systematic pattern seems unlikely to be purely coincidental.

Significantly, the southern BD reached peak granulite facies conditions while the SSZ was undergoing SE-directed extension (ca 1042-1019 Ma; Ketchum et al., 1998), predating Rigolet phase metamorphism and thrusting in the GFTZ by ca. 20-30 My (Fig. 5.8). This northward younging trend in peak metamorphic age is consistent with progressive burial and prograde metamorphism of the Britt Domain during propagation of the orogen toward the Laurentian foreland.

Chapter 6: Discussion and Conclusions

6.1 Sudbury metadiabase in the Britt Domain

This study presents new late-Grenvillian P-T-t information from a critical region of the parautochthonous belt, the Britt Domain (BD), situated between the GFTZ to the NW and the allochthonous Shawanaga Domain to the SE. The widely distributed and readily identifiable ca. 1235 Ma Sudbury metadiabase (SmD) records exclusively Grenvillian metamorphic histories throughout parautochthonous domains of the Central Gneiss Belt (CGB), and serves as an unambiguous monitor of the timing and conditions of peak metamorphism. Figure 6.1 summarises P-T-t data plotted vs. distance (km) from the Grenville Front (GF).

6.1.1 Field Relations

Sudbury metadiabase segments are widely distributed throughout the GFTZ and BD, and readily identifiable by a set of features related to primary igneous characteristics. These include a relict subophitic texture, chilled margins, and, commonly, the presence of megacrystic, subhedral plagioclase. New characteristic features described in this study, not previously associated with Sudbury affinity, include the presence of internal contacts related to dyke-in-dyke sheeting and, locally, magma mingling.

Within the BD, SmD segments appear to be progressively reworked from NW to SE. Despite progressive reworking, coronitic granulite facies metamorphic assemblages overprinting relict diabase texture are preserved in the strain-resistant cores of large, 100-m-scale, segments of SmD hosted in orthogneiss. In the Key Harbour archipelago,

Sudbury metadiabase hosted in ca. 1694 Ma leucogranite orthogneiss crops out as rectangular blocks roughly 100 m long and 50 m wide. Nearby paragneiss-hosted SmD segments are, in contrast, smaller, more strongly deformed, and retrogressed to amphibolite. In the central BD, large SmD segments hosted in ca. 1456 Britt monzogranite orthogneiss are roughly 120 m long and 60 m wide and lenticular. This shape reflects a degree of deformation related to boudin necking, but segments still preserve granulite-facies peak assemblages overprinting relict sub-ophitic textures in the strain-resistant core. In contrast, the 4-m-wide dyke segment on H A Gray Island near Point au Baril in the southern BD is exceedingly well preserved, transecting the host orthogneiss continuously for 240 m.

6.1.2 P-T variations

Previous work in the GFTZ described a steady increase in peak P across the GFTZ from ca. 6 kbar near the GF to ca. 14 kbar in the northern BD, reflecting NW-directed thrusting and exhumation of progressively deeper crust to the SE (Fig. 6.1b) (Haggart et al., 1993; Jamieson et al., 1995; Bethune and Davidson, 1997). In this study, peak P-T conditions calculated for coronitic granulite-facies assemblages in SmD indicate roughly consistent metamorphic conditions across the BD.

The peak P calculated for the northern BD, 13.8 kbar, is consistent with previously published P estimates (ca. 14 kbar; Jamieson et al., 1995) for the Key Harbour area (Fig 6.1b). A slight decrease in peak P to 13.1 kbar was calculated for the central BD, though estimates overlap well within expected uncertainties (~1 kbar). The peak P calculated for the southern BD, 15 kbar, is notably higher than the northern and central BD; it is possible that peak P exceeded 16 kbar, given the lack of stable orthopyroxene (Pattison,

2003). In contrast to the relatively high and consistent P estimates from across the Britt domain, there is a pronounced difference between peak P recorded in the BD and the adjacent Shawanaga domain (ca. 8 kbar; Ketchum, 1994), corresponding to burial differences of ca. 20-25 km. This P difference is interpreted to reflect normal-sense ductile shear on the SSZ accommodating ca. 40 km of down-dip displacement along the structure (Fig 6.1b).

Peak T estimates from SmD in the BD from this study are consistent with previous estimates from SmD across both the GFTZ and northern BD (ca. 720-870 °C; Jamieson et al., 1995; Bethune and Davidson, 1997), and peak T calculated from the monocyclic coronitic metagabbro throughout nearby allochthonous domains (ca. 650-800 °C; Grant, 1987; Ketchum, 1994; Timmerman, 1998; Kendrick, 2015) (Fig. 6.1a). A slight increase in peak T is indicated from ca. 720 °C in the NW to 780°C in the SE. In contrast to peak P, no conspicuous discrepancy is indicated in peak T between the southern BD and the Shawanaga Domain.

6.1.3 Age variations

The timing of metamorphism across the BD is a crucial test of alternative models explaining late-stage orogenic propagation into the Laurentian foreland. If the Rigolet phase was a short-lived event affecting the PB from ca. 1000-980 Ma, then either all regions of the BD, as little-transported, reworked Laurentian crust, should have undergone metamorphism within this age range, and at roughly the same time, or should have undergone cooling and exhumation before this time.

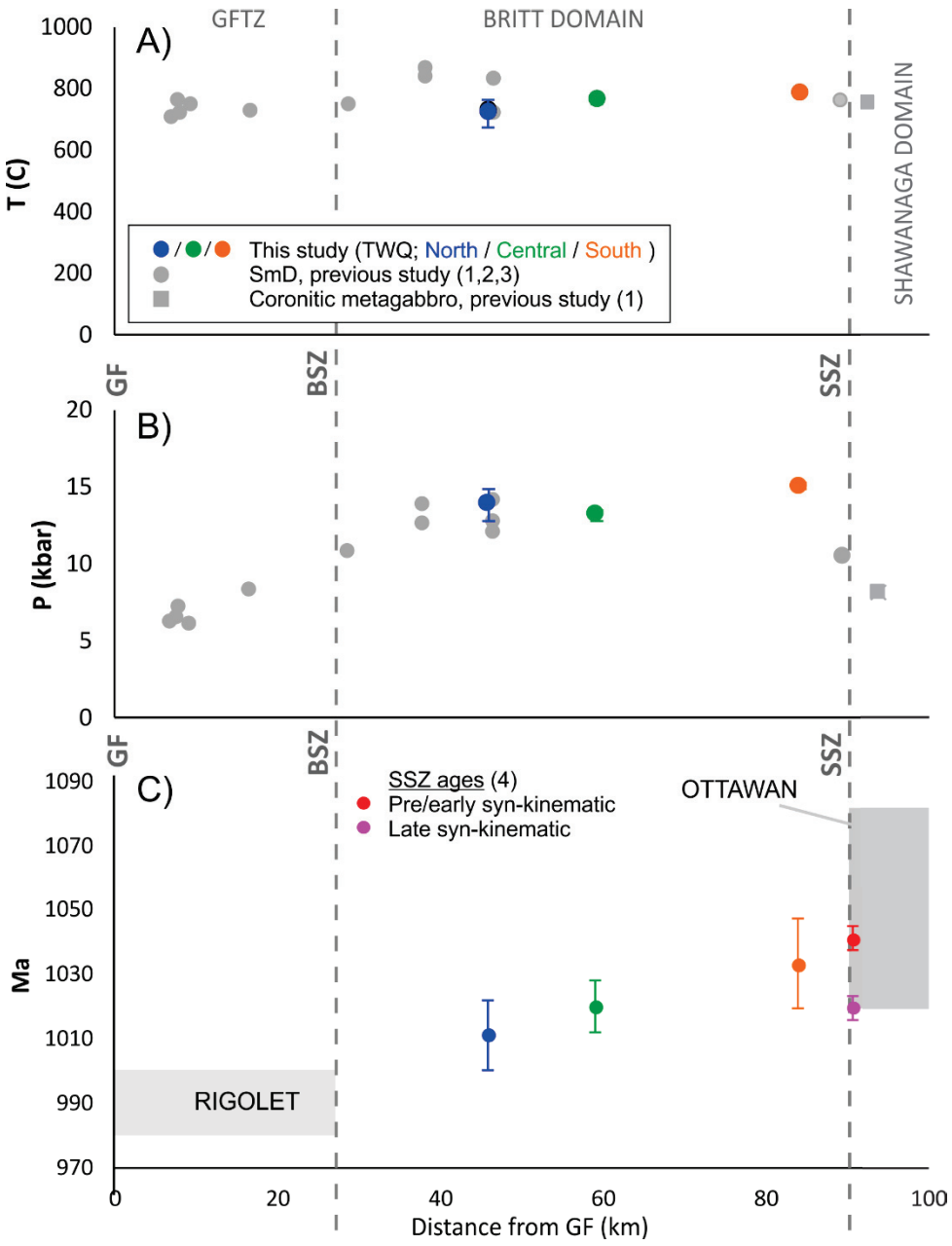

Figure 6.1 Summary of P-T-t data vs. distance relative to domain-bounding structures (GF, Grenville Front; BSZ, Boundary Shear Zone; SSZ, Shawanaga Shear Zone). A) T vs. distance; previous studies in grey dots, this study in coloured dots. Note roughly comparable peak-T throughout. B) P vs. distance; symbols as for (A). Note the steady increase in peak-P across the GFTZ and northern BD and sharp decrease across the SSZ. C) SmD with metamorphic ages, with errors, from this study; symbols as for (A). Metamorphic ages across the parautochthonous Britt Domain young toward the GFTZ, and overlap significantly with metamorphic ages from allochthonous domains (Ottawan phase) and pre/early- and late-syn-kinematic ages of extension on the SSZ (Ketchum et al., 1998). P-T-t references for previous studies: 1. Ketchum (1994); 2. Jamieson et al. (1995); 3. Bethune and Davidson (1997); 4. Ketchum et al. (1998).

Significant scatter among isotopic data, owing to the exceedingly fine-grained habit of metamorphic zircon, resulted in significant overlap in age uncertainties between samples. Nevertheless, U-Pb geochronology of zircon associated with granulite-facies coronitic asssemblages in SmD strongly suggests a metamorphic age gradient younging from 1033 ± 12 Ma in the SE, to 1020 ± 8.7 Ma in the central BD, to 1011 ± 11 Ma in the NW (Fig 6.1c). Together, these ages are consistent with progressive burial and metamorphism of the BD, representing propagation of deformation from SE to NW at a rate of ca. 2 mm/yr.

6.2 What was the Rigolet phase?

6.2.1 Models and model predictions

Was the Rigolet phase of the Grenvillian Orogeny a late, discrete tectonic event involving renewed convergence (e.g., Rivers, 2008), or the natural progression of post-convergent ductile flow (e.g. Jamieson et al., 2010)? The Rigolet phase was originally defined by metamorphic U-Pb ages interpreted to represent a relatively short interval of thrusting and metamorphism from ca. 1000-980 Ma that affected the GFTZ and other parts of the parautochthonous belt near the GF (Rivers, 1997). This age range, post-dating metamorphism during the Ottawan phase (ca. 1090-1050 Ma) in the allochthonous belt by > 20 Myr, led Rivers (1997) to posit a hiatus in tectonic activity in the mid-crust, following which deformation shifted from the orogenic core to the NW flank of the orogen in response to renewed convergence. According to conceptual models for late-stage evolution of the Grenvillian Orogeny (Rivers, 2008, 2009; Rivers and Schwerdtner, 2015), this hiatus represents the cessation of ductile flow characteristic of large hot

orogens, and a transition to critical-wedge mechanics, characteristic of smaller, relatively cold orogens. As ductile, foreland-directed flow was presumed to have ceased near the end of the Ottawan phase (ca. 1050-1020 Ma) this model implies renewed convergence driving thrusting in the foreland.

Results from numerical models designed to analyse the behaviour of the Laurentian margin during collisional orogenesis (Jamieson et al., 2007, 2010; Jamieson and Beaumont, 2013) are consistent with the current geometry of the CGB along the Georgian Bay transect. Predicted P-T paths recorded by tracking particles are roughly consistent with previously published estimates for the GFTZ, the northern BD, and the Shawanaga Domain (Jamieson et al., 2010). The models predict that, following the end of Ottawan convergence, hot, thick, melt-weakened mid-crust would have flowed outward, driving thrusting at the flanks of the orogen and accompanied by coeval ductile thinning in the orogenic core (Jamieson & Beaumont, 2011). These models also predict progressive burial and metamorphism of the parautochthonous belt following the end of Ottawan convergence. In the models, ductile flow propagates toward the foreland at a rate of ca. 7 mm/yr, progressively deforming and metamorphosing crustal blocks correlative first with the BD, then the GFTZ. This process for late-stage propagation differs fundamentally from the conceptual models summarised above in that no hiatus in tectonism between "Ottawan phase" deformation in the orogenic core and late "Rigolet phase" deformation of the parautochthon in the NW flank is predicted. The Ottawan and Rigolet phases are simply early and late expressions of mid-crustal ductile flow, syn-convergent in the case of the Ottawan phase, and post-convergent in the case of the Rigolet phase.

Robust P-T estimates for the BD serve to validate domain-scale model predictions. Conceptual models (e.g. Rivers, 2008) cannot make quantitative predictions, but medium- and high-grade metamorphism for the Rigolet phase are limited to the relatively short-lived time frame of 1000-980 Ma. Cooling and exhumation are predicted to accompany normal-sense extension along the SSZ.

Coupled thermal-mechanical numerical models (Jamieson et al., 2010) involving post-convergent gravitational spreading predict progressive burial and prograde metamorphism of the parautochthon as ductile flow propagates into the Laurentian foreland from the orogenic plateau. Tracking particles in the model predict peak T for the BD correlative blocks on the order of ca. 730 °C at 9.6 kbar (Jamieson et al., 2010). While the predicted temperatures are consistent with the data presented in this study, the differences in pressure suggest a significant difference in the degree of crustal thinning during ductile spreading. The models also predict progressively younger peak metamorphic ages toward the foreland associated with a propagation rate on the order of ca. 7 mm/yr.

The timing of peak metamorphism across the BD serves to distinguish, definitively, between the conflicting models presented above. In summary, the conceptual model (e.g. Rivers, 2008) predicts approximately isochronous deformation and metamorphism, post-dating extension in the orogenic core by ca. 20 My, prior to which cooling and exhumation accompany normal-sence displacement on the SSZ. In contrast, coupled thermal-mechanical numerical models involving post-convergent gravitational-spreading predict progressive NW-directed deformation and metamorphism of the parautochthon, continuous with extension in the orogenic core.

6.2.2 Relation of U-Pb ages to model predictions

Results from this study indicate that peak granulite facies metamorphism affected the parautochthonous BD diachronously from SE to NW. Metamorphism in the footwall of the SSZ (ca 1030 Ma) predated thrusting and metamorphism in the GFTZ by ca 20-30 Myr, and also predates the upper age limit (ca. 1005-1010 Ma) suggested for the Rigolet phase (Rivers, 1997, 2009). Moreover, the age of peak metamorphism in the central and SE BD, the latter located in the footwall of the SSZ, coincides with pre/early-to-late syn-kinematic ages (1042 +4/-2 Ma and 1019 ± 4 Ma, respectively) of SE-directed, normal-sense movement on the SSZ (Ketchum, 1994; Ketchum et al., 1998). This demonstrates that metamorphism in the parautochthon coincided with ductile extension in the orogenic core. Thus, no hiatus in tectonic activity separated Ottawan deformation in the Shawanaga Domain and propagation of deformation and metamorphism through the parautochthon during the Rigolet phase.

In summary, the observed times and grades of metamorphism in the BD are compatible with predictions of models for post-convergent ductile flow. However, the discrepancy between predicted model rate of propagation, ~ 7 mm/yr (Jamieson et al., 2010), and the rate indicated by timing of peak metamorphism in this study, ~ 2 mm/yr, indicate that model viscosities are slightly too low. Discrepancies between model-predicted peak P and the data presented in this study corroborate this, as higher viscosities, less susceptible to ductile spreading, should facilitate greater crustal thickening and deeper burial depths.

6.3 Implications

6.3.1 The Grenvillian Orogeny

Rivers (2008, 2009) characterized ductile gravitational spreading beneath the Grenvillian orogenic plateau as a heterogeneous channel of melt-weakened mid-crust. He contended, however, that models predict roughly coeval deformation in the orogenic foreland (the parautochthon) and extension along the base of the mid-crustal channel (the ABT). As this violated the premise that the Rigolet phase post-dated extension on the ABT by ca. 20 My, it was suggested that late extension cooled the mid-crustal channel, lowering the viscosity and ceasing ductile flow. Following ca. 20 My of tectonic quiescence, rapid burial and metamorphism was taken up in the parautochthon in response to renewed convergence (Rivers, 2008). Based, in part, on this concept of disparate phases of convergence, a new interpretation of the western CGB as a giant metamorphic core complex was proposed (Rivers 2012; Rivers and Schwerdtner, 2015; Schwerdtner et al., 2016).

Peak metamorphic ages presented here show that the premise that Grenvillian deformation and metamorphism in the PB was limited to ca. 1000 – 980 Ma is demonstrably false for the western CGB. Rather, the P-T-t data for the BD presented in this study are consistent with diachronous burial and metamorphism that progressed from the SE, near the SSZ, to the NW, near the GFTZ, as predicted by numerical models for post-convergent ductile flow in the Grenvillian Orogeny (Fig. 6.2) (Jamieson et al., 2007, 2010; Jamieson and Beaumont, 2011, 2013).

This study demonstrates that the current definition of the Rigolet phase as a discrete, short-lived phase of convergence from ca. 1000-980 Ma is inaccurate at least in the context of the western CGB. However, the division of the Grenvillian Orogeny *sensu stricto* into early and late phases relating to the main (Ottawan) plateau building convergent phase (Fig. 6.2a,b), and a later (Rigolet) phase characterized by post-convergent foreland-directed flow (Fig. 6.2b,c) is still useful. It is suggested here that the Rigolet phase be redefined as the response of Laurentia to foreland-directed post convergent ductile flow. A new age range of 1040-980 Ma for the Rigolet phase, defined by onset of metamorphism in the parautochthon, is proposed, with the understanding that the Ottawan and Rigolet phases are continuous and simply represent syn- and post-convergent phases of the Grenvillian orogenic system.

In summary, first-order processes involved in foreland-directed gravitational-spreading of hot, ductile, melt-weakened mid-crust, progressively incorporated from the continental margin, and progressive reworking of crust of above a basal decollement (Fig. 6.2). Lateral flow ultimately drove metamorphism and exhumation toward the flank of the orogen within a broad ductile shear zone (the GFTZ). The GFTZ developed when deformation driven by lateral flow was taken up in colder, stronger continental crust at the end of the orogenic cycle.

6.3.2 Other examples of post-convergent ductile flow

Another example coeval ductile extension and foreland thrusting can seen in Late Jurassic to Eocene deformation in the southern Canadian Cordillera. Terrane accretion during the Early Jurrasic resulted in the formation of the Rocky Mountain Thrust and Fold Belt. Parts of what is now the Omineca Belt were deeply buried and subsequently

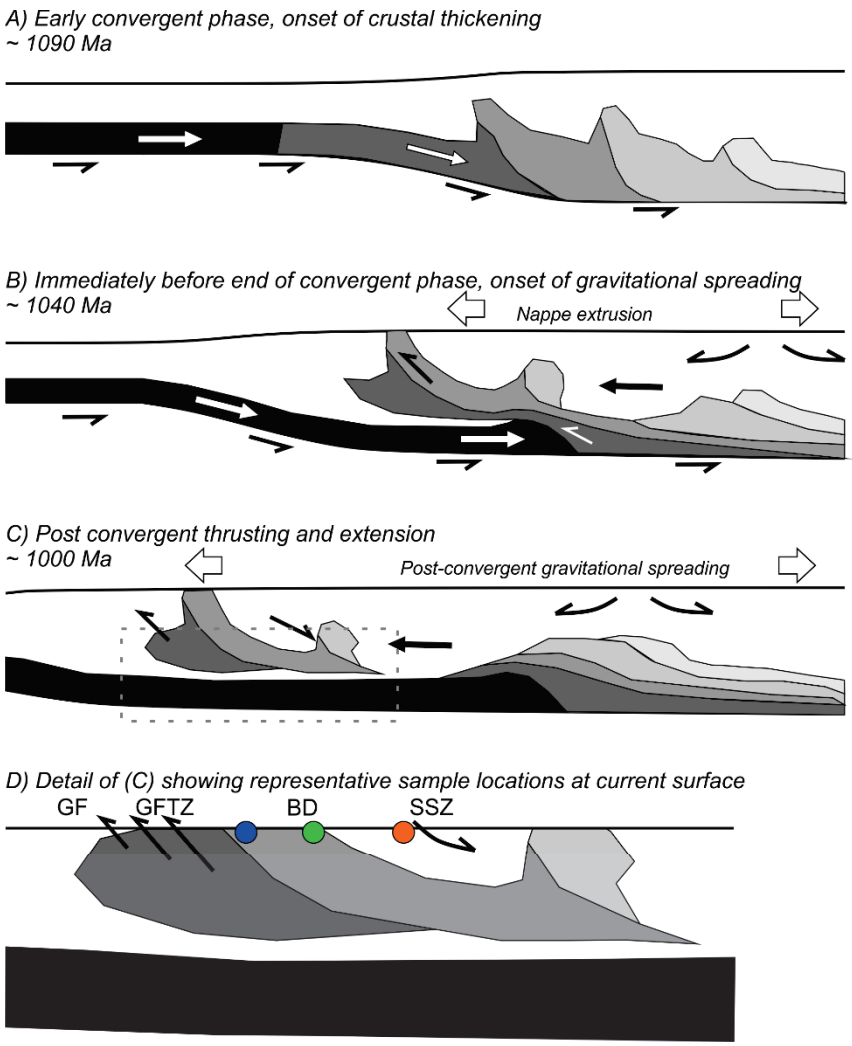

Figure 6.2 Tectonic evolution of the Grenvillian Orogeny, drawn from numerical model results (modified after Jamieson et al., 2011). A) Early convergent phase showing crustal thickening. B) Immediately before the end of the convergence, showing stacking and heterogeneous extrusion of lower crustal nappes and regional foreland-directed flow driven by onset of gravitational spreading. C) Late-stage showing post-convergent gravitational extension and coeval thrusting in the foreland. D) Detail of panel (C; dashed box) showing the locations (to scale) of representative samples from Key Harbour (blue), Byng Inlet (green), and Point au Baril (orange) across the Britt Domain (BD).

exhumed prior to the Cretaceous (Parrish, 1995; Colpron et al., 1998). Other areas of the Omineca Belt, representing a 10-20 km thick zone of hot and weak mid-crust called the Lower Selkirk allochthon, were not exhumed until the Late Cretaceous and Paleocene. It is argued that this zone is bounded at the top by the SW-directed normal-sense Selkirk Detachment Fault, and at the base by the NE-directed Purcell Thrust Fault, a splay of the

Monashee Decollement (Brown and Gibson, 2006; Gervais and Brown, 2011). Both were active during the Late Cretaceous, and while it is unclear whether the upper and lower boundaries were discrete shear zones throughout the Cretaceous, high-T deformation within the mid-crust was active for approximately 100 My (Brown and Gibson, 2006; Gervais and Brown, 2011). Strong arguments have been made that this system did not involve Himalayan-style channel flow, but rather ductile thrusting of coherent crystalline thrust sheets (Carr and Simony, 2006; van Rooyen et al., 2016) that is more consistent with the Grenvillian system of heterogeneous nappe extrusion (Beaumont et al., 2010).

The deformation of hot, melt-weakened mid-crust during the Ottawan and Rigolet phases took place over ca. 100 My (Rivers, 1997, 2009, and references therein), comparable to the duration of high T mid-crustal activity in the Omineca Belt of southern Canadian Cordillera (Brown and Gibson, 2006; Gervais and Brown, 2011). Like numerical models for the western GP, coeval extension and thrusting of the Lower Selkirk allochthon above a crustal ramp drove ductile flow and thrusting ahead of the Upper Selkirk allochthon which sole into the Monashee Decollement, similar to NW-directed thrusting in the GFTZ. The obvious difference between the two regions is the lack of collisional orogenesis in the southern Cordillera. Here, accreted terranes to the west behave as the "other side" of the orogen with westward-directed underthrusting of the Proterozoic basement of the western North American continental margin. This strong lower crustal ramp is analogous to the Laurentian margin lower crustal indentor over which post-convergent gravitational spreading drove heterogeous ductile flow of mid-crust during Rigolet phase propagation Grenvillian orogenesis (Beaumont et al., 2010; Jamieson et al., 2007, 2010).

6.3.3 Future Work

More data are needed on the timing and conditions of peak metamorphism and associated structural and textural styles. Determining the timing of metamorphism in SmD east of the Georgian Bay transect, particularly near the inferred location of the ABT, would provide a test of the hypothesis presented here by determining whether the age gradient indicated in this study is replicated elsewhere. If orogen-wide thrusting and metamorphism within the GFTZ occurred between ca 1000-980 Ma, do other parautochthonous domains adjacent to the GFTZ also record a similar SE-to-NW-younging trend?

Further efforts to produce forward thermodynamic models of equilibrium assemblages are strongly recommended. In particular, thermodynamic models for a progressively changing effective bulk-composition should be developed to track the progressive development and P-T evolution of the coronitic assemblages. This could be done by using x-ray chemical maps of textural sub-domains and image analysis to calculate modal proportions and bulk compositions for sub-assemblages demonstrated to be in compositional equilibrium (Berman, 1991; Schneider et al., 2012).

Significant scatter among isotopic data produced in this study resulted from the exceedingly small metamorphic zircon available for *in situ* LA-ICP-MS analysis. As there is virtually no hope of separating such fine-grained zircons for ID-TIMS analysis, the higher spatial resolution and sensitivity of a sensitive high-resolution ion microprobe (SHRIMP) would be ideally suited for dating zircons of this kind (Ireland and Williams, 2003). Alternatively, split-stream LA-ICP-MC would allow simultaneous collection of

isotopic age data and trace element data, providing better constraints on the mineral assemblage coexisting with zircon during growth (Kylander-Clark et al., 2013).

The ~ 1m wide, very coarse-grained anorthositic xenolith observed in outcrop GC14-023 (Fig. 2.3) deserves further study. There is good field evidence that megacrystic plagioclase in this outcrop is related to this xenolith. By analogy, the megacrystic plagioclase commonly found along the margins of SD dykes and SmD segments may also have been derived from disaggregation of anorthosite enclaves or larger bodies at depth. It is not clear whether this xenolith was actually related to the magma which formed the dykes, or was incorporated from wall rocks shortly before dyke injection. The ca. 1240 Ma St. Charles anorthosite (Prevec, 1992) is located roughly 60 km to the NE of this locality. Major and trace element geochemistry could indicate a correlation, beyond age, between the two.

6.4 Conclusions

The main scientific contributions of this study are as follows:

1. Reliable peak P-T information can be obtained from coronitic metamorphic assemblages preserved in the strain-resistant cores of SmD dyke segments by the careful selection of mineral sub-groups demonstrating compositional equilibrium despite strong textural evidence for general disequilibrium.
2. Peak P estimates suggest that most of the Britt Domain was buried ca. 40 km (corresponding to 13.1-13.8 kbar) during late Grenvillian metamorphism. The P difference recorded by SmD in the footwall of the SSZ and coronitic metagabbro in the hangingwall (ca 15 kbar vs ca 8 kbar) corresponds to a roughly 25 km

difference in burial depth, consistent with SE-directed normal-sense shear on the reactivated ABT.

3. Peak T estimates indicate that the entire Britt Domain saw comparable temperatures throughout, between 720 – 780 °C. This is consistent with lateral advective heat transfer during progressive burial and metamorphism of the parautochthon predicted by results from coupled thermal-mechanical numerical models (Jamieson et al. 2007, 2010). No significant difference in peak T between the BD and the Shawanaga Domain is indicated, which is also consistent with predictions of the numerical models.
4. U-Pb ages of peak metamorphism, as recorded by metamorphic zircons associated with granulite facies coronitic assemblages in SmD, indicate an ages young from SE to NW across the BD. Granulite-facies was reached in Point au Baril at ca. 1033 Ma, in Byng Inlet at ca. 1020 Ma, and in Key Harbour at ca. 1011 Ma. Given a transect length of roughly 40 km, this corresponds to a deformation propagation rate of ~2 mm/yr.
5. The interpretation that the Rigolet phase of the Grenvillian Orogeny represents a short-lived system of rapid burial and exhumation affecting the PB during renewed convergence following a tectonically quiescent period between ca. 1020-980 Ma (Rivers, 2008, 2009, 2015) is inconsistent with data produced for this study.
6. Data for this study support the characterization of the Rigolet phase as the response of Laurentian to foreland-directed ductile flow of hot, melt-weakened mid-crust driven by post-convergent gravitational spreading beneath the orogenic

plateau. It is recommended that the Rigolet phase be redefined to reflect the continuity between the Ottawan and Rigolet phases as the early convergent and post-convergent phases of a continuous process defining the Grevillian Orogeny *sensu stricto*.

Reference List

Andersen, T. 2002. Correction of common lead in U-Pb analyses that do not report 204Pb. Chemical Geology, **192**: 59–79. doi:10.1016/S0009-2541(02)00195-X.

Aranovich, L.Y., and Berman, R.G. 1996. Optimized standard state and solution properties of minerals. Contributions to Mineralogy and Petrology, **126**: 25–37. doi:10.1007/s004100050233.

Austrheim, H., Putnis, C. V., Engvik, A.K., and Putnis, A. 2008. Zircon coronas around Fe-Ti oxides: A physical reference frame for metamorphic and metasomatic reactions. Contributions to Mineralogy and Petrology, **156**: 517–527. doi:10.1007/s00410-008-0299-8.

Baldwin, J.A., Bowring, S.A., and Williams, M.L. 2003. Petrological and geochronological constraints on high pressure, high temperature metamorphism in the Snowbird tectonic zone, Canada. Journal of Metamorphic Geology, **21**: 81–98. doi:10.1046/j.1525-1314.2003.00413.x.

Beaumont, C., Nguyen, M.H., Jamieson, R.A., and Ellis, S. 2006. Crustal flow modes in large hot orogens. Geological Society, London, Special Publications, **268**: 91–145. doi:10.1144/gsl.sp.2006.268.01.05.

Beaumont, C., Jamieson, R., and Nguyen, M. 2010. Models of large, hot orogens containing a collage of reworked and accreted terranes. Canadian Journal of Earth Sciences, **47**: 485–515.

Berman, R.G., Aranovich, L.Y., Rancourt, D.G., and Mercier, P.H.J. 2007. Reversed phase equilibrium constraints on the stability of Mg-Fe-Al biotite. American Mineralogist, **92**: 139–150. doi:10.2138/am.2007.2051.

Berman, R.G., and Aranovich, L.Y. 1996. Optimized standard state and solution properties of minerals .1. Model calibration for olivine, orthpyroxene, cordierite, garnet, ilmenite in the system FeO-MgO-CaO-Al_2O_3-TiO_3-SiO_2. Contributions to Mineralogy and Petrology, **126**: 1–24. doi:10.1007/s004100050233.

Berman, R., Aranovich, L., and Pattison, D. 1995. Reassessment of the garnet-clinopyroxene Fe− Mg exchange thermometer: II. Thermodynamic analysis. Contributions to Mineralogy and Petrology, **119**: 30–42. doi:10.1007/BF00310715.

Berman, R.G. 1990. Mixing properties of Ca-Mg-Fe-Mn garnets. American Mineralogist, **75**: 328–344.

Berman, R.G. 1991. Thermobarometry using multi-equilibrium calculations: a new technique, with petrological applications. Canadian Mineralogist, **29**: 833–855.

Berman, R.G. 2007. WinTWQ (version 2.3) a software package for performing internally-consistent thermobarometric calculations. Open File 5462. Geological Survey of Canada. doi:10.4095/223425.

Bethune, K.M. 1989. Deformation, metamorphism, diabase dykes, and the Grenville Front southwest of Sudbury, Ontario. *In* Current Research, Part C., 89-1C, Geological Survey of Canada. pp. 19–28.

Bethune, K.M. 1993. Evolution of the Grenville Front in the Tyson Lake area, southwest of Sudbury, Ontario, with emphasis on the tectonic significance of the Sudbury diabase dykes. Unpublished PhD thesis, Queen's University, Kingston, Ontario, Canada. 263 p.

Bethune, K.M. 1997. The Sudbury dyke swarm and its bearing on the tectonic development of the Grenville Front, Ontario, Canada. Precambrian Research, **85**: 117–146. doi:10.1016/S0301-9268(96)00052-6.

Bethune, K.M., and Davidson, A. 1988. Diabase dykes and the Grenville Front southwest of Sudbury, Ontario. *In* Current Research, Part A., 88-1C, Geological Survey of Canada. pp. 151–159.

Bethune, K.M., and Davidson, A. 1997. Grenvillian Metamorphism of the Sudbury diabase dyke-swarm: from protolithe to two-pyroxene - garnet coronite. The Canadian Mineralogist, **35**: 1191–1220.

Bhattacharya, A., Mohanty, L., Maji, A., Sen, S.K., and Raith, M. 1992. Non-ideal mixing in the phlogopite-annite binary: constraints from experimental data on Mg-Fe partitioning and a reformulation of the biotite-garnet geothermometer. Contributions to Mineralogy and Petrology, **111**: 87–93. doi:10.1007/BF00296580.

Bingen, B., Austrheim, H., and Whitehouse, M. 2001. Ilmenite as a source for zirconium in high-grade metamorphism? Textural evidence from the Caledonides of Western Norway and implications for zircon geochronology. Journal of Petrology, **42**: 355–375.

Blonde, J.A. 1996. Petrology and Metamorphism of Nipissing Diabase of May Township, Ontario. Unpublished MSc thesis, Carleton University, Ottawa, 160 p.

Breemen, O. van, and Corriveau, L. 2005. U–Pb age constraints on arenaceous and volcanic rocks of the Wakeham Group, eastern Grenville Province. Canadian Journal of Earth Sciences, **42**: 1677–1697. doi:10.1139/e05-079.

Brown, R.L., and Gibson, H.D. 2006. An argument for channel flow in the southern Canadian Cordillera and comparison with Himalayan tectonics. Geological Society, London, Special Publications, **268**: 543–559. doi:10.1144/GSL.SP.2006.268.01.25.

Buchan, K.L., Mortensen, J.K., Card, K.D., and Percival, J.A. 1998. Paleomagnetism and U-Pb geochronology of diabase dyke swarms of Minto block, Superior Province, Quebec, Canada. Canadian Journal of Earth Sciences, **35**: 1054–1069.

Carr, S.D., Easton, R.M., Jamieson, R.A., and Culshaw, N.G. 2000. Geological transect across the Grenville orogen of Ontario and New York. Canadian Journal of Earth Sciences, **37**: 193–216.

Colpron, M., Warren, M.J., and Price, R.A. 1998. Selkirk fan structure, southeastern Canadian Cordillera: Tectonic wedging against an inherited basement ramp. Geological Society of America Bulletin, **110**: 1060–1074.

Condie, K.C., Bobrow, D.J., and Card, K.D. 1987. Geochemistry of Precambrian mafic dykes from the southern Superior Province of the Canadian Shield. In Mafic Dyke Swarms. Edited by H.C. Halls and W.F. Fahrig. Geological Association of Canada Special Paper 34. pp. 95–108.

Connolly, J.A.D. 2005. Computation of phase equilibria by linear programming: A tool for geodynamic modeling and its application to subduction zone decarbonation. Earth and Planetary Science Letters, **236**: 524–541. doi:10.1016/j.epsl.2005.04.033.

Connolly, J.A.D. 1990. Multi-variable phase diagrams: an algorithm based on generalized thermodynamics. Journal of Science, **290**: 666–718.

Corfu, F., and Andrews, A.J. 1986. A U–Pb age for mineralized Nipissing diabase, Gowganda, Ontario. Canadian Journal of Earth Sciences, **23**: 107–109. doi:10.1139/e86-011.

Corfu, F., Hanchar, J.M., Hoskin, P.W.O., and Kinny, P. 2003. Atlas of Zircon Textures. Reviews in Mineralogy and Geochemistry, **53**: 469–500. doi:10.2113/0530469.

Corrigan, D. 1990. Geology and U-Pb Geochronology of the Key Harbour Area, Britt Domain, Southwest Grenville Province. Unpublished MSc Thesis, Dalhousie University. 165 p.

Corrigan, D., Culshaw, G., and Mortensen, J.K. 1994. Pre-Grenvillian evolution and Grenvillian overprinting of the Parautochthonous Belt in Key Harbour, Ontario : U-Pb and field constraints. Canadian Journal of Earth Sciences, **31**: 583–596. doi:10.1139/e94-051.

Culshaw, N.G., Davidson, A., and Nadeau, L. 1983. Structural subdivisions of the Grenville Province in the Parry Sound-Algonquin region, Ontario. *In* Geological Survey of Canada 83-1B. pp. 243–252.

Culshaw, N.G., Corrigan, D., Drage, J., and Wallace, P. 1988. Georgian Bay geological synthesis, Key Harbour to Dillon, Grenville Province of Ontario. *In* Current Research Part C. Geological Survey of Canada. pp. 129–134.

Culshaw, N.G., Corrigan, D., Jamieson, R.A., Ketchum, J.W.F., Wallace, P., and Wodicka, N. 1991. Traverse of the Central Gneiss Belt, Grenville Province, Georgian Bay. Field Guide B3, Geological Association of Canada, Toronto, Ontario. 32p.

Culshaw, N.G., Corrigan, D., Ketchum, J.W.F., Wallace, P. and Wodicka, N. 2004. Precambrian geology, Key Harbour area; Ontario Geological Survey, Preliminary Map P.3548, scale 1:50000.

Culshaw, N.G., Corrigan, D., Ketchum, J.W.F., Wallace, P. and Wodicka, N. 2004. Precambrian geology, Naiscoot area; Ontario Geological Survey, Preliminary Map P.3549, scale 1:50000.

Culshaw, N.G., Jamieson, R.A., Ketchum, J.W.F., Wodicka, N., Corrigan, D., and Reynolds, P.H. 1997. Transect along the northwestern Grenville orogen, Georgian Bay, Ontario: polystage convergence and extension in the lower orogenic crust. Tectonics, **16**: 966–982.

Culshaw, N.G., Ketchum, J.W.F., Wodicka, N., and Wallace, P. 1994. Deep crustal ductile extension following thrusting in the southwestern Grenville Province, Ontario. Canadian Journal of Earth Sciences, **31**: 160–175. doi:10.1139/e94-013.

Culshaw, N., and Dostal, J. 1997. Sand Bay gneiss association, Grenville Province, Ontario: a Grenvillian rift- (and -drift) assemblage stranded in the Central Gneiss Belt? Precambrian Research, **85**: 97–113. doi:10.1016/S0301-9268(97)00036-3.

Davidson, A. 2008. Late Paleoproterozoic to mid-Neoproterozoic history of northern Laurentia: An overview of central Rodinia. Precambrian Research, **160**: 5–22. doi:10.1016/j.precamres.2007.04.023.

Davidson, A., and Bethune, K.M. 1988. Geology of the north shore of Georgian Bay, Grenville Province of Ontario. *In* Current Research, Part C, 88-1C, Geological Survey of Canada, pp. 135-144.

Davidson, A., and van Breemen, O. 1988. Baddeleyite-zircon relationships in coronitic metagabbro, Grenville Province, Ontario: Implications for geochronology. Contributions to Mineralogy and Petrology, **100**: 291–299. doi:10.1007/BF00379740.

Davidson, A., and van Breemen, O. 1994. U-Pb ages of granites near the Grenville Front. In Radiogenic Age and Isotope Studies: Report 8. Geological Survey of Canada. Paper, 1994-F, 1-8.

Davidson, A., and van Breemen, O. 2001. Baddeleyite U-Pb age of metadiabase near Key Harbour, Britt domain, Grenville Province, Ontario; Radiogenic age and isotopic studies: Report 14. Geological Survey of Canada, Current Research 2001-F7, 6 p. doi:10.4095/212674.

de Capitani, C., and Brown, T.H. 1987. The computation of chemical equilibrium in complex systems containing non-ideal solutions. Geochimica et Cosmochimica Acta, **51**: 2639–2652. doi:10.1016/0016-7037(87)90145-1.

de Capitani, C., and Petrakakis, K. 2010. The computation of equilibrium assemblage diagrams with Theriak/Domino software. American Mineralogist, **95**: 1006–1016. doi:10.2138/am.2010.3354.

Dolivo-Dobrovolsky, D. 2016. PTQuick, a ©MS Windows program for the estimation of equilibrium parameters for mineral parageneses using methods of classical thermobarometry. www.dimadd.ru/en/Programs/ptquick. (accessed Sept. 2016)

Dudàs, F.O., Davidson, A., and Bethune, K.M. 1994. Age of the Sudbury diabase dykes and their metamorphism in the Grenville Province, Ontario. *In* Radiogenic Age and Isotopic Studies: Report 8. Geological Survey of Canada. pp. 97-106.

Essene, E.J. 1989. The current status of thermobarometry in metamorphic rocks. Geological Society, London, Special Publications, **43**: 1–44. doi:10.1144/GSL.SP.1989.043.01.02.

Fuhrman, M.L., and Lindsley, D.H. 1988. Ternary-feldspar modeling and thermometry. American Mineralogist, **73**: 201–215.

Gower, C.F., and Krogh, T.E. 2002. A U–Pb geochronological review of the Proterozoic history of the eastern Grenville Province. Canadian Journal of Earth Sciences, **39**: 795–829. doi:10.1139/e01-090.

Gower, C.F., Kamo, S.L., Kwok, K., and Krogh, T.E. 2008. Proterozoic southward accretion and Grenvillian orogenesis in the interior Grenville Province in eastern Labrador: Evidence from U-Pb geochronological investigations. Precambrian Research, **165**: 61–95. doi:10.1016/j.precamres.2008.06.007.

Graham, C.M., and Powell, R. 1984. A garnet - hornblende gethermometer: Calibration, testing, and application to the Pelona Schist, Southern California. Journal of Metamorphic Geology, **2**: 13–31.

Grant, S.M. 1989. Tectonic implications from sapphirine-bearing lithologies, south-west Grenville Province, Canada. Journal of Metamorphic Geology, **7**: 583–598. doi:10.1111/j.1525-1314.1989.tb00620.x.

Grujic, D., Hollister, L.S., and Parrish, R.R. 2002. Himalayan metamorphic sequence as an orogenic channel: Insight from Bhutan. Earth and Planetary Science Letters, **198**: 177–191. doi:10.1016/S0012-821X(02)00482-X.

Haggart, M.J., Jamieson, R.A., Reynolds, P.H., Krogh, T.E., Beaumont, C., and Culshaw, N.G. 1993. Last gasp of the Grenville orogeny: Thermochronology of the Grenville Front tectonic zone near Killarney, Ontario. Journal of Geology, **101**: 575–589.

Harley, S.L. 1984a. An experimental study of the partitioning of Fe and Mg between garnet and orthopyroxene. Contributions to Mineralogy and Petrology, **86**: 359–373. doi:10.1007/BF01187140.

Harley, S.L. 1984b. The solubility of alumina in orthopyroxene coexisting with garnet in FeO-MgO-Al_2O_3-SiO_2 and CaO-FeO-MgO-Al_2O_3-SiO_2. Journal of Petrology, **25**: 665–696. doi:10.1093/petrology/25.3.665.

Harley, S.L. 1984. Comparison of the garnet-orthopyroxene geobarometer with recent experimental studies, and applications to natural assemblages. Journal of Petrology, 25: 697–712. doi:10.1093/petrology/25.3.697.

Heaman, L.M., and LeCheminant, A.N. 1993. Paragenesis and U-Pb systematics of baddeleyite (ZrO_2). Chemical Geology, **110**: 95–126. doi:10.1016/0009-2541(93)90249-I.

Hodges, K. V., and McKenna, L.W. 1987. Realistic propagation of uncertainties in geologic thermobarometry. American Mineralogist, **72**: 671–680.

Hoffman, P.F. 1991. Did the breakout of Laurentia turn Gondwanaland inside-out? Science, 252: 1409–1412.

Holdaway, M.J. 2000. Application of new experimental and garnet Margules data to the garnet-biotite geothermometer. American Mineralogist, **85**: 881–892. doi:10.2138/am-2000-0701.

Ireland, T.R., and Williams, I.S. 2003. Considerations in zircon geochronology by SIMS. Reviews in Mineralogy and Geochemistry, **53**: 215–241. doi:10.2113/0530215.

Jamieson, R.A., Beaumont, C., Nguyen, M.H., and Culshaw, N.G. 2007. Synconvergent ductile flow in variable-strength continental crust: Numerical models with application to the western Grenville orogen. Tectonics, **26**. doi:10.1029/2006TC002036.

Jamieson, R.A., Beaumont, C., Warren, C.J., and Nguyen, M.H. 2010. The Grenville Orogen explained? Applications and limitations of integrating numerical models with geological and geophysical data. Canadian Journal of Earth Sciences, **47**: 517–539.

Jamieson, R.A., Culshaw, N.G., and Corrigan, D. 1995. Northwest Propegation of the Grenville Orogen: Grenvillian structure and metamorphism near Key Harbour, Georgian Bay, Ontario, Canada. Journal of Metamorphic Geology, **13**: 185–207.

Jamieson, R.A., Culshaw, N.G., Wodicka, N., Corrigan, D., and Ketchum, J.W.F. 1992. Timing and tectonic setting of Grenvillian metamorphism - Constraints from a transect along Georgian Bay, Ontario. Journal of Metamorphic Geology, **10**: 321–332. doi:10.1111/j.1525-1314.1992.tb00087.x.

Kamo, S.L., Krogh, T.E., and Kumarapeli, P.S. 1995. Age of the Grenville dyke swarm, Ontario-Quebec: Implications for the timing of lapetan rifting -. Canadian Journal of Earth Sciences, **32**: 273–280.

Ketchum, J.W.F. 1994. Extentional shear zones and lithotectonic domains in the southwest Grenville orogen: structure, metamorphism, and U–Pb geochronology of the Central Gneiss Belt near Pointe-au-Baril, Ontario. Unpublished PhD thesis, Dalhousie University, Halifax, N.S, Canada. 341 p.

Ketchum, J.W.F., and Davidson, A. 2000. Crustal architecture and tectonic assembly of the Central Gneiss Belt, southwestern Grenville Province, Canada: A new interpretation. Canadian Journal of Earth Sciences, **37**: 217–234. doi:10.1139/cjes-37-2-3-217.

Ketchum, J.W.F., Heaman, L.M., Krogh, T.E., Culshaw, N.G., and Jamieson, R.A. 1998. Timing and thermal influence of late orogenic extension in the lower crust: a U-Pb geochronological study from the southwest Grenville orogen, Canada. Precambrian Research, **89**: 25–45. doi:10.1016/S0301-9268(97)00079-X.

Ketchum, J.W.F., Jamieson, R.A., Heaman, L.M., Culshaw, N.G., and Krogh, T.E. 1994. 1.45 Ga granulite in the southwest Grenville Province: Geological setting, P-T conditions, and U-Pb geochronology. Geology, **22**: 215–218.

Ketchum, J.W.F., and Krogh, T.E. 1997. U–Pb constraints on high-pressure metamorphism in the Central Gneiss Belt, southwestern Grenville orogen. *In* Geological Association of Canada – Mineralogical Association of Canada, Program with Abstracts volume 22. p. A78.

Ketchum, J.W.F., and Krogh, T.E. 1998. U–Pb constraints on high-pressure metamorphism in the southwestern Grenville orogen. *In* Goldschmidt Conference 1998, Abstracts volume, Mineralogical Magazine, **62A**. pp. 775–776.

Ketchum, J.W.F., Wodicka, N., Culshaw, N.G., and Jamieson, R.A. 1999. Polystage convergence and extension in the mid- to lower orogenic crust: an examination of the Central Gneiss Belt, Grenville Province, along Georgian Bay. Field Trip B10 Guidebook, Geological Association of Canada, Sudbury, Ontario. 65 p.

Kleemann, U., and Reinhardt, J. 1994. Garnet-biotite thermometry revisited: the effect of Al(VI) and Ti in biotite. European Journal of Mineralogy, **85**: 925–941.

Kohn, J., and Spear, F. 1990. Two new geobarometers for garnet amphibolites, with applications to southeastern Vermont. The American Mineralogist, **75**: 89–96.

Krogh Ravna, E.J. 1988. The garnet-clinopyroxene Fe-Mg geothermometer - a reinterpretation of existing experimental data. Contributions to Mineralogy and Petrology, **99**: 44–48. doi:10.1007/BF00399364.

Krogh Ravna, E.J.. 2000. The garnet-clinopyroxene Fe^{2+}-Mg geothermometer: An updated calibration. Journal of Metamorphic Geology, **18**: 211–219. doi:10.1046/j.1525-1314.2000.00247.x.

Krogh Ravna, E.J. 2000. Distribution of Fe^{2+} and Mg between coexisting garnet and hornblende in synthetic and natural systems: An empirical calibration of the garnet-hornblende Fe-Mg geothermometer. Lithos, **53**: 265–277. doi:10.1016/S0024-4937(00)00029-3.

Krogh, T.E. 1982. Improved accuracy of U-Pb zircon ages by the creation of more concordant systems using an air abrasion technique. Geochimica et Cosmochimica Acta, **46**: 637–649. doi: 10.1016/0016-7037(82)90165-X.

Krogh, T.E. 1994. Precise U-Pb ages for Grenvillian and pre-Grenvillian thrusting of Proterozoic and Archean metamorphic assemblages in the Grenville Front tectonic zone, Canada. Tectonics, **13**: 963–982.

Krogh, T.E., Corfu, F., Davis, D.W., Dunning, G.R., Heaman, L.M., Kamo, S.L., Machado, N., Greenough, J.D., and Nakamura, E. 1987. Precise U-Pb isotopic ages of diabase dykes and mafic to ultramafic rocks using trace amounts of baddeleyite and zircon. *In* Mafic Dyke Swarms. *Edited by* H.C. Halls and W.F. Fahrig. Geological Association of Canada, Special Paper 34. pp. 147–152.

Krogh, T., Gower, C., and Wardle, R. 1996. Pre-Labradorian crust and later Labradorian, Pinwarian and Grenvillian metamorphism in the Mealy Mountains terrane, Grenville Province, eastern Labrador, paper presented at Proterozoic Evolution in the North Atlantic Realm COPENA-ECSOOT-IBTA conference, Goose Bay, Labrador. pp. 106–107.

Kylander-Clark, A.R.C., Hacker, B.R., and Cottle, J.M. 2013. Laser-ablation split-stream ICP petrochronology. Chemical Geology, **345**: 99–112. doi:10.1016/j.chemgeo.2013.02.019.

Leake, B.E. 1997. Nomenclature of Amphiboles: Report of the Subcommittee on Amphiboles of the International Mineralogical Association Commission on New Minerals and Mineral Names. Mineralogical Magazine, **61**: 295–321. doi:10.1180/minmag.1997.061.405.13.

Lightfoot, P.C., Souza, H.D., and Doherty, W. 1993. Differentiation and source of the Nipissing Diabase intrusions, Ontario, Canada. Canadian Journal of Earth Sciences, **30**: 1123–1140. doi:10.1139/e93-095.

Ludwig, K.R. 2012. Users manual for Isoplot version 4.15. A geochronological toolkit for Microsoft Excel. Berkeley Geochronology Center, Special Publication 5. Available from http://www.bgc.org/isoplot_etc/isoplot.html.

Marsh, J.H., and Culshaw, N.G. 2014. Timing and conditions of high-pressure metamorphism in the western Grenville Province: Constraints from accessory mineral composition and phase equilibrium modeling. Lithos, **200–201**: 402–417. doi:10.1016/j.lithos.2014.04.016.

Mattinson, J.M. 2005. Zircon U-Pb chemical abrasion ("CA-TIMS") method: Combined annealing and multi-step partial dissolution analysis for improved precision and accuracy of zircon ages. Chemical Geology, **220**: 47–66. doi:10.1016/j.chemgeo.2005.03.011.

McDonough, W.F., and Sun, S-S. 1995. The composition of the Earth. Chemical Geology, **120**: 223–253. doi:10.1016/0009-2541(94)00140-4.

Moore, J.M., and Thompson, H. 1980. The Flinton Group: A late Precambrian metasedimentary succession in the Grenville Province of eastern Ontario. Canadian Journal of Earth Sciences, **17**: 1685–1707. doi:10.1139/e80-178.

Nakamura, D. 2009. A new formulation of garnet-clinopyroxene geothermometer based on accumulation and statistical analysis of a large experimental data set. Journal of Metamorphic Geology, **27**: 495–508. doi:10.1111/j.1525-1314.2009.00828.x.

Newton, R.C., and Perkins, D. 1982. Thermodynamic calibration of geobarometers based on the assemblages garnet - plagioclase - orthopyroxene (clinopyroxene) - quartz. American Mineralogist, **67**: 203–222.

Noble, S.R., and Lightfoot, P.C. 1992. U-Pb baddeleyite ages of the Kerns and Triangle Mountain intrusions, Nipissing Diabase, Ontario. Canadian Journal of Earth Sciences, **29**: 1424–1429.

Parrish, R.R. 1995. Thermal evolution of the southeastern Canadian Cordillera. Canadian Journal of Earth Sciences, **32**: 1618–1642. doi:10.1139/e95-130.

Parrish, R.R. 2003. Zircon U-Th-Pb geochronology by isotope dilution - thermal ionization mass spectrometry (ID-TIMS). Reviews in Mineralogy and Geochemistry, **53**: 183–213. doi:10.2113/0530183.

Pattison, D.R.M. 2003. Petrogenetic significance of orthopyroxene-free garnet + clinopyroxene + plagioclase +- quartz-bearing metabasites with respect to the amphibolite and granulite facies. Journal of Metamorphic Geology, **21**: 21–34. doi:10.1046/j.1525-1314.2003.00415.x.

Powell, R. 1985. Geothermometry and geobarometry: A discussion. Journal of the Geological Society, **142**: 29–38. doi:10.1144/gsjgs.142.1.0029.

Powell, R. 1985. Regression diagnostics and robust regression in geothermometer / geo barometer calibration: the garnet-clinopyroxene geothermometer revisited. Journal of Metamorphic Geology, **3**: 231–243. doi:10.1111/j.1525-1314.1985.tb00319.x.

Powell, R., Holland, T., and Worley, B. 1998. Calculating phase diagrams using solid solutions via non-linear equations, with examples using THERMOCALC. Journal of Metamorphic Geology, **16**: 577–588.

Powell, R., and Holland, T. 1994. Optimal geothermometry and geobarometry. American Mineralogist, **79**: 120–133.

Powell, R., and Holland, T.J.B. 2008. On thermobarometry. Journal of Metamorphic Geology, **26**: 155–179.

Powell, R., and Holland, T. 2010. Using Equilibrium Thermodynamics to Understand Metamorphism and Metamorphic Rocks. Elements, **6**: 309–314. doi:10.2113/gselements.6.5.309.

Rivers, T. 1997. Lithotectonic elements of the Grenville Province: Review and tectonic implications. Precambrian Research, **86**: 117–154. doi:10.1016/S0301-9268(97)00038-7.

Rivers, T. 2008. Assembly and preservation of lower, mid, and upper orogenic crust in the Grenville Province - Implications for the evolution of large hot long-duration orogens. Precambrian Research, **167**: 237–259. doi:10.1016/j.precamres.2008.08.005.

Rivers, T. 2009. The Grenville Province as a large hot long-duration collisional orogen - Insights from the spatial and thermal evolution of its orogenic fronts. Geological Society, London, Special Publications, **327**: 405–444. doi:10.1144/sp327.17.

Rivers, T., and Corrigan, D. 2000. Convergent margin on southeastern Laurentia during the Mesoproterozoic: tectonic implications. Canadian Journal of Earth Sciences, **37**: 359–383. doi:10.1139/e99-067.

Rivers, T., Culshaw, N.G., Hynes, A., Indares, A., Jamieson, R.A., and Martignole, J. 2012. The Grenville Orogen - A post-lithoprobe perspective. *In* Tectonic Styles in Canada: The Lithoprobe Perspective. *Edited by* J.A. Percival, F.A. Cook, and R.M. Clowes. Geological Association of Canada, Special Paper 49. pp. 97–236.

Rivers, T., Martignole, J., Gower, C.F., and Davidson, A. 1989. New tectonic divisions of the Grenville Province, southern Canadian Shield. Tectonics, **8**: 63–84.

Rivers, T. 2012. Upper-crustal orogenic lid and mid-crustal core complexes: signatures of a collapsed orogenic plateau in the hinterland of the Grenville Province. Canadian Journal of Earth Sciences, **49**: 1–42. doi:10.1139/e11-014.

Rivers, T., and Schwerdtner, W. 2015. Post-peak evolution of the Muskoka Domain, western Grenville Province: Ductile detachment zone in a crustal-scale metamorphic core complex. Geoscience Canada, **42**: 403–436. doi:10.12789/geocanj.2015.42.080.

Schneider, C.A., Rasband, W.S., and Eliceiri, K.W. 2012. NIH Image to ImageJ: 25 years of image analysis. Nature Methods, **9**: 671–675. doi:10.1038/nmeth.2089.

Schoene, B. 2014. U–Th–Pb Geochronology. *In* Treatise on Geochemistry. Elsevier. pp. 341–378. doi:10.1016/B978-0-08-095975-7.00310-7.

Schumacher, J.C. 1991. Empirical ferric iron corrections: Necessity, assumptions, and effects on selected geothermobarometers. Mineralogical Magazine, **55**: 3–18. doi:10.1180/minmag.1991.055.378.02.

Schwerdtner, W.M., Rivers, T., Tsolas, J., Waddington, D.H., Page, S., and Yang, J. 2016. Transtensional origin of multi-order cross-folds in a high-grade gneiss complex, southwestern Grenville Province: Formation during post-peak gravitational collapse. Canadian Journal of Earth Sciences, **53**: 1511–1538. doi:10.1139/cjes-2015-0212.

Sengupta, P., Dasgupta, S., Bhattacharya, P.K., and Hariya, Y. 1989. Mixing behavior in quaternary garnet solid solution and an extended Ellis and Green garnet-clinopyroxene geothermometer. Contributions to Mineralogy and Petrology, **103**: 223–227. doi:10.1007/BF00378508.

Seymour, K.S., and Kumarapeli, S.P. 1995. Geochemistry of the Grenville dyke swarm: Role of plume-source mantle in magma genesis. Contributions to Mineralogy and Petrology, **120**: 29–41. doi:10.1007/BF00311006.

Slagstad, T., Culshaw, N.G., Jamieson, R.A., and Ketchum, J.W.F. 2004. Early Mesoproterozoic tectonic history of the southwestern Grenville Province, Ontario: Constraints from geochemistry and geochronology of high-grade gneisses. *Edited by* R.P. Tollo, J. McLelland, L. Corriveau, and M.J. Bartholomew. *In* Proterozoic Tectonic Evolution of the Grenville Orogen. Geological Society of America Memoir 197. pp. 209–241. doi:10.1130/0-8137-1197-5.209.

Spear, F.S. 1993. Metamorphic Phase Equilibria and Pressure-Temperature-Time Paths. Mineralogical Society of America, Monograph Series. 799 p.

Tera, F., and Wasserburg, G.J. 1972. U-Th-Pb systematics in three Apollo 14 basalts and the problem of initial Pb in lunar rocks. Earth and Planetary Science Letters, **14**: 281–304. doi:10.1016/0012-821X(72)90128-8.

Tera, F., and Wasserburg, G.J. 1972. U-Th-Pb systematics in lunar highland samples from the Luna 20 and Apollo 16 missions. Earth and Planetary Science Letters, **17**: 36–51. doi:10.1016/0012-821X(72)90257-9.

Tohver, E., Teixeira, W., van der Pluijm, B., Geraldes, M.C., Bettencourt, J.S., and Rizzotto, G. 2006. Restored transect across the exhumed Grenville orogen of Laurentia and Amazonia, with implications for crustal architecture. Geology, **34**: 669. doi:10.1130/G22534.1.

Tollo, R.P., Corriveau, L., McLelland, J., and Bartholomew, M.J. 2004. Proterozoic tectonic evolution of the Grenville orogen in North America: An introduction. *Edited by* R.P. Tollo, J. McLelland, L. Corriveau, and M.J. Bartholomew. *In* Proterozoic Tectonic Evolution of the Grenville Orogen. Geological Society of America Memoir 197. pp. 1–18. doi:10.1130/0-8137-1197-5.1.

Tuccillo, M.E., Mezger, K., Essene, E.J., and van der Pluijm, B.A. 1992. Thermobarometry, geochronology and the interpretation of P-T-t data in the Britt domain, Ontario Grenville Orogen, Canada. Journal of Petrology, **33**: 1225–1259. doi:10.1093/petrology/33.6.1225.

van Breemen, O., Davidson, A., Loveridge, W.D., and Sullivan, R.W. 1986. U-Pb zircon geochronology of Grenville tectonites, granulites and igneous precursors, Parry Sound, Ontario. *Edited by* Moore, J.M., Davidson, A., Baer, A.J. *In* The Grenville Province. Geological Association of Canada, Special Paper 31. pp. 191–207.

van Breemen, O., and Davidson, A. 1988. Northeast extension of Proterozoic terranes of mid-continental North America. Geological Society of America Bulletin, **100**: 630–638. doi:10.1130/0016-7606(1988).

van Breemen, O., and Davidson, A. 1990. U-Pb zircon and baddeleyite ages from the Central Gneiss Belt, Ontario. In Radiogenic Age and Isotope Studies: Report 3. Geological Survey of Canada. pp. 85–92.

van Rooyen, D., and Carr, S.D. 2016. Deconstructing the infrastructure: A complex history of diachronous metamorphism and progressive deformation during the late Cretaceous to Eocene in the Thor-Odin-Pinnacles area of southeastern British Columbia. Geoscience Canada, **43**: 103–122.

van Schmus, W.R. 1980. Chronology of igneous rocks associated with the Penokean orogeny in Wisconsin. *Edited by* G.B. Morey and G.N. Hanson. *In* Selected studies of Archean gneisses and lower Proterozoic rocks, southern Canadian Shield: Geological Society of America Special Paper 182. pp. 159–168. doi:10.1130/SPE182-p159.

Wetherill, G.W. 1956. Discordant uranium-lead ages, I. Transactions, American Geophysical Union, **37**: 320. doi:10.1029/TR037i003p00320.

White, D.J., Forsyth, D.A., Asudeh, I., Carr, S.D., Wu, H., Easton, R.M., and Mereu, R.F. 2000. A seismic-based cross-section of the Grenville Orogen in southern Ontario and western Quebec. Canadian Journal of Earth Sciences, **37**: 183–192. doi:10.1139/cjes-37-2-3-183.

Wynne-Edwards, H.R. 1972. The Grenville Province. *Edited by* R.A. Price and R.J.W. Douglas. *In* Variations in Tectonic Styles in Canada. Geological Association of Canada, Special Paper 11. pp. 263–334.

Appendix A. Table of Coordinates

Sudbury metadiabase key sample locations. UTM Zone 17, NAD 83

	Easting	*Northing*
GC14-057	518225	5081051
GC14-024	526568	5069122
GC14-048	539185	5043624

Appendix B. Whole-Rock Geochemistry, Major Elements

Sample (wt %)	SiO2	Al2O3	Fe2O3	MgO	CaO	Na2O	K2O	TiO2	P2O5	MnO	Cr2O3	LOI	Sum
GC14-001	44.7	15.52	16.82	6.8	7.92	2.74	1.09	2.9	0.59	0.22	0.011	0.4	99.71
GC14-001-duplicate	45.11	15.41	16.72	6.84	7.82	2.78	1.1	2.82	0.59	0.22	0.01	0.3	99.71
GC14-008	43.57	14.19	17.71	6.16	7.41	3.2	1.38	4.06	1.13	0.22	0.01	0.5	99.56
GC14-008-duplicate	43.37	14.23	17.87	6.2	7.45	3.21	1.39	4.04	1.14	0.22	0.009	0.4	99.55
GC14-009	44.6	15.56	16.3	5.9	7.63	3.27	1.3	3.57	1.11	0.23	0.013	0.1	99.59
GC14-011	46.58	17.48	11.63	7.59	9.88	3.01	0.51	1.8	0.15	0.16	0.008	0.9	99.67
GC14-024	43.9	13.68	18.28	4.9	7.75	3.57	1.81	3.94	1.78	0.28	<0.002	-0.4	99.54
GC14-046	46.06	17.05	12.83	7.22	8.91	3.19	0.64	1.92	0.3	0.17	0.009	1.4	99.66
GC14-048	46.26	16.98	13.91	6.63	8.49	3.36	1.05	2.44	0.39	0.18	0.006	-0.1	99.6
GC14-057	46.42	15.41	16.19	6.03	7.94	3.32	1.13	2.87	0.56	0.2	0.015	-0.4	99.7
GC14-058	44.55	16.16	16.23	5.24	7.37	3.47	1.21	3.18	0.97	0.2	0.01	1.1	99.66
GC14-060	46.62	15.22	16.73	5.67	7.94	2.75	1.19	2.95	0.6	0.21	0.007	-0.3	99.6
GC14-064a	46.72	15.03	16.56	5.45	9.72	2.73	0.49	2.04	0.36	0.24	0.002	0.4	99.73
GC14-079	47.38	14.89	16.13	5.56	7.72	3.27	1.23	2.79	0.6	0.2	0.017	-0.1	99.7
GC14-084a	46.64	14.86	16.39	5.6	7.62	3.4	1.28	3.1	0.65	0.21	0.014	-0.1	99.69
SV14-0503	43.44	14.27	18.98	4.95	6.92	3.42	1.6	4.46	1.09	0.25	0.004	0.3	99.68

Whole-Rock Geochemistry, Minor and Trace Elements

sample (ppm)	Ni	Sc	Ba	Be	Co	Cs	Ga	Hf	Nb	Rb	Sn	Sr	Ta	Th	U	V
GC14-001	102	27	594	<1	82.3	0.4	19.7	4.8	12.4	20.7	1	397.3	1.1	2.2	0.6	244
GC14-001-duplicate	107	27	615	<1	80.9	0.3	21	4.5	12.2	20.4	1	385.3	0.9	2.2	0.7	246
GC14-008	70	35	1071	3	66.7	0.2	20	5.1	14	15.5	<1	477.1	0.9	1.3	0.5	298
GC14-008-duplicate	69	35	1051	<1	68.1	0.2	19.9	4.7	13.7	15.2	1	476.1	1	1.4	0.3	301
GC14-009	83	26	964	2	72.5	0.2	19.1	3.3	11.4	13.3	<1	590.6	1	1	0.3	255
GC14-011	78	23	189	<1	71.4	<0.1	19.6	2.7	10.3	6.8	1	602.9	0.8	0.8	0.2	258
GC14-024	<20	28	1286	2	51.2	0.3	21.6	9.8	33.4	28.4	2	475.9	2.1	3.1	0.7	130
GC14-046	127	23	329	<1	72.6	0.1	19	3.3	6.1	6.7	<1	558	0.7	0.5	0.2	241
GC14-048	95	21	554	2	77.1	<0.1	19.7	4.6	13.3	13.8	1	763.1	1.1	1.2	0.4	249
GC14-057	83	28	601	2	71.4	0.3	20	4	11.8	21.5	1	402.2	0.9	1.9	0.6	273
GC14-058	45	27	829	2	61.6	0.3	19.9	4.2	13.9	18.4	1	561.3	0.9	1.7	0.4	311
GC14-060	77	26	822	2	77.2	0.4	20.3	5.2	12.7	19.9	<1	422.8	0.8	2	0.2	276
GC14-064a	<20	43	326	2	66.8	0.2	19.6	1.8	3	6.4	<1	394.8	0.5	0.6	0.1	463
GC14-079	63	30	678	1	70.9	0.4	21.2	5.3	12.2	22.5	1	399.1	0.9	2.4	0.7	248
GC14-084a	75	28	711	1	70.3	0.4	22.7	5.7	14.5	24.5	1	389	1	2.8	0.8	240
SV14-0503	28	27	789	<1	65	0.2	21.2	7.8	20	23.8	2	353.1	1.5	2.1	0.5	211

Whole-Rock Geochemistry, Minor and Trace Elements, cont.

sample (ppm)	W	Zr	Y	La	Ce	Pr	Nd	Sm	Eu	Gd	Tb	Dy	Ho	Er	Tm	Yb	Lu	TOT/C	TOT/S
GC14-001	211.2	194.6	33.1	22	51.6	6.9	30.8	6.82	2.05	7.06	1.11	6.25	1.19	3.38	0.48	3.03	0.49	<0.02	0.1
GC14-001-duplicate	211	188.5	31.7	23.5	53.6	6.82	29.7	6.75	2.14	6.61	1.08	6.07	1.15	3.37	0.49	3.04	0.49	<0.02	0.11
GC14-008	188	201.7	35.8	32.3	74.9	9.89	43	9.01	3.28	8.81	1.26	6.86	1.26	3.64	0.5	3.3	0.52	0.04	0.11
GC14-008-duplicate	192.4	202.8	35.5	31.9	72.5	9.72	45.7	8.82	3.13	8.7	1.25	6.69	1.29	3.83	0.52	3.39	0.5	0.04	0.11
GC14-009	193.8	154.1	25.2	26.1	59.6	8	36.9	7.35	2.63	6.59	0.96	5.07	0.97	2.61	0.36	2.38	0.35	0.04	0.1
GC14-011	212.3	103.4	13.2	11	27.7	3.72	16.8	3.76	1.35	3.74	0.59	3.26	0.52	1.48	0.17	1.17	0.17	0.11	0.13
GC14-024	137.6	421.4	68.4	55.2	130.7	17.5	80.1	16.24	4.69	16.28	2.42	12.94	2.57	6.99	1.02	6.13	0.99	<0.02	0.07
GC14-046	198.7	128.4	21.9	13.8	32.1	4.42	20.2	4.64	1.56	4.99	0.79	4.38	0.81	2.15	0.32	2.06	0.32	0.2	0.16
GC14-048	233.8	180.2	24.1	21.8	48.3	6.65	29.7	6.28	1.95	5.69	0.86	4.68	0.85	2.3	0.31	2	0.3	0.08	0.06
GC14-057	218.6	183.4	30.5	22.8	51.1	6.72	30.7	6.05	2.02	6.35	1	5.62	1.09	3.21	0.45	2.88	0.45	0.02	0.11
GC14-058	171.4	193.1	32.8	31.9	71.3	8.95	37.6	7.29	2.31	7.02	1.09	6.12	1.14	3.35	0.48	2.97	0.48	0.03	0.02
GC14-060	207.9	213.4	34	23.8	56.6	7.04	32.7	6.91	2.53	7.41	1.19	6.73	1.32	3.69	0.52	3.65	0.51	0.19	0.1
GC14-064a	216.6	64.2	26.9	10.7	26.6	3.78	18.6	4.65	1.68	5.04	0.88	5.42	1.04	3.25	0.42	2.78	0.43	0.07	0.21
GC14-079	187.6	209.1	32.6	25	57.8	7.57	33.3	7	2.23	6.88	1.09	6.11	1.16	3.39	0.47	3.11	0.48	0.03	0.13
GC14-084a	174.6	237	36.9	28.9	63.4	8.36	36.3	8.07	2.3	7.57	1.21	7.02	1.35	3.87	0.54	3.57	0.54	0.03	0.14
SV14-0503	167.2	328.9	50.8	34.2	80	11.02	49.6	10.85	3.21	10.93	1.74	9.45	1.82	5.55	0.8	4.95	0.76	0.03	0.04

Appendix C. Electron Microprobe Data: GC14-057, Key Harbour

GC14-057 : Garnet

Analysis	057_1_9	057_1_10	057_1_11	057_1_12	057_1_13	057_1_14	057_1_38	057_1_39	057_1_40
Oxide (wt%)									
SiO_2	38.53	38.53	38.48	38.80	38.82	38.78	38.88	38.64	38.57
TiO_2	0.06	0.01	0.05	0.03	0.04	0.05	0.02	0.04	0.04
Al_2O_3	21.91	21.97	22.21	21.68	22.18	21.95	21.71	22.03	21.89
Cr_2O_3	0.00	0.01	0.01	0.00	0.03	0.01	0.00	0.00	0.01
FeO	27.70	27.50	27.01	27.70	27.43	27.28	26.88	26.85	28.38
MnO	0.72	0.69	0.68	0.71	0.70	0.62	0.72	0.70	0.76
MgO	5.82	6.44	6.38	6.22	6.50	6.45	6.52	6.53	5.66
CaO	6.36	5.87	5.79	5.98	5.81	5.78	6.20	6.01	5.91
BaO	0.13	0.11	0.09	0.06	0.08	0.16	0.02	0.00	0.04
Na_2O	0.02	0.04	0.03	0.02	0.02	0.02	0.00	0.00	0.00
K_2O	0.04	0.02	0.04	0.03	0.03	0.04	0.01	0.03	0.02
Total	101.28	101.19	100.78	101.22	101.63	101.13	100.97	100.84	101.27
Cations p.f.u (O = 12)									
Si	2.978	2.974	2.974	2.994	2.977	2.988	2.998	2.981	2.984
Ti	0.004	0.001	0.002	0.002	0.002	0.002	0.001	0.002	0.002
Al	1.997	1.999	2.023	1.972	2.005	1.994	1.973	2.004	1.997
Cr	0.000	0.000	0.000	0.000	0.001	0.000	0.000	0.000	0.001
Fe	1.792	1.775	1.746	1.788	1.759	1.759	1.734	1.732	1.836
Mn	0.047	0.044	0.044	0.046	0.046	0.041	0.047	0.046	0.049
Mg	0.670	0.740	0.736	0.715	0.743	0.740	0.749	0.751	0.653
Ca	0.527	0.486	0.480	0.494	0.478	0.478	0.512	0.497	0.490
Ba	0.004	0.004	0.002	0.002	0.002	0.005	0.001	0.000	0.001
Na	0.002	0.005	0.005	0.002	0.004	0.002	0.000	0.000	0.000
K	0.005	0.002	0.004	0.004	0.002	0.004	0.001	0.002	0.002
Total	8.024	8.030	8.016	8.020	8.020	8.015	8.016	8.015	8.016

GC14-057 : Plagioclase

Analysis	057_1_19	057_1_20	057_1_21	057_1_22	057_1_23	057_1_24	057_1_25	057_1_26	057_1_35	057_1_36	057_1_37
Oxide (wt%)											
SiO_2	63.94	65.11	63.90	63.78	54.48	60.63	63.82	63.80	63.45	64.26	63.11
TiO_2	0.00	0.00	0.00	0.00	0.00	0.00	0.00	0.00	0.00	0.00	0.00
Al_2O_3	21.76	21.57	22.51	22.35	25.90	24.78	18.99	18.80	22.23	21.86	22.62
Cr_2O_3	0.00	0.00	0.00	0.00	0.00	0.00	0.00	0.00	0.00	0.00	0.00
FeO	0.23	0.26	0.32	0.39	4.56	0.05	0.04	0.00	0.17	0.26	0.12
MnO	0.00	0.00	0.00	0.00	0.00	0.00	0.00	0.00	0.00	0.00	0.00
MgO	0.00	0.00	0.00	0.00	0.42	0.00	0.00	0.00	0.00	0.00	0.00
CaO	2.75	2.53	3.29	3.26	5.39	6.07	0.08	0.10	3.48	2.92	3.91
BaO	0.00	0.00	0.00	0.00	0.00	0.00	1.17	1.03	0.00	0.00	0.00
Na_2O	10.00	10.05	9.62	9.62	7.55	8.08	1.42	1.29	9.41	9.78	8.99
K_2O	0.42	0.48	0.46	0.46	0.34	0.25	14.40	14.57	0.62	0.40	0.42
Total	99.10	100.00	100.10	99.86	98.64	99.87	99.93	99.58	99.36	99.48	99.16
Cations p.f.u (O = 8)											
Si	2.850	2.873	2.824	2.826	2.526	2.701	2.962	2.970	2.826	2.852	2.813
Ti	0.000	0.000	0.000	0.000	0.000	0.000	0.000	0.000	0.000	0.000	0.000
Al	1.143	1.122	1.172	1.167	1.416	1.301	1.039	1.031	1.167	1.144	1.189
Cr	0.000	0.000	0.000	0.000	0.000	0.000	0.000	0.000	0.000	0.000	0.000
Fe	0.008	0.010	0.012	0.014	0.177	0.002	0.002	0.000	0.006	0.010	0.005
Mn	0.000	0.000	0.000	0.000	0.000	0.000	0.000	0.000	0.000	0.000	0.000
Mg	0.000	0.000	0.000	0.000	0.030	0.000	0.000	0.000	0.000	0.000	0.000
Ca	0.131	0.119	0.156	0.154	0.268	0.290	0.004	0.005	0.166	0.139	0.186
Ba	0.000	0.000	0.000	0.000	0.000	0.000	0.022	0.019	0.000	0.000	0.000
Na	0.865	0.860	0.825	0.826	0.679	0.698	0.127	0.116	0.813	0.842	0.777
K	0.024	0.027	0.026	0.026	0.020	0.014	0.853	0.865	0.035	0.022	0.024
Total	5.022	5.011	5.015	5.016	5.116	5.006	5.009	5.006	5.014	5.010	4.994

GC14-057 : Clinopyroxene

Analysis	057_1_5	057_1_6	057_1_7	057_1_8	057_1_31	057_1_32	057_1_33	057_1_34	057_1_41	057_1_46	057_1_47	057_1_48
Oxide (wt%)												
SiO_2	51.91	52.42	51.99	52.31	52.65	52.67	52.28	52.71	51.71	52.34	52.50	51.53
TiO_2	0.16	0.13	0.18	0.17	0.13	0.15	0.16	0.03	0.27	0.20	0.33	0.27
Al_2O_3	4.80	5.67	4.68	4.92	4.96	3.29	5.26	4.69	4.58	3.21	2.20	4.04
Cr_2O_3	0.00	0.00	0.00	0.00	0.00	0.00	0.00	0.00	0.14	0.00	0.00	0.06
FeO	10.38	10.34	10.43	10.60	9.71	10.30	9.86	9.77	10.16	9.36	10.26	9.84
MnO	0.10	0.10	0.06	0.08	0.08	0.08	0.06	0.08	0.09	0.09	0.08	0.09
MgO	11.31	10.63	11.26	10.83	11.26	12.19	11.17	11.53	11.45	12.59	12.60	11.88
CaO	19.29	17.61	19.00	18.25	18.25	19.34	18.76	19.05	19.20	21.02	20.38	19.89
BaO	0.07	0.07	0.03	0.06	0.00	0.00	0.00	0.00	0.01	0.00	0.00	0.00
Na_2O	2.31	3.19	2.45	2.89	2.84	2.24	2.69	2.58	2.25	1.39	1.62	1.98
K_2O	0.01	0.01	0.02	0.02	0.01	0.01	0.01	0.01	0.02	0.00	0.01	0.07
Total	100.35	100.15	100.10	100.13	99.89	100.25	100.24	100.45	99.89	100.20	99.97	99.65
Cations p.f.u (O = 6)												
Si	1.933	1.946	1.939	1.949	1.955	1.961	1.939	1.951	1.933	1.948	1.966	1.933
Ti	0.005	0.004	0.005	0.005	0.004	0.004	0.005	0.001	0.008	0.005	0.010	0.007
Al	0.211	0.248	0.206	0.216	0.217	0.144	0.230	0.205	0.202	0.140	0.097	0.179
Cr	0.000	0.000	0.000	0.000	0.000	0.000	0.000	0.000	0.004	0.000	0.000	0.002
Fe	0.323	0.321	0.325	0.330	0.301	0.321	0.306	0.302	0.318	0.291	0.321	0.308
Mn	0.003	0.003	0.002	0.002	0.002	0.002	0.002	0.002	0.003	0.003	0.002	0.003
Mg	0.628	0.589	0.626	0.601	0.623	0.677	0.617	0.636	0.638	0.699	0.703	0.664
Ca	0.770	0.700	0.759	0.728	0.726	0.772	0.745	0.755	0.769	0.838	0.818	0.799
Ba	0.001	0.001	0.001	0.001	0.000	0.000	0.000	0.000	0.000	0.000	0.000	0.000
Na	0.167	0.229	0.178	0.209	0.205	0.161	0.194	0.185	0.163	0.101	0.117	0.144
K	0.001	0.001	0.001	0.001	0.001	0.001	0.001	0.001	0.001	0.000	0.001	0.004
Total	4.042	4.041	4.042	4.042	4.034	4.044	4.039	4.040	4.039	4.027	4.035	4.043

GC14-057 : Biotite

Analysis	057_1_15	057_1_16	057_1_17	057_1_18	057_1_43	057_1_44	057_1_45
Oxide (wt%)							
SiO_2	36.15	36.08	36.14	35.98	36.44	36.45	36.32
TiO_2	6.36	6.34	6.32	6.58	5.95	5.15	7.00
Al_2O_3	14.46	14.40	14.76	14.91	14.01	14.30	13.97
Cr_2O_3	0.02	0.00	0.00	0.00	0.04	0.03	0.03
FeO	13.76	14.57	13.97	14.76	16.86	15.66	16.96
MnO	0.00	0.03	0.00	0.02	0.02	0.00	0.00
MgO	14.32	13.48	14.14	13.55	12.54	13.51	11.94
CaO	0.05	0.05	0.09	0.08	0.01	0.01	0.02
BaO	1.32	1.11	1.05	1.25	0.40	0.32	0.35
Na_2O	0.03	0.01	0.07	0.05	0.14	0.12	0.09
K_2O	9.03	9.53	9.27	9.48	9.47	9.48	9.80
Total	95.49	95.61	95.81	96.64	95.88	95.04	96.47
Cations p.f.u (O = 22)							
Si	5.42	5.43	5.40	5.37	5.50	5.51	5.46
Ti	0.72	0.72	0.71	0.74	0.68	0.59	0.79
Al	2.56	2.56	2.60	2.62	2.49	2.55	2.48
Cr	0.00	0.00	0.00	0.00	0.00	0.00	0.00
Fe	1.73	1.83	1.75	1.84	2.13	1.98	2.13
Mn	0.00	0.00	0.00	0.00	0.00	0.00	0.00
Mg	3.20	3.03	3.15	3.01	2.82	3.04	2.67
Ca	0.01	0.01	0.02	0.01	0.00	0.00	0.00
Ba	0.08	0.07	0.06	0.07	0.02	0.02	0.02
Na	0.01	0.00	0.02	0.01	0.04	0.04	0.02
K	1.73	1.83	1.77	1.80	1.82	1.83	1.88
Total	15.45	15.48	15.48	15.49	15.51	15.56	15.46

BSE Image of GC14-057, Key Harbour

SmD, EMP analysis points. Numbers below are suffix to 057_1_

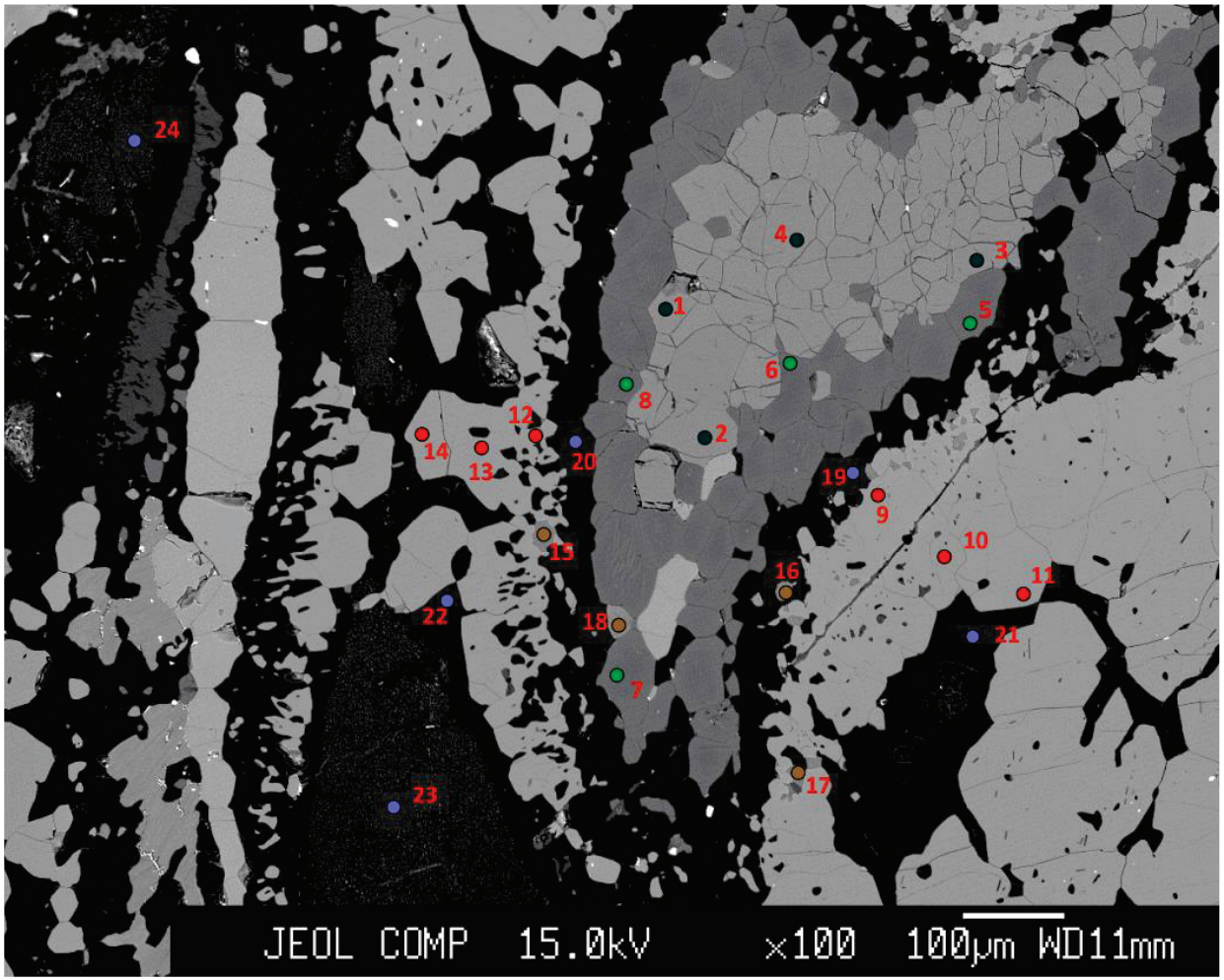

BSE Image of GC14-057, Key Harbour

SmD, EMP analysis points. Numbers below are suffix to 057_1_

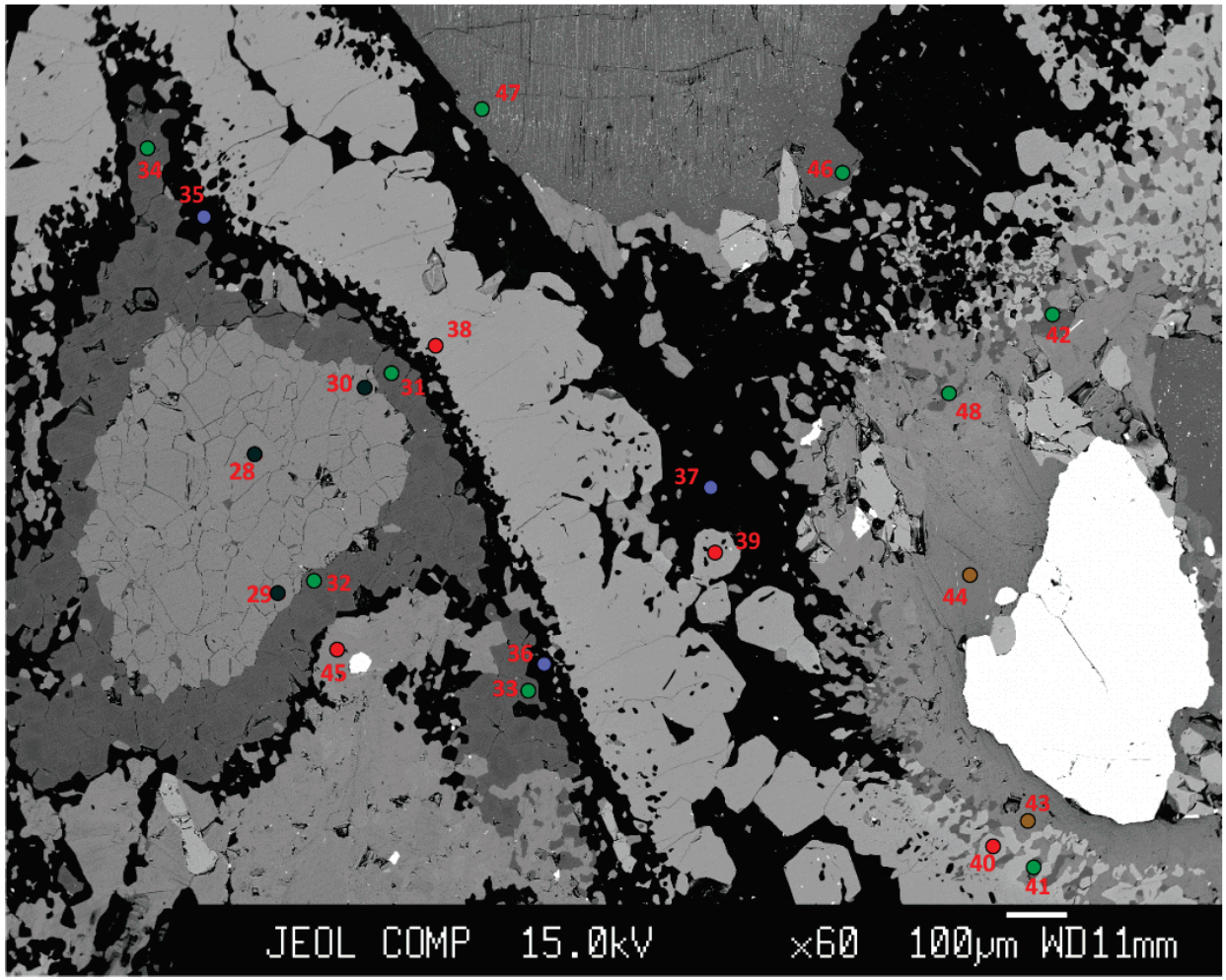

Electron Microprobe Data : GC14-024, Byng Inlet

GC14-024 : Garnet

Analysis	024C_1_18	024C_1_19	024C_1_20	024C_1_21	024C_1_22	024C_1_23	024C_2_44	024C_2_51	024C_2_52	024C_2_53	024C_2_54	024C_2_55
Oxide (wt%)												
SiO_2	36.78	36.86	36.91	36.58	37.04	36.83	36.72	36.52	36.82	36.80	36.75	36.61
TiO_2	0.07	0.01	0.05	0.05	0.03	0.01	0.18	0.11	0.08	0.09	0.09	0.09
Al_2O_3	20.59	20.55	20.81	20.65	20.85	20.69	20.33	20.98	20.93	20.59	20.62	20.55
Cr_2O_3	0.00	0.01	0.00	0.02	0.01	0.02	0.00	0.01	0.02	0.03	0.03	0.00
FeO	29.99	29.82	30.39	30.31	30.32	29.62	31.76	30.66	30.70	30.77	30.67	30.50
MnO	1.61	1.50	1.64	1.61	1.53	1.46	1.84	1.59	1.60	1.60	1.61	1.59
MgO	3.11	3.18	3.28	2.80	3.81	3.49	2.88	2.89	3.03	2.80	2.75	3.08
CaO	6.82	6.84	6.28	6.87	5.74	6.69	5.62	6.91	6.66	6.94	7.03	6.75
BaO	0.00	0.01	0.04	0.03	0.01	0.00	0.01	0.00	0.07	0.05	0.06	0.09
Na_2O	0.01	0.00	0.01	0.00	0.01	0.01	0.02	0.02	0.00	0.00	0.00	0.00
K_2O	0.05	0.03	0.02	0.02	0.01	0.02	0.05	0.02	0.04	0.04	0.04	0.02
ZrO_2	0.00	0.00	0.05	0.00	0.00	0.03	0.05	0.00	0.00	0.00	0.00	0.00
Total	99.03	98.82	99.47	98.95	99.35	98.86	99.46	99.71	99.95	99.71	99.65	99.28
Cations p.f.u (O = 12)												
Si	2.972	2.981	2.969	2.965	2.974	2.972	2.974	2.940	2.954	2.965	2.963	2.960
Ti	0.005	0.001	0.004	0.004	0.001	0.000	0.011	0.006	0.005	0.005	0.006	0.006
Al	1.961	1.960	1.973	1.973	1.973	1.968	1.940	1.991	1.980	1.956	1.960	1.958
Cr	0.000	0.001	0.000	0.001	0.001	0.001	0.000	0.000	0.001	0.002	0.002	0.000
Fe	2.027	2.017	2.045	2.054	2.035	1.999	2.150	2.065	2.060	2.074	2.069	2.063
Mn	0.110	0.103	0.112	0.110	0.104	0.100	0.126	0.108	0.109	0.109	0.110	0.109
Mg	0.374	0.383	0.394	0.338	0.456	0.420	0.348	0.347	0.362	0.337	0.330	0.371
Ca	0.590	0.593	0.541	0.596	0.493	0.578	0.488	0.596	0.572	0.599	0.607	0.584
Ba	0.000	0.000	0.001	0.001	0.000	0.000	0.000	0.000	0.002	0.001	0.001	0.002
Na	0.002	0.000	0.001	0.000	0.001	0.001	0.002	0.002	0.000	0.000	0.000	0.000
K	0.005	0.004	0.002	0.001	0.001	0.002	0.005	0.002	0.004	0.004	0.004	0.002
Zr	0.000	0.000	0.002	0.000	0.000	0.001	0.002	0.000	0.000	0.000	0.000	0.000
Total	8.048	8.042	8.044	8.045	8.040	8.045	8.048	8.059	8.051	8.053	8.053	8.058

GC14-024 : Garnet cont.

Analysis	024C_2_56	024C_2_57	024C_2_58
Oxide (wt%)			
SiO_2	36.56	36.77	36.54
TiO_2	0.09	0.06	0.12
Al_2O_3	20.71	20.72	20.71
Cr_2O_3	0.01	0.04	0.01
FeO	30.78	31.02	30.70
MnO	1.65	1.55	1.51
MgO	2.66	3.47	3.09
CaO	6.95	6.02	6.61
BaO	0.05	0.18	0.07
Na_2O	0.02	0.02	0.01
K_2O	0.03	0.04	0.04
ZrO_2	0.02	0.01	0.03
Total	99.53	99.88	99.45
Cations p.f.u (O = 12)			
Si	2.954	2.956	2.950
Ti	0.006	0.004	0.007
Al	1.973	1.963	1.970
Cr	0.001	0.002	0.001
Fe	2.080	2.084	2.074
Mn	0.113	0.106	0.103
Mg	0.320	0.415	0.372
Ca	0.602	0.518	0.571
Ba	0.001	0.006	0.002
Na	0.004	0.002	0.002
K	0.004	0.004	0.004
Zr	0.000	0.000	0.001
Total	8.058	8.062	8.058

GC14-024 : Plagioclase

Analysis	024C_1_24	024C_1_25	024C_1_26	024C_1_27	024C_1_28	024C_1_29	024C_2_66	024C_2_67	024C_2_68	024C_2_69
Oxide (wt%)										
SiO_2	64.57	65.02	64.88	65.13	65.14	64.47	64.46	64.43	64.84	64.08
TiO_2	0.00	0.00	0.00	0.00	0.00	0.00	0.00	0.00	0.00	0.00
Al_2O_3	21.41	21.71	21.85	21.65	21.49	21.86	21.62	21.90	21.81	22.07
Cr_2O_3	0.00	0.00	0.00	0.00	0.00	0.00	0.00	0.00	0.00	0.00
FeO	0.61	0.09	0.56	0.51	0.47	0.58	0.95	0.76	0.49	0.39
MnO	0.00	0.00	0.00	0.00	0.00	0.00	0.00	0.01	0.00	0.00
MgO	0.00	0.00	0.00	0.00	0.00	0.04	0.07	0.00	0.00	0.01
CaO	2.60	2.61	2.93	2.60	2.64	3.05	2.82	2.83	2.49	3.20
BaO	0.00	0.00	0.00	0.00	0.00	0.00	0.00	0.00	0.00	0.00
Na_2O	10.00	10.43	10.21	10.74	10.41	9.94	10.12	10.20	10.44	10.21
K_2O	0.33	0.33	0.34	0.24	0.39	0.25	0.41	0.31	0.39	0.22
ZrO_2	0.00	0.00	0.02	0.00	0.00	0.00	0.00	0.00	0.00	0.00
Total	99.53	100.20	100.79	100.87	100.55	100.20	100.45	100.43	100.45	100.18
Cations p.f.u (O = 8)										
Si	2.866	2.864	2.850	2.858	2.866	2.846	2.847	2.842	2.855	2.833
Ti	0.000	0.000	0.000	0.000	0.000	0.000	0.000	0.000	0.000	0.000
Al	1.120	1.127	1.131	1.120	1.114	1.138	1.126	1.139	1.132	1.150
Cr	0.000	0.000	0.000	0.000	0.000	0.000	0.000	0.000	0.000	0.000
Fe	0.022	0.003	0.021	0.019	0.018	0.022	0.035	0.028	0.018	0.014
Mn	0.000	0.000	0.000	0.000	0.000	0.000	0.000	0.000	0.000	0.000
Mg	0.000	0.000	0.000	0.000	0.000	0.002	0.004	0.000	0.000	0.001
Ca	0.123	0.123	0.138	0.122	0.125	0.145	0.134	0.134	0.118	0.151
Ba	0.000	0.000	0.000	0.000	0.000	0.000	0.000	0.000	0.000	0.000
Na	0.861	0.891	0.870	0.914	0.888	0.851	0.866	0.872	0.891	0.874
K	0.019	0.018	0.019	0.014	0.022	0.014	0.023	0.018	0.022	0.012
Zr	0.000	0.000	0.001	0.000	0.000	0.000	0.000	0.000	0.000	0.000
Total	5.013	5.028	5.030	5.047	5.033	5.018	5.036	5.033	5.037	5.035

GC14-024 : Orthopyroxene

Analysis	024C_1_4	024C_1_5	024C_1_6	024C_1_7	024C_1_8	024C_1_9	024C_2_39	024C_2_40	024C_2_41	024C_2_42	024C_2_43	024C_2_45
Oxide (wt%)												
SiO_2	50.58	50.57	50.68	50.58	50.46	50.81	50.77	50.39	50.58	50.58	50.89	50.47
TiO_2	0.09	0.16	0.07	0.06	0.56	0.33	0.14	0.07	0.07	0.08	0.03	0.07
Al_2O_3	0.55	0.56	0.61	0.63	0.49	0.51	0.57	0.61	0.63	0.61	0.62	0.64
Cr_2O_3	0.04	0.05	0.06	0.06	0.05	0.06	0.01	0.01	0.00	0.00	0.00	0.00
FeO	32.76	32.77	33.13	33.06	33.00	33.05	33.10	32.67	33.02	33.44	33.75	33.25
MnO	0.49	0.53	0.47	0.51	0.48	0.54	0.49	0.46	0.46	0.48	0.54	0.50
MgO	15.49	15.17	15.32	15.33	15.38	15.35	15.29	15.63	15.50	15.29	15.23	15.19
CaO	0.60	0.55	0.52	0.60	0.46	0.53	0.45	0.55	0.49	0.56	0.55	0.51
BaO	0.07	0.00	0.00	0.08	0.03	0.02	0.00	0.01	0.00	0.00	0.04	0.00
Na_2O	0.01	0.03	0.01	0.00	0.01	0.01	0.01	0.03	0.02	0.02	0.02	0.01
K_2O	0.03	0.02	0.02	0.03	0.03	0.00	0.05	0.02	0.02	0.02	0.01	0.01
ZrO_2	0.03	0.00	0.00	0.00	0.02	0.05	0.00	0.02	0.02	0.02	0.02	0.06
Total	100.74	100.41	100.89	100.92	100.98	101.24	100.88	100.45	100.80	101.09	101.70	100.71
Cations p.f.u (O = 6)												
Si	1.972	1.976	1.973	1.970	1.964	1.971	1.976	1.968	1.970	1.969	1.970	1.970
Ti	0.003	0.005	0.002	0.002	0.017	0.010	0.004	0.002	0.002	0.002	0.001	0.002
Al	0.025	0.026	0.028	0.029	0.022	0.023	0.026	0.028	0.029	0.028	0.028	0.029
Cr	0.001	0.001	0.002	0.002	0.002	0.002	0.001	0.000	0.000	0.000	0.000	0.000
Fe	1.068	1.071	1.078	1.077	1.074	1.072	1.078	1.067	1.076	1.088	1.093	1.085
Mn	0.016	0.017	0.016	0.017	0.016	0.017	0.016	0.015	0.015	0.016	0.017	0.017
Mg	0.899	0.884	0.889	0.890	0.892	0.887	0.887	0.910	0.900	0.887	0.879	0.884
Ca	0.025	0.023	0.022	0.025	0.019	0.022	0.019	0.023	0.020	0.023	0.023	0.021
Ba	0.001	0.000	0.000	0.001	0.001	0.000	0.000	0.000	0.000	0.000	0.001	0.000
Na	0.001	0.002	0.001	0.000	0.001	0.001	0.001	0.002	0.002	0.002	0.002	0.001
K	0.001	0.001	0.001	0.001	0.001	0.000	0.002	0.001	0.001	0.001	0.001	0.001
Zr	0.001	0.000	0.000	0.000	0.001	0.001	0.000	0.001	0.001	0.001	0.001	0.001
Total	4.014	4.007	4.011	4.013	4.009	4.006	4.009	4.016	4.015	4.017	4.015	4.012

GC14-024 : Clinopyroxene

Analysis	024C_1_1	024C_1_2	024C_1_3	024C_1_30	024C_1_31	024C_1_32	024C_1_33	024C_1_34	024C_1_35	024C_2_36	024C_2_37	024C_2_38
Oxide (wt%)												
SiO_2	51.22	51.43	51.35	51.73	52.00	51.05	52.08	51.63	51.63	51.68	51.54	51.43
TiO_2	0.18	0.22	0.31	0.22	0.21	0.23	0.17	0.29	0.23	0.27	0.26	0.29
Al_2O_3	2.85	2.35	3.72	2.37	2.27	3.02	1.86	2.81	3.12	3.65	3.33	3.49
Cr_2O_3	0.03	0.04	0.03	0.03	0.01	0.01	0.00	0.00	0.00	0.00	0.00	0.00
FeO	13.52	13.30	13.71	13.74	13.55	13.50	13.18	13.46	13.19	13.90	13.62	15.98
MnO	0.20	0.17	0.22	0.20	0.17	0.16	0.19	0.16	0.19	0.21	0.20	0.25
MgO	10.49	10.99	9.82	10.73	10.59	10.19	11.04	10.58	10.38	9.85	10.20	10.32
CaO	20.77	21.27	19.81	20.87	21.14	19.95	21.68	20.89	20.17	19.35	20.04	17.80
BaO	0.00	0.00	0.00	0.00	0.00	0.00	0.00	0.04	0.00	0.00	0.00	0.00
Na_2O	1.49	1.32	2.02	1.49	1.49	1.64	1.17	1.52	1.80	1.93	1.77	1.80
K_2O	0.01	0.01	0.01	0.02	0.04	0.05	0.04	0.05	0.05	0.00	0.04	0.01
ZrO_2	0.00	0.00	0.10	0.00	0.00	0.01	0.00	0.05	0.01	0.15	0.07	0.12
Total	100.74	101.08	101.09	101.39	101.47	99.80	101.42	101.47	100.77	101.00	101.08	101.50
Cations p.f.u (O = 6)												
Si	1.938	1.939	1.934	1.946	1.953	1.946	1.956	1.939	1.946	1.945	1.940	1.936
Ti	0.005	0.007	0.009	0.006	0.006	0.007	0.005	0.008	0.007	0.008	0.007	0.008
Al	0.127	0.104	0.165	0.105	0.100	0.136	0.083	0.124	0.139	0.162	0.148	0.155
Cr	0.001	0.001	0.001	0.001	0.001	0.000	0.000	0.000	0.000	0.000	0.000	0.000
Fe	0.428	0.419	0.431	0.432	0.425	0.430	0.414	0.422	0.416	0.437	0.428	0.503
Mn	0.007	0.005	0.007	0.006	0.005	0.005	0.006	0.005	0.006	0.007	0.007	0.008
Mg	0.592	0.618	0.551	0.602	0.593	0.578	0.618	0.592	0.583	0.553	0.572	0.579
Ca	0.842	0.859	0.799	0.841	0.851	0.815	0.872	0.841	0.815	0.780	0.808	0.718
Ba	0.000	0.000	0.000	0.000	0.000	0.000	0.000	0.001	0.000	0.000	0.000	0.000
Na	0.110	0.096	0.147	0.109	0.109	0.121	0.085	0.110	0.131	0.141	0.130	0.132
K	0.001	0.000	0.001	0.001	0.002	0.002	0.002	0.002	0.002	0.000	0.002	0.001
Zr	0.000	0.000	0.002	0.000	0.000	0.000	0.000	0.001	0.000	0.003	0.001	0.002
Total	4.049	4.049	4.047	4.049	4.045	4.040	4.041	4.046	4.045	4.035	4.043	4.043

GC14-024 : Clinopyroxene cont.

Analysis	024C_2_46	024C_2_47	024C_2_48	024C_2_49	024C_2_50
Oxide (wt%)					
SiO_2	51.59	51.52	51.49	51.33	51.27
TiO_2	0.18	0.54	0.19	0.20	0.25
Al_2O_3	3.03	3.27	2.82	2.52	2.58
Cr_2O_3	0.00	0.00	0.00	0.00	0.00
FeO	13.89	14.10	13.84	13.91	13.66
MnO	0.19	0.22	0.25	0.24	0.19
MgO	10.46	10.04	10.42	10.52	10.51
CaO	20.40	19.52	20.17	20.75	20.47
BaO	0.00	0.00	0.00	0.00	0.00
Na_2O	1.48	2.02	1.70	1.55	1.63
K_2O	0.01	0.02	0.01	0.01	0.04
ZrO_2	0.02	0.06	0.00	0.04	0.01
Total	101.24	101.29	100.89	101.08	100.61
Cations p.f.u (O = 6)					
Si	1.941	1.938	1.945	1.940	1.943
Ti	0.005	0.016	0.005	0.005	0.007
Al	0.134	0.145	0.125	0.112	0.115
Cr	0.000	0.000	0.000	0.000	0.000
Fe	0.437	0.443	0.437	0.440	0.433
Mn	0.006	0.007	0.008	0.008	0.006
Mg	0.587	0.563	0.587	0.593	0.594
Ca	0.823	0.787	0.817	0.841	0.832
Ba	0.000	0.000	0.000	0.000	0.000
Na	0.108	0.147	0.124	0.114	0.120
K	0.001	0.001	0.001	0.001	0.002
Zr	0.000	0.001	0.000	0.001	0.000
Total	4.041	4.048	4.049	4.054	4.052

GC14-024 : Biotite

Analysis	024C_1_10	024C_1_11	024C_1_12	024C_1_13	024C_2_62	024C_2_63	024C_2_64	024C_2_65
Oxide (wt%)								
SiO_2	35.70	35.63	35.73	35.47	35.74	35.51	35.02	35.63
TiO_2	6.74	6.47	6.56	6.50	6.44	6.29	6.40	6.35
Al_2O_3	13.75	13.81	13.78	13.97	14.02	13.98	13.72	13.90
Cr_2O_3	0.04	0.04	0.05	0.05	0.00	0.01	0.00	0.02
FeO	21.87	22.16	21.93	21.92	21.82	21.62	21.55	21.79
MnO	0.07	0.05	0.07	0.07	0.05	0.03	0.03	0.07
MgO	9.47	9.27	9.49	9.47	9.72	9.87	9.59	9.59
CaO	0.03	0.02	0.04	0.02	0.01	0.02	0.03	0.04
BaO	0.85	0.86	0.69	0.96	0.76	0.87	0.82	0.83
Na_2O	0.07	0.18	0.18	0.14	0.11	0.08	0.22	0.09
K_2O	9.62	9.29	9.39	9.57	9.42	9.70	8.89	9.18
ZrO_2	0.00	0.00	0.00	0.00	0.00	0.00	0.01	0.00
Total	98.22	97.77	97.91	98.13	98.09	97.98	96.28	97.49
Cations p.f.u (O = 22)								
Si	5.419	5.432	5.430	5.397	5.416	5.401	5.405	5.432
Ti	0.770	0.741	0.750	0.744	0.735	0.719	0.744	0.728
Al	2.462	2.482	2.468	2.506	2.504	2.506	2.495	2.497
Cr	0.004	0.004	0.004	0.007	0.000	0.002	0.000	0.002
Fe	2.776	2.825	2.787	2.787	2.765	2.750	2.783	2.779
Mn	0.009	0.007	0.009	0.009	0.007	0.004	0.004	0.009
Mg	2.143	2.105	2.149	2.147	2.196	2.237	2.207	2.178
Ca	0.004	0.004	0.007	0.004	0.002	0.004	0.004	0.007
Ba	0.051	0.051	0.042	0.057	0.044	0.051	0.051	0.051
Na	0.020	0.051	0.055	0.042	0.033	0.022	0.066	0.026
K	1.863	1.806	1.819	1.857	1.822	1.883	1.749	1.784
Zr	0.000	0.000	0.000	0.000	0.000	0.000	0.000	0.000
Total	15.521	15.508	15.521	15.556	15.523	15.580	15.508	15.492

GC14-024 : Amphibole

Analysis	024C_1_14	024C_1_15	024C_1_16	024C_1_17	024C_2_59	024C_2_60	024C_2_61
Oxide (wt%)							
SiO_2	40.74	40.77	40.15	40.57	40.50	40.20	40.61
TiO_2	2.94	3.03	3.13	2.90	3.14	3.26	3.14
Al_2O_3	11.92	11.73	11.83	11.78	11.82	11.97	11.59
Cr_2O_3	0.03	0.02	0.00	0.00	0.02	0.00	0.00
FeO	19.62	19.77	19.40	19.79	19.69	19.79	19.60
MnO	0.12	0.12	0.09	0.08	0.13	0.11	0.11
MgO	8.16	8.10	8.03	8.21	8.22	8.07	8.19
CaO	11.09	11.26	10.89	11.06	11.19	11.16	11.16
BaO	0.00	0.00	0.00	0.00	0.03	0.04	0.06
Na_2O	2.85	2.75	2.82	2.75	2.89	2.80	2.84
K_2O	1.46	1.44	1.39	1.41	1.39	1.42	1.35
ZrO_2	0.04	0.03	0.04	0.02	0.02	0.00	0.02
Total	98.96	99.02	97.77	98.57	99.02	98.80	98.66
Cations p.f.u (O = 23)							
Si	6.194	6.201	6.176	6.194	6.162	6.134	6.196
Ti	0.336	0.347	0.363	0.334	0.359	0.375	0.361
Al	2.137	2.102	2.146	2.121	2.118	2.153	2.084
Cr	0.002	0.002	0.000	0.000	0.002	0.000	0.000
Fe	2.493	2.514	2.496	2.528	2.505	2.525	2.500
Mn	0.016	0.014	0.012	0.012	0.016	0.014	0.014
Mg	1.849	1.835	1.842	1.868	1.863	1.835	1.863
Ca	1.808	1.835	1.796	1.810	1.824	1.824	1.826
Ba	0.000	0.000	0.000	0.000	0.002	0.002	0.005
Na	0.840	0.812	0.842	0.812	0.851	0.828	0.842
K	0.283	0.278	0.271	0.274	0.271	0.276	0.262
Zr	0.002	0.002	0.002	0.002	0.000	0.000	0.002
Total	15.960	15.944	15.946	15.953	15.974	15.967	15.955

BSE Image of GC14-024, Byng Inlet

SmD, EMP analysis points. Numbers below are suffix to 024_1_

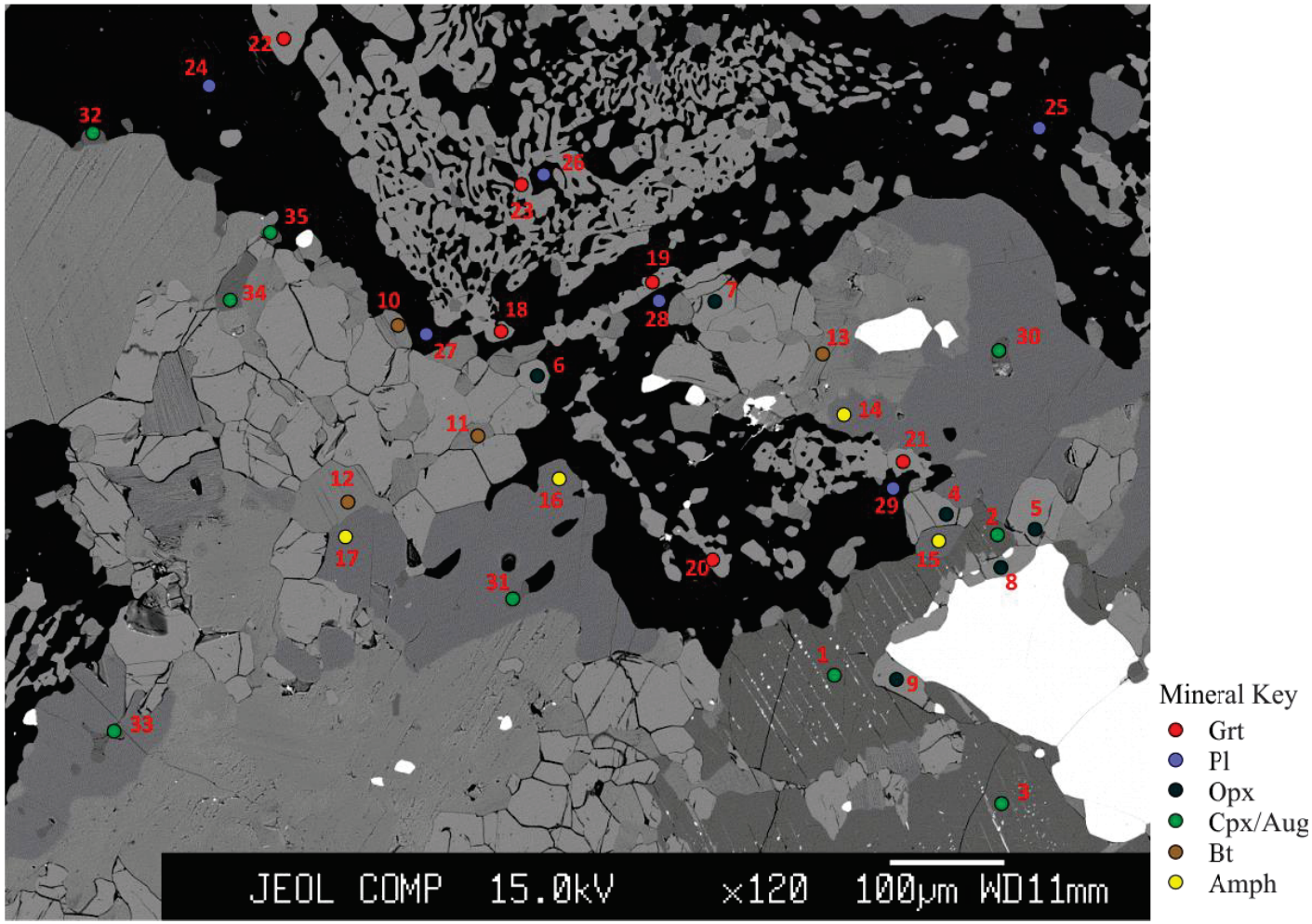

BSE Image of GC14-024, Byng Inlet

SmD, EMP analysis points. Numbers below are suffix to 024C_2_

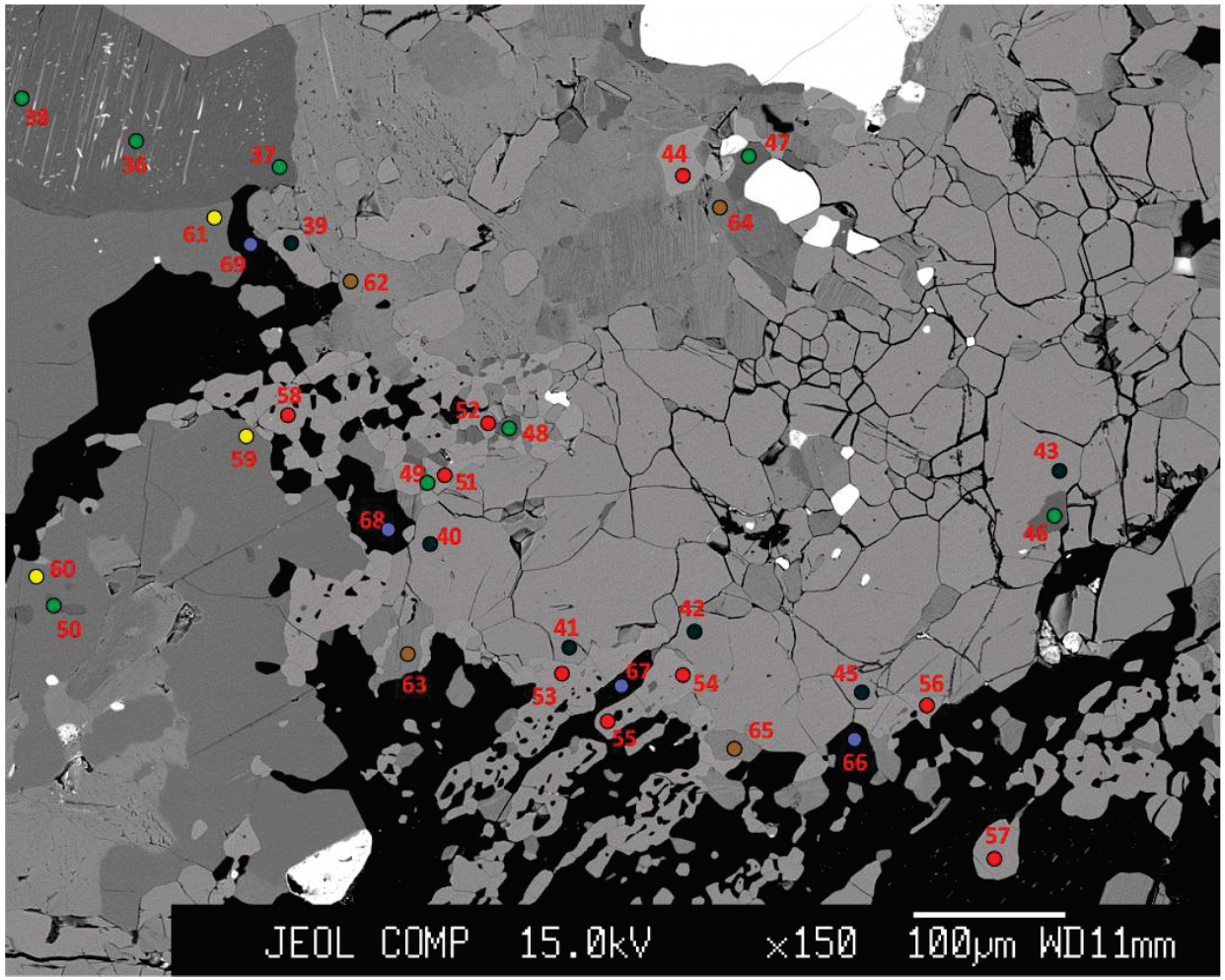

Mineral Key
- Grt
- Pl
- Opx
- Cpx/Aug
- Bt
- Amph

Electron Microprobe Data : GC14-048, Point au Baril

GC14-048 : Garnet

Analysis	048_1_9	048_1_10	048_1_11	048_1_12	048_1_13	048_2_25	048_2_26	048_2_27	048_2_28	048_2_29
Oxide (wt%)										
SiO_2	39.22	39.24	39.17	38.81	39.13	39.10	38.95	39.39	39.32	39.07
TiO_2	0.05	0.06	0.08	0.11	0.04	0.07	0.21	0.08	0.06	0.11
Al_2O_3	22.15	22.21	22.06	21.57	22.03	22.29	22.01	22.20	22.12	21.91
Cr_2O_3	0.00	0.00	0.00	0.02	0.00	0.03	0.10	0.04	0.05	0.04
FeO	26.07	25.43	26.19	25.13	26.06	25.40	27.85	25.42	26.71	27.45
MnO	0.60	0.56	0.64	0.60	0.60	0.63	0.69	0.61	0.60	0.67
MgO	7.22	7.25	6.79	7.43	6.95	7.15	6.04	7.25	7.49	6.23
CaO	6.07	6.37	6.15	5.77	6.05	6.74	6.12	6.79	5.86	6.13
BaO	0.06	0.00	0.05	0.05	0.08	0.02	0.02	0.02	0.07	0.01
Na_2O	0.00	0.00	0.00	0.01	0.00	0.00	0.00	0.00	0.00	0.00
K_2O	0.03	0.03	0.03	0.02	0.03	0.02	0.09	0.01	0.03	0.07
Total	101.49	101.14	101.15	99.50	100.95	101.46	102.06	101.81	102.31	101.70
Cations p.f.u (O = 12)										
Si	2.992	2.995	3.000	3.010	3.001	2.981	2.982	2.990	2.982	2.995
Ti	0.004	0.004	0.005	0.006	0.002	0.004	0.012	0.005	0.004	0.006
Al	1.992	1.998	1.992	1.972	1.992	2.003	1.986	1.986	1.978	1.980
Cr	0.000	0.000	0.000	0.001	0.000	0.002	0.006	0.002	0.004	0.002
Fe	1.663	1.622	1.678	1.630	1.672	1.620	1.783	1.614	1.694	1.760
Mn	0.038	0.036	0.041	0.040	0.040	0.041	0.044	0.040	0.038	0.043
Mg	0.821	0.826	0.775	0.859	0.794	0.812	0.689	0.821	0.846	0.713
Ca	0.497	0.521	0.505	0.479	0.497	0.550	0.503	0.552	0.476	0.504
Ba	0.002	0.000	0.001	0.001	0.002	0.001	0.000	0.000	0.002	0.000
Na	0.000	0.000	0.000	0.001	0.000	0.000	0.000	0.000	0.000	0.000
K	0.002	0.002	0.002	0.002	0.002	0.002	0.008	0.001	0.002	0.006
Total	8.011	8.005	7.999	8.002	8.003	8.016	8.014	8.012	8.027	8.011

GC14-048 : Plagioclase

Analysis	048_1_14	048_1_15	048_1_16	048_1_17	048_2_37	048_2_38	048_2_39	048_2_40	048_2_41
Oxide (wt%)									
SiO_2	63.12	59.77	63.29	59.31	59.06	63.38	63.51	63.04	60.83
TiO_2	0.12	0.00	0.00	0.00	0.00	0.00	0.00	0.25	0.00
Al_2O_3	22.65	25.66	22.91	25.97	25.77	23.17	22.94	22.98	24.43
Cr_2O_3	0.00	0.00	0.00	0.00	0.00	0.00	0.00	0.00	0.00
FeO	0.20	0.35	0.37	0.35	0.13	0.24	0.28	0.60	0.12
MnO	0.00	0.00	0.00	0.00	0.00	0.00	0.00	0.00	0.00
MgO	0.00	0.00	0.00	0.00	0.00	0.00	0.00	0.00	0.00
CaO	3.94	7.20	4.15	7.48	7.45	4.36	4.07	4.15	5.96
BaO	0.00	0.00	0.00	0.00	0.00	0.00	0.00	0.00	0.00
Na_2O	9.11	7.53	9.03	7.28	7.32	9.00	9.12	8.98	8.06
K_2O	0.30	0.19	0.23	0.21	0.20	0.24	0.26	0.32	0.21
Total	99.44	100.71	99.98	100.58	99.93	100.40	100.18	100.31	99.62
Cations p.f.u (O = 8)									
Si	2.807	2.651	2.802	2.636	2.639	2.794	2.804	2.787	2.714
Ti	0.004	0.000	0.000	0.000	0.000	0.000	0.000	0.008	0.000
Al	1.187	1.342	1.195	1.360	1.358	1.204	1.194	1.198	1.285
Cr	0.000	0.000	0.000	0.000	0.000	0.000	0.000	0.000	0.000
Fe	0.007	0.013	0.014	0.013	0.005	0.009	0.010	0.022	0.005
Mn	0.000	0.000	0.000	0.000	0.000	0.000	0.000	0.000	0.000
Mg	0.000	0.000	0.000	0.000	0.000	0.000	0.000	0.000	0.000
Ca	0.187	0.342	0.197	0.356	0.357	0.206	0.193	0.197	0.285
Ba	0.000	0.000	0.000	0.000	0.000	0.000	0.000	0.000	0.000
Na	0.786	0.648	0.775	0.627	0.634	0.770	0.781	0.770	0.698
K	0.017	0.010	0.013	0.012	0.011	0.014	0.015	0.018	0.012
Total	4.995	5.007	4.995	5.005	5.004	4.996	4.997	5.001	4.998

GC14-048 : Clinopyroxene

Analysis	048_1_1	048_1_2	048_1_3	048_1_4	048_1_8	048_2_20	048_2_21	048_2_22	048_2_24
Oxide (wt%)									
SiO_2	53.37	52.56	52.16	52.48	51.86	53.24	52.25	52.29	53.26
TiO_2	0.24	0.39	0.41	0.44	0.36	0.26	0.46	0.33	0.21
Al_2O_3	4.18	6.26	5.85	6.76	4.16	3.75	5.21	5.26	2.78
Cr_2O_3	0.00	0.00	0.00	0.00	0.00	0.01	0.02	0.02	0.03
FeO	7.86	7.32	7.62	7.16	7.53	7.75	7.74	7.76	8.93
MnO	0.07	0.06	0.06	0.08	0.08	0.10	0.09	0.08	0.10
MgO	12.51	11.52	11.77	11.26	12.78	12.95	12.20	12.40	13.26
CaO	19.79	19.69	20.03	19.02	21.67	21.33	20.63	20.51	20.52
BaO	0.02	0.00	0.01	0.00	0.04	0.00	0.00	0.00	0.00
Na_2O	2.18	2.50	2.25	2.90	1.40	1.62	1.99	1.89	1.64
K_2O	0.02	0.02	0.01	0.02	0.02	0.02	0.03	0.03	0.02
Total	100.23	100.32	100.18	100.12	99.90	101.04	100.60	100.57	100.75
Cations p.f.u (O = 6)									
Si	1.963	1.927	1.921	1.925	1.925	1.950	1.921	1.922	1.964
Ti	0.007	0.011	0.011	0.012	0.010	0.007	0.013	0.009	0.005
Al	0.181	0.271	0.254	0.292	0.182	0.162	0.226	0.228	0.121
Cr	0.000	0.000	0.000	0.000	0.000	0.001	0.001	0.001	0.001
Fe	0.242	0.224	0.235	0.220	0.234	0.238	0.238	0.238	0.275
Mn	0.002	0.002	0.002	0.002	0.002	0.003	0.002	0.002	0.003
Mg	0.686	0.629	0.646	0.616	0.707	0.707	0.668	0.679	0.729
Ca	0.780	0.773	0.791	0.748	0.862	0.837	0.812	0.808	0.811
Ba	0.000	0.000	0.000	0.000	0.001	0.000	0.000	0.000	0.000
Na	0.155	0.178	0.161	0.206	0.101	0.115	0.142	0.135	0.117
K	0.001	0.001	0.001	0.001	0.001	0.001	0.001	0.002	0.001
Total	4.018	4.016	4.022	4.021	4.025	4.021	4.024	4.024	4.028

GC14-048 : Biotite

Analysis	048_1_6	048_2_32	048_2_33	048_2_34	048_2_35	048_2_36	048_2_43
Oxide (wt%)							
SiO_2	36.39	36.84	36.83	39.11	37.13	36.96	37.34
TiO_2	6.52	5.36	6.36	4.77	5.63	5.35	5.20
Al_2O_3	14.32	14.62	14.29	12.76	14.33	14.95	14.48
Cr_2O_3	0.00	0.06	0.04	0.00	0.04	0.02	0.00
FeO	13.74	13.24	14.18	13.62	13.92	12.65	13.90
MnO	0.01	0.02	0.02	0.03	0.03	0.02	0.00
MgO	13.71	14.38	13.81	15.40	14.56	15.41	13.74
CaO	0.10	0.05	0.21	1.63	0.05	0.01	0.26
BaO	0.89	0.67	0.84	0.55	0.59	0.59	0.79
Na_2O	0.11	0.06	0.15	0.17	0.16	0.18	0.28
K_2O	9.23	9.63	9.31	8.22	9.46	9.44	8.88
Total	95.01	94.94	96.05	96.25	95.91	95.58	94.87
Cations p.f.u (O = 22)							
Si	5.474	5.524	5.489	5.749	5.522	5.478	5.597
Ti	0.737	0.605	0.713	0.528	0.629	0.596	0.585
Al	2.539	2.585	2.510	2.209	2.512	2.611	2.559
Cr	0.000	0.007	0.004	0.000	0.004	0.002	0.000
Fe	1.727	1.661	1.767	1.674	1.731	1.569	1.742
Mn	0.002	0.002	0.002	0.004	0.002	0.002	0.000
Mg	3.073	3.214	3.067	3.375	3.227	3.406	3.071
Ca	0.018	0.009	0.033	0.255	0.007	0.002	0.042
Ba	0.053	0.040	0.048	0.031	0.035	0.033	0.046
Na	0.033	0.018	0.044	0.048	0.046	0.051	0.081
K	1.771	1.841	1.771	1.540	1.795	1.786	1.698
Total	15.426	15.508	15.448	15.413	15.514	15.539	15.422

GC14-048 : Amphibole

Analysis	048_1_5	048_1_7	048_2_23	048_2_31	048_2_42
Oxide (wt%)					
SiO_2	41.33	41.93	45.95	41.86	41.54
TiO_2	3.13	3.38	0.21	3.06	3.29
Al_2O_3	13.07	12.73	3.46	13.48	12.66
Cr_2O_3	0.00	0.00	0.03	0.07	0.00
FeO	12.65	12.65	8.13	12.04	13.46
MnO	0.04	0.01	0.06	0.05	0.04
MgO	11.82	11.73	13.00	12.07	10.90
CaO	11.54	11.62	20.13	11.61	11.53
BaO	0.00	0.00	0.00	0.03	0.02
Na_2O	2.56	2.66	0.91	2.72	2.52
K_2O	1.34	1.27	0.11	1.27	1.30
Total	97.48	97.98	91.99	98.25	97.24
Cations p.f.u (O = 23)					
Si	6.157	6.208	7.183	6.164	6.222
Ti	0.352	0.375	0.023	0.338	0.370
Al	2.295	2.222	0.637	2.339	2.233
Cr	0.000	0.000	0.005	0.009	0.000
Fe	1.576	1.566	1.063	1.481	1.686
Mn	0.005	0.002	0.007	0.007	0.005
Mg	2.627	2.590	3.029	2.650	2.433
Ca	1.842	1.842	3.372	1.831	1.852
Ba	0.000	0.000	0.000	0.002	0.002
Na	0.738	0.764	0.276	0.777	0.731
K	0.255	0.242	0.023	0.239	0.248
Total	15.847	15.810	15.617	15.840	15.785

GC14-048 : Spinel

Analysis	048_1_18	048_1_19
Oxide (wt%)		
SiO_2	3.22	2.58
TiO_2	0.05	0.07
Al_2O_3	58.55	58.74
Cr_2O_3	0.00	0.00
FeO	28.99	29.03
MnO	0.07	0.07
MgO	8.47	8.61
CaO	0.33	0.29
BaO	0.04	0.02
Na_2O	0.49	0.35
K_2O	0.05	0.05
Total	100.25	99.81
Cations p.f.u (O = 4)		
Si	0.087	0.070
Ti	0.001	0.002
Al	1.867	1.884
Cr	0.000	0.000
Fe	0.656	0.661
Mn	0.002	0.002
Mg	0.342	0.349
Ca	0.010	0.008
Ba	0.000	0.000
Na	0.026	0.018
K	0.002	0.002
Total	2.992	2.997

BSE Image of GC14-048, Point au Baril

SmD, EMP analysis points. Numbers below are suffix to 048_1_

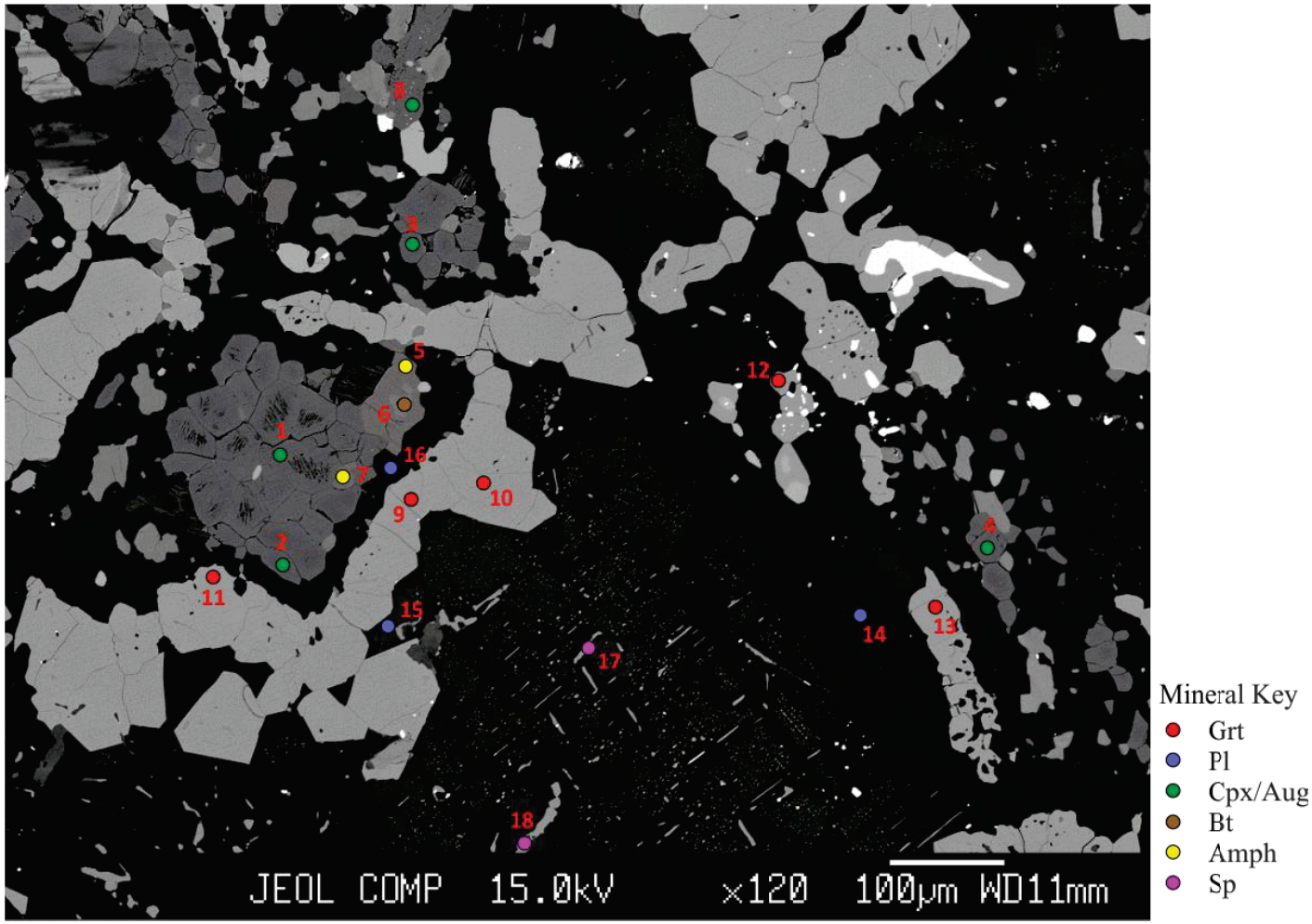

BSE Image of GC14-048, Point au Baril

SmD, EMP analysis points. Numbers below are suffix to 048_2_

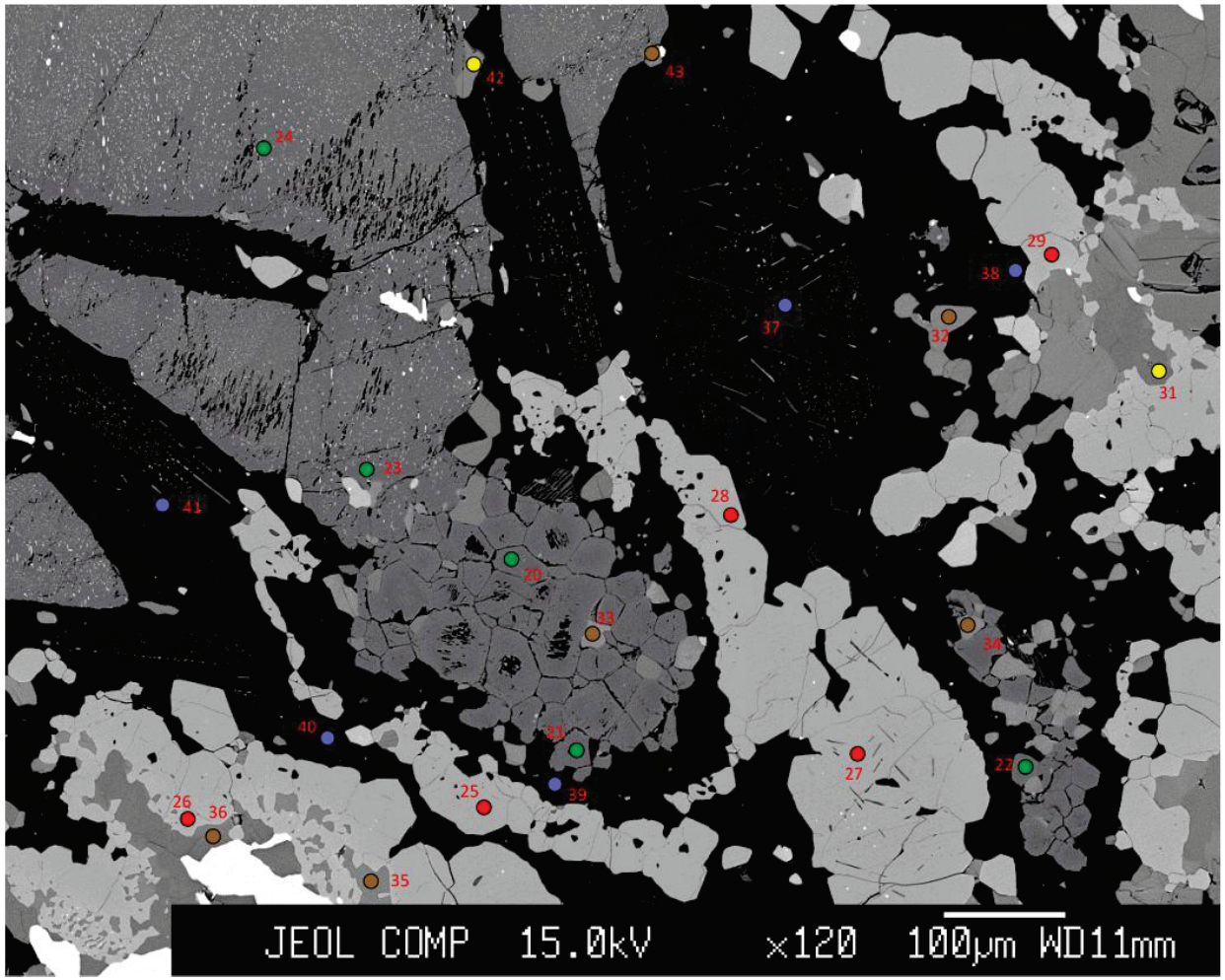

Appendix D. LA-ICP-MS U-Pb Isotopic Data, Uncorrected for Pb_c

Sample	Isotopic Ratios (uncorrected) Concordia (Wetherill) $^{207}Pb/^{235}U$	± 2σ abs.	$^{206}Pb/^{238}U$	± 2σ abs.	Error Correl.	Inv. concordia (Tera-Wasserburg) $^{238}U/^{206}Pb$	± 2σ abs.	$^{207}Pb/^{206}Pb$	± 2σ abs.
GC14-057: Key Harbour									
GC14-057C - 9	2.220	0.230	0.171	0.008	0.360	5.85	0.26	0.092	0.009
GC14-057C - 8	3.860	0.460	0.167	0.007	0.410	6.00	0.24	0.164	0.017
GC14-057C - 7	2.490	0.190	0.170	0.009	0.496	5.89	0.30	0.104	0.007
GC14-057C - 6	2.140	0.140	0.172	0.006	0.195	5.81	0.19	0.089	0.006
GC14-057C - 5	2.430	0.140	0.180	0.005	0.185	5.57	0.16	0.097	0.006
GC14-057C - 4	4.500	0.270	0.190	0.007	0.269	5.27	0.20	0.173	0.010
GC14-057C - 3	2.340	0.230	0.176	0.006	0.460	5.70	0.20	0.095	0.008
GC14-057C - 2	2.190	0.120	0.175	0.005	0.188	5.70	0.17	0.092	0.005
GC14-057C - 15	2.400	0.140	0.177	0.005	0.325	5.64	0.17	0.097	0.005
GC14-057C - 13	2.550	0.130	0.193	0.005	0.070	5.19	0.14	0.095	0.005
GC14-057C - 12	3.660	0.260	0.180	0.007	0.319	5.55	0.21	0.145	0.010
GC14-057C - 11	2.280	0.150	0.175	0.005	0.257	5.70	0.17	0.093	0.006
GC14-057C - 10	2.170	0.170	0.165	0.005	0.354	6.08	0.20	0.093	0.007
GC14-057C - 1	1.880	0.170	0.153	0.006	0.418	6.54	0.26	0.092	0.007
GC14-024: Byng Inlet									
GC14-024B - 6	8.700	0.990	0.226	0.010	0.749	4.42	0.19	0.269	0.024
GC14-024C - 7	6.880	0.830	0.223	0.014	0.634	4.48	0.28	0.225	0.022
GC14-024C - 24	3.850	0.420	0.215	0.013	0.316	4.65	0.28	0.130	0.014
GC14-024C - 12	7.390	0.950	0.215	0.011	0.649	4.65	0.24	0.242	0.024
GC14-024B - 2	3.840	0.370	0.201	0.008	0.189	4.97	0.20	0.137	0.013
GC14-024B - 22	3.600	0.430	0.199	0.009	0.235	5.03	0.23	0.133	0.015
GC14-024C - 6	2.840	0.290	0.196	0.009	0.190	5.10	0.24	0.105	0.011
GC14-024C - 18	2.780	0.300	0.192	0.008	0.283	5.20	0.20	0.111	0.010
GC14-024C - 16	5.120	0.530	0.191	0.012	0.335	5.24	0.33	0.200	0.021
GC14-024C - 17	2.600	0.330	0.190	0.011	0.146	5.26	0.30	0.103	0.014
GC14-024C - 22	3.380	0.280	0.187	0.009	0.270	5.34	0.25	0.132	0.011
GC14-024C - 2	2.660	0.200	0.187	0.007	0.253	5.35	0.20	0.105	0.008
GC14-024B - 14	4.600	0.420	0.187	0.011	0.205	5.35	0.31	0.184	0.018
GC14-024B - 18	3.510	0.280	0.185	0.006	0.519	5.41	0.18	0.139	0.009
GC14-024C - 13	2.220	0.170	0.185	0.006	0.105	5.42	0.19	0.087	0.007
GC14-024B - 11	2.180	0.160	0.183	0.006	0.062	5.46	0.17	0.086	0.006
GC14-024C - 21	2.270	0.250	0.183	0.009	0.204	5.47	0.26	0.091	0.010
GC14-024C - 14	3.310	0.280	0.182	0.006	0.280	5.49	0.19	0.133	0.010
GC14-024C - 1	2.900	0.260	0.182	0.006	0.322	5.49	0.19	0.117	0.010
GC14-024C - 15	2.950	0.330	0.181	0.009	0.546	5.52	0.27	0.124	0.014
GC14-024C - 8	1.920	0.220	0.181	0.008	0.080	5.53	0.24	0.078	0.009
GC14-024B - 4	2.150	0.190	0.181	0.007	0.193	5.53	0.22	0.086	0.007
GC14-024A-Zr2 - 1	1.882	0.091	0.181	0.005	0.237	5.54	0.15	0.075	0.004
GC14-024C - 9	2.730	0.190	0.180	0.006	0.236	5.56	0.19	0.110	0.007
GC14-024A-Zr13 - 4	2.460	0.180	0.179	0.004	0.086	5.58	0.12	0.099	0.007
GC14-024B - 12	2.370	0.220	0.179	0.007	0.389	5.59	0.23	0.097	0.010
GC14-024B - 3	2.660	0.270	0.178	0.007	0.290	5.62	0.23	0.110	0.010
GC14-024B - 15	2.980	0.220	0.178	0.006	0.287	5.62	0.20	0.122	0.009
GC14-024B - 17	2.900	0.220	0.177	0.006	0.136	5.64	0.19	0.124	0.010
GC14-024A-Zr13 - 3	1.827	0.110	0.177	0.006	0.225	5.65	0.18	0.075	0.004

Sample	Isotopic Ratios (uncorrected) Concordia (Wetherill) $^{207}Pb/^{235}U$	± 2σ abs.	$^{206}Pb/^{238}U$	± 2σ abs.	Error Correl.	Inv. concordia (Tera-Wasserburg) $^{238}U/^{206}Pb$	± 2σ abs.	$^{207}Pb/^{206}Pb$	± 2σ abs.
GC14-024: Byng Inlet, cont.									
GC14-024C - 4	1.950	0.230	0.177	0.010	0.115	5.65	0.31	0.082	0.010
GC14-024C - 10	1.810	0.120	0.176	0.006	0.199	5.69	0.18	0.074	0.005
GC14-024A-Zr13 - 1	1.815	0.075	0.175	0.004	0.151	5.70	0.12	0.075	0.003
GC14-024C - 5	2.050	0.240	0.175	0.008	0.078	5.71	0.26	0.086	0.010
GC14-024C - 3	1.910	0.150	0.175	0.006	0.284	5.73	0.20	0.082	0.006
GC14-024A-Zr5 - 1	1.866	0.077	0.174	0.005	0.381	5.74	0.15	0.078	0.003
GC14-024B - 7	2.620	0.190	0.174	0.006	0.128	5.76	0.19	0.109	0.008
GC14-024B - 20	1.820	0.190	0.174	0.007	0.303	5.76	0.24	0.080	0.008
GC14-024A-Zr4 - 1	1.780	0.120	0.174	0.005	0.124	5.76	0.17	0.076	0.005
GC14-024A-Zr13 - 2	1.780	0.100	0.174	0.004	0.185	5.76	0.14	0.075	0.004
GC14-024B - 9	2.050	0.190	0.174	0.006	0.282	5.76	0.21	0.087	0.008
GC14-024A-Zr12 - 1	2.780	0.410	0.173	0.014	0.227	5.79	0.47	0.116	0.008
GC14-024B - 21	2.420	0.170	0.173	0.006	0.435	5.80	0.20	0.104	0.007
GC14-024B - 8	2.120	0.170	0.172	0.005	0.116	5.81	0.18	0.090	0.007
GC14-024B - 1	2.140	0.160	0.172	0.005	0.197	5.81	0.18	0.090	0.006
GC14-024A-Zr5 - 2	2.180	0.390	0.172	0.024	0.141	5.81	0.81	0.092	0.007
GC14-024A-Zr2 - 2	1.867	0.090	0.172	0.004	0.042	5.82	0.13	0.079	0.004
GC14-024C - 11	3.150	0.270	0.170	0.007	0.069	5.87	0.24	0.134	0.012
GC14-024B - 13	2.330	0.180	0.169	0.006	0.201	5.93	0.20	0.100	0.008
GC14-024A-Zr13 - 5	1.928	0.089	0.168	0.004	0.237	5.96	0.14	0.084	0.004
GC14-024B - 5	2.490	0.210	0.167	0.005	0.514	5.98	0.17	0.106	0.008
GC14-024B - 19	2.580	0.200	0.162	0.008	0.342	6.16	0.31	0.123	0.010
GC14-024C - 23	1.960	0.150	0.162	0.006	0.217	6.18	0.21	0.088	0.006
GC14-048: Point au Baril									
GC14-048C - 9	4.620	0.340	0.183	0.008	0.343	5.47	0.23	0.184	0.013
GC14-048C - 8	2.990	0.290	0.177	0.008	0.018	5.67	0.26	0.124	0.012
GC14-048C - 6	2.810	0.230	0.189	0.007	0.157	5.30	0.20	0.106	0.009
GC14-048C - 5	2.140	0.160	0.179	0.006	0.283	5.58	0.20	0.085	0.006
GC14-048C - 4	4.330	0.300	0.192	0.008	0.316	5.21	0.21	0.160	0.010
GC14-048C - 3	4.910	0.400	0.191	0.007	0.332	5.23	0.19	0.183	0.014
GC14-048C - 2	2.510	0.150	0.193	0.006	0.149	5.17	0.16	0.091	0.005
GC14-048C - 13	3.680	0.310	0.192	0.008	0.305	5.21	0.23	0.142	0.012
GC14-048C - 12	1.890	0.140	0.161	0.004	0.279	6.21	0.17	0.084	0.006
GC14-048C - 11	2.320	0.160	0.189	0.007	0.220	5.28	0.20	0.090	0.006
GC14-048C - 10	4.600	0.400	0.195	0.008	0.445	5.12	0.20	0.172	0.013
GC14-048C - 1	3.980	0.590	0.186	0.011	0.396	5.38	0.32	0.152	0.019
GC14-048B - 5	2.040	0.130	0.174	0.006	0.337	5.76	0.19	0.086	0.005
GC14-048B - 4	1.840	0.150	0.177	0.006	0.225	5.66	0.21	0.076	0.006
GC14-048B - 3	2.050	0.150	0.173	0.006	0.031	5.79	0.19	0.086	0.007
GC14-048B - 2	2.160	0.150	0.182	0.006	0.213	5.50	0.18	0.087	0.006
GC14-048B - 1	2.530	0.170	0.162	0.006	0.050	6.16	0.23	0.114	0.008
GC14-048A - 8	2.550	0.170	0.168	0.006	0.080	5.96	0.23	0.113	0.008
GC14-048A - 7	3.080	0.200	0.195	0.006	0.160	5.12	0.17	0.116	0.008
GC14-048A - 6	2.460	0.150	0.182	0.006	0.204	5.50	0.17	0.100	0.006
GC14-048A - 5	2.720	0.250	0.180	0.009	0.466	5.57	0.27	0.114	0.010
GC14-048A - 3	3.470	0.310	0.190	0.010	0.463	5.27	0.27	0.133	0.010